GESP-650
NASA-CR-72897

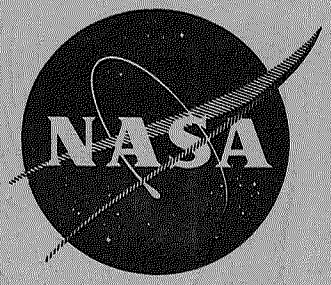

TOPICAL REPORT NO. 7
SNAP-8 REFRACTORY BOILER DEVELOPMENT PROGRAM

ANALYSIS AND TESTING OF A SINGLE TUBE MERCURY BOILER

By
Edward S. Hsia

prepared for
NATIONAL AERONAUTICS AND SPACE ADMINISTRATION

NASA Lewis Research Center
Contract NAS 3-10610
Edward R. Furman, Project Manager

September 1971

NUCLEAR SYSTEMS PROGRAMS
SPACE DIVISION
GENERAL ELECTRIC
CINCINNATI, OHIO 45215

NOTICE

This report was prepared as an account of Government sponsored work. Neither the United States, nor the National Aeronautics and Space Administration (NASA), nor any person acting on behalf of NASA:

A.) Makes any warranty or representation, expressed or implied, with respect to the accuracy, completeness, or usefulness of the information contained in this report, or that the use of any information, apparatus, method, or process disclosed in this report may not infringe privately owned rights; or

B.) Assumes any liabilities with respect to the use of, or for damages resulting from the use of any information, apparatus, method or process disclosed in this report.

As used above, "person acting on behalf of NASA" includes any employee or contractor of NASA, or employee of such contractor, to the extent that such employee or contractor of NASA, or employee of such contractor prepares, disseminates, or provides access to, any information pursuant to his employment or contract with NASA, or his employment with such contractor.

Requests for copies of this report should be referred to:

National Aeronautics and Space Administration
Scientific and Technical Information Division
Attention: USS-A
Washington, D.C. 20546

650

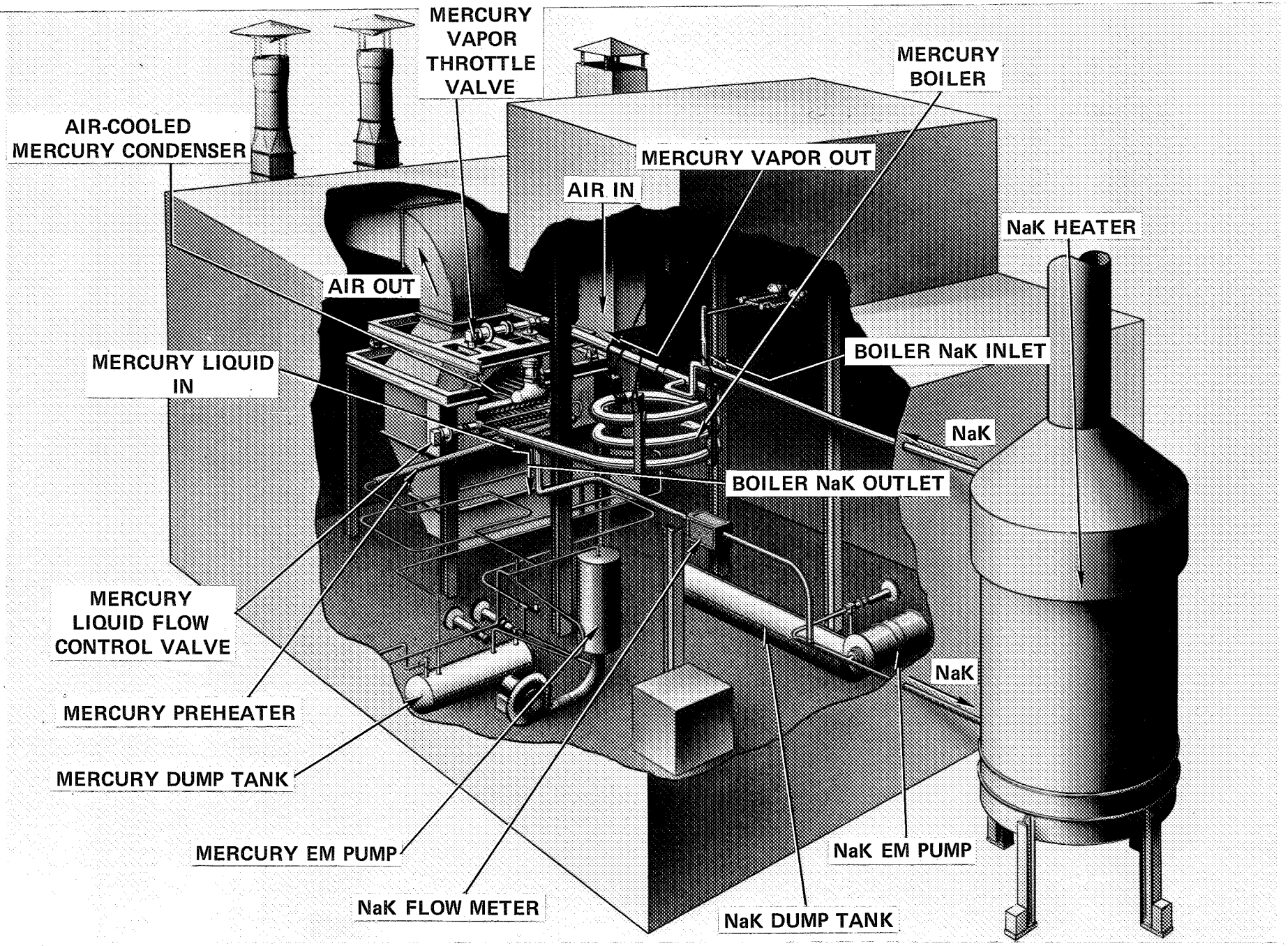

FIG. 1 90% 650

Figure 1. 500 KW SNAP-8 Refractory Boiler Test Loop Model (Single Tube Boiler Located at the Position Shown for SNAP-8 Test Boiler. (CDC11711)

Fig. 5 857 650

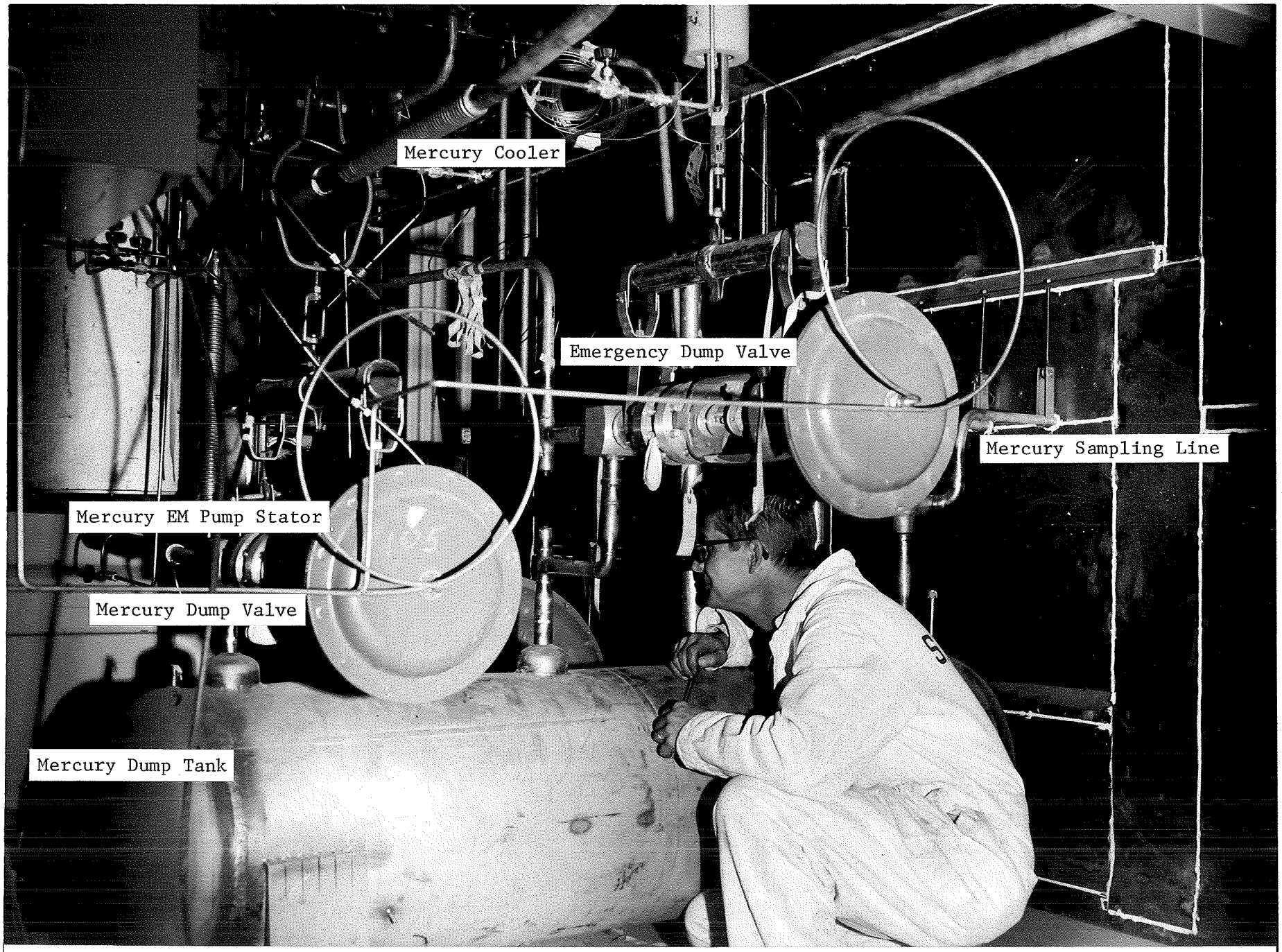

Figure 5. SNAP-8 Refractory Boiler Development Facility Showing Mercury Dump Tank, with Dump Valves, EM Pump Stator and Sampling Line. (C67112008)

857

Fig. 6 857 650

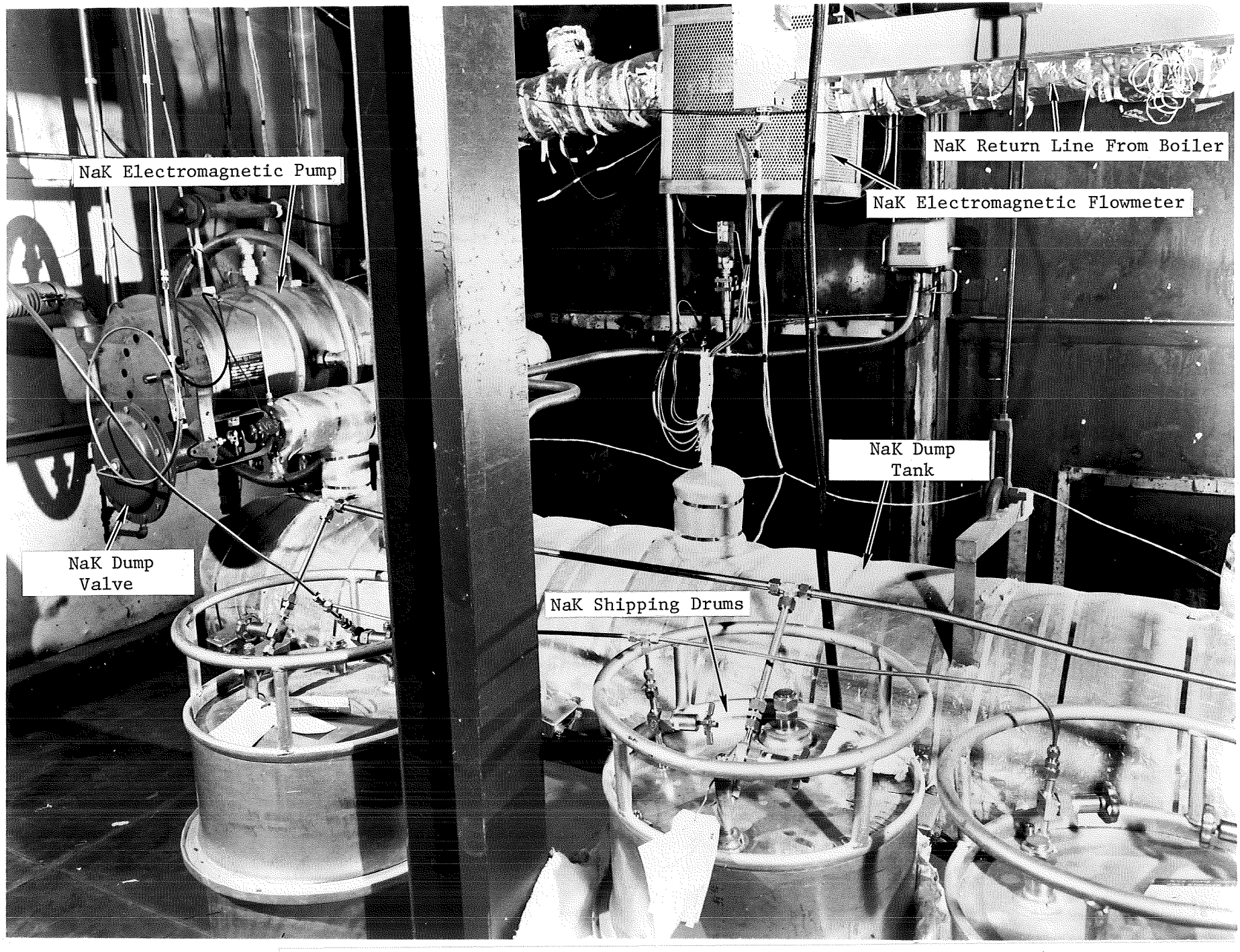

Figure 6. NaK Loop During Filling Operation. C68010411

Fig. 7 85% 650

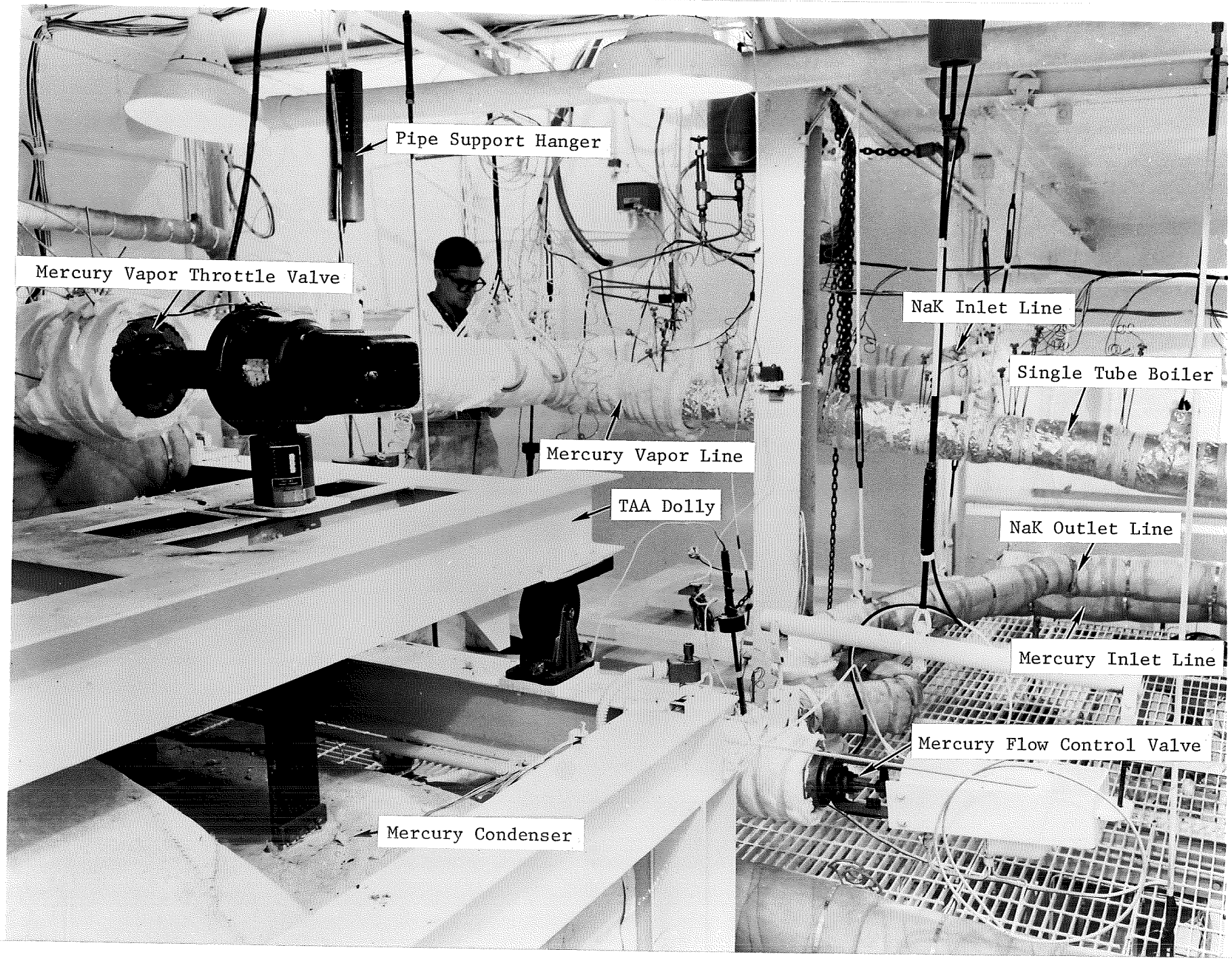

Figure 7. Photographic View of the Single Tube Test Boiler Installed in the 500 KW SNAP-8 Refractory Boiler Development Facility Loop. C68010413

Fig. 10 100% 650

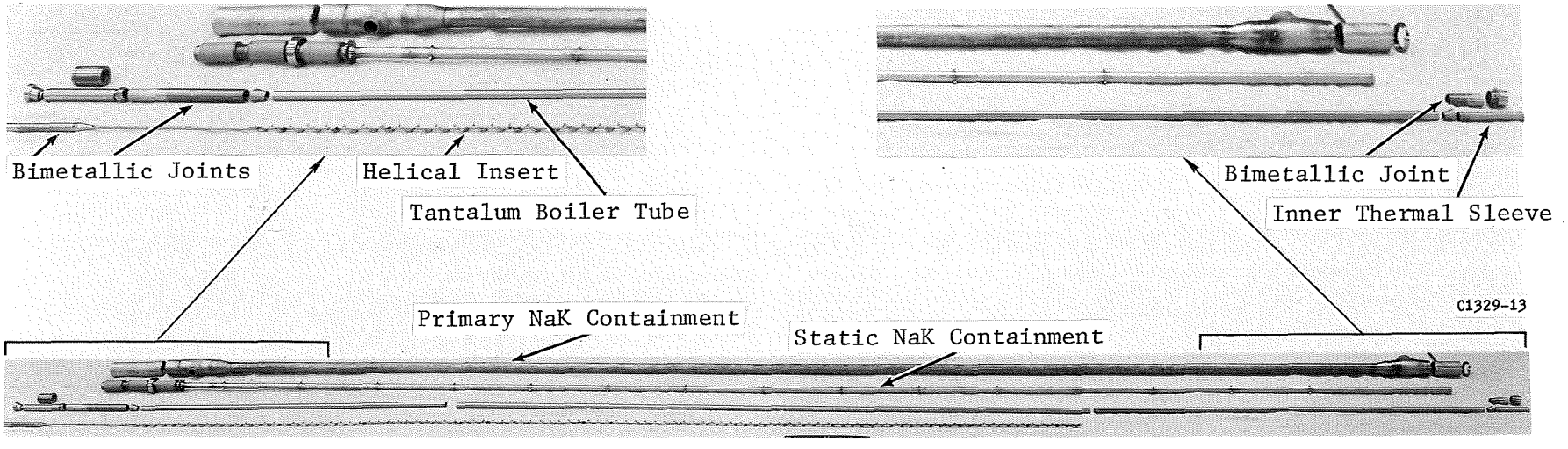

Figure 10. SNAP-8 Single Tube Test Boiler. C68011583

FIG. 11 100% 650

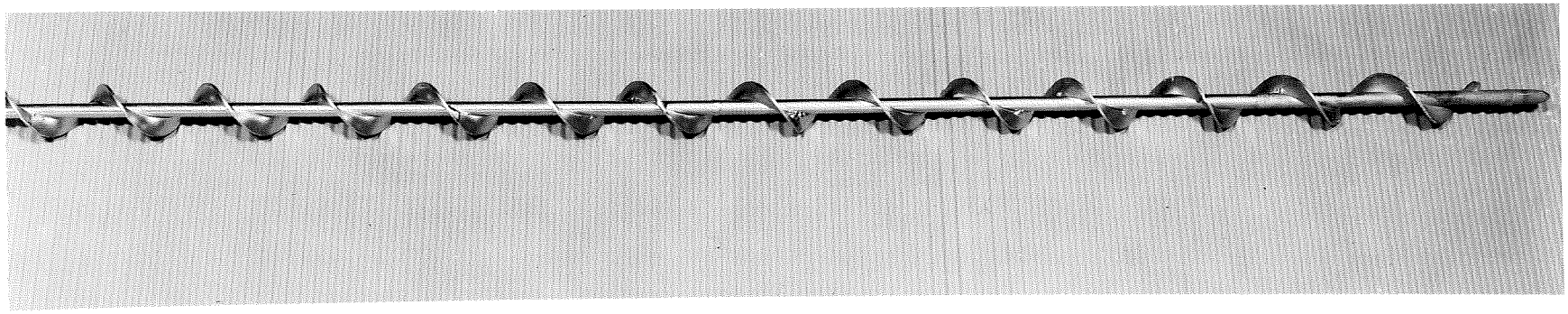

Figure 11. Helical Insert P/D 2.0, 1/4 - Inch Center Body. (C68011582)

C68011582

Fig. 12 85% 650

Figure 12. Photographic View of the Test Section Inlet Portion (Exposed Before Insulation). C67120770

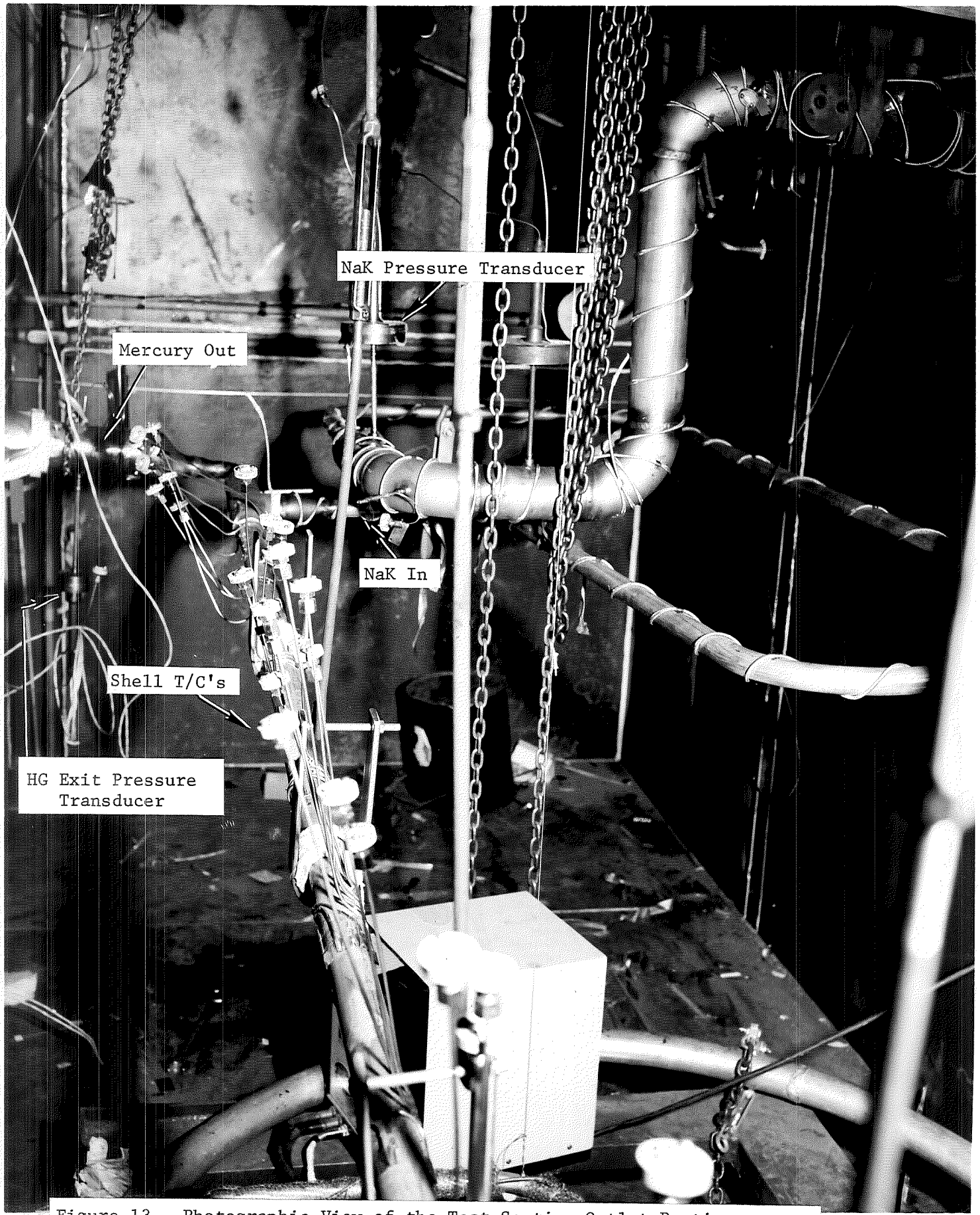

Figure 13. Photographic View of the Test Section Outlet Portion. (Exposed Before Insulation). C67120768

FIG. 13 850.

650

106

TOPICAL REPORT NO. 7

SNAP-8 REFRACTORY BOILER DEVELOPMENT PROGRAM

ANALYSIS AND TESTING OF A SINGLE TUBE MERCURY BOILER

prepared by

E. S. Hsia

approved by

R. D. Brooks

NUCLEAR SYSTEMS PROGRAMS
SPACE DIVISION
GENERAL ELECTRIC COMPANY
Cincinnati, Ohio 45215

September 1971

prepared for

NATIONAL AERONAUTICS AND SPACE ADMINISTRATION

NASA Lewis Research Center
Contract NAS 3-10610
Edward R. Furman, Project Manager

TABLE OF CONTENTS

FOREWORD

The work described in this report is part of the SNAP-8 Refractory Metal Boiler Development Program, NASA Contract NAS 3-10610, conducted by the General Electric Company. The work was done under the technical management of R.D. Brooks of the General Electric Company and E. R. Furman of the Lewis Research Center, NASA.

Principal technical contribution to the single tube mercury boiling program, within the General Electric Company, was done by the following individuals: Dr. J.R. Peterson, Manager of Heat Transfer Engineering, provided constant guidance and helpful discussions in the heat transfer analysis; Mr. R.A. Fuller contributed the testing of the boiler and the design of the mercury helical EM pump; Mr. J.L. Pride made the data reduction computer program; and Mr. W.H. Bennethum helped in the loop instrumentations.

ABSTRACT

The results of an experimental investigation of heat transfer and fluid flow during forced convection boiling of wetted mercury in a single tantalum tube with composite vortex generator insert are presented. The experiments were conducted with a NaK-heated and highly-instrumented test section at mercury saturation temperature up to 1130°F. Exploratory local two-phase forced convection boiling results for mercury are presented for nucleate boiling, the critical heat flux condition, transition boiling and superheated vapor regions in a once-through boiling process. The experimental data and the associated correlations are directly applicable for the design and optimization of once-through boilers for Space Power Rankine Cycle Systems employing mercury as the working fluid.

LIST OF ILLUSTRATIONS

LIST OF ILLUSTRATIONS (Cont'd)

LIST OF ILLUSTRATIONS (Cont'd)

LIST OF ILLUSTRATIONS (Cont'd)

LIST OF ILLUSTRATIONS (Cont'd)

LIST OF ILLUSTRATIONS (Cont'd)

LIST OF TABLES

NOMENCLATURE

Symbols		Units
A	Area	ft^2
A_R	Radial Acceleration	g's
C_p	Constant Pressure Heat Capacity	$Btu/lb_m-°F$
D	Diameter	ft
d	Diameter of Liquid Droplet or Wire Coil	ft
E	Fraction of Entrained Liquid	--
f	Darcy-Weisbach Friction Factor	--
G	Mass Velocity	$lb_m/sec-ft^2$
g_c	Gravitational Conversion Factor	32.2 $ft-lb_m/sec^2-lb_f$
h	Heat Transfer Coefficient	$Btu/hr-ft^2-°F$
h_{LV}	Latent Heat of Vaporization	Btu/lb_m
J	Energy Conversion Factor	$778-ft-lb_m/Btu$
K	Slip Ratio	--
k	Thermal Conductivity	Btu/hr-ft-°f
K_h	Heat Transfer Parameter for Helical Flow	--
K_p	Pressure Drop Parameter for Helical Flow	--
L	Boiler Tube Length	ft
n	Number of Liquid Droplets per Unit Area	$(ft^2)^{-1}$
N_{Nu}	Nusselt Number, $\frac{hD}{k}$	--
N_{Pe}	Peclet Number, $\frac{DGC_P}{k}$	--
N_{Pr}	Prandtl Number $\frac{\mu C_P}{k}$	--
N_{Re}	Reynolds Number $\frac{DG}{\mu}$	--
P	Pressure	psia
P/D	Insert Twist Ratio	--
Q	Rate of Heat Transfer	Btu/sec

Symbols		Units
q''	Heat Flux	$Btu/hr-ft^2$
T	Temperature	°F
U	Overall Heat Transfer Coefficient	$Btu/hr-ft^2-°F$
V	Velocity	ft/sec
x	Flowing Quality	--
z	Distance Along Boiler Tube from Mercury Inlet	ft
α	Void Fraction	--
Δ	Difference	--
ϵ_m	Eddy Diffusion for Momentun	ft^2/hr
θ	Elevation Angle	degree
μ	Dynamic Viscosity	$lb_m/ft-hr$
ν	Kinematic Viscosity	ft^2/hr
ρ	Density	lb_m/ft^3
$\overline{\phi}$	Integrated Two-Phase Frictional Pressure Drop Multiplier	--
Ω	Entrainment Parameter Defined in Equation (46)	--
ϕ	Local Two-Phase Frictional Pressure Drop Multiplier	--

Subscripts

a	Axial
B	Boiler or Boiling
b	Bulk Fluid Temperature
BN	Bubble Nucleation
c	Refers to Critical Heat Flux Condition
cb	Refers to Insert Centerbody
cw	Refers to Combined Wall
e	Equivalent or exit or elevation

Subscripts

exp	Experimental Results
f	Frictional Pressure Drop
FE	Refers to Film Evaporation
H	Refers to Helical Flow Condition or Homogeneous Model
Hg	Mercury Flow in Tube
HV	Helical Vane Insert
i	Inside or Inlet
IB	Refers to Boiling Inception Point
IS	Refers to Superheat Inception Point
L	Refers to Liquid Phase
LB	Refers to Liquid Boiling
m	Momentum Pressure Drop
M	Martinelli-Nelson Pressure Drop Model
NaK	NaK-78 Flow in Shell
NB	Refers to Nucleate Boiling Region
o	Outside or Outlet
PB	Refers to Pool Boiling
s	Shell
Sat	Refers to Saturation Condition
sc	Refers to Subcooled Heating Region
SH	Refers to Vapor Superheating Region or Degree of Superheat
SP	Single Phase
ss	Stainless Steel
t,T	Tube or Total
ta	Tantalum

Subscripts

TB	Refers to Transition Boiling Region
TP	Two-Phase
V	Refers to Vapor Phase
w	Tube Wall
wc	Wire Coil Insert
x	Evaluated at Local Quality Condition

Superscripts

$\overline{\quad}$	Averaged Value

I. INTRODUCTION

The once-through boiler holds promise of being highly suitable for liquid metal Rankine Cycle Power Systems. In a typical high-performance version of this concept, liquid enters the boiler at subcooled conditions, where it is heated to boiling temperature, boiled to dry saturated vapor conditions, and then heated to superheated vapor for discharge to the turbine - all in one continuous pass through the boiler. The boiler tube usually contains vortex generator inserts to promote boiling stability and to increase heat transfer performance. Heating of the boiler is provided by a liquid metal reactor coolant. The SNAP-8 Rankine Cycle conversion system has been under development by NASA-LRC since 1963. Mercury is used as the working fluid whereas the energy source is provided by a nuclear reactor coolant, NaK.

In the development of a once-through boiler for the SNAP-8 system, major problems encountered have been mercury and NaK incompatibility with the containment material and the unpredictable thermal and hydraulic performance [1] [2]. In the fall of 1966, NASA-LRC recognized the necessity of changing the boiler tube material and selected tantalum as the new mercury-containment material due to its high resistance to mercury corrosion. The second problem of understanding the nature of boiling mercury in a once-through boiler with vortex generator inserts was not explored until late 1967. Early in 1967, a series of tests were

conducted at the General Electric Company on mercury-tantalum systems to explore the thermal wettability of mercury in contact with tantalum surfaces. An important result [3] of these tests was the high degree of wettability of tantalum exhibited by mercury at elevated temperatures. In addition, the results indicated that once wetting had been obtained, the mercury did not become nonwetting upon cooling in the absence of air. These initial findings were later verified independently by contact angle measurements conducted by Geoscience, Ltd.[4]. Results in Reference (4) indicate that at temperatures greater than 1000°F the contact angle between mercury and tantalum approaches zero (perfect wetting).

Based upon these early findings in 1967, a decision was made to design a single tube tantalum mercury boiler by using the heat transfer and two-phase pressure drop relationships for a wetting fluid. These relationships[5] [6] were developed under NASA contracts 3-2528 and 3-9426 for high temperature potassium, a highly wetting fluid.

Double containment using static NaK as a barrier between the shell side primary NaK flow and the tube side mercury was employed. The static NaK was located in the annulus between an outer stainless steel tube and an inner tantalum tube, with mercury flowing inside the tantalum tube. A composite vortex generator insert, consisting of helical vane and wire coil sections, was positioned inside the boiler tube to increase the heat transfer capacity.

Earlier SNAP-8 boiler designs were based upon nonwetting mercury heat transfer relations[11] and resulted in boiler tube lengths of 30-feet for the SNAP-8 system requirements. The use of wetting heat transfer

relations in the thermal design calculations for the single tube boiler resulted in the selection of a shorter 16-foot tube length for the same system operating conditions.

During the end of 1967 and early in 1968, the single tube mercury boiler was designed, fabricated and successfully tested in the 550 KW capacity liquid metal facility located at the Evendale Plant. Boiler operation included 326 hours of testing and three restart cycles. No deterioration in performance was observed within the specified SNAP-8 power system operating ranges. A large amount of test data was accumulated and subsequently analyzed to explore the heat transfer and pressure loss characteristics for the once-through boiling of mercury inside a tantalum tube with vortex generators.

Detailed descriptions of the single tube boiler assembly, test apparatus and instrumentation are presented in subsequent sections. Local and overall boiling heat transfer results and their correlations are presented for all 16 planned test runs. Individual heat transfer regions, designated as subcooled liquid, nucleate boiling, transition boiling and superheated vapor, were identified from the NaK and mercury temperature profiles established by a large number of calibrated thermocouples installed on both the shell external surface and inside the boiler insert. Local and overall pressure losses and their correlations for boiling mercury are also presented and compared with established predictions. Local two-phase pressure loss gradients, local pressure loss multipliers, and pressure losses for superheated mercury vapor in the wire coil section of the insert were thoroughly analyzed and correlated. Two existing two-phase pressure loss

correlations, the Martinelli model and homogeneous model, are compared with the experimental two-phase pressure loss results.

Performance testing was also accomplished by varying the operating conditions over the expected operating band for the SNAP-8 system to obtain off-design information. Three hundred and twenty-six hours of performance testing and three restart cycles were achieved without any deterioration in performance in the single tube mercury boiling experiment. Accurate temperature profiles of both shell side NaK flow and tube side mercury flow and a large amount of test data were secured and subsequently analyzed. The experimental heat transfer and pressure drop results of boiling mercury are presented in the subsequent chapters.

Complete tabulations of the local and overall heat transfer and pressure losses obtained from the present test are given in the appendix. The ranges of operation for all 326 hours of test and three restart cycles are listed as follows:

Mercury Flow Rate	700 to 1700 lb/hr
NaK Flow Rate	6800 to 7350 lb/hr
Mercury Exit Temperature	1290 to 1335°F
NaK Inlet Temperature	1292 to 1350°F
Mercury Exit Pressure	75 to 267 psia
Mercury Saturation Temperature	975 to 1130°F
Degree of Vapor Superheat	205 to 390°F
Thermal Power	36 to 75 KW

II. TEST APPARATUS

A. Description of the Test Loop

The NaK-mercury test facility employed in the experiment is shown schematically in Figure (1) . The entire facility was constructed of Type 316 stainless steel except the tantalum boiler tube, the L-605 NaK dump tank and the L-605 mercury vapor line. As shown in the figure, the NaK primary loop of the facility, which simulates the reactor coolant loop of an actual SNAP-8 power conversion system, accepted heat from a 550 KW gas fired furnace and rejected heat to boiling mercury in the secondary loop. A reversible helical induction EM pump was used in the single phase primary loop and the NaK flow rate was determined with an electromagnetic flowmeter. The NaK level in the dump tank was indicated by a level probe and was controlled by inert gas pressurization. Mercury flowing in the secondary loop was boiled and superheated inside the tantalum test boiler and was condensed in an air-cooled, finned-tube condenser. An adjustable vapor throttle valve positioned downstream of the boiler was employed to maintain both boiler exit and condenser inlet pressures at the proper system values. The valve normally operated in a choked mode. A valved mercury dump tank connected to the loop downstream of the condenser. The liquid mercury flowed through a helical induction EM pump, a venturi flowmeter and finally a liquid throttle valve upon its return to the test section from the dump tank. The mercury vapor

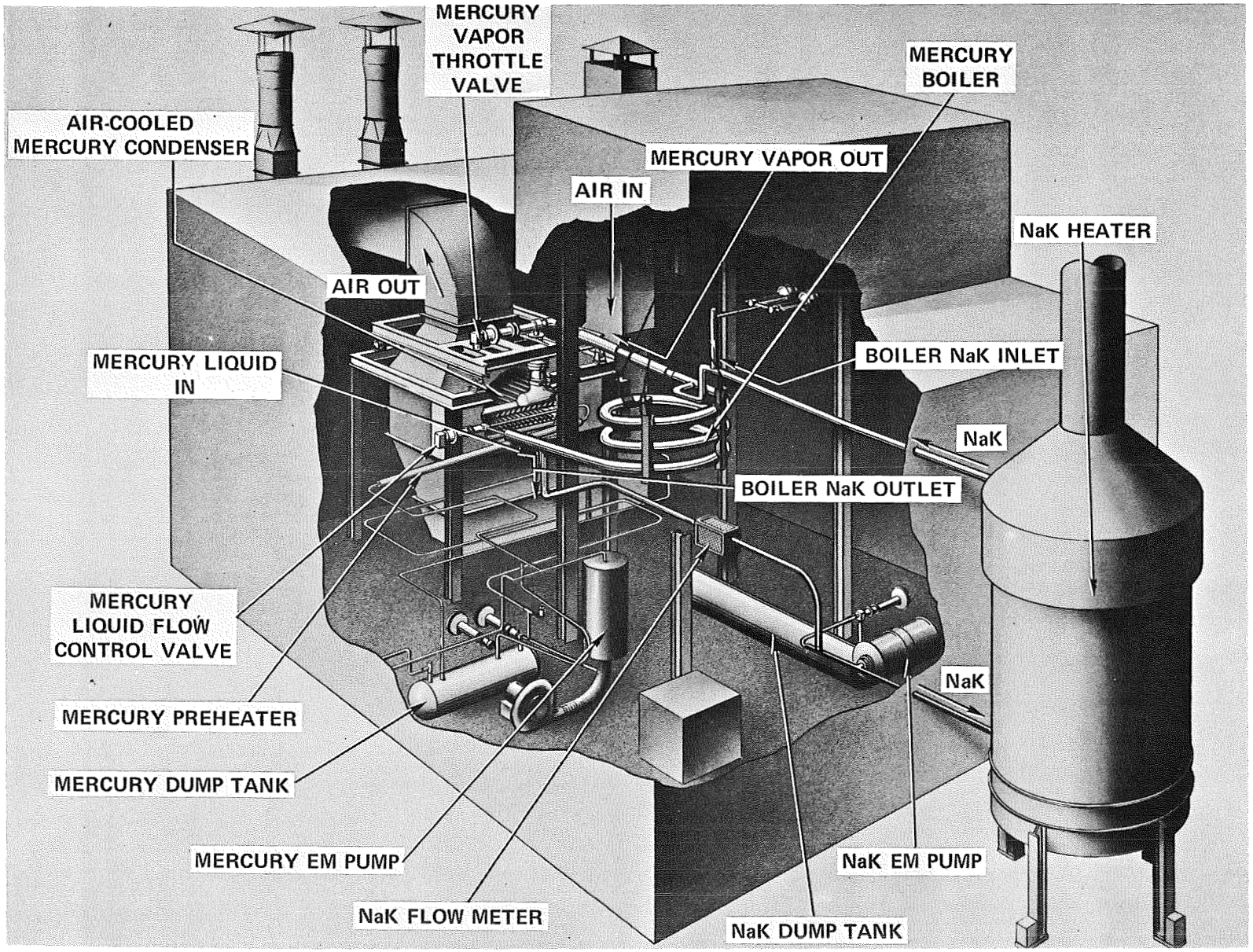

Figure 1. 500 KW SNAP-8 Refractory Boiler Test Loop Model (Single Tube Boiler Located at the Position Shown for SNAP-8 Test Boiler. (CDC11711)

line was a 3 1/2-inch O.D. Haynes-25 seamless pipe. Since the mercury was superheated vapor and the Haynes-25 was chosen for its availability and high strength. The vapor throttle valve was also made of Haynes-25 alloy.

The three-stage mercury helical induction EM pump as shown schematically in Figure (2) was designed, fabricated and tested. The pump consisted essentially of a polyphase stator, a pump duct made up of two concentric tubes with spiral passages in the annulus and suitable enclosing and supporting framework. As shown in Figure (3), testing of the mercury EM pump using a three-stage pump and a 15-inch-long stator, indicated, at the design point, using approximately 560 volts would provide 560 psi developed head at the SNAP-8 system design flow rate of 12,500 lb/hr. No difficulties whatsoever were encountered in the operation of the helical induction pumps for pumping liquid mercury.

The gas-fired furnace employed as the prime heat source is shown schematically in Figure (4). The furnace was designed for a nominal heat load of 550 KW at a NaK exit temperature of 1350°F. The heater shell was air-tight and the flue was valved so that NaK fumes could be contained in the event of a leak. An alternate vent line to a scrubber system insured that no caustic fumes would be released to the atmosphere.

Type 316 stainless steel was selected as the material of construction for the air-cooled, finned-tube mercury condenser. This selection was based on the welding and post-weld annealing

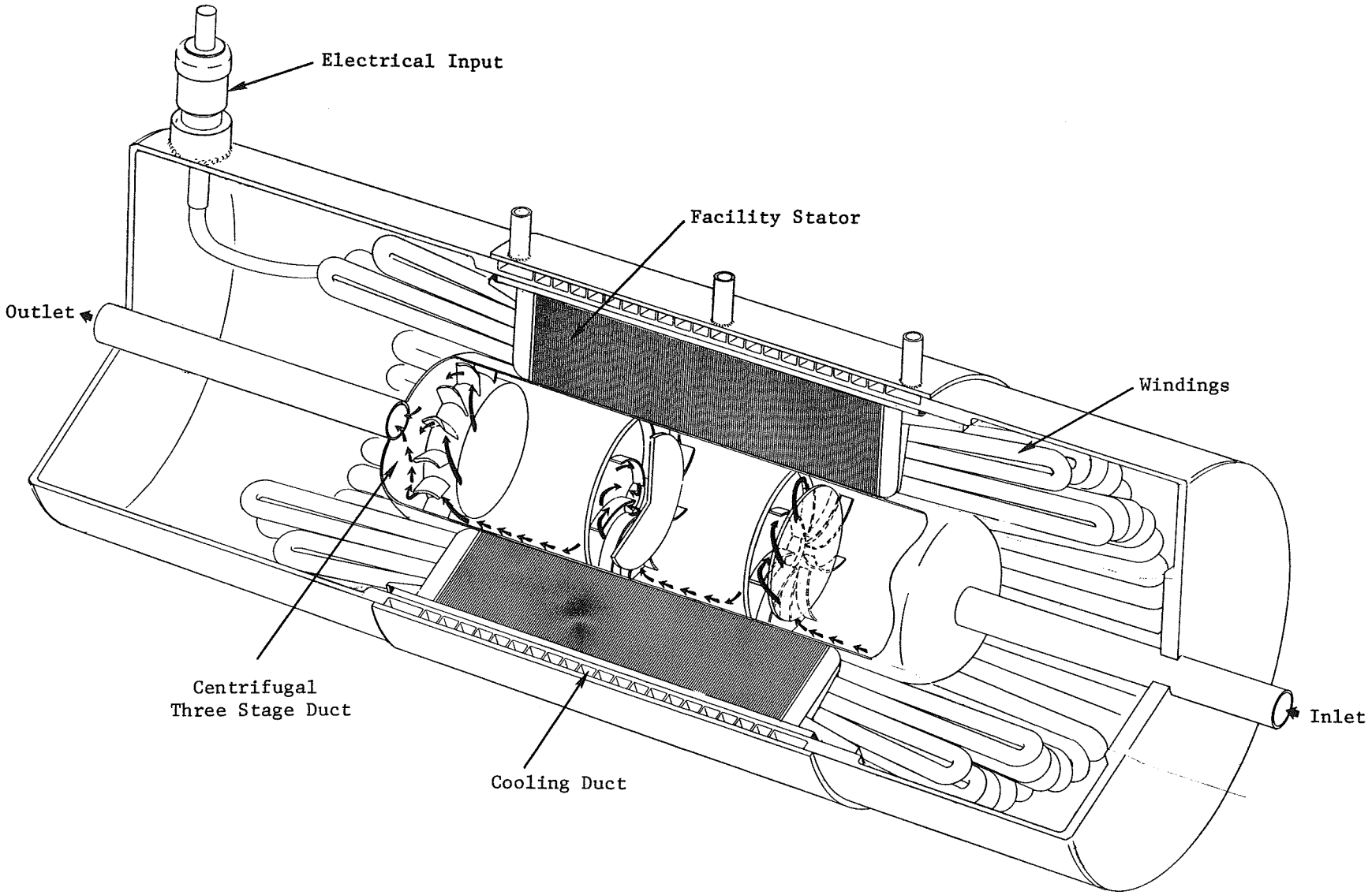

Figure 2. Three-Stage Mercury Helical Induction EM Pump.

AS-873

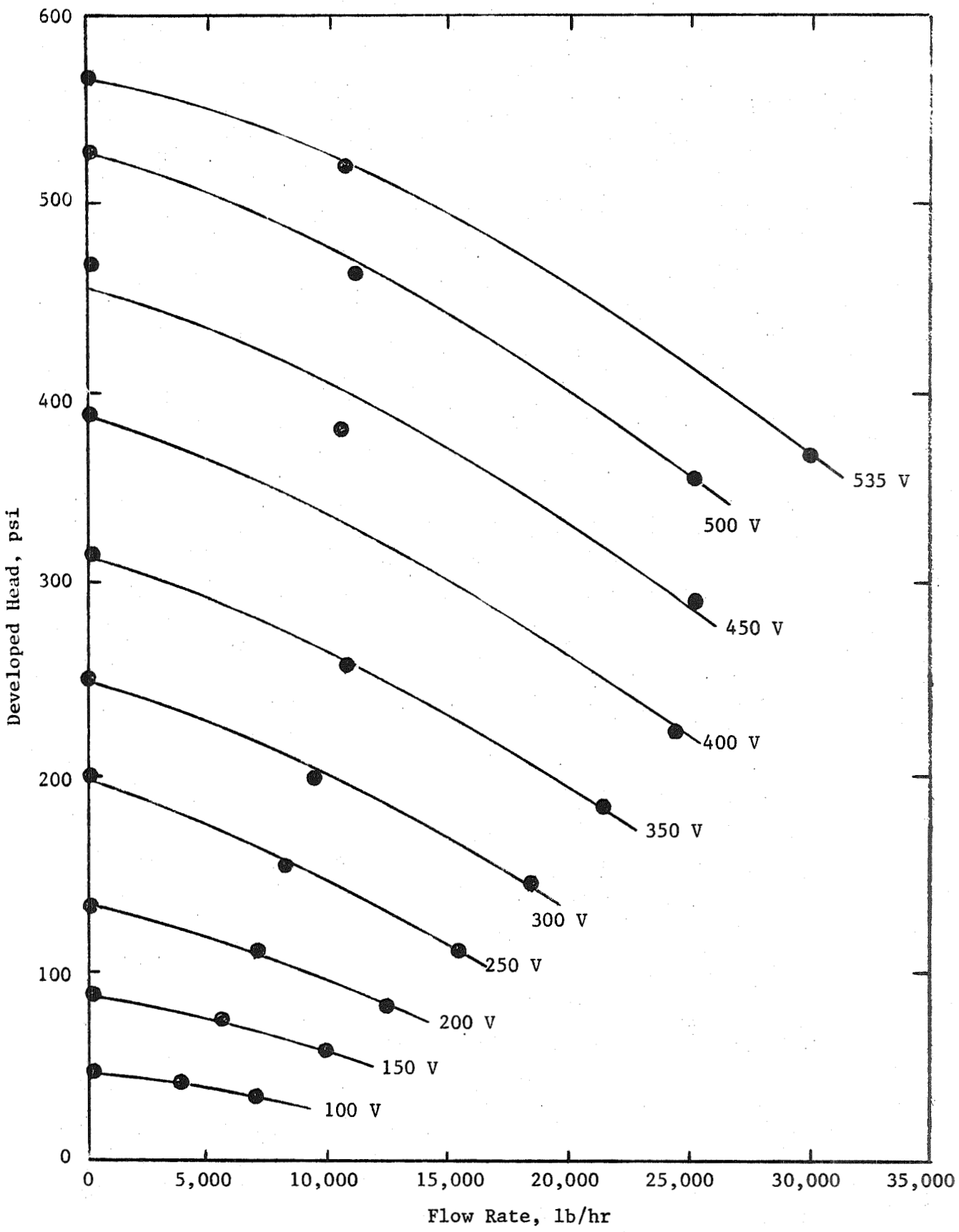

Figure 3. Three Stage Duct Mercury EM Pump Test Data.

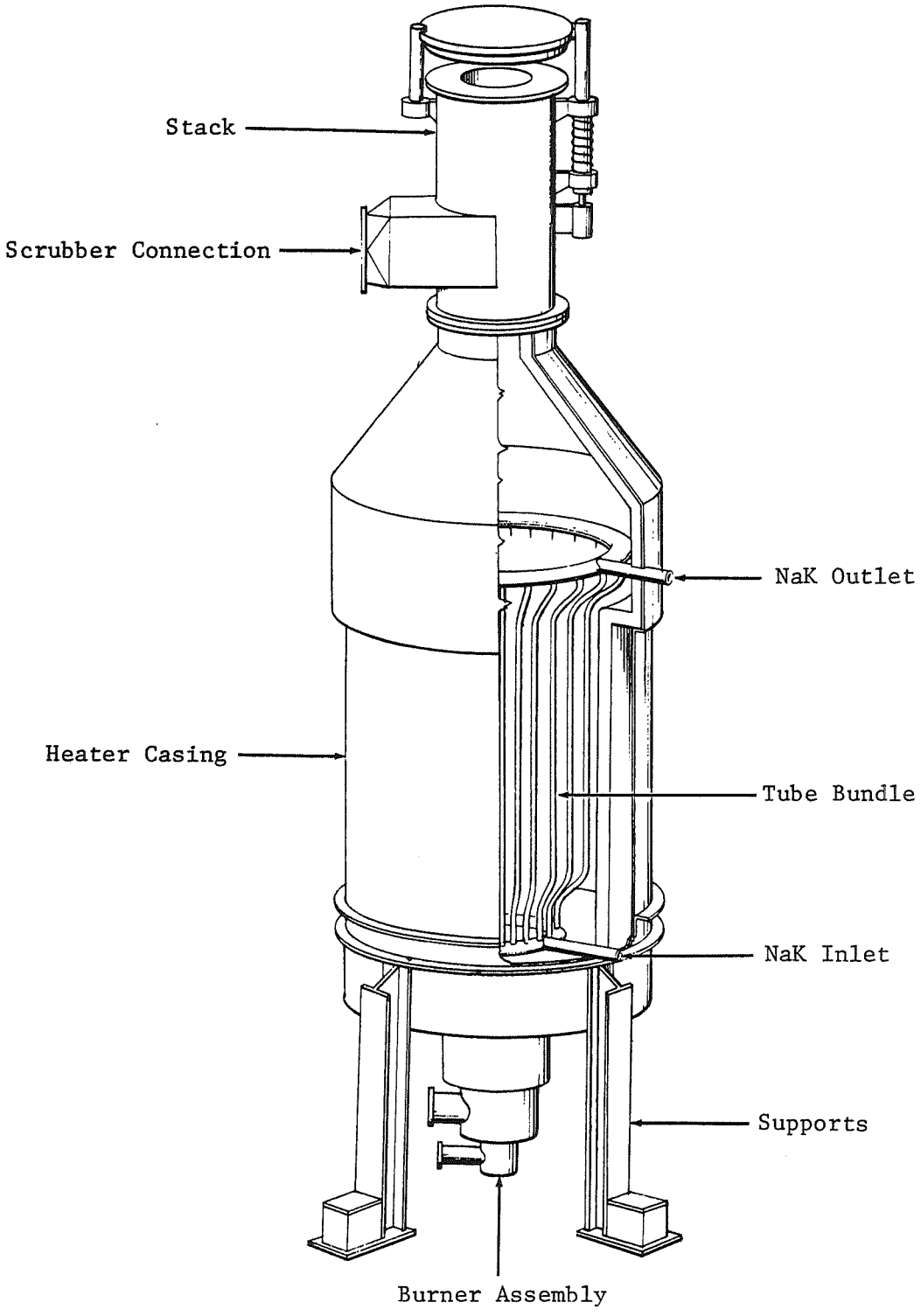

Figure 4. Schematic of Facility Gas Fired NaK Heater.

requirements involved with the use of the more corrosion resistant low alloy steels and the lack of significant corrosion of the austenitic stainless steel at the condenser temperature of 450°F to 600°F. The condenser cooling air was drawn from outside the building to the condenser. Two blowers were used for exhausting air from the condenser to improve the reliability of cooling air to the condenser. In addition, a screen was installed over the air intake duct to minimize any intake of foreign objects.

The mercury dump tank installation with some of the mercury piping and valves is shown in Figure (5). The mercury cooler shown was used to trim the liquid temperature returning to the pump from the condenser. The mercury EM pump stator is shown installed at the left side of the picture and thus operated with a slight negative pressure in the test cell. The air discharge was also connected to the scrubber piping and, in the event of a leak, the air could be discharged to the safety system. On the right side is shown the mercury sampling line to the sample station which was external to the enclosure to permit sampling during operation. Similar connections for sampling were installed to sample primary loop NaK and static NaK from the boiler during the test.

For the purpose of safety, a mercury vapor detector was installed in the condenser air exit ducting. A similar detector was installed to monitor the test cell for mercury vapor.

Figure (6) shows a partial view of the NaK loop during the NaK filling operation for the primary loop. In Figure (7), within the mercury enclosure, the mercury loop had just been completed with the single tube test boiler installed. The interior of this enclosure was coated with two layers of white epoxy paint to facilitate clean-up in the event of a mercury spill.

Electric heaters were provided to preheat the mercury loop and the NaK dump tank during the startup period.

The 550 KW liquid metal test facility and its components are discussed in greater detail in Reference (7) in which the design and calculations are also presented.

B. Description of the Test Boiler

The single tube mercury boiler is shown schematically in Figure (8). The boiler employed a single tube counterflow configuration with a static NaK annular layer acting as a barrier between shell side NaK flow and tube side mercury flow. The boiler shell and the static NaK containment tube were fabricated from 316 SS tubing. A cross sectional view of the test boiler assembly is shown in Figure(9) . The tantalum boiler tube had an inside diameter of 0.67-inch and an outside diameter of 0.75-inch. The static NaK containment tube had an inside diameter of 0.805-inch and a wall thickness of 0.035-inch, while the boiler shell had an inside diameter of 1.38-inches and a wall thickness of 0.062-inch. The overall heat transfer length was 16 feet. A disassembled view of the test boiler is shown in Figure(10) .

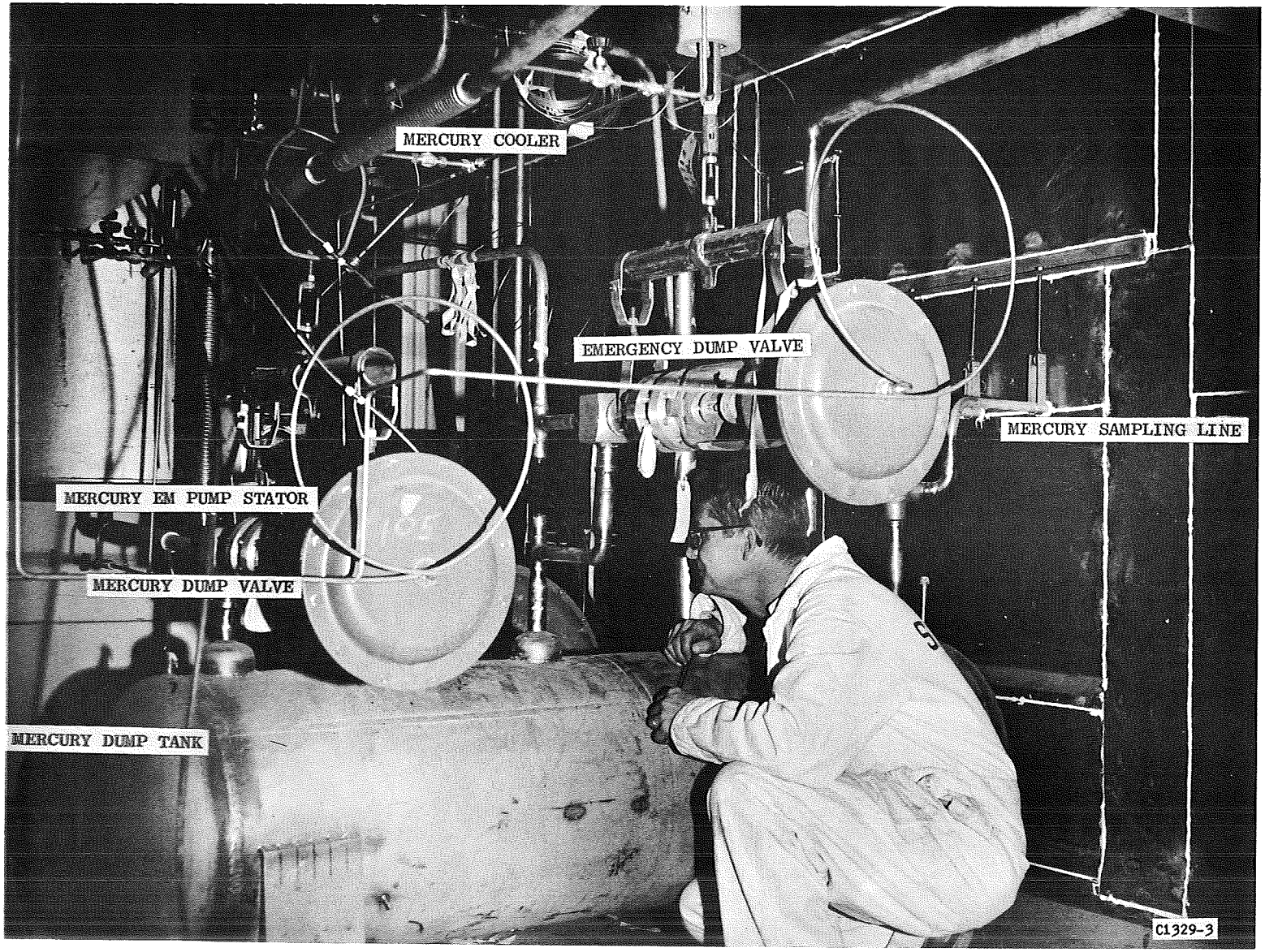

Figure 5. SNAP-8 Refractory Boiler Development Facility Showing Mercury Dump Tank, with Dump Valves, EM Pump Stator and Sampling Line. (C67112008)

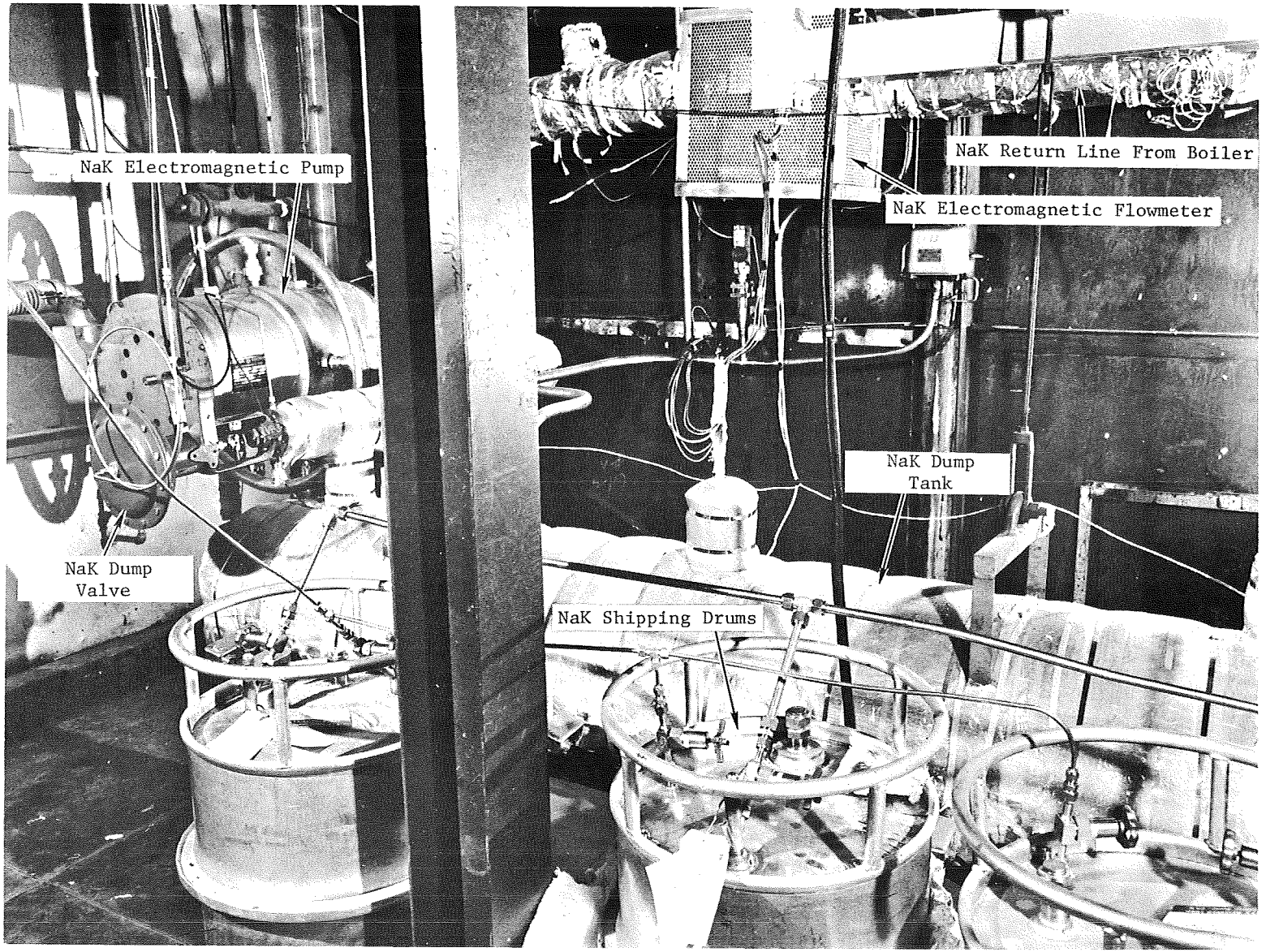

Figure 6. NaK Loop During Filling Operation. (C68010411)

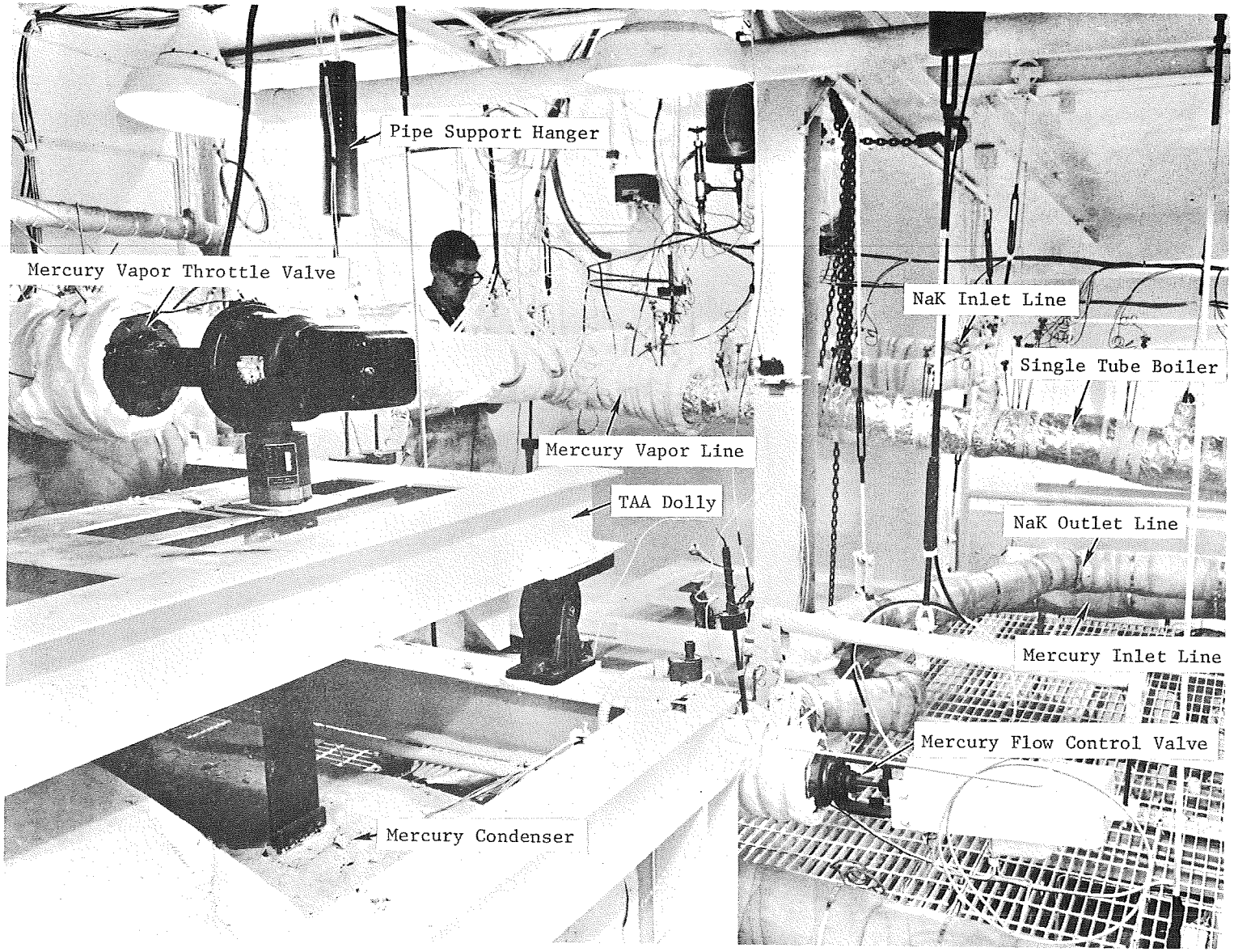

Figure 7. Photographic View of the Single Tube Test Boiler Installed in the 500 KW SNAP-8 Refractory Boiler Development Facility Loop. (C68010413)

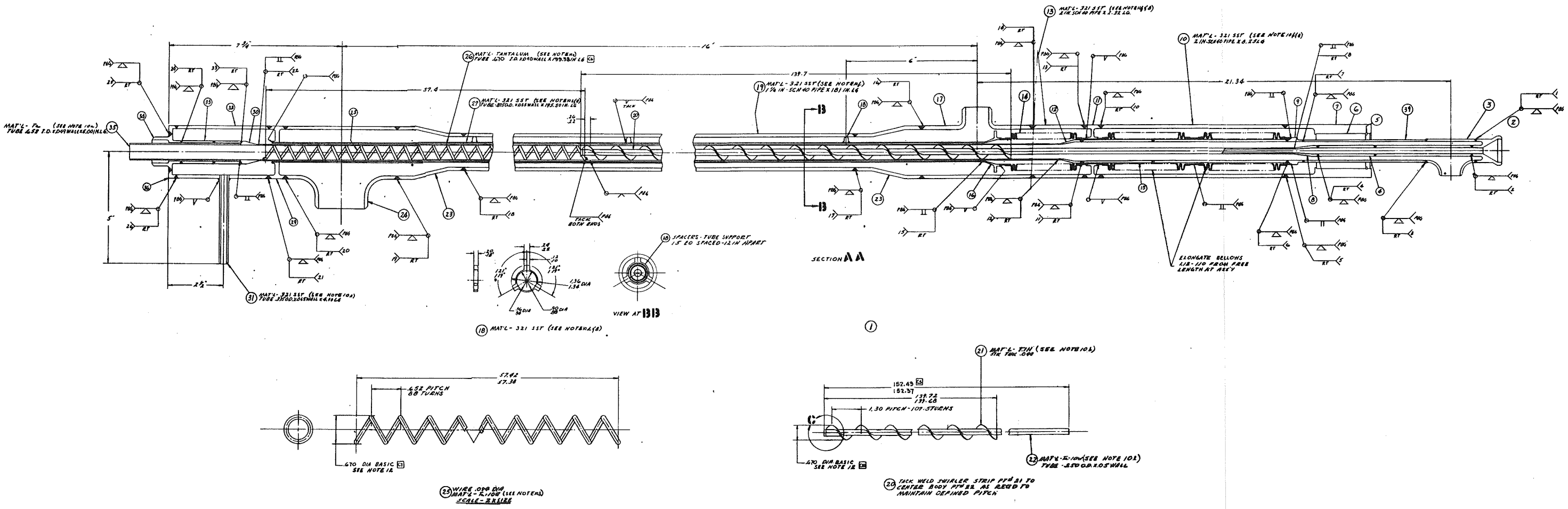

Figure 8. General Electric Single Tube Straight Boiler.

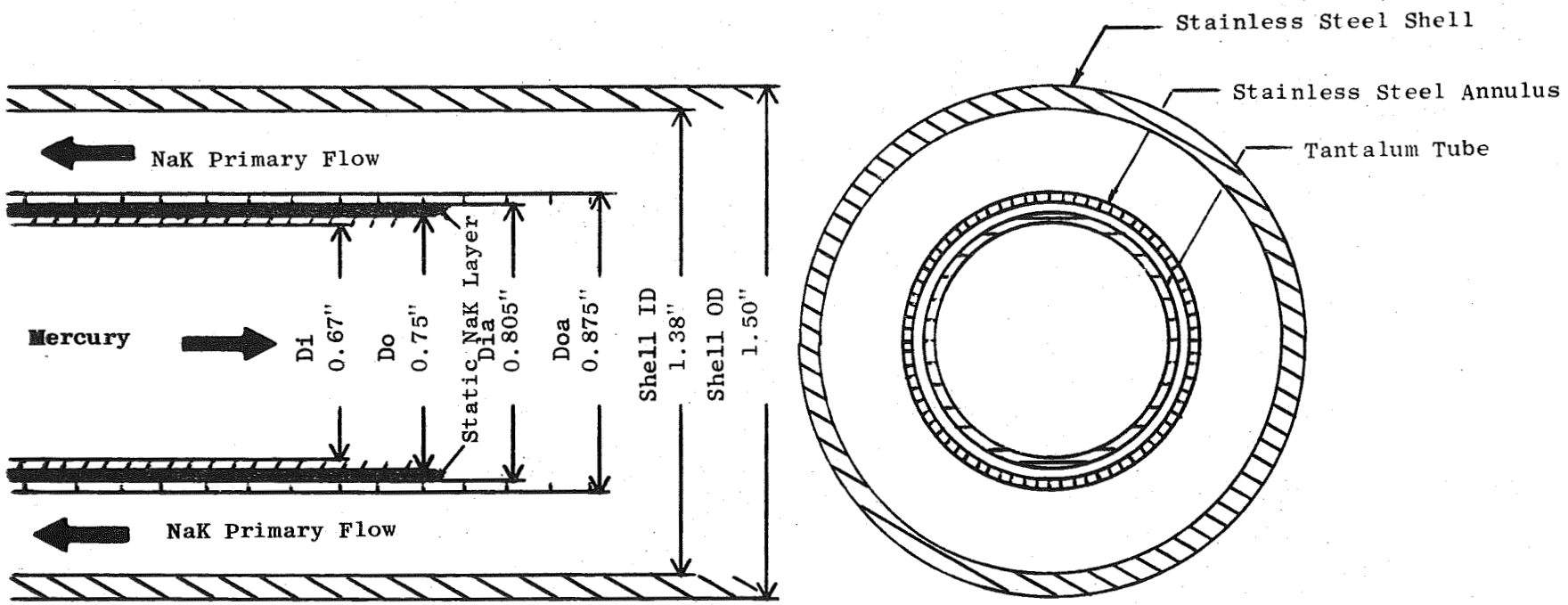

Figure 9. Cross Sectional View of the Single Tube Test Boiler.

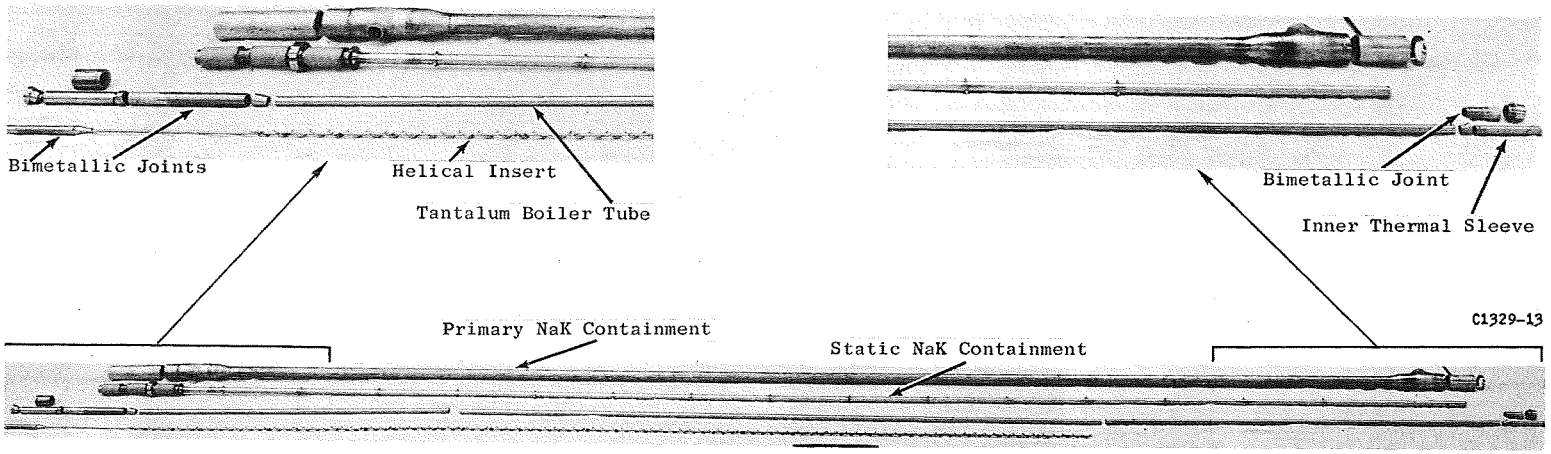

Figure 10. SNAP-8 Single Tube Test Boiler. (C68011583)

Spacer pins welded one foot apart on the static NaK containment tube allowed it to be accurately centered in the shell during assembly. Three bimetallic joints between tantalum and stainless steel were employed. One at each end of the boiler tube and one at the inlet of the helical vane insert. The composite insert employed in the test consisted of a P/D = 2.0* helical vane insert for the first 12 feet and a P/D = 0.97 wire coil insert with wire diameter equal to 0.094-inch in the last four feet of the test boiler. A photographic view of the helical vane insert is shown in Figure (11). It contained a 1/4-inch OD, 0.05-inch thick wall hollow centerbody and 0.035-inch thick helical vane. The hollow centerbody permitted local mercury temperature measurement by the installation of thermocouples inside it. The helical vane insert was terminated before the boiler exit in order to avoid carry-over of any liquid mercury which had adhered to the centerbody. As the mercury flow entered the boiler tube, a helical flow pattern was induced by the insert. The purpose of the arrangement was to increase the heat transfer capacity of the boiling fluid, particularily in the transition region, since the radial acceleration produced by the insert will tend to force the liquid droplets entrained in the vapor core to the partially wetted tube wall.

Photographic views of the boiler inlet and outlet portion just before installing insulation materials are shown in Figures (12) and (13). The shell-side thermocouples are also illustrated by these figures.

As shown in Figure (12), relative expansion between the boiler tube and the shell of the assembly was accommodated by a bellows positioned near the mercury inlet end of the test section.

*See Nomenclature

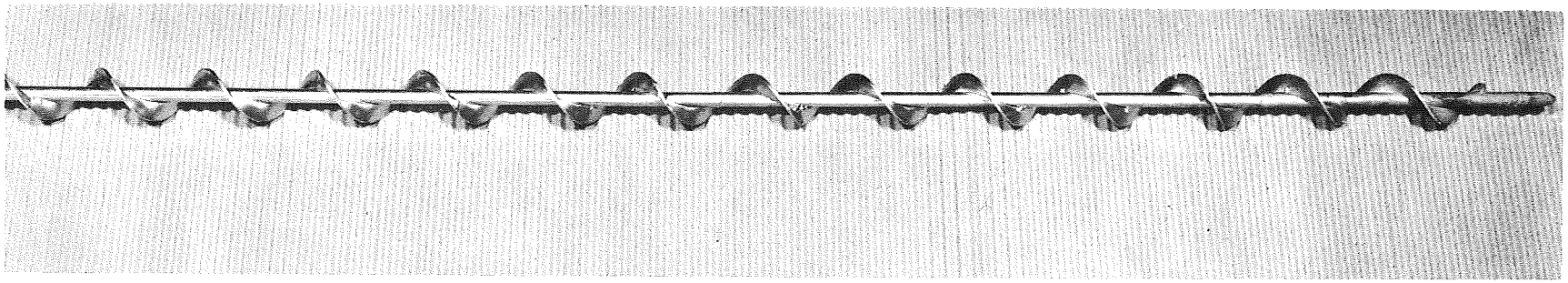

Figure 11. Helical Insert P/D 2.0, 1/4 - Inch Center Body. (C68011582)

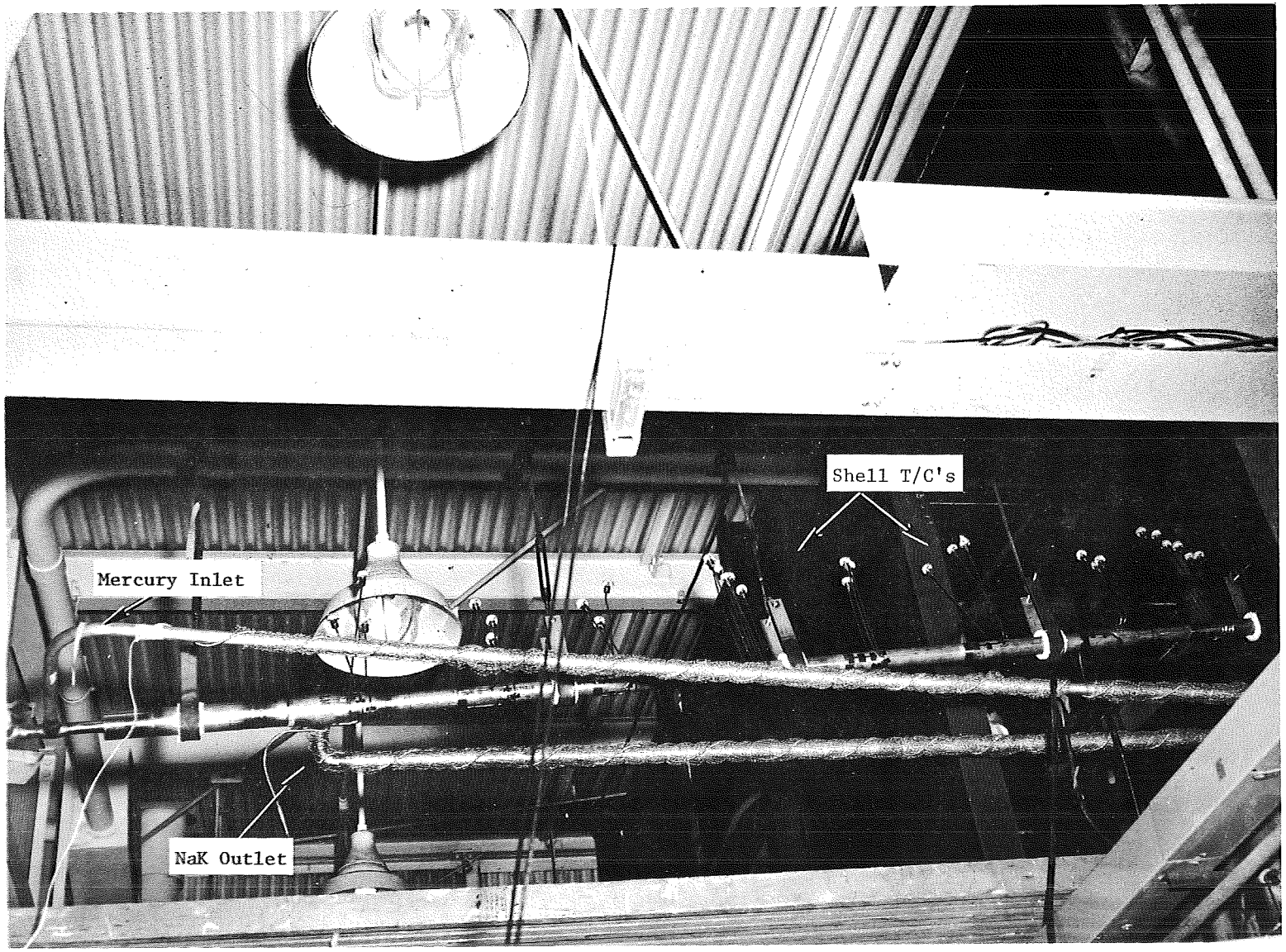

Figure 12. Photographic View of the Test Section Inlet Portion (Exposed Before Insulation). (C67120770)

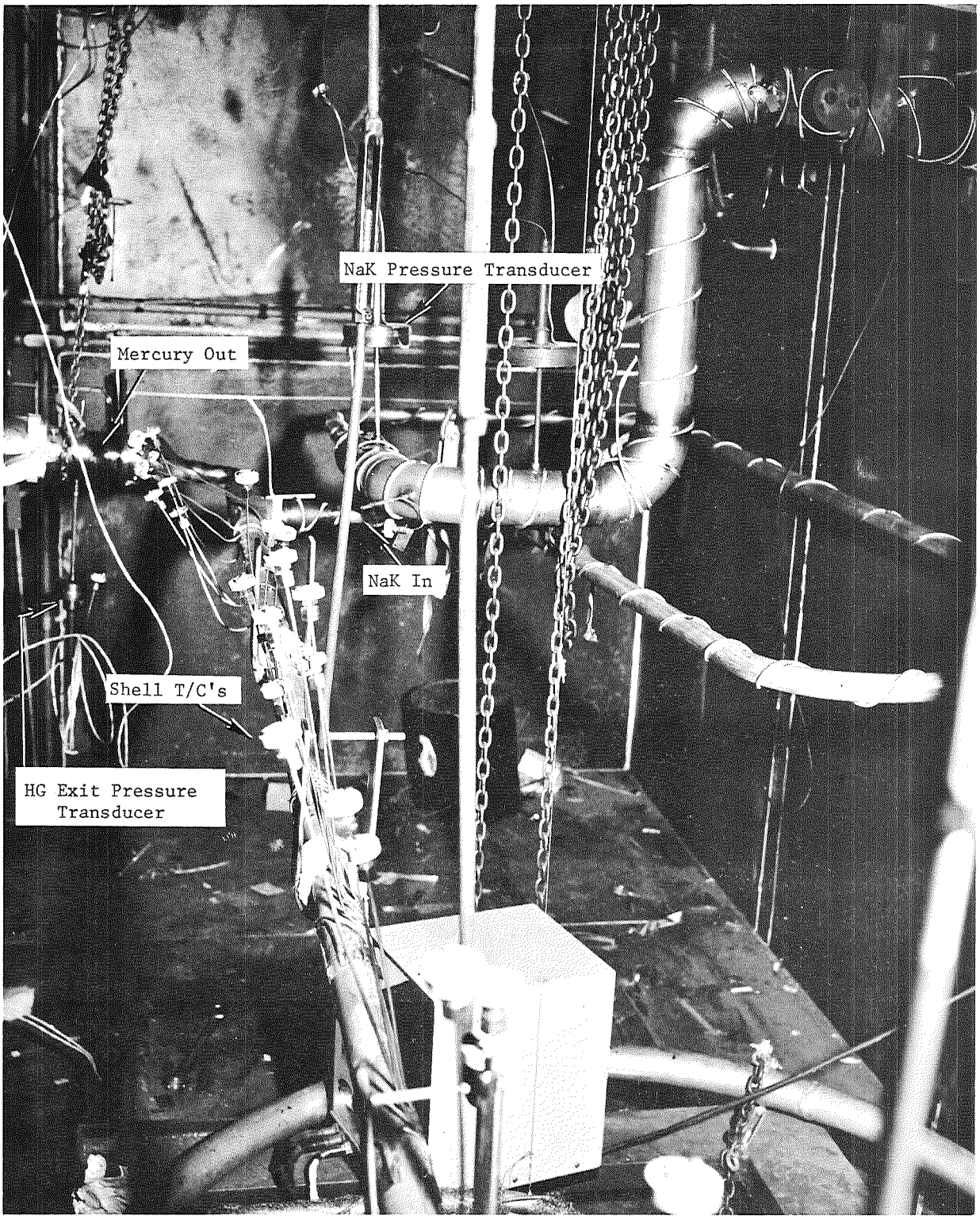

Figure 13. Photographic View of the Test Section Outlet Portion. (Exposed Before Insulation). (C67120768)

III. INSTRUMENTATION AND OPERATING PROCEDURES

A. Loop Instrumentation

A complete instrumentation layout for the NaK-mercury heat transfer loop is shown on the loop schematic drawing in Figure (14). Pressure gauges, flowmeters, thermocouples, level controls and mercury vapor detectors are shown in their approximate locations. The instrumentation installation consists of temperature and pressure instruments which monitor operation and provide data for heat transfer and pressure loss analysis.

A liquid venturi designed to provide 20 psi differential pressure at 1800 lb/hr mercury flow was installed in the loop for the mercury flow rate measurement. Prior to installation water was used to determine the venturi discharge coefficient over appropriate throat Reynolds number range. The mercury flow rate was then determined by the standard venturi flow equation as a function of the differential pressure (inlet pipe to throat static). An on-loop calibration of the venturi differential pressure versus the output signal was done in 10% increment of the full scale (0 to 20 psi) in both direction of increasing and decreasing. A final calibration curve for the liquid venturi, plotted as mercury flow rate versus output signal can thus be established and is presented in Figure(15).

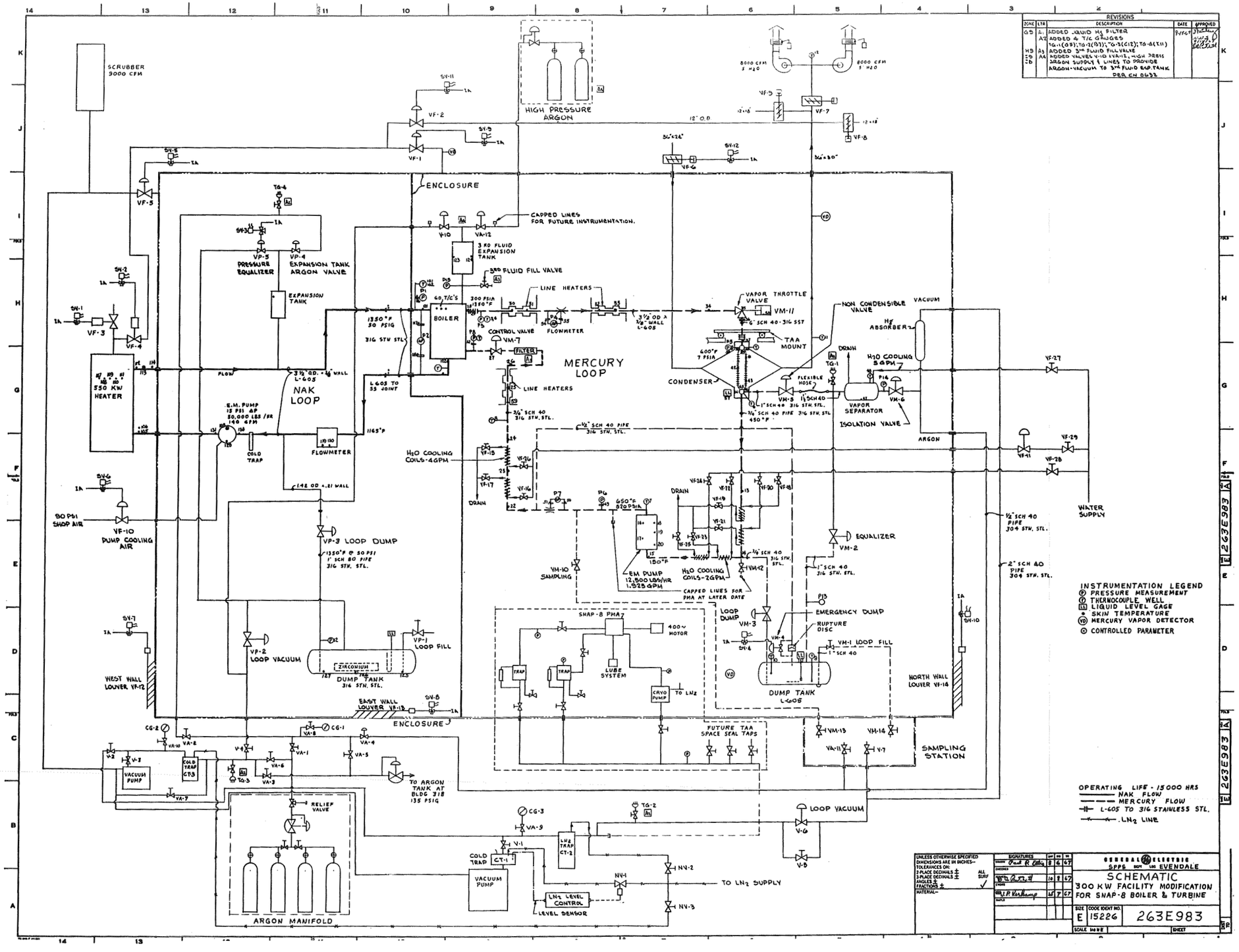

Figure 14. Schematic of 550 KW SNAP-8 Refractory Boiler Test Facility with Instrumentation.

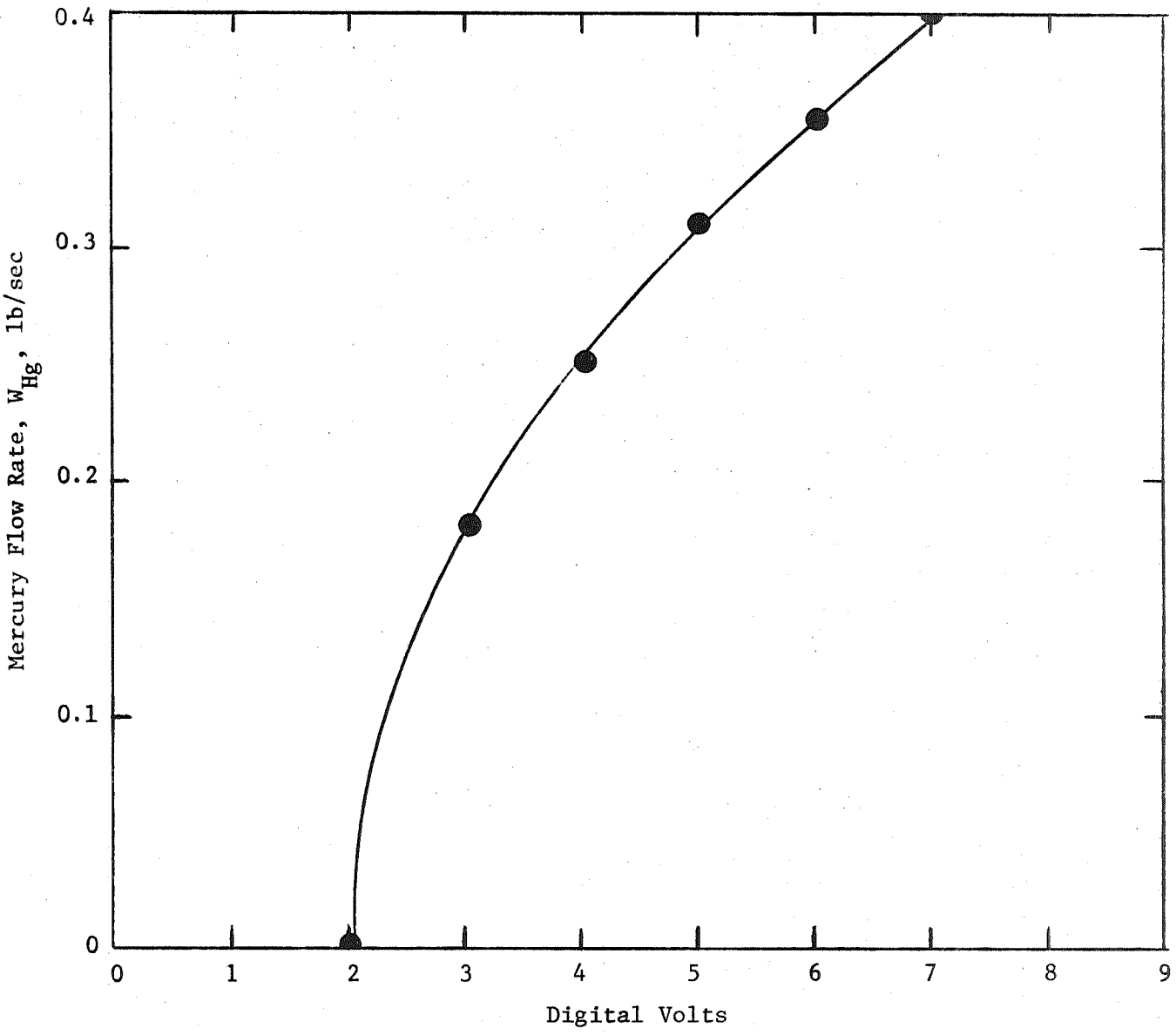

Figure 15. Mercury Liquid Venturi Flowmeter Calibration.

A permanent magnet flowmeter was used to measure NaK flow. This meter consists of a 3.513-inch OD x 2.812-inch ID Haynes-25 cylindrical duct located within a 728 gauss magnetic field to provide a theoretically calculated sensitivity of 13.93 gpm/mv at 500°F. A calibration curve for NaK flowmeter is shown in Figure (16).

At locations where it was necessary to determine fluid temperature, thermocouple wells were provided which were immersed in the fluid stream such that the depth of immersion was at least ten times the well diameter. The wells were made from 0.25-inch OD tubing and 0.062-inch OD sheathed thermocouples with capped, non-grounded junctions installed therein.

With two exceptions, all thermocouples were chromel-alumel type with 0.125-inch, 0.062-inch or 0.04-inch OD. One hundred and fifty thermocouples were installed on the entire test system with 71 on the single tube test boiler. All thermocouples necessary for performance calculations were connected into a digital recording system via a 150 °F controlled temperature reference junction heat block. Two copper constantan thermocouples referenced to an ice bath were used to check the reference block temperature. All other thermocouples were connected to various readout instruments located on the control console for monitoring during operation.

Approximately 50 of the thermocouples, which were required for data reduction, were calibrated prior to installation at the freezing points of zinc (787.1°F) and aluminum (1220°F). The calibrated thermocouples included all the well thermocouples and a representative group of the boiler shell surface thermocouples. Calibration results are summarized as follows:

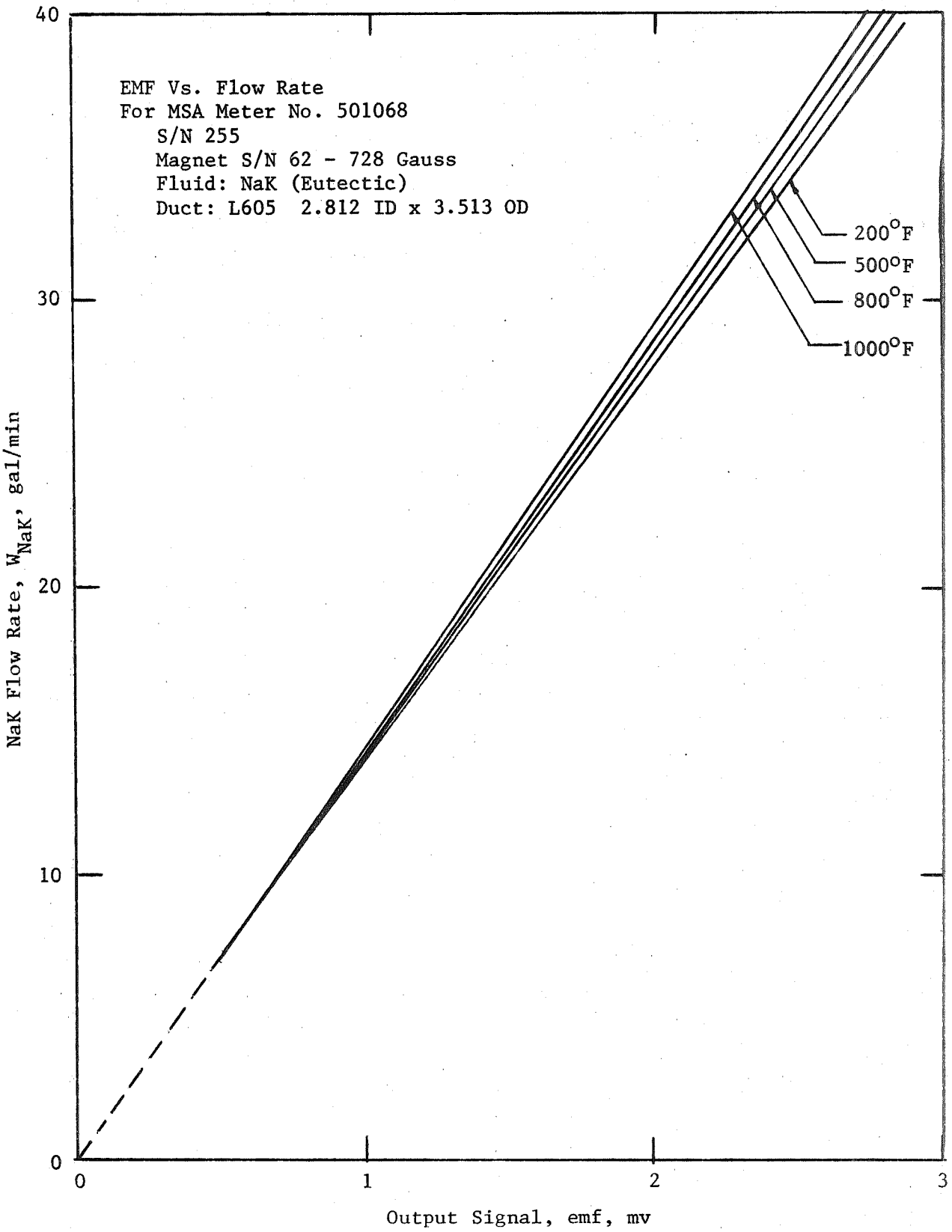

Figure 16. NaK EM Flowmeter Calibration.

0.04-inch OD insert thermocouples	Maximum error 1.1°F with most less than 0.5°F.
0.062-inch OD well thermocouples	Within a $\pm$ 3/8% tolerance in all except two cases which were within $\pm$ 0.5%.
0.125-inch OD Exposed Junction thermocouples	Within a $\pm$ 3/4% tolerance in all cases.

The differential pressure gauges (P4, P7), as shown in Figure (14) were used to measure pressure drop through the two mercury flow nozzles and another (P2) which was used to measure shell side pressure drop for NaK flow are slack diaphragm units. Each unit employed a 0.005-inch thick diaphragm which transmits the pressure forces to a differential sensing chamber (mounted outside the loop enclosure) via a NaK filled capillary tube. The gauges provide a pneumatic output signal which varies from 3 - 15 psi over the calibrated range of the pressure transducer (0-600-inches of water for mercury transducers and 0 - 5 psi for the NaK transducer). The 3 - 15 psi output signal is converted into a 4 - 20 ma dc current by a signal conditioning circuit in the control room. The dc current is then converted into a 10 - 50 mv signal for recording at the control console and a 2 to 10 volts signal for digital recording.

Calibration of the three differential pressure transducers was accomplished prior to installation by subjecting the high side to a series of inert gas pressure steps to cover the calibration range with the low side vented to atmosphere. This was done at both ambient temperature and at 500 °F (nominal). All calibration results showed that the transducers were linear and repeatable within $\pm$ 1% throughout

the calibration range. Typical calibration curves are given in Figure (17). Final zero adjustments were made with the transducers installed on the loop and with the loop full of mercury or NaK to eliminate errors caused by static head variations.

Other slack diaphragm pressure transducers are used to measure absolute pressure at the NaK flow inlet (P1), mercury pump exit (P6), boiler inlet (P8), boiler outlet (P3) and condenser inlet (P5). All of these transducers functioned the same as the differential transducers described above except that they provided a 4 - 20 ma dc signal directly. All except the gauge (P5) on the condenser were calibrated prior to installation into the loop system at operating temperatures.

Liquid level gauges were also provided in the NaK dump tank, mercury dump tank, NaK standpipes and the mercury condenser to permit accurate control of inventory during operation.

Automatic loop safety control circuits were installed on the control console. These provide automatic dump of the mercury loop if pressure limits at the boiler inlet or the condenser are exceeded and automatic shutdown of the gas-fired furnace and all mercury loop heaters if the NaK flow drops below a preset level or if the gas heater tube temperature exceeds a preset limit. Automatic control circuits were also provided for temperatures of the NaK dump tank heater, mercury vapor line heater, mercury preheater and the gas heater exit. Additional warning devices are connected to an annunciator circuit located on the control console to alert loop

operators of the following conditions:

1. Gas-fired furnace overtemperature
2. Static NaK expansion tank overpressure
3. Mercury boiler inlet overpressure
4. Mercury condenser overpressure

As shown in Figure (14), additional pressure transducers P12, P13, P14, and P15 are used in the argon and vacuum piping systems for loop operation requirements. These are all conventional penumatic transmitters with all welded bourdon tube sensing elements.

A detailed description of the thermocouples installed in the test loop is given in Table (I) listed in Appendix (II).

B. Boiler Instrumentation

As shown schematically in Figure (18), sixty 0.125-inch OD thermocouples were installed on the shell surface of the test boiler in 17 circumferential rings at 12-inch intervals along the entire boiler length. All shell thermocouple junctions were formed by surface spot welding. It was found that a small tab of 0.002-inch thick tantalum foil tacked over the exposed junctions would reduce the frequency of thermocouple failure caused by the thermocouple lead lifting off the shell surface. Seven 0.04-inch OD sheathed chromel-alumel thermocouples with capped and nongrounded junctions were installed in the centerbody of the helical insert, with junctions located at evenly space increments along the active boiling region of approximately the first 12 feet of the test

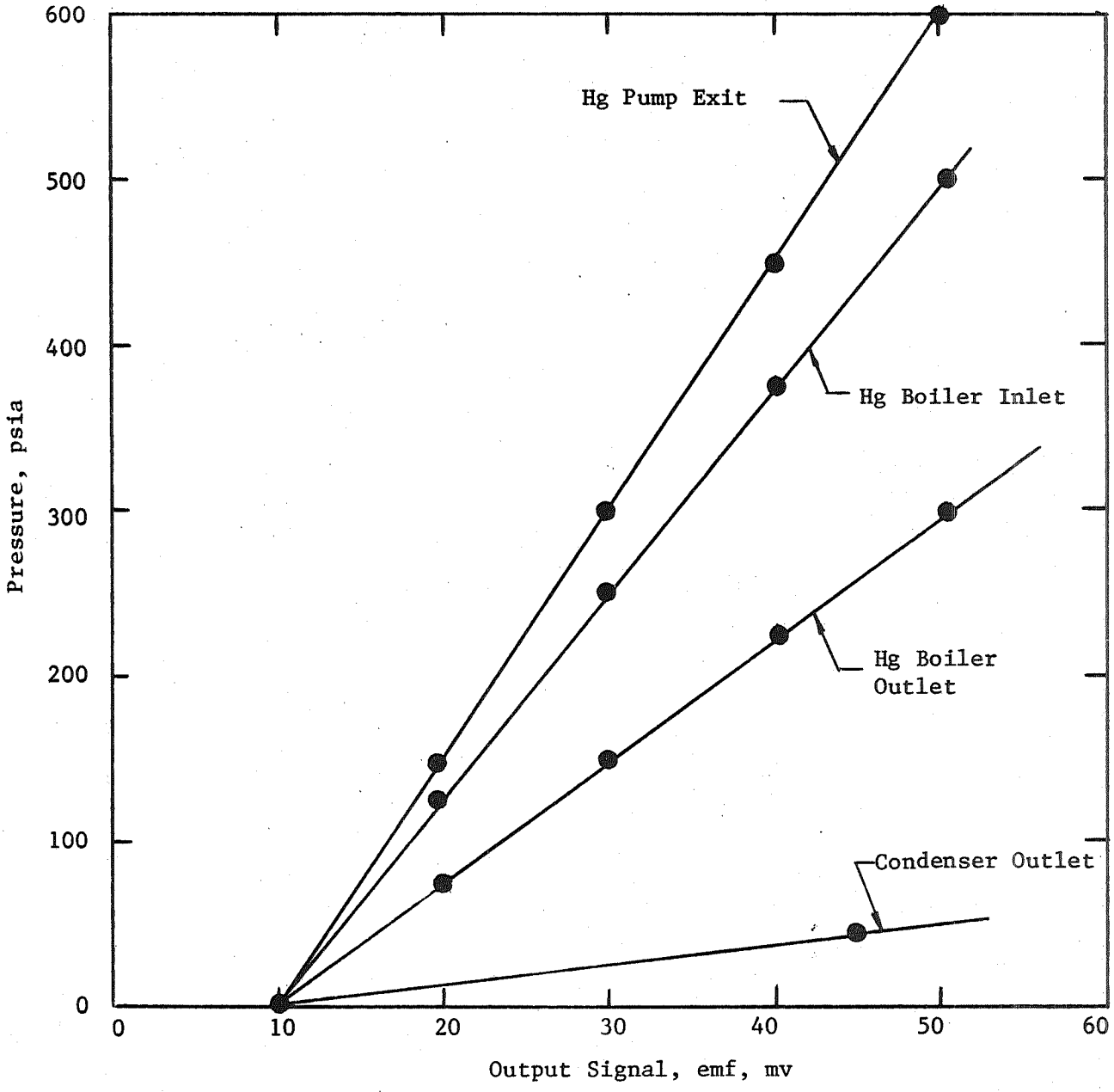

Figure 17. Calibrations of Pressure Transducers.

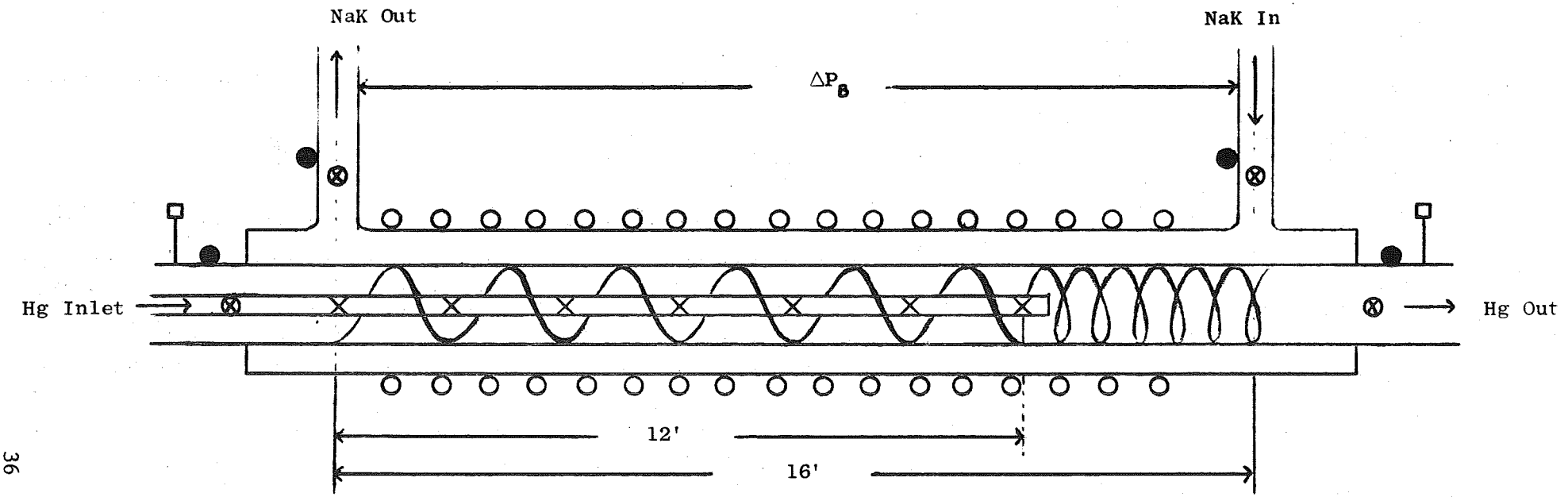

- ✕ Thermocouple Located Inside Insert Support Tube (total of 7)
- ○ 17 Rings of Shell T/C (3 or 6 per ring, total 60)
- ⊗ NaK and Hg Inlet and Outlet Well T/C
- ● NaK and Hg Inlet and Outlet Skin T/C
- □ Taylor Pressure Transducers

Figure 18. Instrumentation of Single Tube Test Boiler.

boiler. These insert thermocouples were then brought out through a "Conax" multi-hole packing gland so that the inside of the centerbody tube could be kept under pressurized argon atmosphere during operation. This arrangement ensures that argon will leak into the mercury loop in the event of any leak along the centerbody tube, rather than mercury leaking into the atmosphere.

Two 0.062-inch OD Cr-Al sheathed thermocouples with capped and nongrounded junctions were positioned in each of the four thermocouple wells located at the inlet and outlet of both the NaK and mercury flows. Two 0.125-inch OD Cr-Al sheathed thermocouples 180 degrees apart were surface spot welded in the inlet and outlet of both the primary and secondary flow pipes to measure the inlet and outlet pipe skin temperatures.

Two slack diaphragm Taylor absolute pressure transducers located at the mercury inlet and exit were employed to measure the total pressure drop across the test boiler. Figure (13) shows the mercury outlet pressure transducer as installed in the test section. The differential pressure gauge used to measure NaK flow pressure drop through the shell side passages was also a slack diaphargm unit.

A detailed description of the shell and insert thermocouples used in the test section is given in Tables (2) and (3) and is listed in Appendix II.

C. Loop Checkout and Operating Procedures

One of the problems of greatest concern was that of particulate matter which might be present in the loop prior to startup. Every precaution was taken to eliminate this possibility, however, it must be appreciated that despite all care the possibility still existed. Consequently, prior to startup the loop was flushed with mercury in both directions and the mercury was returned to the dump tank. The dip leg into the dump tank was then blown down with pressurized argon to make sure that any particulate material floating on the surface was blown into the dump tank. The probability of such contaminants being returned to the loop on refilling will thus be extremely small, since this material would then be floating on the surface of the mercury in the dump tank. In addition to this flushing procedure, a filter having a nominal pore size of 17 microns was placed in the loop just upstream of the liquid throttle valve where the liquid mercury enters the boiler. The filter should prevent particles from reaching and plugging the 0.060-inch orifices of the inlet of each boiler tube.

Oxide and impurity control in the NaK primary loop was achieved by a combination of hot-flushing and hot-trapping. Upon startup, the NaK loop was hot-flushed at 800 °F by several charges of NaK flow, which was discarded. Oxygen content during operation was controlled by hot-trapping the liquid NaK at 1200°F with zirconium gettering grid located in the NaK dump tank.

The static NaK layer system which acted as a barrier between the primary NaK flow and the secondary mercury flow was filled with

793 grams of reactor-grade NaK. The static NaK system was vacuum outgassed for 36 hours at temperatures up to 700°F before filling. During this time, the mercury system was also under vacuum to protect the tantalum test boiler from contamination.

Filling operation proceeded from a condition in which both the primary and secondary loops were evacuated with the facility mechanical vacuum pump and were baked out to approximately 400°F by means of auxiliary electrical heating wire. The mercury and NaK dump tanks were also heated up to approximately 400°F with auxiliary heating equipment. Then by pressurizing the NaK dump tank with argon, NaK was forced to fill the evacuated loop. Level sensors located in the NaK loop standpipes indicated when the proper inventory was obtained. In the meantime, the NaK EM pump was activated and, subsequently, the gas-fired furnace was turned to its minimum heat level.

The secondary mercury loop was filled in a similar manner. The liquid mercury was forced to fill the evacuated mercury loop by pressurizing argon in the mercury dump. When the desired mercury inventory was attained, the mercury EM pump was then activated and, in the meantime, forced cooling air flow into the condenser was started. Boiling was initiated as the mercury was pumped into the NaK heated boiler section where the shell side NaK flow had already been heated to an elevated temperature.

Before filling with mercury, a series of thermocouple calibrations and heat loss runs were conducted. The purpose of these runs was to check

each boiler shell thermocouple against the calibrated well thermocouple in the NaK stream and to obtain the heat loss for the test section. This was accomplished by running the NaK loop at both maximum and minimum flow rates at three different temperature levels with the mercury loop evacuated. The heat loss runs are of vital importance in the heat transfer analysis to determine accurately the exact amount of heat transferred to the tantalum boiler tube. A technique described in detail in Reference (6), employing two NaK flow rates at several temperature levels with the mercury loop evacuated, was used to determine the test section heat losses. These heat losses, so determined, are presented in Figure (19) and range from 6.26 to 7.4 KW depending upon the temperature level of the test section. The shell thermocouple corrections obtained in this manner were generally about 10°F and are believed accurate to approximately $\pm$ 2°F. The reference well thermocouples in the NaK stream are judged to have an accuracy within $\pm$ 1°F on an absolute basis.

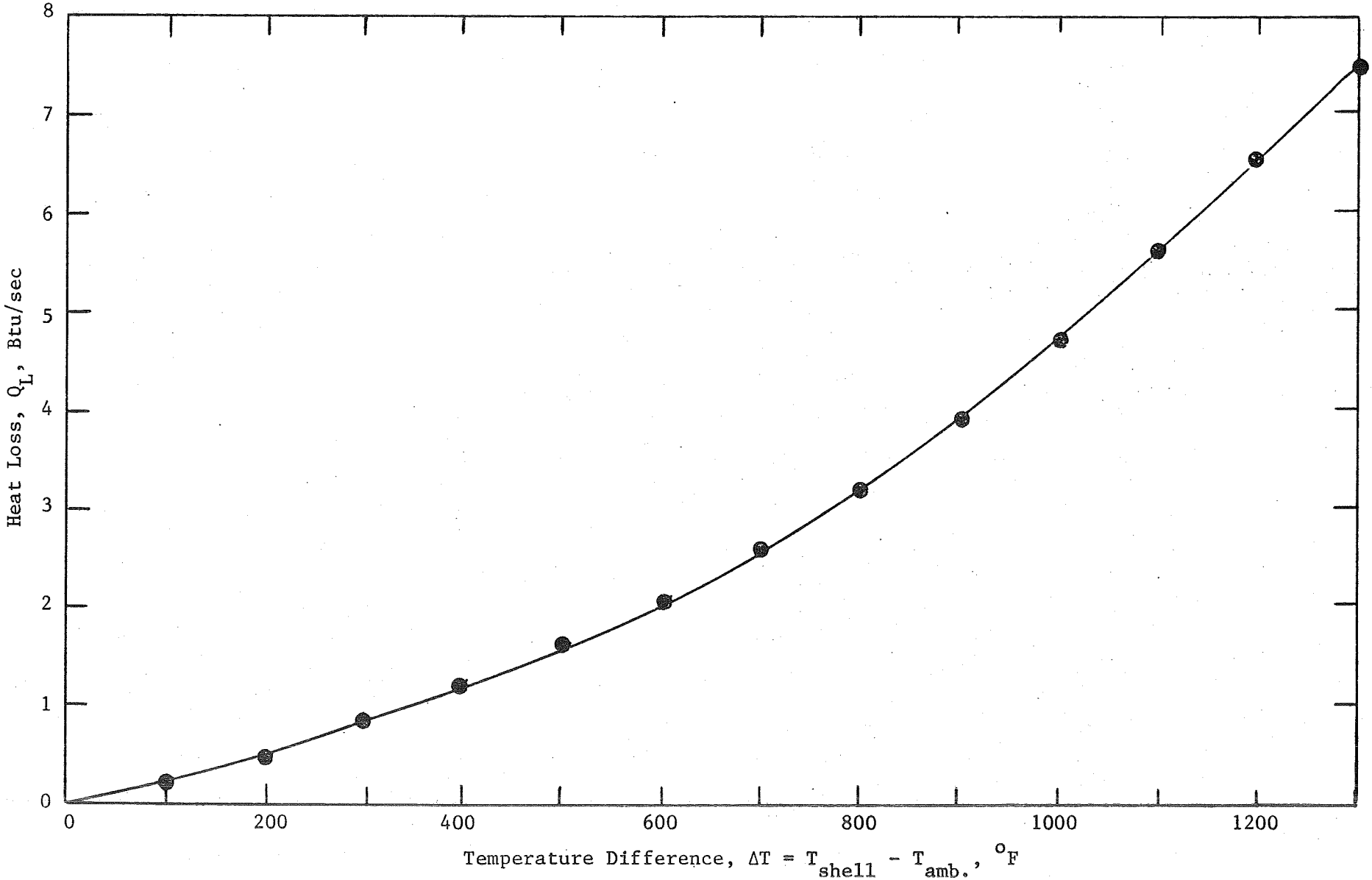

Figure 19. Test Section Total Heat Loss.

IV. EXPERIMENTAL RESULTS AND DISCUSSIONS

Before presenting average and local heat transfer and pressure drop results, a conceptual model of the local boiling conditions as shown in Figure (20) which is thought to occur in the mercury once-through boiler will be briefly described in order to define some of the terminology employed in this report.

In the once-through boiling process as described in Reference (6), the mercury bulk temperature, subcooled at the boiler inlet, is increased by single phase liquid heat transfer in the "subcooled heating region" until boiling is initiated. The point of boiling inception marks the beginning of the "nucleate boiling region" which is mainly characterized by relatively high heat transfer performance. In this region, it is believed that the wall is completely wetted by mercury at the elevated saturation temperatures of the present test. As the quality is increased, it is thought that in this nucleate region part of the liquid flows as a continuous liquid film on the boiler wall and the remainder is entrained in the vapor core. Two heat transfer models are frequently used to describe this nucleate boiling region at high qualities. The "film evaporation" model, which is characterized by totally suppressed bubble formation has the vapor generated by evaporation at the postulated interface. The "bubble nucleation" model neglects liquid-vapor interface vapor generation and assumes heat

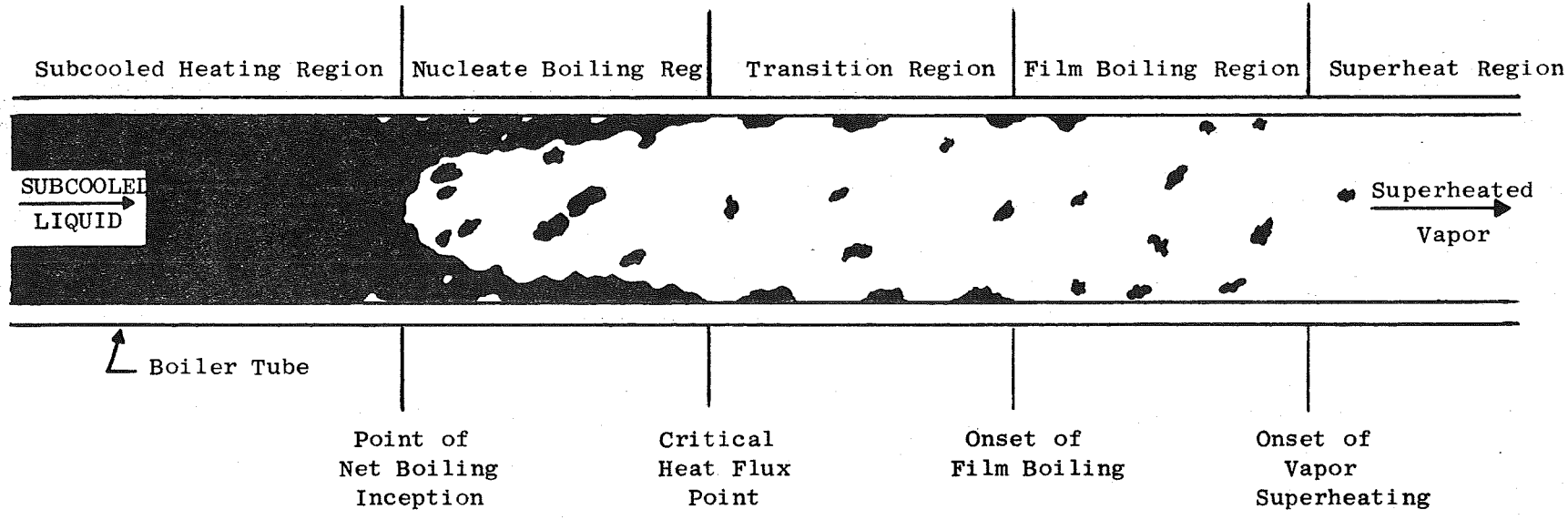

Figure 20. Conceptual Illustration of Once-Through Boiling.

transport through the formation of vapor bubbles from nucleation sites at the boiler tube wall. This nucleate boiling region persists with increasing quality until the onset of the critical heat flux condition, at which point the heat transfer performance begins to deteriorate due to breakdown of the continuous liquid film along the boiler wall. Thus, the critical heat flux condition marks the onset of the lower heat transfer performance "transition boiling region." The transition boiling region is characterized by a lower heat transfer coefficient thought to be caused by the heat transfer surface being partially wetted by liquid patches or droplets and partially exposed to dry vapor. As the quality is further increased, the quantity of liquid patches or droplets wetting the wall decrease and the mean wall temperature increases rapidly until the so-called "spheroidal state" or "film boiling region" is reached. This region is characterized by the wall being blanketed with a continuous layer of locally superheated vapor. The film boiling region extends to the point at which bulk superheating commences, and the subsequent "superheated vapor region" marks the end of the once-through boiling process.

In the film boiling region, heat is transferred by a combination of conduction, convection and radiation through the vapor layer, and the heat fluxes expected at reasonable temperature levels are substantially lower than those in the nucleate boiling region. For a horizontal surface, the film boiling heat transfer correlations have been worked out by several investigators. Chang[8] and Zuber[9] are among the earliest workers. In 1961, Berensen[10] modified and extended the hydrodynamic approach used by Zuber and Chang and obtained relationships for both the heat transfer coefficient and

temperature difference at the minimum heat flux condition for pool boiling. The results are given as follows:

$$(\Delta T)_{min} = 0.127 \left(\frac{\rho_v h_{Lv}}{k_v}\right) \left[\frac{g(\rho_L - \rho_v)}{\rho_L + \rho_v}\right]^{2/3} \left[\frac{g_c \sigma}{g(\rho_L - \rho_v)}\right]^{1/2} \left[\frac{\mu_v}{g_c(\rho_L - \rho_v}\right]^{1/3} \quad (1)$$

The parameter $(\Delta T)_{min}$ is the minimum temperature difference between boiler wall and mercury required for the existence of film boiling. Equation (1) was used to predict the tube wall-to-mercury temperature difference required for mercury having film boiling. It is found that $(\Delta T)_{min}$ is generally in the order of 250°F under the present operating conditions. One should notice that Equation (1) is primarily derived for pool boiling and it might not be useful to predict $(\Delta T)_{min}$ for onset of film boiling under forced convection conditions. However, due to lack of information for forced-convective film boiling for mercury, it is believed that Equation (1) will be adequate to provide at least an order of magnitude analysis. Fortunately, recent film boiling data for mercury from Reference (11) showed that the mean temperature difference for film boiling is in the range of 180 - 270°F under the same temperature level as the present experiment employed. These sources support a conclusion that the film boiling might not have occurred in the present two-fluid mercury boiler, since no tube wall-to-mercury temperature differences as large as 200°F were experienced in the present experiment.

A. Overall and Average Test Results

The digital data system, as previously described, received and recorded raw test data in the form of a millivolt signal. A computer program was written to convert these quantities to useful engineering

units which would permit direct use of the conventional equations for performance analysis. The computations used in the computer program make use of all available calibration factors for thermocouples, pressure gauges, and flowmeters. All physical quantities for mercury liquid and vapor used in the data reduction are obtained from Reference (12). Appendix (III) shows the printout of most of the overall test results for the present 16 test runs, including such factors as power levels, operating temperature bands, degree of superheating, flow rates, and total pressure drops. Indeed, these overall results have illustrated the gross performance for boiling of mercury inside a tantalum tube boiler. Figures (21) to (36) show the temperature profiles for NaK and mercury flows in the test section for all 16 test runs. Exit superheats of the mercury vapor are also illustrated in these figures. Overall results of the operating temperature band for primary and secondary flows, as shown in these figures, are quite useful in that they indicate the feasibility of compact once-through boilers and permit the design of multiple-tube boilers with enhanced thermal power levels by direct scale-up. For example, the design of a compact once-through 19-tube boiler[13] which was proposed for the SNAP-8 power conversion system was based on the overall result of a 1/19th scale test run (Figure 35). This compact 19-tube boiler with only 6.68 feet long will meet the SNAP-8 power conversion system requirements, i.e., a power level of 500 KW and a specified exit pinch point temperature difference of 30°F.

Following the computational procedures given in Appendix (I), the average values of $\bar{U}$, $\bar{h}$, and $\bar{q}''$ for each individual heat transfer region were calculated, and the results for all 16 test runs, are listed in Table (4). The ranges of the average values are as follows:

G_{Hg}	$0.294 \times 10^6 - 0.695 \times 10^6$	$lb/hr\text{-}ft^2$
T_{Sat}	970 - 1120	°F
Q_T	36 - 75.5	KW
Q_B	24.5 - 56	KW
$\overline{q''}_{sc}$	24,000 - 25,000	$Btu/hr\text{-}ft^2$
$\overline{q''}_{NB}$	110,000 - 258,000	$Btu/hr\text{-}ft^2$
$\overline{q''}_{TB}$	25,000 - 214,000	$Btu/hr\text{-}ft^2$
$\overline{q''}_{SH}$	2,700 - 7,700	$Btu/hr\text{-}ft^2$
$\overline{h}_B$	938 - 3,790	$Btu/hr\text{-}ft^2\text{-}°F$
$\overline{h}_{sc}$	980 - 1,850	$Btu/hr\text{-}ft^2\text{-}°F$
$\overline{h}_{NB}$	5,000 - 9,050	$Btu/hr\text{-}ft^2\text{-}°F$
$\overline{h}_{TB}$	2,320 - 5,700	$Btu/hr\text{-}ft^2\text{-}°F$
$\overline{h}_{SH}$	38 - 125	$Btu/hr\text{-}ft^2\text{-}°F$
$(\triangle T)_{SH}$	205 - 400	°F

The length for each individual heat transfer region except the subcooled heating region was calculated following the procedures presented in Appendix (I). The length of the subcooled liquid heating region, L_{SC}, was obtained directly from the mercury temperature profile determined from the insert thermocouples. As shown in Figures (21) to (36), the subcooled heating region is generally short (less than 7% of the total boiler length) for all test runs.

The values of overall pressure drops recorded from the two Taylor gauges are listed in Table (5) and are plotted in Figures (21) to (36). The pressure drop profiles in Figures (21) to (36) were obtained with the saturation curves from the saturation temperature of mercury measured with insert thermocouples. The dotted lines in these figures are estimates for mercury vapor in the superheated region. Following the calculational procedures described in Appendix (I) for $(\triangle P)_{misc.}$,

$(\Delta P)_{elev.}$, $(\Delta P)_{SPL}$, and $(\Delta P)_{SPV}$, the two pressure drops were obtained, and these results are given in Table (5). The values of $(\Delta P)_{TP}$ obtained from saturation curves by insert thermocouples readings are also listed in Table (6) for comparison to those data obtained from Equation (A38). As shown in Figure (37), the comparison indicates that the values of $(\Delta P)_{TP}$ obtained from two different sources generally agreed $\pm$ 16%. In Figure (38) the frictional and momentum components of $(\Delta P)_{TP}$ are plotted along with the value of $(\Delta P)_{TP}$ obtained from insert thermocouples. The momentum component $(\Delta P)_{TPm}$ is calculated from Equation (A57).

The values of $(\Delta P)_{TP}$ obtained from insert thermocouples were used in Equation (A38), and the mercury vapor pressure drop, $(\Delta P)_{SPV}$ was obtained. By using Equation (A39), the frictional term, $(\Delta P)_{SPVf}$, was then obtained by subtracting the momentum term, ΔP_{SPVm}. Again a comparison between these experimentally-determined $(\Delta P)_{SPVf}$ and the values calculated by Equations (A46) and (A53) was made and the result is presented in Figure (39). The comparison indicates that these two $(\Delta P)_{SPVf}$ generally agree within $\pm$ 22% and the predicted values are generally smaller than those obtained from the test results. The momentum parts calculated by Equation (A41) are found to be a small fraction of the total mercury vapor pressure drop (less than 10%), and their values are plotted in Figure (40) together with $(\Delta P)_{TP}$, $(\Delta P)_{SPV}$, and total pressure drop across the boiler $(\Delta P)_{T}$. The rather large $\pm$ 22% discrepancy in $(\Delta P)_{SPVf}$ between tested and predicted values is attributed mainly to the uncertainty of using the frictional pressure multiplier K_p, especially in the wire coil region. The use of Equation (A52) for predicting K_p values in the helical vane insert region has recently been verified by a series of water and air tests.[29] In other words, the

empirical K_p curve obtained for a wire coil in reference (29) is believed to be correct within $\pm$ 22% when using it to predict frictional pressure loss of mercury vapor flowing through the wire coil insert region.

It was also found that a rather large fraction of pressure drop occurred in the wire coil insert region as compared with other portions along the boiler. This is clearly shown in Figures (21) to (36). A wire coil insert at the end of the boiler (the superheated region) was used to turbulate the liquid mercury which might remain on the center-body at the helical vane insert end and to enhance the superheated vapor heat transfer coefficient. As the pressure drop data shows, the penalty for this performance was an increase of pumpin g power for the working fluid.

B. Local Test Results

The overall and average heat transfer and pressure drop data presented previously are only useful for design studies at conditions near those at which the test data were obtained. These data were generally obtained by averaging over one or more heat transfer regions of the once-through boiling process and thus can not be extrapolated with confidence for general design purposes beyond the range of the present test conditions. For these reasons, local mercury boiling heat transfer and pressure drop data were needed, and consequently a considerable effort was devoted to the calculation and correlation of the local results. These local results not only enhanced understanding of the once-through boiling mercury in a single tube with inserts, but also provided a general means for extrapolating data outside the range of test conditions.

1. Heat Flux Distribution, Quality and Overall Heat Transfer Coefficient

Values of the local heat flux distribution were obtained by differentiation of the smooth temperature curves at one-foot intervals, using Equation (A64) for the regions up to the transition boiling and Equation (A66) for the region of superheated vapor. The results are presented in Figures (41) to (56). The values of q" obtained in this manner were not sufficient to give the entire axial heat flux profile, since near the end of the active heat transfer length the local differentiation of the mercury temperature profiles could not be made with accuracy. However, with the known values of the average heat flux in the superheated region, the shape of local heat flux distributions could be estimated in the end region. The estimated profiles are shown in Figures (41) to (56).

Also shown in these figures, the points IB, C, and IS indicate the approximate location of boiling inception, critical heat flux condition, and initiation of superheating for each test run. It can be seen from these figures that, if the "entrance effect" is excluded before and after these points, the local heat flux in the individual heat transfer regions increases or decreases almost linearly. This effect can be more clearly seen from those runs with long boiling sections in Figures (52), (53), and (54).

Local qualities calculated from Equation (A70) are plotted in Figures (21) to (36). The results show that the conventional assumption of linear variation in quality versus length is not always correct, especailly for the low and high quality regions and is acceptable only in the intermediate quality range, i.e., 0.2 to 0.8.

Local values of the overall heat transfer coefficient, U, were calculated from Equation (A73), and the results are presented in Figures (41) to (56). Due to the lack of reliable q" values near the end of the test section, the distribution of U is extended by dotted lines to the known value at the boiler exit. At the boiler exit, the superheated vapor heat transfer coefficient was estimated by the conventional Dittus-Boelter equation, modified for helical flow as follows:

$$h_v = 0.023 \left(\frac{k_b}{D_e}\right)\left(\frac{C_p \mu}{k}\right)_b^{0.4} \left(\frac{G_H D_e}{\mu_b}\right)^{0.8} \qquad (2)$$

where the subscript b denotes the fluid properties evaluated at fluid bulk temperature.

The local values of U were then used to calculate the local mercury heat transfer coefficients from Equation (A74). All the local h_{Hg} results were tabulated for each individual heat transfer region (Tables 7, 8, 10, 11). In the following section, a more detailed discussion of these h_{Hg} values is given.

2. Local Heat Transfer Coefficients and Correlations

Subcooled Liquid Region, h_L

Results of subcooled liquid heat transfer coefficients are summarized in Table (7). Figure (57) shows a comparison of the present data to the conventional predictions by Lyon[14] and Lubarsky and Kaufman[15]. When written in terms of helical flow parameters, these two equations are:

$$\frac{h_L D_e}{k_L} = 7 + 0.025\left(\frac{G_H D_e C_{PL}}{k_L}\right)^{0.8} \quad \text{(Lyon's Equation)} \qquad (3)$$

$$\frac{h_L D_e}{k_L} = 0.625\left(\frac{G_H D_e C_{PL}}{k_L}\right)^{0.4} \quad \text{(Lubarsky - Kaufman Equation)} \qquad (4)$$

As shown in the figure, the mercury data fit well with the Lubarsky-Kaufman equation when the Peclet number, $N_{Pe} = \left(\frac{G_H D_e C_{PL}}{k_L}\right)$, was less thant 250; when the Peclet number was larger than 250, the data were close to the prediction of Lyon's equation.

Nucleate Boiling Region, h_{NB}

Sixty-six local nucleate boiling data points were obtained by the procedure discussed in Appendix (I) and were tabulated (Table 8). Figure (58) presents the calculated heat transfer coefficients in the nucleate boiling region, h_{NB}, versus the local heat flux, q", with mass velocity, G_{Hg}, and saturation temperature, T_{Sat}, used as parameters. From these curves, it is clear that the mass velocity and saturation temperature (or pressure) both have an effect in increasing the nucleate boiling heat transfer coefficient. This can be seen more clearly by comparing curves (5) and (7) for the mass velocity effect, and curves (7) and (8) for the boiling temperature effect. Figure (59) presents q" versus ΔT, where ΔT, the temperature difference between the wall temperature and fluid saturation temperature, was obtained by the following equation:

$$\Delta T = T_{wall} - T_{Sat} = \frac{q''}{h} \qquad (5)$$

The approximate liquid metal forced convection heat transfer equation (Nu = 7) and available mercury pool boiling data are also presented in Figure (59) for comparison. The pool boiling curve and data point at $T_{Sat} = 950^{o}F$ were cited from the test reported by Atomics International[16]. Another set of pool boiling curves for elevated saturation temperature levels were obtained by extending the Russian pool boiling equation[17] at 14.7 psia or $680^{o}F$. The pool boiling equation[17] reads:

$$h_{PB} = 10.4\ (q''_{PB})^{0.57}\ \text{Btu/hr-ft}^2\text{-}^{o}\text{F} \qquad (6)$$

The Cichelli-Bonilla correlation [18]:

$$\left(\frac{q''}{q''_c}\right)_{PB} = \left(\frac{\Delta T}{\Delta T_c}\right)^n \tag{7}$$

was employed to obtain:

$$q''_{PB} = q''_c \left(\frac{(\Delta T)}{\Delta T_c}\right)^{2.33} \tag{8}$$

where the critical heat flux and ΔT_c were obtained from Zuber's Equation[19] for selected saturation temperatures.

To examine the dependence of h_{NB} on heat flux and quality, h_{NB} was plotted versus q" for selected data ponts having approximately the same qualities, and verus x for selected data points having approximately the same heat fluxes. Figure (60) shows that h_{NB} increases with increasing heat flux, whereas Figure (61) shows that h_{NB} is virtually independent of the local qualities for selected constant heat flux levels. Moreover, the increase in h_{NB} with mass velocity as shown in these figures can be attributed to a heat flux effect since, in the two-fluid heat exchanger, heat flux increases in proporation to mass velocity at constant quality.

To ascertain if any detectable trend existed in the data of h_{NB}, as a function of radial acceleration developed by the helical insert, Figure (62) was constructed by plotting h_{NB} versus $(1 + A_R)$, where A_R denotes the radial acceleration of the annular liquid at the wall surface and is given by the following expression [6]:

$$A_R = \frac{2}{D_i g_c} \left[\frac{xG_{Hg}}{\rho_V \sqrt{\rho_L / \rho_V}} \left(\frac{\pi D_i}{P}\right)\right]^2 \tag{9}$$

As shown in Figure (62), the effect of local radial acceleration A_R is an increase in the nucleate boiling heat transfer coefficient at the low acceleration field or the low quality region, $x < 0.10$ (since $A_R \sim x^2$). It can be seen from this figure that the degree of increasing h_{NB} by radial acceleration is gradually decreased as the quality is increased. For $x > 0.35$, there is almost no effect on h_{NB} by A_R. Somewhat similarly, the pool boiling data of Merte and Clark[20] showed the effect of acceleration field on nucleate pool boiling of water. Their results showed an increase in h_{NB} with increasing acceleration fields at low heat fluxes, and a decrease in h_{NB} with increasing acceleration fields at high heat fluxes. However, in the present experiments the reverse effect at higher qualities was not observed, i.e., h_{NB} did not decrease as the acceleration field increased.

The evidence in Figures (60) and (61) that h_{NB} was strongly influenced by heat flux and much less influenced by quality, led to a further investigation of the heat transfer mechanism of wetted mercury boiling inside a tantalum tube. As noted in Reference (21), a boiling mechanism termed as "film evaporation", which is based upon conduction through the thin liquid film with subsequent evaporation from the film surface, predicts the h_{NB} to be markedly influenced by quality and to decrease with increasing temperature levels. References (21) and (22)note another boiling mechanism, "bubble nucleation", in which h_{NB} increases with both heat flux and temperature level. Hence, Figures (60) and (61) suggest that there may be bubble nucleation for mercury in forced convection bulk boiling. Below is a more detailed analytical study of these two heat transfer models. The analytical flow pattern is assumed to consist of a thin, continuous, and concentric layer of mercury liquid on the wall, with the remaining liquid entrained

in the vapor core and traveling with the vapor.

Film Evaporation Model - The heat transfer mechanism is assumed to be conduction from the wall to the liquid-vapor interface through the thin layer of liquid on the wall. The vapor is then generated by evaporation at existing liquid-vapor interfaces. Evaporation of the entrained liquid droplets is neglected, and the interface is assumed to be at the local saturation temperature. By utilizing the heat conduction equation through the annulus liquid layer, the following expression was obtained:

$$\frac{h_{FE} D_i}{k_L} = \frac{2}{\ell n \left(\frac{D_i}{D_V} \right)} \tag{10}$$

where D_V denotes the diameter of the vapor core.

Equation (10), rewritten in terms of the average void fraction and mass fraction of the entrained liquid is as follows:

$$\frac{h_{FE} D_i}{k_L} = \frac{-4}{\ell n \left[1 - \left(\frac{1-x}{x} \right) \frac{\rho_V}{\rho_L} \alpha \, (K-E) \right]} \tag{11}$$

where

K = the slip ratio obtained from the continuity equation

$$= \frac{\rho_L}{\rho_V} \left(\frac{x}{1-x} \right) \left(\frac{1-\alpha}{\alpha} \right) \tag{12}$$

E = the fraction of the entrained liquid flowing in the vapor core.

By assuming E = 0, Equation (11) reduced to the following simple expression:

$$h_{FE} = -\frac{4k_L}{D_i \ell n\,(\alpha)} \tag{13}$$

The relationship between quality and void fraction is given by the momentum exchange model from Reference (23):

$$\frac{1 - x}{1 - \alpha} + \frac{x^2}{\alpha}\left(\frac{\rho_L}{\rho_V}\right) - \frac{1}{2}\left(\frac{1 - x}{1 - \alpha}\right)^2 = \frac{1}{2} \tag{14}$$

By simply letting the slip ratio equal one, the following was obtained:

$$\left(\frac{1 - \alpha}{\alpha}\right)\left(\frac{x}{1 - x}\right)\frac{\rho_L}{\rho_V} = 1 \quad \text{(homogeneous model)} \tag{15}$$

Equations (14) and (15) are plotted in Figure (63) for each saturation temperature level. The void fraction α was then obtained from Figure (63) by knowing the local quality. Subsequently, the heat transfer coefficient due to film evaporation alone was calculated from Equation (13). To obtain agreement between the heat transfer coefficient at zero quality and the fully developed single-phase liquid value, an interpolation equation was proposed to obtain the heat transfer coefficient for the film evaporation model in the nucleate boiling region. This equation reads:

$$(h_{TP})_{FE} = \left[h_L^2 + h_{FE}^2\right]^{\frac{1}{2}} \tag{16}$$

with h_L calculated by Equation (3). As indicated by Equation (16), h_{TP} approaches the single-phase liquid value at low qualities and approaches the film evaporation value at high qualities.

Bubble Nucleation Model - In this model, vapor is assumed to be generated by the formation of bubbles at the wall of the tube, with subsequent growth and transport of these bubbles through the liquid

layer into the vapor core. The heat transfer coefficient was obtained by a superposition of nucleate pool boiling and liquid forced convection as recommended by Kutateladze[24], i.e.,:

$$(h_{TP})_{BN} = \left[h_L^2 + h_{PB}^2 \right]^{\frac{1}{2}} \qquad (17)$$

where h_L and h_{PB} were evaluated by Equations (3) and (6), respectively.

The calculated h_{TP} from Equations (16) and (17) were used for comparison with the present nucleate boiling data. The ratio of $\frac{h_{exp}}{h_{TP}}$ is shown versus vapor quality and versus heat flux in Figures (64) and (65), respectively.

As shown in these figures, the data correlated with the film evaporation model are more scattered than those correlated with the bubble nucleation model. In Figure (65), the well-grouped data of the bubble nucleation model show the independence of vapor quality. This strongly indicates that the mechanism of forced-convection boiling mercury might be the bubble nucleation in the nucleate boiling region. Furthermore, based upon the present results, a rather generalized correlation equation for mercury heat transfer coefficient in the nucleate boiling region is:

$$h_{NB} = 0.6 \left[h_L^2 + h_{PB}^2 \right]^{\frac{1}{2}} \qquad (18)$$

with h_L, h_{PB} given in Equations (3) and (6), respectively.

A correlation of the nucleate boiling heat transfer coefficients was attempted, based upon the following reasoning :

(1) The results from Figure (64) and (65) suggest that there may be bubble nucleation for mercury in forced convection bulk boiling. It is a known fact that a boiling mechanism based upon this bubble nucleation model predicts the heat transfer coefficent to be markedly influenced by heat flux, virtually unaffected by the vapor quality, and increased with increasing temperature level[21] Furthermore, the liquid metal pool boiling data of Bonilla[22], for which bubble nucleation is presumed to occur, show an increase in heat transfer coefficient with both heat flux and temperature level. On the contrary, a boiling mechanism based upon the film evaporation model predicts the heat transfer coefficient to be increased with increasing vapor quality, decreased with increasing temperature level[21], and, probably, influenced by heat flux, depending upon the particular analytical flow model chosen. Therefore, the heat flux and saturation temperature (or saturation pressure) are thought to be important parameters affecting the heat transfer coefficient in the nucleate boiling region. The local vapor quality is presumed to have no effect upon the heat transfer coefficient in this region for all saturation temperatures.

(2) The mass velocity, G, must also be a significant parameter affecting the heat transfer coefficient. Physically, in the nucleate boiling region with a thin liquid layer on the wall, the high flow rate would shear off liquid from this annular layer to increase the heat transfer coefficient.

(3) The effect of the local acceleration field on the heat transfer coefficient in the nucleate boiling region is neglected.

These three considerations resulted in the following functional relation:

$$h_{NB} = (\text{constant})\ (G)^{a}\ (P_{Sat})^{b}\ (q'')^{c} \qquad (19)$$

The expondent "c" was determined by taking an average slope from lines 1, 2 & 3 presented in Figure (58). The parameters G and P_{Sat} did not vary significantly among these lines in the determination of "c". Followiing this approach, "c" was found to be approximately 0.85. The exponent "b" was then determined by plotting $\frac{h_{NB}}{(q'')^{0.85}}$ versus P_{Sat} on a log-log scale at approximate constant values of G. As shown in Figure (66), "b" was thus determined to be 0.54. Similarly, the exponent "a" was determined from Figure (67) by plotting $\frac{h_{NB}}{(q'')^{0.85}(P_{sat})^{0.54}}$ versus G on a log-log scale and was found to be approximately 0.65. Finally, from the correlating plot in Figure (68), the dimensional constant was determined. The correlation equation has the following final form:

$$h_{NB} = 3.09 \times 10^{-4}\ (G)^{0.65}(P_{sat})^{0.54}(q'')^{0.85} \qquad \frac{Btu}{hr\text{-}ft^{2}} \qquad (20)$$

with a scatter band of $\pm$ 20%.

Further effort was made to detect if any trend existed in h_{NB} as a function of the local acceleration field generated by the boiler insert. Figure (69) is a plot of the expression $h_{NB}/(G)^{0.65}(P_{Sat})^{0.54}(q'')^{0.85}$ versus the local acceleration field, $(1 + A_R)$, where A_R is

obtained from Equation (9). The data in Figure (69) suggests that the effect of the induced acceleration field upon h_{NB} is either negligible or is less than the data scatter of about $\pm$ 20% over the range covered.

Critical Heat Flux, q''_c As described in Appendix (I), the onset of the critical flux condition was determined by finding an inflection point along the shell temperature profile. The critical heat flux data obtained in this manner are tabulated in Table (9). Experiments in pool boiling have indicated that the critical heat flux is proportional to the fourth root of the local acceleration [25] [26]; therefore, the radial acceleration produced by the helical insert might logically have a similar effect on the critical heat flux in forced convection boiling. As recommended in Reference (6), the crtical heat flux data can be correlated in the following form,

$$q''_c = \frac{\left(1 + A_R\right)^{\frac{1}{4}} q''_{PBc}}{1+n\left(\frac{x_c}{1 - x_c}\right)} \qquad (21)$$

where q''_{PBc} is the critical heat flux for pool boiling, and the empirical constant, n, can be determined by experiment.

References (5) and (6) correlated forced convection potassium critical heat flux data reasonably well by using the form of Equation (21). The value of q''_{PBc} was taken to be 10^6 Btu/ hr-ft^2, and the constant, n, was empirically determined to be 2.

Following this procedure, the present Mercury critical heat flux data can be reasonably well represented by the following equation:

$$q''_c = \frac{(1 + A_R)^{\frac{1}{4}} (10)^6}{1 + 4\left(\frac{x_c}{1 - x_c}\right)} \qquad (22)$$

In Figure (70) the critical heat flux data are presented by a plot of the expression $\frac{q''_c}{(1 + A_R)^{\frac{1}{4}}}$ versus x_c, the quality at critical heat flux condition. Also in this figure, the boiling potassium critical heat flux data from References (5) and (6) are plotted for comparison.

To determine the effect of boiling temperature and mass velocity on the critical heat flux, Figure (71) was prepared. The result shows that there is no definite grouping of the data with respect to either mass velocity or boiling temperature.

Transition Boiling Region, h_{TB}

As described before, after onset of the critical heat flux condition and before establishment of the superheated vapor condition, the test section was in the transition boiling region. This region was distinguished by the shell side temperature profile as shown in Figures (21) to (36). In the constant heat flux boiling potassium experiments,[5] the transition boiling region was observed by relatively large tube wall temperature oscillations which increased in amplitude when the quality was increased. However, as pointed out by Peterson[6] in his two-fluid boiling potassium experiment, these temperature oscillations were less in magnitude in the transition boiling region for the two fluid case and the local heat flux decreased with increasing quality. Furthermore, as concluded in Reference (6), the maximum possible wall temperature was limited by the local primary

fluid temperature, and it was possible that the film boiling region was never reached.

The transition boiling data calculated following the procedures in Appendix (I) are presented in Table (10). An attempt to seek an empirical correlation of this data was made by considering the following analytical flow model which is thought to exist in the transition boiling region. The flow is assumed to consist of liquid droplets or patches on the wall surface positioned in a random manner with the remainder of the wall surface that is not covered by liquid to be exposed to dry mercury vapor at local saturation temperatures. If the heat transfer

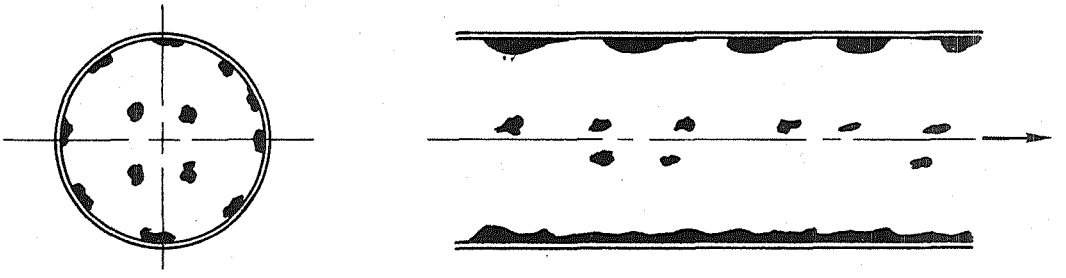

of the entrained mercury liquid is neglected in the vapor core, the heat transfer mechanism for this analytical model can be assumed to be local boiling for the liquid droplet and forced convection for the dry vapor areas. Therefore, the average heat transfer rate can be written by combining these contributions as;

$$q''_{ave} = q''_{LB}\left(\frac{A_L}{A_T}\right) + q''_{V}\left(\frac{A_V}{A_T}\right) \qquad (23)$$

or

$$h_{TB} = \frac{q''_{ave}}{T_w - T_{Sat}} = h_{LB}\left(\frac{A_L}{A_T}\right) + h_{Vx}\left(\frac{A_V}{A_T}\right) \qquad (24)$$

where h_{Vx} indicates the vapor forced convection heat transfer coefficient evaluated at local conditions with fractional mass of mercury vapor. Alternately, the equation can be rewritten as:

$$\frac{h_{TB} - h_{Vx}}{h_{LB} - h_{Vx}} = \frac{A_L}{A_T} \tag{25}$$

since $A_L + A_V = A_T$.

The single-phase vapor forced convection heat transfer coefficient evaluated at local conditions can be simply calculated by the equation:

$$h_{Vx} = h_V (x)^{0.8} \tag{26}$$

with h_V given by the conventional Dittus-Boelter or Colburn equations modified for helical flow. The local liquid boiling heat transfer coefficient, h_{LB}, can be approximately calculated by using the Cichelli-Bonilla relation:

$$h_{LB} = h_{LBc} \left(\frac{\Delta T}{\Delta T_c}\right)^{1.33} \tag{27}$$

where h_{LBc} is defined as the heat transfer coefficient at the critical heat flux condition. For the purpose of simplification, if $h_{Vx} \approx h_V$, and $h_{LB} \approx h_{LBC}$, then Equation (25) reduces to

$$\frac{h_{TB} - h_V}{h_{LBc} - h_V} = \frac{A_L}{A_T} \tag{28}$$

The problem remaining is to evaluate the area ratio $\frac{A_L}{A_T}$. It is necessary to specify the size and density of the liquid droplets. To avoid complication in this respect, two simple approaches to evaluate $\frac{A_L}{A_T}$ are proposed.

Case I Liquid Droplets with Constant Size - In this case, the liquid droplets are all assumed to have a disk-shape with diameter, d, and height, d. The number of droplets per unit area, n, is assumed to decrease when the droplets start to boil. Considering the liquid volume within a small tube length, ΔL, the following equation is obtained:

$$(\pi D_i \Delta L)\ n\ \frac{\pi d^3}{4} = (1 - \alpha)\ A_F \Delta L \tag{29}$$

where A_F = flow area perpendicular to tube axis.

Solving for n, Equation (29) yields:

$$n = \frac{(1 - \alpha)\ A_F}{\pi D_i \left(\frac{\pi d^3}{4}\right)} \tag{30}$$

The ratio of liquid area to the total heat transfer area can thus be written as:

$$\frac{A_L}{A_T} = \frac{(\pi D_i \Delta L)\ n \left(\frac{\pi d^2}{4}\right)}{\pi D_i \Delta L} = \frac{n \pi d^2}{4} \tag{31}$$

Combining Equations (30) and (31) yields:

$$\frac{A_L}{A_T} = \frac{(1 - \alpha) A_F}{\pi D_i d} \tag{32}$$

The assumed droplet diameter, d, can be eliminated from Equation (32) by using the condition at $\alpha = \alpha_c$, and $\frac{A_L}{A_T} = 1$ (continuous liquid film up to critical heat flux point). Hence:

$$d = \left(\frac{1 - \alpha_c}{\pi D_i}\right) A_F \tag{33}$$

Since the size of the droplet is assumed to be unchanged, Equations (32) and (33) can be combined to yield a final expression for the area ratio:

$$\frac{A_L}{A_T} = \left(\frac{1 - \alpha}{1 - \alpha_c}\right) \tag{34}$$

Case II Liquid Droplet with Constant Density - In this case, the number of liquid droplets per unit area is assumed constant, and the disk-shaped liquid droplets shrink as fluid evaporates. From equation (29):

$$d = \left[\frac{4\ (1 - \alpha)\ A_F}{n\ \pi^2\ D_i}\right]^{1/3} \tag{35}$$

Combining the above expression into Equation (31) yields:

$$\frac{A_L}{A_T} = \frac{n\pi}{4} \left[\frac{4(\ 1 - \alpha)\ \ A_F}{n\ \pi^2\ D_i}\right]^{2/3} \tag{36}$$

Using the condition at $\alpha = \alpha_c$, and $\frac{A_L}{A_T} = 1$ gives:

$$n = 4\pi \left[\frac{D_i}{(1 - \alpha_c)\ A_F}\right]^2 \tag{37}$$

Finally, since n is assumed to remain unchanged as the fluid evaporates, Equations (36) and (37) are combined yielding:

$$\frac{A_L}{A_T} = \left(\frac{1 - \alpha}{1 - \alpha_c}\right)^{2/3} \tag{38}$$

With the expression in Equations (32) and (36) for $\frac{A_L}{A_T}$, the final form for correlating the transition boiling heat transfer coefficient can be written as:

Case I Constant Droplet Size

$$\frac{h_{TB} - h_{Vx}}{h_{LBC} - h_{Vx}} = \left(\frac{1 - \alpha}{1 - \alpha_c}\right) \tag{39}$$

Case II Constant Droplet Density

$$\frac{h_{TB} - h_{Vx}}{h_{LBc} - h_{Vx}} = \left(\frac{1 - \alpha}{1 - \alpha_c}\right)^{2/3} \tag{40}$$

The ratio $\frac{1-\alpha}{1-\alpha_c}$ can be written in terms of local quality and fluid properties by using the continuity equation for two-phase mixtures. This is:

$$\frac{1 - \alpha}{1 - \alpha_c} = \left[\frac{1 + K_c\left(\frac{\rho_V}{\rho_L}\right)_c\left(\frac{1 - x_c}{x_c}\right)}{1 + K\left(\frac{\rho_V}{\rho_L}\right)\left(\frac{1 - x}{x}\right)}\right]\left(\frac{1 - x}{1 - x_c}\right)\left(\frac{x_c}{x}\right)\left[\frac{K\left(\frac{\rho_V}{\rho_L}\right)}{K_c\left(\frac{\rho_V}{\rho_L}\right)_c}\right] \tag{41}$$

For mercury, the ratio $\frac{\rho_V}{\rho_L}$ is negligibly small when compared with the values of one: If also $\left(\frac{\rho_V}{\rho_L}\right)_c = \frac{\rho_V}{\rho_L}$, and if K is assumed to be constant and numerically equal to K_c, the equation can be simplified to:

$$\frac{1 - \alpha}{1 - \alpha_c} = \frac{(1 - x)\, x_c}{(1 - x_c)\, x} \tag{42}$$

Consequently the predictions for h_{TB} can be further simplified from Equations (39) and (40). For the constant droplet size case:

$$\frac{h_{TB}}{h_v} = 1 + \left(\frac{h_{LBc}}{h_V} - 1 \right) \frac{(1 - x)\, x_c}{(1 - x_c)\, x} \tag{43}$$

and for the constant droplet density case:

$$\frac{h_{TB}}{h_V} = 1 + \left(\frac{h_{LBc}}{h_V} - 1 \right) \left[\frac{(1 - x)x_c}{(1 - x_c)x} \right]^{2/3} \tag{44}$$

These two equations fit two boundary points of the transition boiling region, i.e.,

as $x \longrightarrow x_c$ $\qquad$ $h_{TB} \longrightarrow h_{LBc}$ (critical heat flux condition)

and

as $x \longrightarrow 1.0$ $\qquad$ $h_{TB} \longrightarrow h_V$ (superheated vapor starts)

Figure (72) shows a plot of $\left(\frac{h_{TB} - h_{Vx}}{h_{LBc} - h_{Vx}} \right)$ versus $\frac{(1 - x)x_c}{(1 - x_c)x}$ using the transition boiling data listed in Table (10). The values of h_{LBc} were taken from the critical heat flux results in Table (9), and h_{Vx} was calculated for mercury vapor at local temperatures by the modified Dittus-Boelter Equation (2). This figure shows a remarkably good correlation of the transition boiling data. Except for the regions near the two boundary points, i.e., critical heat flux condition and superheated vapor starting point, all the data can be represented linearly by the following empirical expression:

$$\frac{h_{TB} - h_{Vx}}{h_{LBc} - h_{Vx}} = 0.4805 \left[\frac{(1 - x)\, x_c}{(1 - x_c)x} \right]^{0.68} \tag{45}$$

To see how good the analytical predictions would be for h_{TB} in Equations (43) and (44), Figures (73) and (74) were plotted using those equations together with the present data. These figures show that the analytical predictions yield much higher values when compared to the experimental results.

Since the major assumption used in the derivation of these analytical predictions was the negligible effect from entrained liquid droplets, the discrepancies between the analytical predictions and the experimental results might be attributed mainly to the liquid entrainment effect. Following this argument, a parameter, Ω, was considered as the entrainment effect and was defined as:

$$\Omega = \frac{\text{Entrainment at any location in the transition boiling region}}{\text{Entrainment at critical flux condition}} \qquad (46)$$

Hence a series of parametric lines were added to Figures (75) and (76) by introducing the parameter, Ω, to Equations (43) and (44). The parameter Ω shows the inadequacy of the analytical flow models to account for the actual picture of transition boiling. The parametric line with $\Omega = 1.0$ implies that the liquid entrainment throughout the transition boiling region is kept virtually unchanged, and its value is inherited from the critical heat flux condition throughout the transition boiling region. In this way, all the data points were identified from these figures as having their own individual Ω values. A plot of Ω versus $(1 + A_R)$ for each data point was then constructed, as shown in Figure (75), for both analytical flow models considered. It can be seen from Figure (75) that the entrainment parameter, Ω, is strongly influenced by local radial accelerations developed by the helical insert. Moreover, the value of Ω seems to approach its lower

limit asymptotically as the value of $(1 + A_R)$ goes higher. This result tends to confirm the interpretation of Ω as an entrainment effect, since the radial acceleration should reduce entrainment. The result also suggests that vortex inserts tend to eliminate the liquid entrainment in the transition boiling region. However, the present results only provide a qualitative conclusion about the entrainment effect, and it is believed that more experiments with various sizes of inserts should be carried out in this area before drawing a complete picture of the entrainment behavior in the transition boiling region.

Empirical expressions for Ω in terms of radial accelerations were obtained from Figure (75). For the constant density model:

$$\Omega = 2.62\ (1 + A_R)^{-0.45} \tag{47}$$

and for the constant size model:

$$\Omega = 3.465\,(1 + A_R)^{-0.6} \tag{48}$$

It should be noticed that the expressions for Ω in Equations (47) and (48) were obtained only on an experimental basis and under the present test conditions.

Correlations for liquid metal in the transition boiling region were available from current literature[5] [6]. As suggested in Reference (6), the following expression was used to correlate potassium transition boiling data:

$$\frac{\left(\frac{h_{TB}}{h_v} - 1\right)}{(1 + A_R)^a} = B \left(\frac{1 - x}{x}\right)^b \left(\frac{1}{\Delta T}\right)^c \tag{49}$$

Following a conclusion from pool boiling results in the gravity field[24], the exponent a was given values of 1/4 to 1/5. B, b, and c were determined purely by the best fit with the data. As shown in Figure (76) all the data grouped nicely when represented by the following equation:

$$\frac{\left(\frac{h_{TB}}{h_V} - 1\right)}{(1 + A_R)^{1/5}} = 4.75 \times 10^3 \left(\frac{1 - x}{x}\right)^{0.35} \left(\frac{1}{\Delta T}\right) \qquad (50)$$

It must be emphasized, however, that Equation (50) is primarily an empirical expression covering only the present data range. Any extrapolation outside the data range should be made with caution.

Superheated Vapor Region, h_V

The superheated region is defined in the mercury temperature profile as the region initiated by a sudden temperature rise. The local heat transfer coefficients in this region were obtained by the calculational procedure discussed in Appendix (I), and the local data are summarized in Table (11).

The conventional single-phase prediction, the Dittus-Boelter equation, was used for comparison with the data. To account for the effect of the vortex insert, helical parameters were introduced. The modified Dittus-Boelter equation[6] for helical flow through tubes is therefore:

$$\left(\frac{h_{VH}}{C_{pb} G_H}\right) \left(\frac{c_p \mu}{k}\right)_b^{0.6} = 0.023 \left(\frac{G_H D_e}{\mu_b}\right)^{-0.2} \qquad (51)$$

where the subscript b indicates evaluation at local bulk temperature. As discussed in Appendix (I), the helix parameter for heat transfer was obtained for Equation (51) by employing the following relationship:

$$\frac{G_H}{G_a} = \frac{L_H}{L} = \sqrt{1 + \left(\frac{\pi D_i}{P}\right)^2} \tag{52}$$

Hence, Equation (51) was reduced to:

$$h_{VH} = h_{Va}\left[\left(\frac{L_H}{L}\right)^{0.8} \left(\frac{D_i}{D_e}\right)^{0.2}\right] \tag{53}$$

with h_{Va} given, for axial flow only, as:

$$h_{Va} = \left(\frac{k_b}{D_i}\right) 0.023\left(\frac{G_a D_i}{\mu_b}\right)^{0.8}\left(\frac{C_p \mu}{k}\right)_b^{0.4} \tag{54}$$

To account for the helical flow effect, a heat transfer parameter, K_h, was obtained from Equation (53), as follows:

$$\frac{h_{VH}}{h_{Va}} = K_h = \left(\frac{L_H}{L}\right)^{0.8}\left(\frac{D_i}{D_e}\right)^{0.2} \tag{55}$$

This is similar to the pressure parameter, K_p, which was defined in Equation (A52).

Figure (77) shows a plot of the superheated vapor data together with the prediction from Equation (55). The results shows that the modified Dittus-Boelter equation with the heat transfer parameter K_h is quite adequate to predict the heat transfer coefficient for mercury vapor flowing in a tube with a helical insert. However, the parameter K_h in Equation (55) is good only for certain types of

inserts; for instance, the use of K_h to predict h_{VH} failed in the wire coil insert region in the present test.

The mercury temperature profiles and the heat transfer data for the wire coil insert region (beyond the tube length of 12 feet) are recorded in Table (11) under Run Nos. 9, 10, 11, 12, 13 and 14. It was found that introducing K_h as expressed in Equation (55) gives an underestimate of the test results. Since there is no analytical expression for K_h applicable to the wire coil insert, the only evaluation for K_h is experimental. From Figure (78) which shows results for heated air heat transfer coefficients with various types of inserts in tubes[27], an experimentally-determined heat transfer parameter was obtained for the presently employed wire coil insert geometry ($d/D_i = 0.1428$, $P/D_i = 0.97$). The K_h value was found to be approximately 2.6. The heat transfer data in the wire coil region are shown in Figure (79) together with Equation (53) (using K_h equal to 2.6), and the agreement is quite good. To show the deviation of flow with a wire coil insert from axial flow, Equation (54) was also plotted in Figure (79). This result indicates that single phase tests with air can be employed to predict mercury superheated vapor heat transfer coefficients, even without an established theoretical forumulation.

3. Local Two-Phase Pressure Drop

The local saturation pressures of boiling mercury at the measured mercury saturation temperatures were obtained from the vapor pressure curve, and the results were plotted in Figures (21) to (36) for all the test runs. The local two-phase pressure gradients in the boiling region, obtained through Equation (A75), are tabulated in

Table (12) for various positions along the boiling length.

Figure (80) shows that the local two-phase pressure gradient varies along the normalized boiling length, in the low and intermediate quality regions and becoming constant in the high quality region. In Figures (81) and (82), the effects of saturation temperature and mass velocity on the local variation of $\left(\frac{dp}{dz}\right)_{TP}$ are presented. The two-phase momentum pressure gradients $\left(\frac{dp}{dz}\right)_{TPm}$ calculated by using Equation (A77) are tabulated in Table (12), and selcted values are plotted in Figure (82) for comparison. The two-phase frictional pressure gradients $\left(\frac{dp}{dz}\right)_{TPf}$, calculated by subtracting the momentum pressure gradient from the total gradient, are tabulated in Table (12) and represented in Figures (83) to (85). In these figures, the predictions from the modified Martinelli-Nelson model and the homogeneous model were also plotted for comparison. The data fall generally between the two predictions in the higher quality region, $x > 0.3$. The general trend of the present data, however, is closer to the modified Martinelli-Nelson prediction; the homogeneous model gives an underestimation of the two-phase frictional pressure gradient. The elevation pressure gradient given in Equation (A78) was found to be a small fraction of the total pressure gradient, particularly in the high quality region. Hence, its contribution is neglected when computing $\left(\frac{dp}{dz}\right)_{TPf}$ from Equation (A76). Using the experimentally-determined $\left(\frac{dp}{dz}\right)_{TPf}$, the local two-phase pressure multipler ϕ defined in Equation (A88) was calculated, and the results are tabulated in Table (12). Figures (86) to (91) compare these experimentatlly-determined values with the modified Martinelli-Nelson model and the homogeneous model predictions, showing that the present data of $\phi_{exp.}$ fall between these two predictions and show better agreement with the modified Martinelli-Nelson model. In the low

quality region, both models underestimate the actual test data.

The final conclusion drawn from the present results is that the pressure loss during forced convection boiling of mercury in tubes containing helical inserts can be fairly well predicted by the modified Martinelli-Nelson model, provided the single-phase liquid pressure losses are known. Predictions for single-phase pressure drop through tubes containing helical inserts currently are available in References (28) and (29).

C. Discussion

Certain assumptions were made in reducing the data as described in the calculational procedures in Appendix (I). These assumptions are summarized here and their effects on the accuracy of the data are discussed.

Assumptions

(1) The outer shell wall temperature is taken as an average value over the measurements by the five calibrated thermocouples located at equal intervals circumferentially on the outer shell wall.

(2) The axial NaK bulk temperature gradient is equal to the axial shell wall temperature gradient in the boiling region.

(3) The Dwyer's equation (Equation A5) for calculating the shell-side NaK film coefficient is valid.

(4) Effects of the axial conduction in the shell-side NaK flow and in both the tantalum tube and stainless steel NaK layer containment tube walls are negligible.

(5) Effects of uneven thickness of the boiler tube wall, NaK layer, and NaK containment tube wall are neglected.

(6) Axial variation of heat flux on the shell-side film coefficient is neglected.

(7) Heat transfer through the NaK layer is considered as conduction only. Hence, the effect from natural convection of this thin layer (0.0275-inch) is neglected.

(8) Eccentricity of the shell and tube alignment and its effects on data measurement are not considered.

Validity of Assumptions

The validity of these assumptions was carefully examined. It was found that the major uncetainty arose from the prediction of the shell-side film coefficient by using Dwyer's equation. Dwyer's prediction for concentric annuli (Equation A5) is based upon the conditions (1) uniform heat flux at the inner wall, (2) fully developed temperature and velocity profiles, (3) negligible axial conduction, and (4) no effect of transverse temperature variation on the physical properties of the flowing metal. Of course, none of these conditions exist in the shell-side flow of the present two-fluid test. It is possible to calculate the axial variation in the local heat transfer coefficient for any arbitrary axial variation in wall heat flux, but the calculations are difficult and, consequently, few results are available. For the case of turbulent flow of low-Prandtl-number liquids, there are even fewer analytical predictions available to account for the variable wall heat flux effect. Hsu[30] carried out computations for the case of sinusoidal wall heat flux distribution and slug-flow condition in pipes. It is believed that the slug-flow results in Reference (30) can be used to estimate the axial variation of the heat transfer coefficient for turbulent flow if the Peclet number is not too large (< 500). As shown in Figures (41) to (56),

the present heat flux distribution for several test runs were roughly approximated by sinusoidal distribution, excluding the end regions. Figure (92), as cited from Hsu's results, shows the axial variation of the local Nusselt number as a function of the non-dimensional pipe length, z/L, and a parameter, $\frac{N_{Pe}D}{L}$. At z/L = 0.5, the local Nusselt number value is the same as that for uniform-wall heat flux, because the heat flux in that region is relatively uniform. Excluding the end regions, the axial variation of the local Nusselt number diminishes as the parameter $\frac{N_{Pe}D}{L}$ decreases. For example, curve No. 1 $\left(\frac{N_{Pe}D}{L} = 2.0\right)$ shows that the local Nusselt number could be replaced by the value calculated for uniform-wall heat flux (at z/L = 0.5) over most of the pipe length without producing any appreciable errors. For the present test where the parameter $\frac{N_{Pe}D}{L}$ is equal to 1.52, the degree of uncertainty in calculating the shell-side NaK film coefficient through Dwyer's equation (based on uniform-wall heat flux) is approximately $\pm$ 8% over most of the axial length.

Additional analytical estimates were made which verify this conclusion. A Nu profile plot analogous to that in Figure (92) is not known to be available for any prescribed heat flux distribution and turbulent flow conditions. Stein[31] has outlined a procedure for determining the local Nusselt number for flow through pipes, annuli, and parallel plates, where the velocity profile is established and where the wall heat flux may vary as any arbitrary function of the axial distance. For relatively long channel and axial distance not too close to the end regions, Stein developed the equation:

$$q'' + \sum_{n=1}^{\infty} R_n \frac{d^n q''}{d(z/D_e)^n} = h_{U\text{-}W\text{-}H\text{-}F} (t_w - t_b) \qquad (56)$$

where $h_{U-W-H-F}$ = fully developed heat transfer coefficient for uniform wall heat flux. The coefficient R_n generally is a function of N_{Pr}, N_{Re}, and channel geometry.

Unforunately, Stein's work is only verified for the infinite flat-plate case for which R_n can be computed from the relationship:

$$R_n = (-1)^n \left(\frac{N_{Nu}}{2}\right) \left(\frac{N_{Pe}}{2}\right)^n \sum_{m=1}^{\infty} \frac{C_m}{\lambda_m^{2n}} \tag{57}$$

The first five values of the coefficients C_m and λ_m^2 are given in Reference (31) for turbulent flow.

From Equation (56) we get:

$$(N_{Nu})_{local} = \frac{(N_{Nu})_{U-W-H-F}}{1 + \frac{1}{q''} \sum_{n=1}^{\infty} R_n \frac{d^n q''}{d(z/D_e)^n}} \tag{58}$$

Equation (58) was used in several runs of the present test to check the effect of axial variation of heat flux upon shell-side NaK conductance. In general, the results were consistent with the trend indicated by curve No. 1 in Figure (92). Clearly, the computed Equation (58) is not exactly for an annulus, in which case the coefficients C_m and λ_m^2 are not available at this time. It is felt, however, that Equation (58) does indicate how the local Nusselt number would vary with axial length for the annular case since it is known that the infinite flat-plate case is one of the limiting cases of an annulus.

Recent work on double heat exchangers also provides useful information on the prediction of local heat transfer coefficients. Nunge and Gill[32] in a pioneering analytical study calculated the heat transfer characteristics for laminar counter current flow in double-pipe heat exchangers. They based their analysis on a fully developed flow condition and assumed negligible axial conduction in both the heat exchanger walls and fluid streams. They obtained local and asymptotic Nusselt number changes as functions of several standard parameters. The results indicated that for long exchangers, say $\frac{L}{N_{Pe} D_e} > 0.5$, (in the present test $\frac{L}{N_{Pe} D_e} = 0.67$) a fully-developed U-W-H-F coefficient may be used along almost the entire axial length. However, Nunge and Gill's results are only true for laminar flow and all liquids.

In the case of liquid metal, for turbulent flow as for laminar flow, the local heat transfer coefficient is very much dependent on the thermal boundary conditions. For this reason, the results drawn for laminar flow of any liquids in Reference (32) can be applied to turbulent flow of liquid metal. In the absence of turbulent flow results, it is probably appropriate to assume that the turbulent-flow coefficient normalized with respect to the fully-developed turbulent flow U-W-H-F coefficient is the same as the comparable normalized coefficient for the laminar flow case.

Summarizing all the foregoing discussions on the validity of Dwyer's equation to calculate NaK film coefficient, it is felt that the degree of uncertainty on h_{NaK} would approximately be 8%. This uncertainty is probably greater if the axial conduction in the shell-side stream and eccentricity are present.

Estimates were also made of the axial tube wall conductions and were found to be negligible.

No estimation was made on the heat transfer mechanism through the very confined static-NaK layer with an average thickness of 0.0275-inch. It is conceivable that some unstable, free-convection cells might set up and some temperature fluctuations might prevail at any axial and lateral positions. However, the complex flow patterns and thermal conditions which might exist in this layer generally preclude the feasibility of any analytical attack.

The assumption of the axial shell wall temperature gradient in calculating local heat flux in the boiling region was justified through several heat balance calculations. The results generally checked within 5%.

Finally, it is believed that the average shell wall temperature taken over the five wall thermocouples would definitely eliminate part of the effect coming from eccentricity of the tube-and-shell alignment.

Accuracy of Data

Local Heat Flux, q'' - The degree of accuracy on the local heat flux calculation depends upon the assumption of the local shell wall temperature gradient and the way to obtain it. Through occasional heat balance checks and very careful performance on graphical differentiation in obtaining the local temperature gradient, it is believed that the accuracy on local heat flux is approximately 6%.

Local Overall Heat Transfer Coefficient, U - The accuracy of U, obtained from the local heat flux and the shell- and tube-side

fluid temperatures, depends primarily on the accuracy of those values. It is estimated that the present data for U may have a probable error of 10%. The local mercury saturation temperature required is the calculation for U is determined from the temperature profile measured by insert thermocouples. The helical insert employed in the present test induces a swirling motion in the flow and imposes radial acceleration on the fluid. If the flow pattern is visualized as a relatively thin layer of liquid adjacent to the wall with a vapor core, then there exists a radial pressure difference between the fluid close to the wall and that at the centerline. If it is assumed that the vapor is saturated at the centerline then the centerline temperature (measured by insert thermocouples) must be corrected to obtain the saturation temperature close to the wall for use in the calculation of U. Such corrections can be made through using the following equation from Reference (5):

$$T_w - T_{cb} = \frac{A_R}{2}\left(\frac{\rho_L D_i}{2}\right)\frac{T\, v_{LV}}{J\, h_{LV}}\left[1 - \left(\frac{D_{cb}}{D_i}\right)^2\right] \qquad (59)$$

However, it is found that such corrections are generally not necessary when evaluating the local overall heat transfer coefficient U.

Combined Wall Conductance, U_{cw} - The combined wall conductance, including those thermal resistances from the NaK film coefficient, stainless steel tube wall, static-NaK layer, and tantalum tube wall, has a variety of implicit errors. The major portion of error (approximately 10%) comes from the method of predicting h_{NaK} as previously discussed. No analytical estimates were made on tube and annuli wall thermal resistances, as they may be effected by their uneven wall thicknesses. Also, no estimate was made on the natural convection

effect on the heat transfer rate through the very thin static-NaK layer. The relative thermal resistances for this composite structure are presented in Figure (93) and the one for the static-NaK layer was obtained by treating it as conduction only. As the figure shows the NaK film coefficient resistance occupied almost of the total combined resistances. The resistance of the static-NaK layer, in which the natural convection effect was not considered, only occupied about 15% of the total resistance. In this respect, uncertainty in predicting the static-NaK thermal resistance will not appreciably affect the accuracy of U_{cw}. Allowing additional uncertainty due to these unknown effects, the probable error in U_{cw} is estimated to be 15%.

Local Mercury Heat Transfer Coefficient, h_{Hg} - The mercury heat transfer coefficients for various regions throughout the boiler were obtained by subtracting the combined thermal resistance U_{cw} from the overall resistance U calculated from local heat flux and temperature measurements. Hence, the accuracy of h_{Hg} will vary for different heat transfer regions. In Figure (94) typical data of h_{Hg} are presented and the subtraction performed to obtain these local values of h_{Hg} is also illustrated. Consequently, a detailed error analysis can be performed on h_{Hg} by using Figure (94) and the probable maximum errors for U and U_{cw} discussed before. In general, the analysis indicated that no serious error (less than 15%) can be made in h_{Hg} obtained in the transition, subcooled liquid, and superheated vapor regions, since over these regions the mercury thermal resistance is a relatively large fraction of the overall heat transfer coefficient. However, for the nucleate boiling region, as shown in Figure (94), the accuracy on h_{Hg} decreases as h_{Hg} is taken from locations closer to the critical heat flux point where the thermal resistance is small.

The worst case might happen as the expected errors in the prediction of U_{cw} are larger than the indicated mercury heat transfer coefficient taken close to the end of the nucleate boiling region. Typical examples showed that when h_{Hg} was 5500 Btu/hr-ft^2-°F or larger, the estimated error for h_{Hg} might exceed 35% if a 10% error for U and a 15% error for U_{cw} were assumed. For this reason, when establishing the correlation equation for h_{Hg} in the nucleate boiling region, h_{Hg} values over 5500 Btu/hr-ft^2-°F were not employed.

Critical Heat Flux, q''_c - The critical heat flux data is believed more accurate than h_{Hg} data and is estimated to have a probable error of 15%. The accuracy of q''_c primarily depends on how well the local graphical differentiation is performed along the shell temperature profile and on how accurate the critical heat flux point is located.

V CONCLUDING REMARKS

A considerable amount of experimental and analytical information on forced convection boiling of mercury in a tantalum tube has been obtained from the present investigation. The results presented in this report include both local and average heat transfer and pressure drop data from subcooled liquid to superheated vapor conditions for mercury at saturation temperatures from 975°F to 1120°F. The experimental data and the associated correlations are directly applicable to the design of once-through boilers for Space Power Rankine Cycle Systems employing mercury as a working fluid. Specific conclusions with respect to the heat transfer and pressure drop of boiling mercury follow.

A. Heat Transfer

(1) Liquid mercury heat transfer coefficients, h_L, were found to be in the range of 980 to 1850 Btu/hr-ft^2-°F. They are in fair agreement with the Lubarsky-Kaufman equation[15] when the modified Peclet Number, $N_{Pe} = \frac{G_H D_e C_p}{k}$, is less than 250, and with Lyon's equation[14] when P_e is greater than 250. Both equations were evaluated using helical flow parameters.

(2) The mercury nucleate boiling heat transfer coefficient, h_{NB}, was found to be in the range of 2100 to 7050 Btu/hr-ft^2-°F. Generally, they increase with increased heat flux (Figure 60) and are virtually

independent of quality (Figure 61). However, for quality less than 0.15, h_{NB} increases slightly with increasing quality.

(3) Vortex generator inserts were found to increase h_{NB} for the quality range less than 0.10. In the quality range $0.10 < x < x_c$, the increase in h_{NB} due to insert is gradually diminished.

(4) The heat transfer mechanism in the nucleate boiling region is believed to be bubble nucleation. This conclusion is supported by the fact that the measured h_{NB} increases with increasing heat flux and is virtually independent of quality (Figures 60 and 61). A qualitative study concerning the heat transfer model also affirmed this conclusion (Figures 64 and 65).

(5) Empirical correlation of h_{NB} (Figure 68) shows that h_{NB} increases as the mass velocity and saturation pressure increase and approximately in proportion to the 0.85 power of the heat flux under the present test conditions.

(6) The critical heat flux q''_c was found to be in the range of 1.86×10^5 to 4.5×10^5 Btu/hr-ft^2. The value of q''_c was found to decrease with increasing local vapor quality (Figure 70) and to increase approximately in proportion to the fourth root of the local acceleration field.

(7) Effects of mass velocity and saturation temperature on the critical heat flux were not observed within the present range of experimental data.

(8) The transition boiling heat transfer coefficient, h_{TB}, was found to be in the range of 1530 to 6500 Btu/hr-ft^2-°F. The values of h_{TB} generally decrease with increasing quality or with decreasing heat flux.

(9) Local data of h_{TB} were successfully correlated by the equation suggested in Reference (6). The correlation (Equation 50) states that h_{TB} decreases with increasing vapor quality, increases with increasing local acceleration field, and decreases with increasing wall to fluid temperature difference.

(10) Liquid droplet entrainment was suggested to be significant in the transition boiling region and to be strongly dependent upon the local acceleration field developed by the insert (Figure 75).

(11) An analysis based on adopting a flow model of constant droplet number in the transition boiling region was successful in correlating the present transition boiling heat transfer data after introducing the entrainment parameter (Figure 72).

(12) The large differences between wall and fluid temperature which characterize the film boiling region were not observed in the present two-fluid, temperature-controlled experiment.

(13) The superheated vapor heat transfer coefficient, h_V, is in the range of 45 to 110 Btu/hr-ft^2-°F. The h_V values can be generally correlated in the helical insert region by the conventional Dittus-Boelter equation after introducing the helical flow heat transfer parameter, K_h (Equation 55).

(14) In the case of the wire coil insert, the Dittus-Boelter equation fails to correlate the test data for h_v even after being modified for helical flow. The heat transfer parameter, K_h, was found to be 2.6 for the present wire coil insert geometry, $P/D_i = 0.97$ and $d/D_i = 0.1428$, agreeing with measurements made with air reported in Reference (27).

B. Pressure Drop

(1) Single-phase pressure drop for the helical insert can be predicted with reasonable accuracy by using the conventional Fanning equation after introducing a pressure parameter, K_p, for the helical flow condition.

(2) Single-phase pressure drop for the wire coil insert can not be predicted by the same method as the helical insert. The pressure parameter, K_p, was found to be $23 \pm 22\%$ for the present wire coil insert geometry $P/D_i = 0.97$ and $d/D_i = 0.1428$, agreeing roughly with measurements made with air reported in Reference (27).

(3) Local two-phase pressure gradients were found to be dependent upon the boiling length. They increase rapidly as the boiling starts and gradually become constant as the end of the boiling region is reached.

(4) Local two-phase momentum pressure gradients were found to be only about 10 percent of the total two-phase pressure gradients. Hence, the frictional pressure gradients dominate the pressure drop in the two-phase region.

(5) Local two-phase pressure gradients were found to fall generally between the prediction of the modified Martinelli-Nelson model and the homogeneous model.

(6) In the low quality region, both predictions give an underestimate of the two-phase frictional pressure gradient data.

(7) The two-phase frictional pressure gradients were found to increase with decreasing saturation temperature in the low quality region and to decrease with decreasing saturation temperature in the high quality region.

(8) Experimental results show that the two-phase frictional pressure drop multiplier can be predicted with reasonable accuracy by using the Martinelli-Nelson correlation modified for mercury. The homogeneous model, though simpler in use, was found to be inadequate to predict the multiplier.

(9) Effects of mass velocity on the two-phase pressure drop multiplier were apparently not significant in the present test ranges.

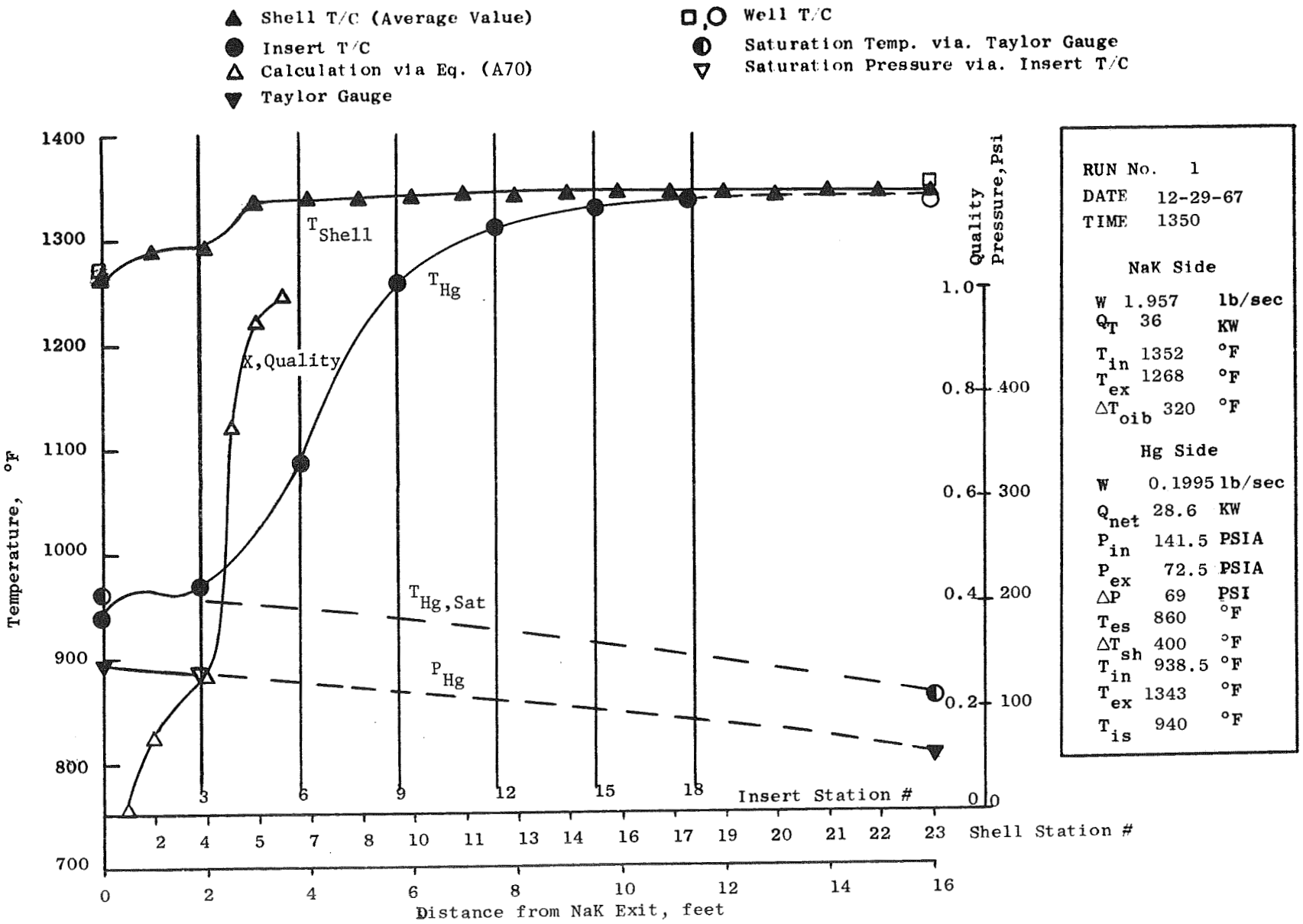

Figure 21. SNAP-8 Single Tube Boiler Temperature and Pressure Profile.

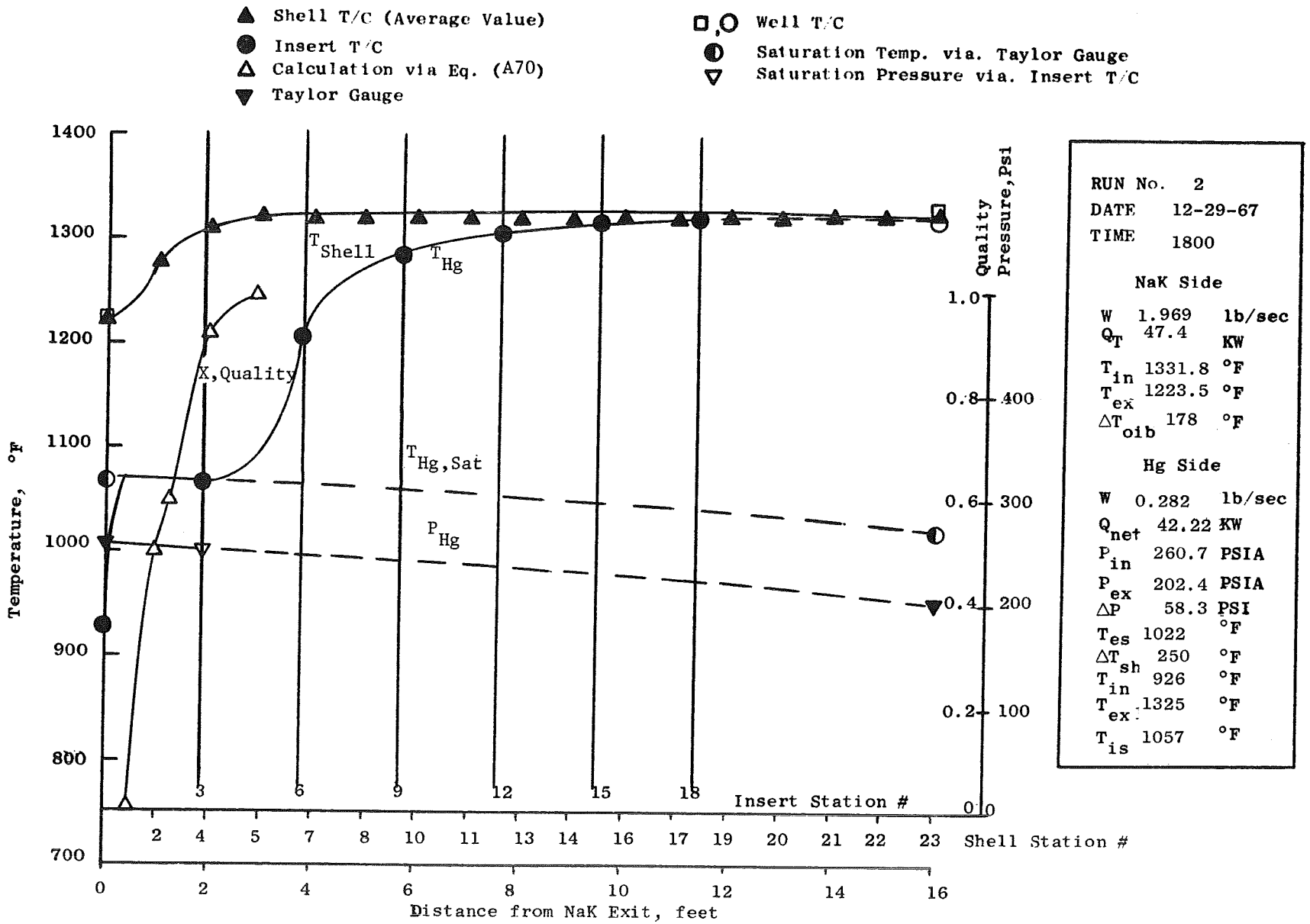

Figure 22. SNAP-8 Single Tube Boiler Temperature and Pressure Profile.

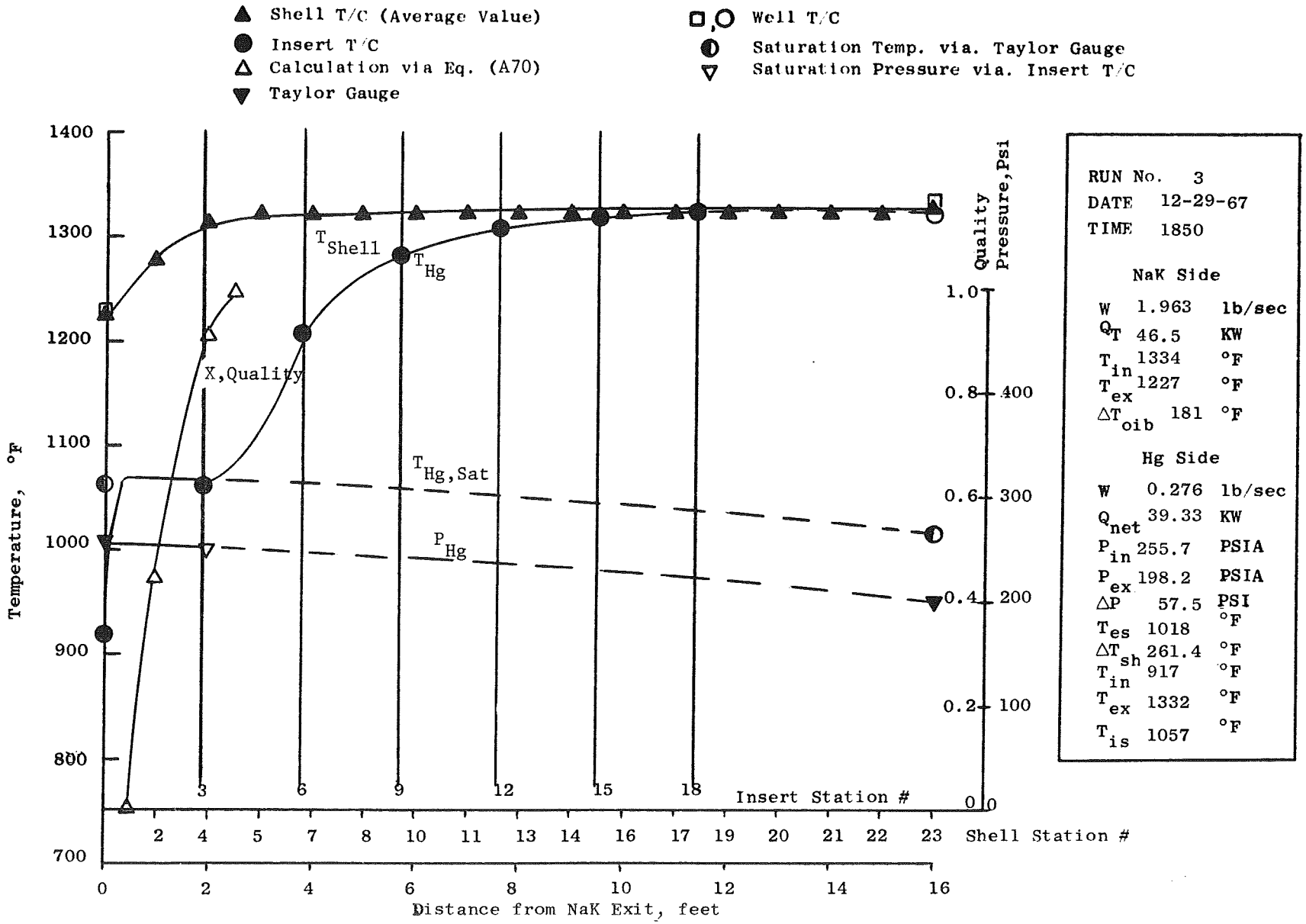

Figure 23. SNAP-8 Single Tube Boiler Temperature and Pressure Profile.

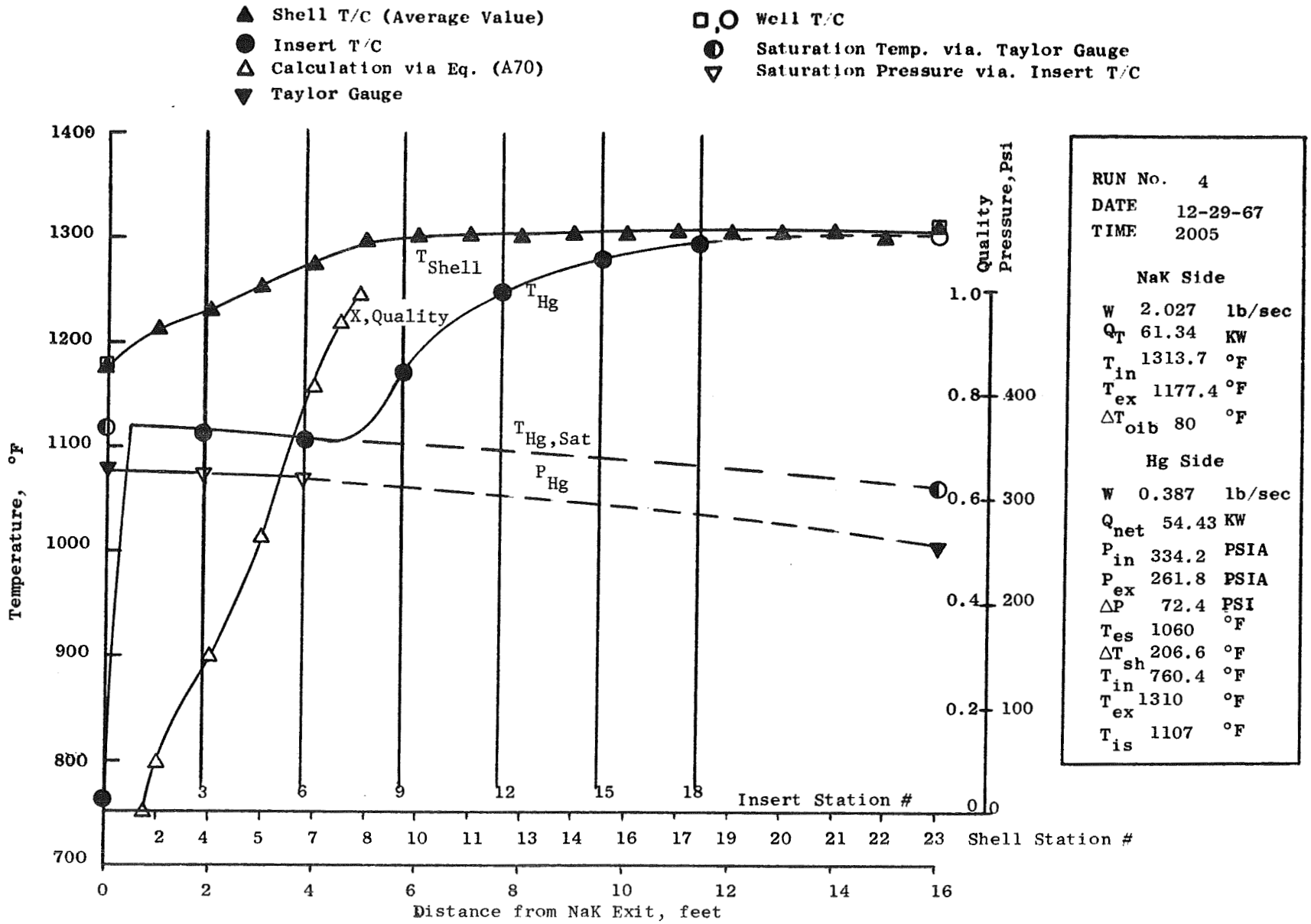

Figure 24. SNAP-8 Single Tube Boiler Temperature and Pressure Profile.

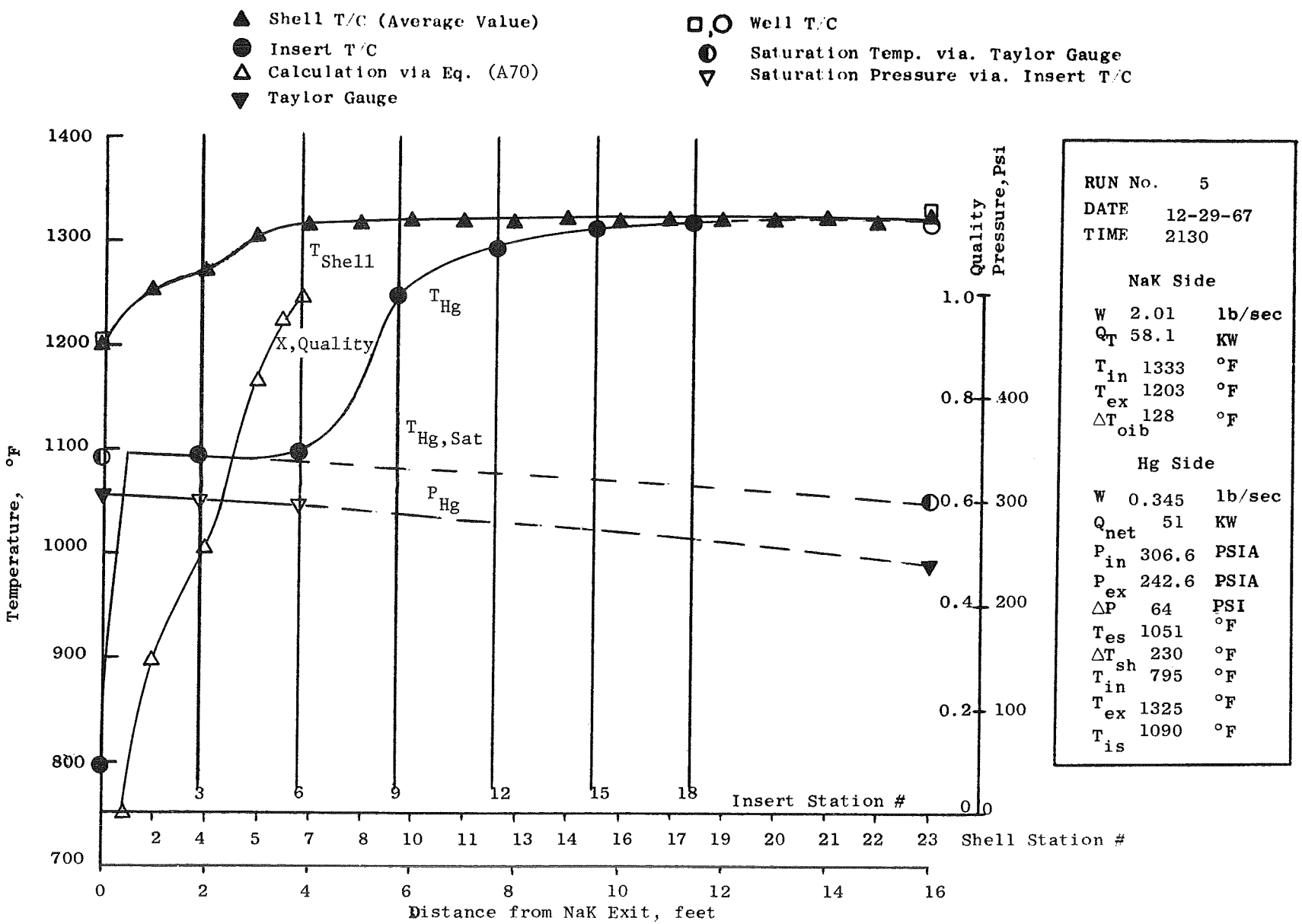

Figure 25. SNAP-8 Single Tube Boiler Temperature and Pressure Profile.

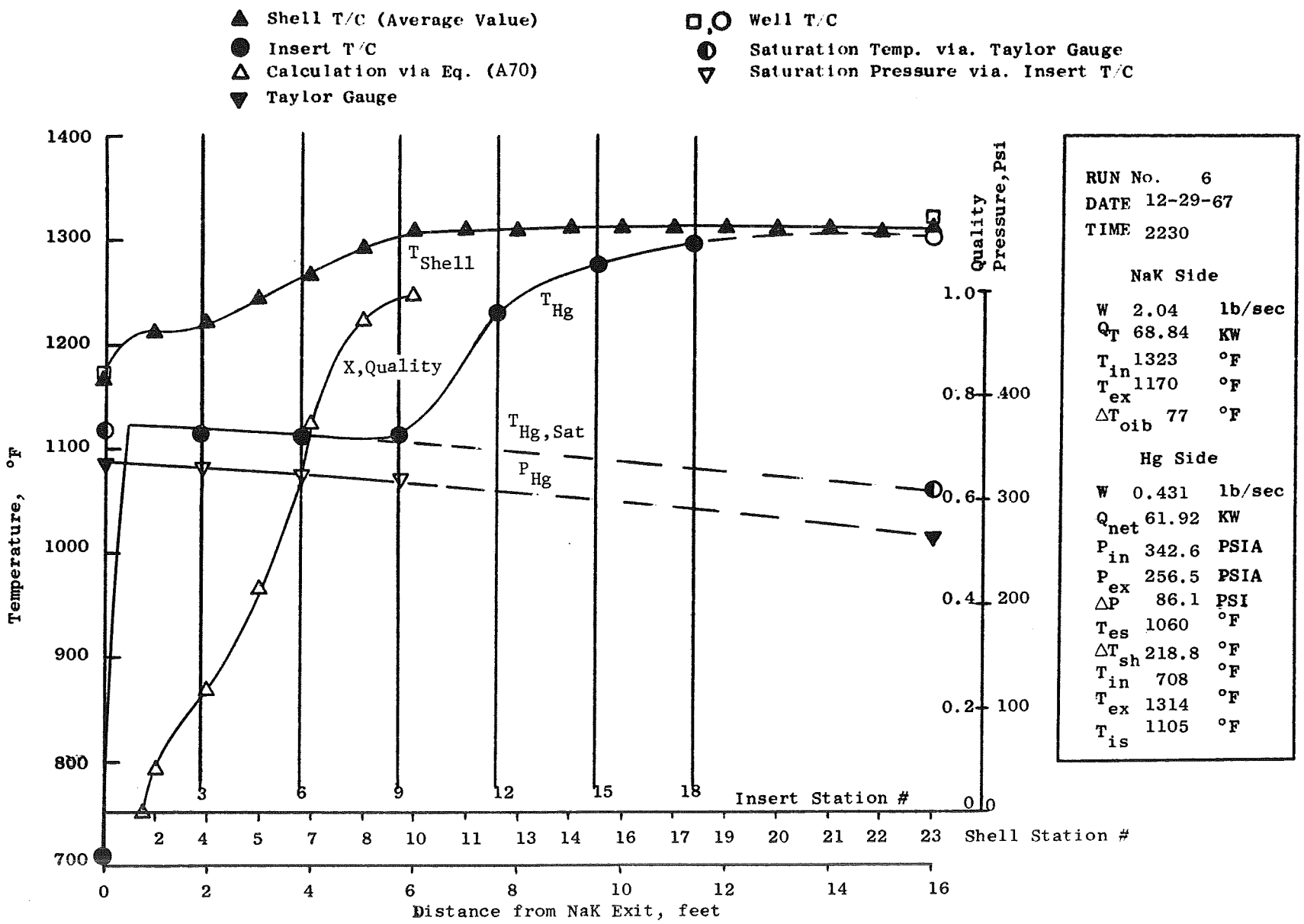

Figure 26. SNAP-8 Single Tube Boiler Temperature and Pressure Profile.

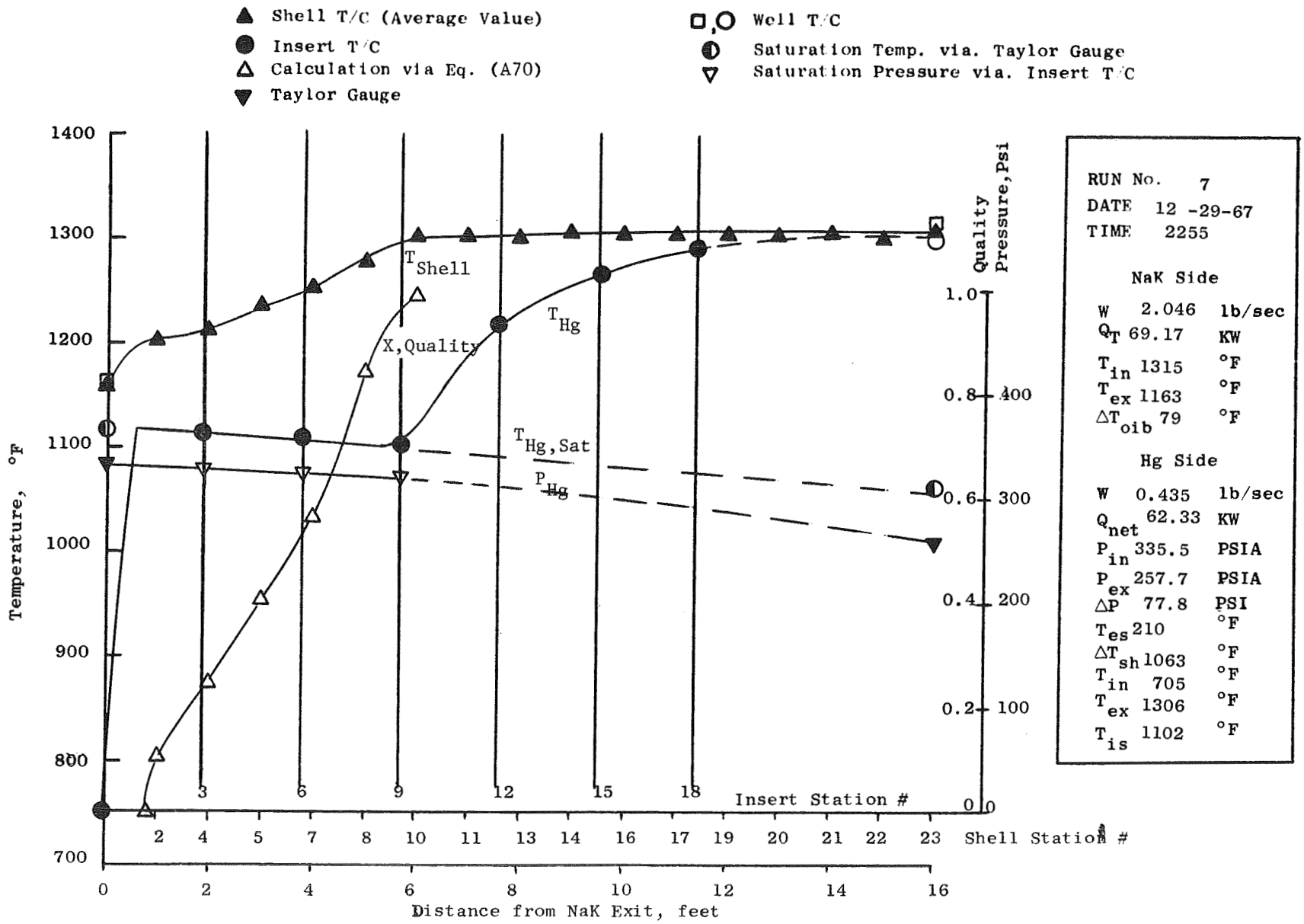

Figure 27. SNAP-8 Single Tube Boiler Temperature and Pressure Profile.

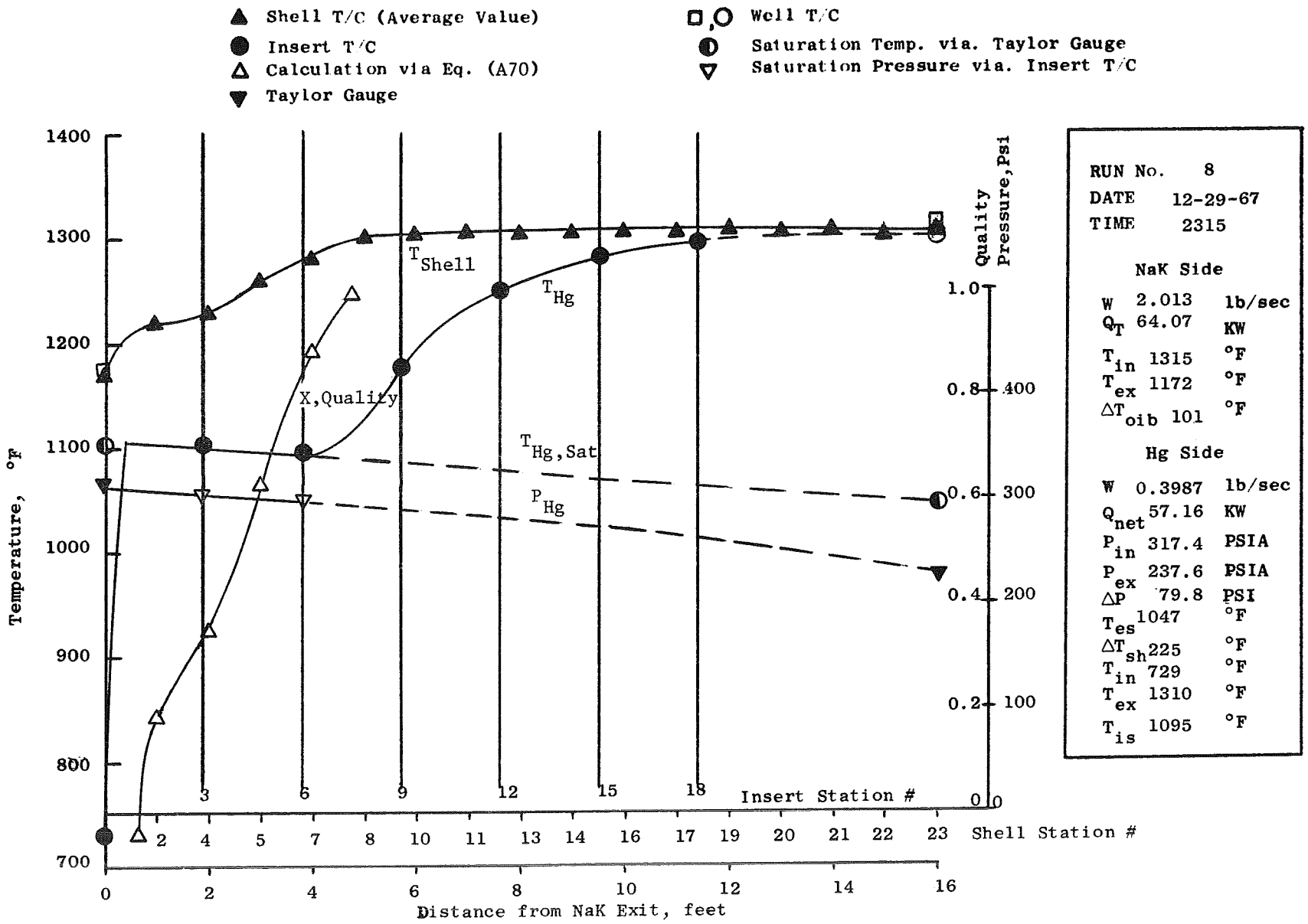

Figure 28. SNAP-8 Single Tube Boiler Temperature and Pressure Profile.

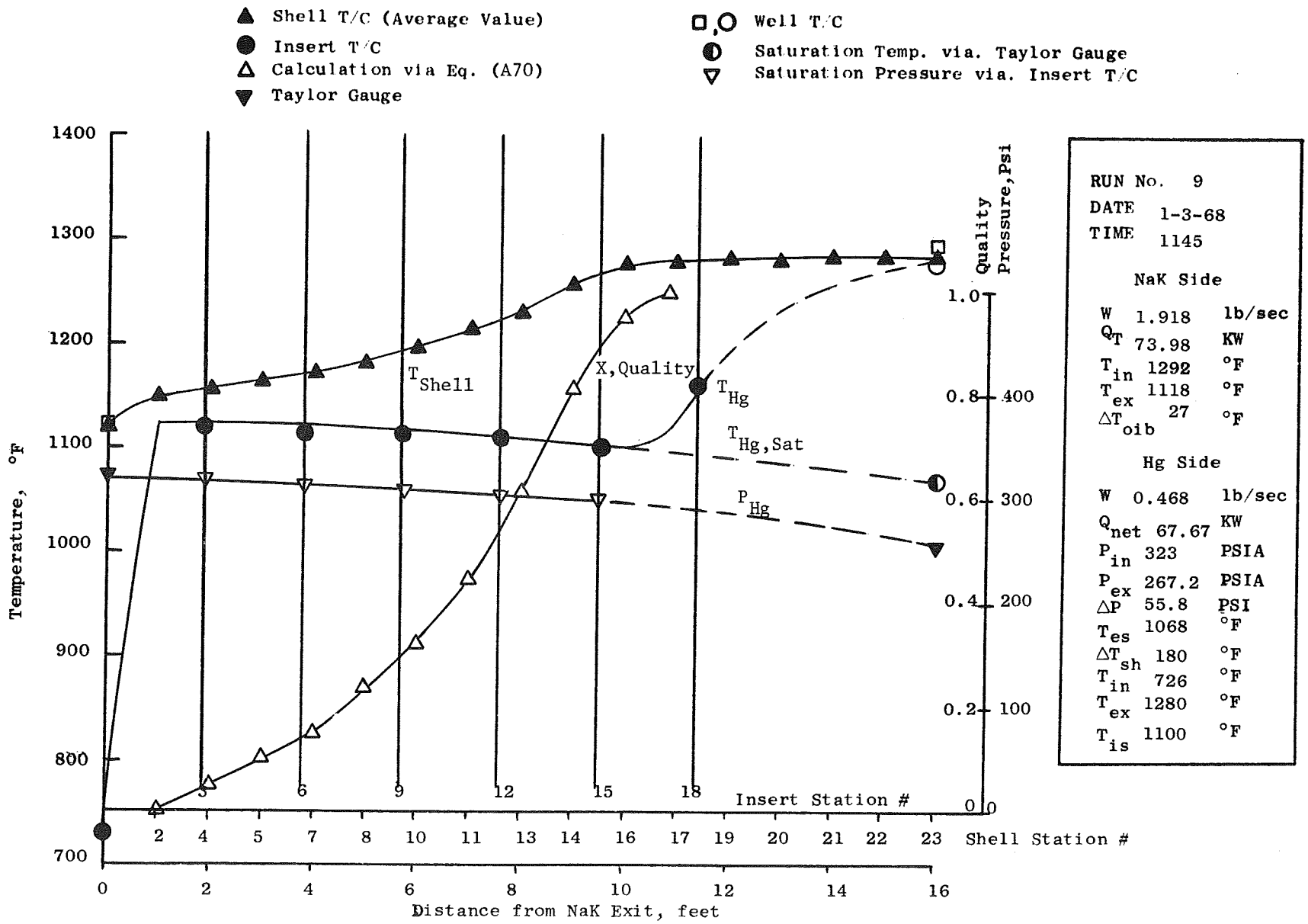

Figure 29. SNAP-8 Single Tube Boiler Temperature and Pressure Profile.

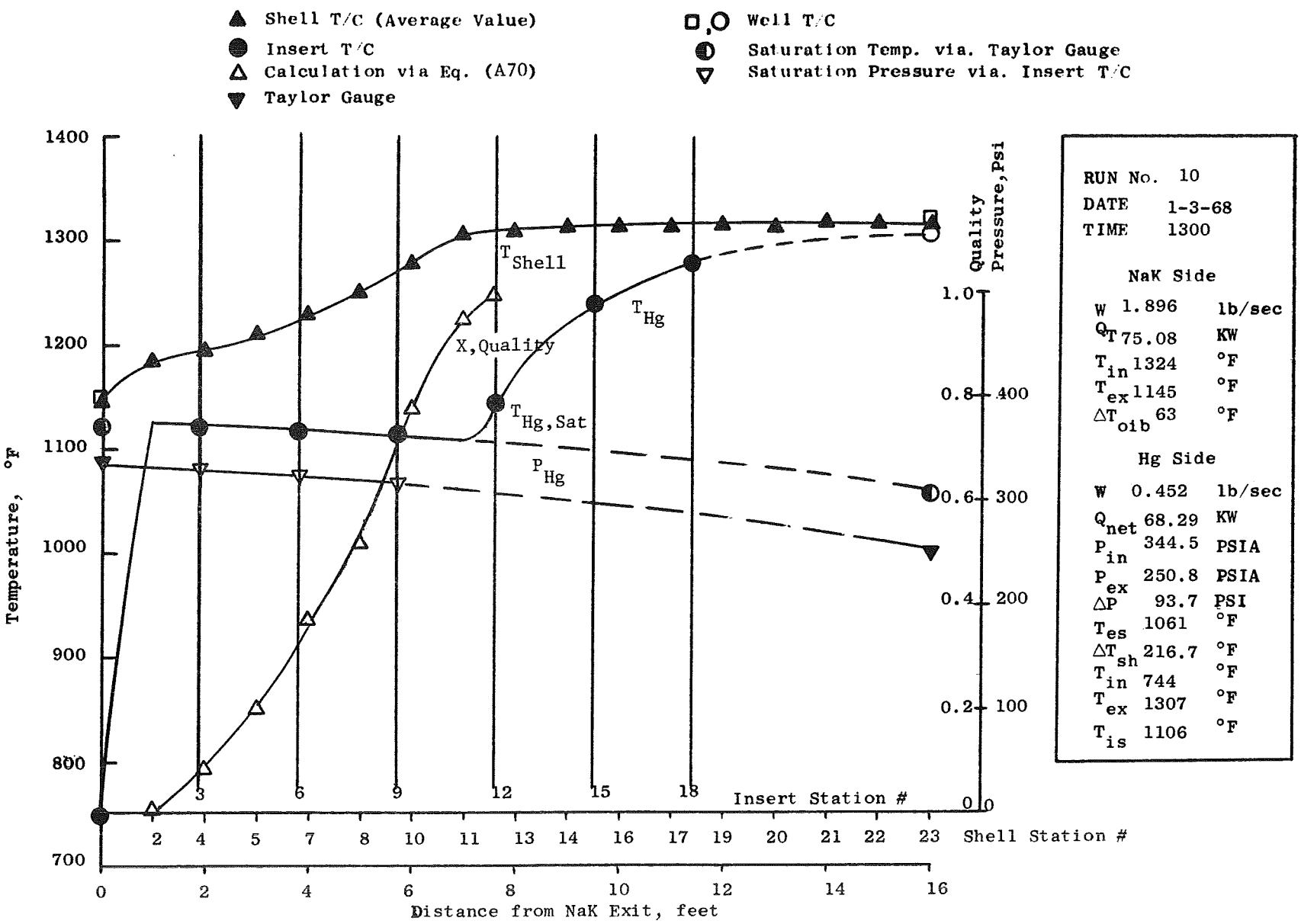

Figure 30. SNAP-8 Single Tube Boiler Temperature and Pressure Profile.

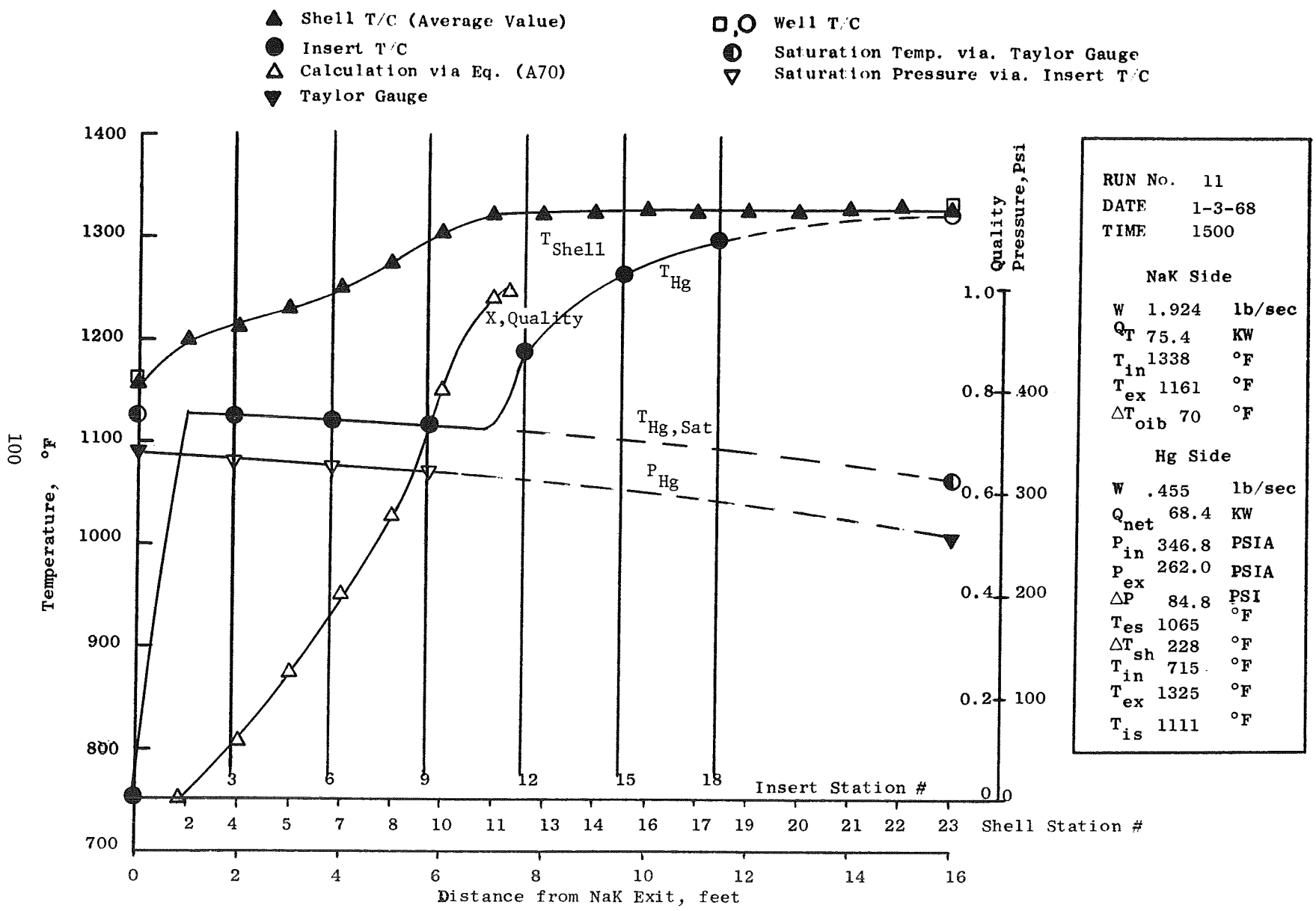

Figure 31. SNAP-8 Single Tube Boiler Temperature and Pressure Profile.

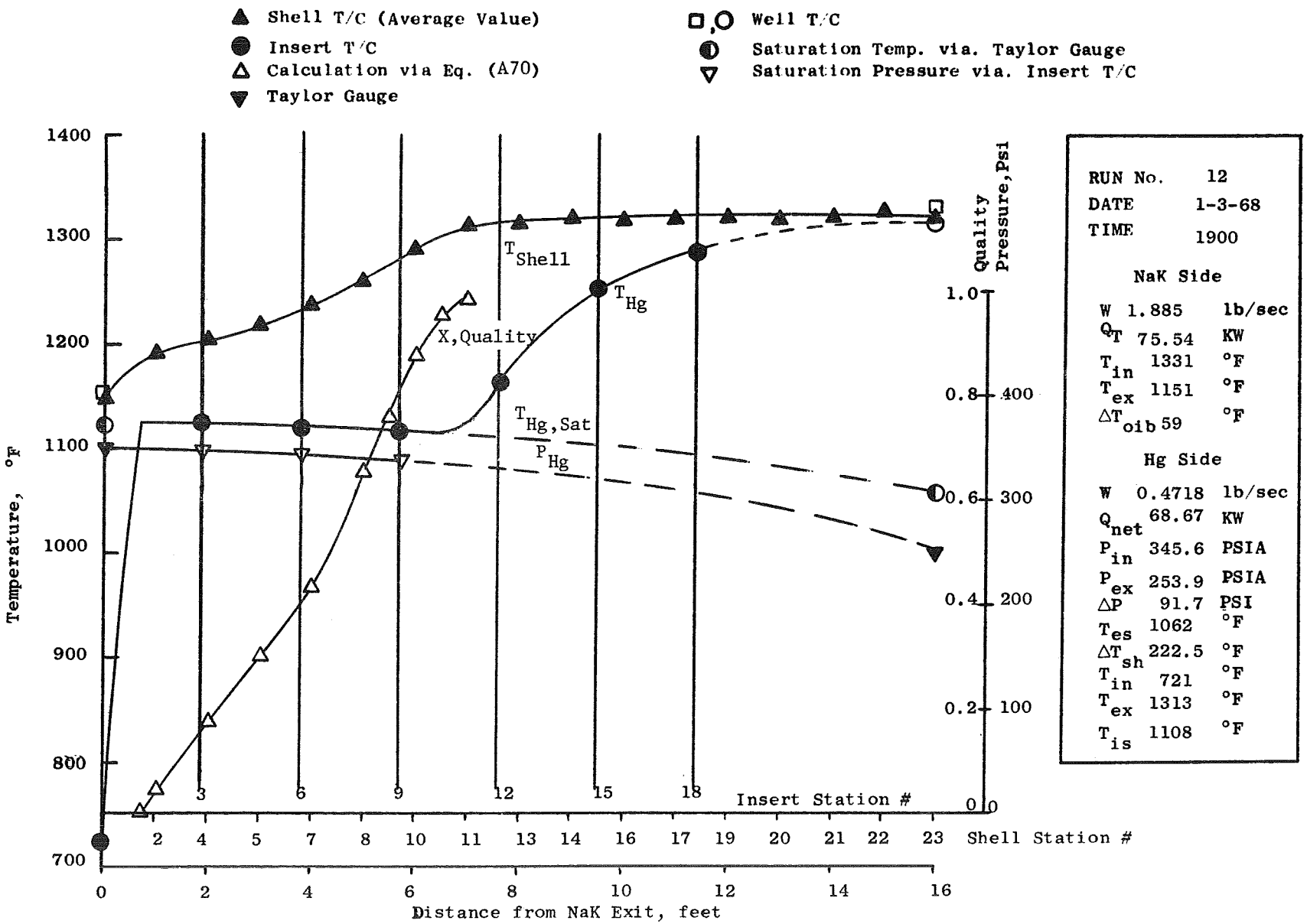

Figure 32. SNAP-8 Single Tube Boiler Temperature and Pressure Profile.

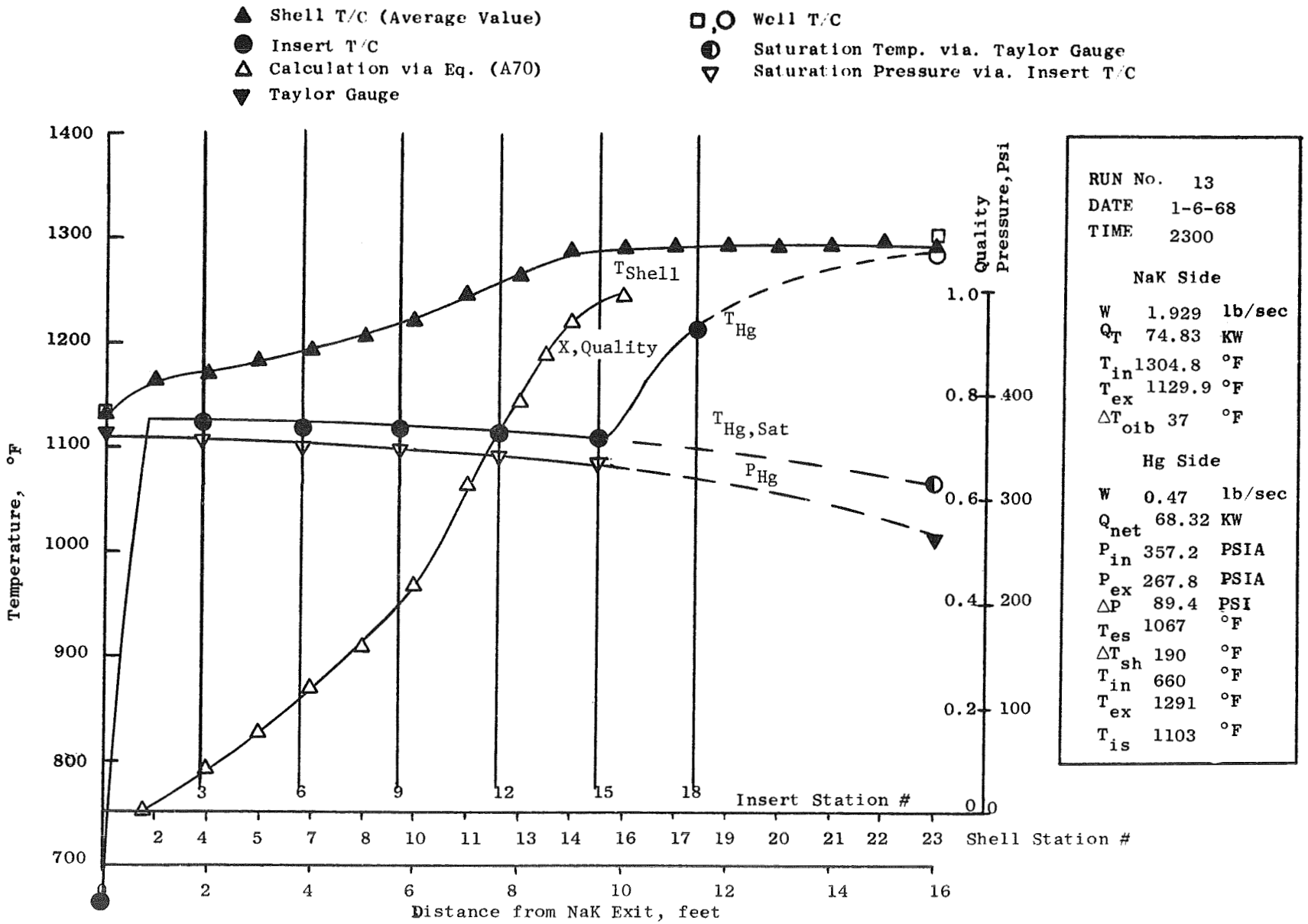

Figure 33. SNAP-8 Single Tube Boiler Temperature and Pressure Profile.

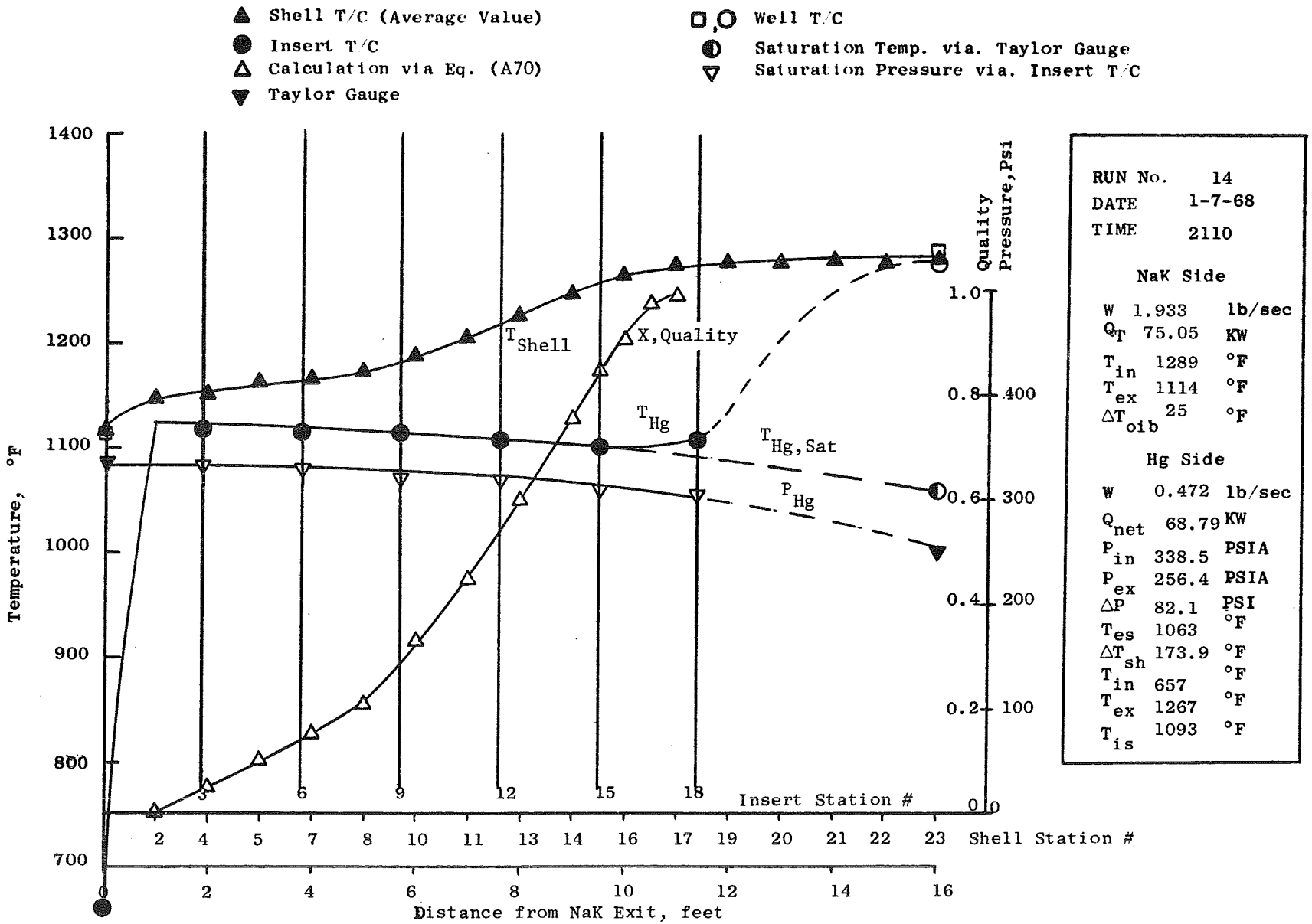

Figure 34. SNAP-8 Single Tube Boiler Temperature and Pressure Profile.

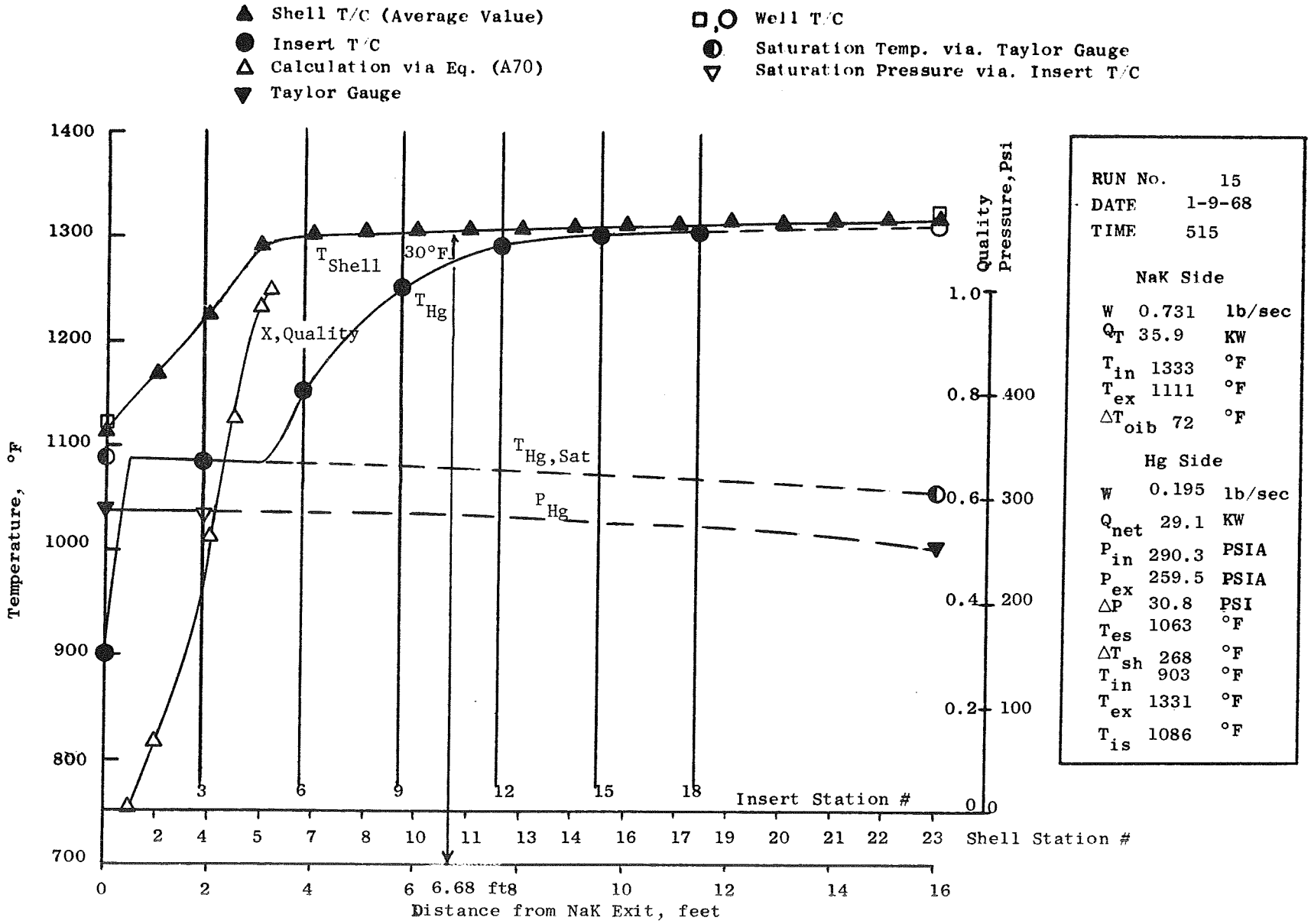

Figure 35. SNAP-8 Single Tube Boiler Temperature and Pressure Profile.

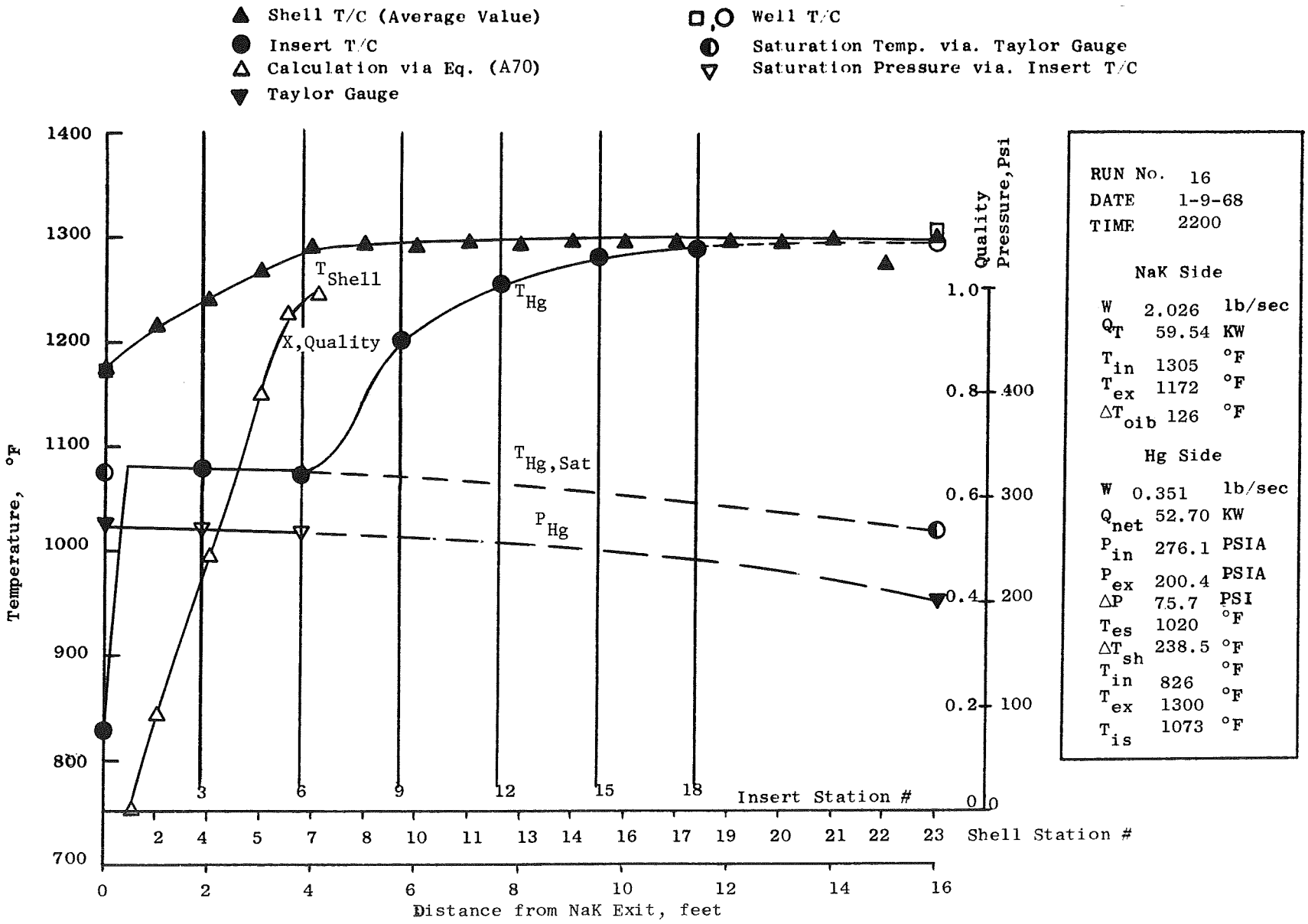

Figure 36. SNAP-8 Single Tube Boiler Temperature and Pressure Profile.

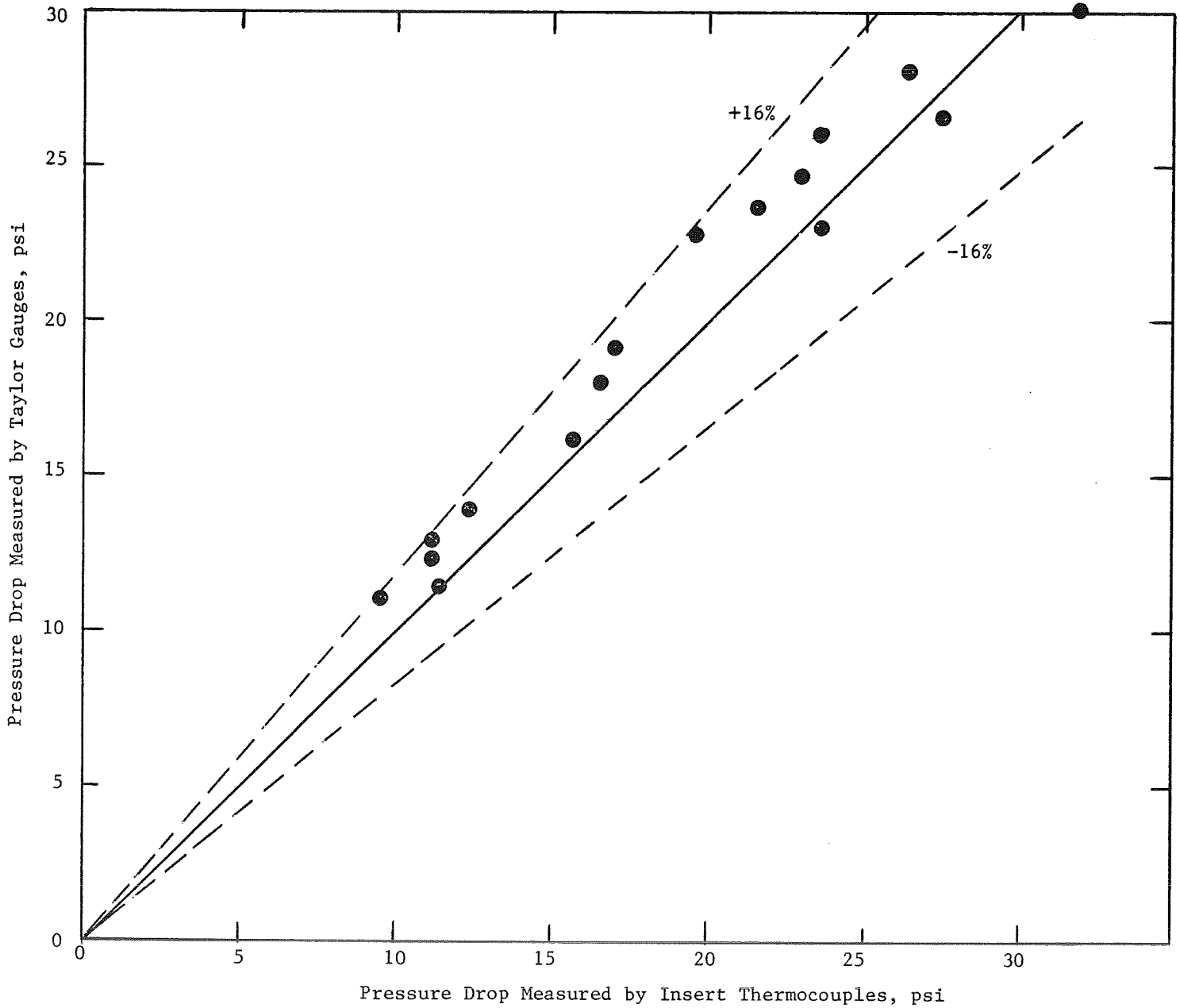

Figure 37. Comparison of Two-Phase Pressure Drop Measured by Insert Thermocouples and Taylor Gauges.

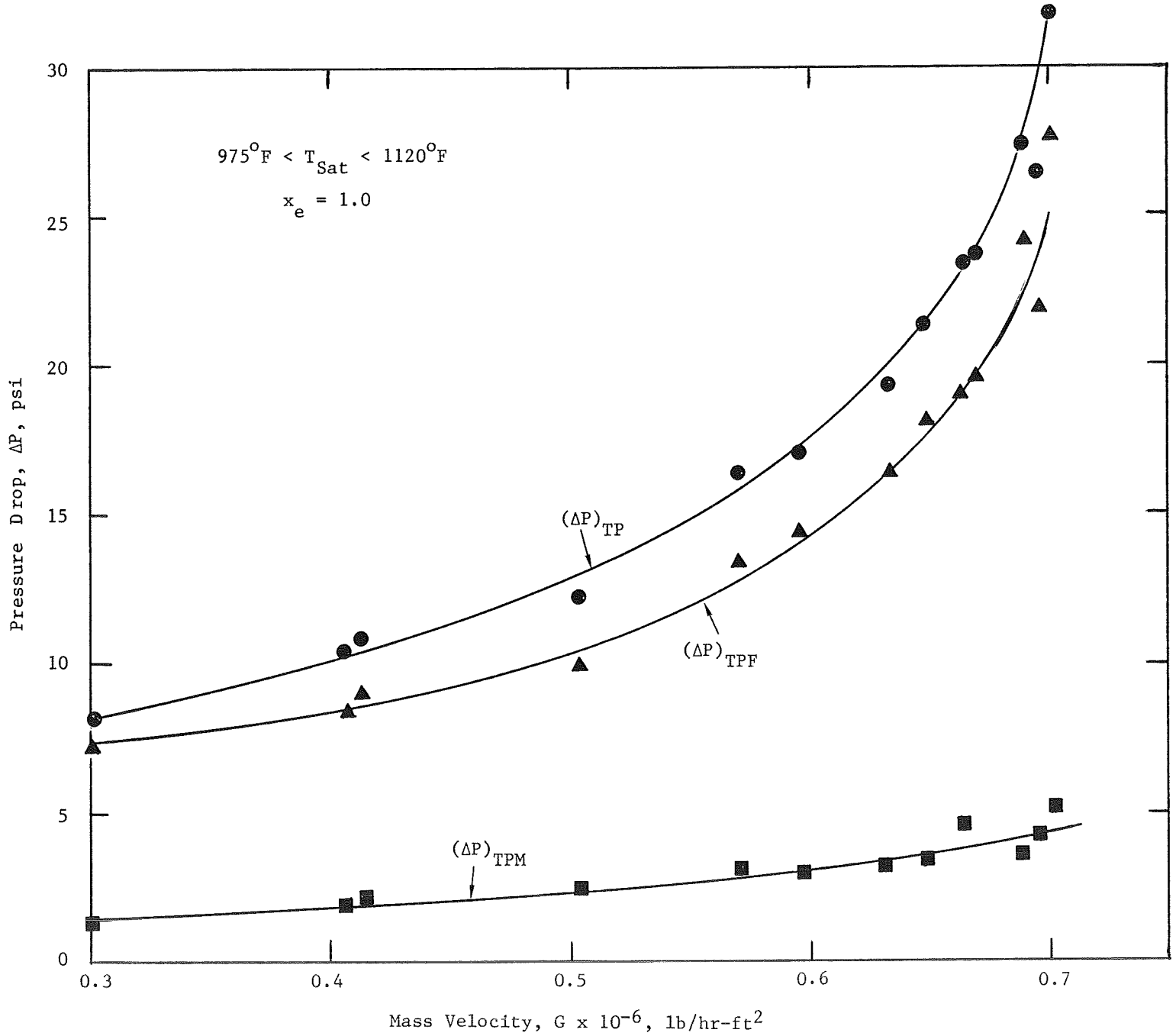

Figure 38. Two-Phase Pressure Drop Results Obtained from a 0.67-inch ID Tube With Helical Insert.

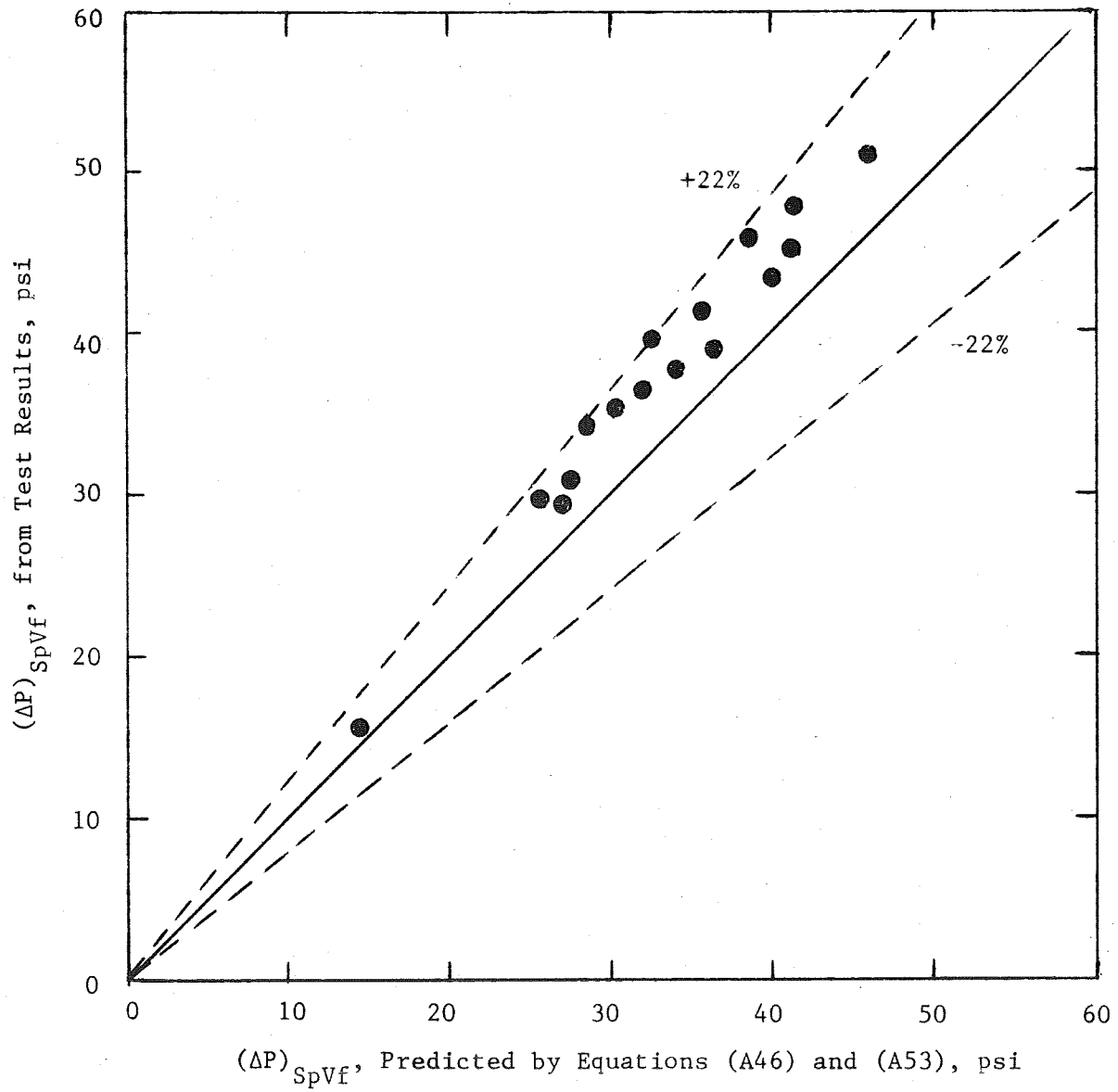

Figure 39. Comparison of Mercury Single-Phase Vapor Frictional Pressure Drop Between Test Results and Predicted Values.

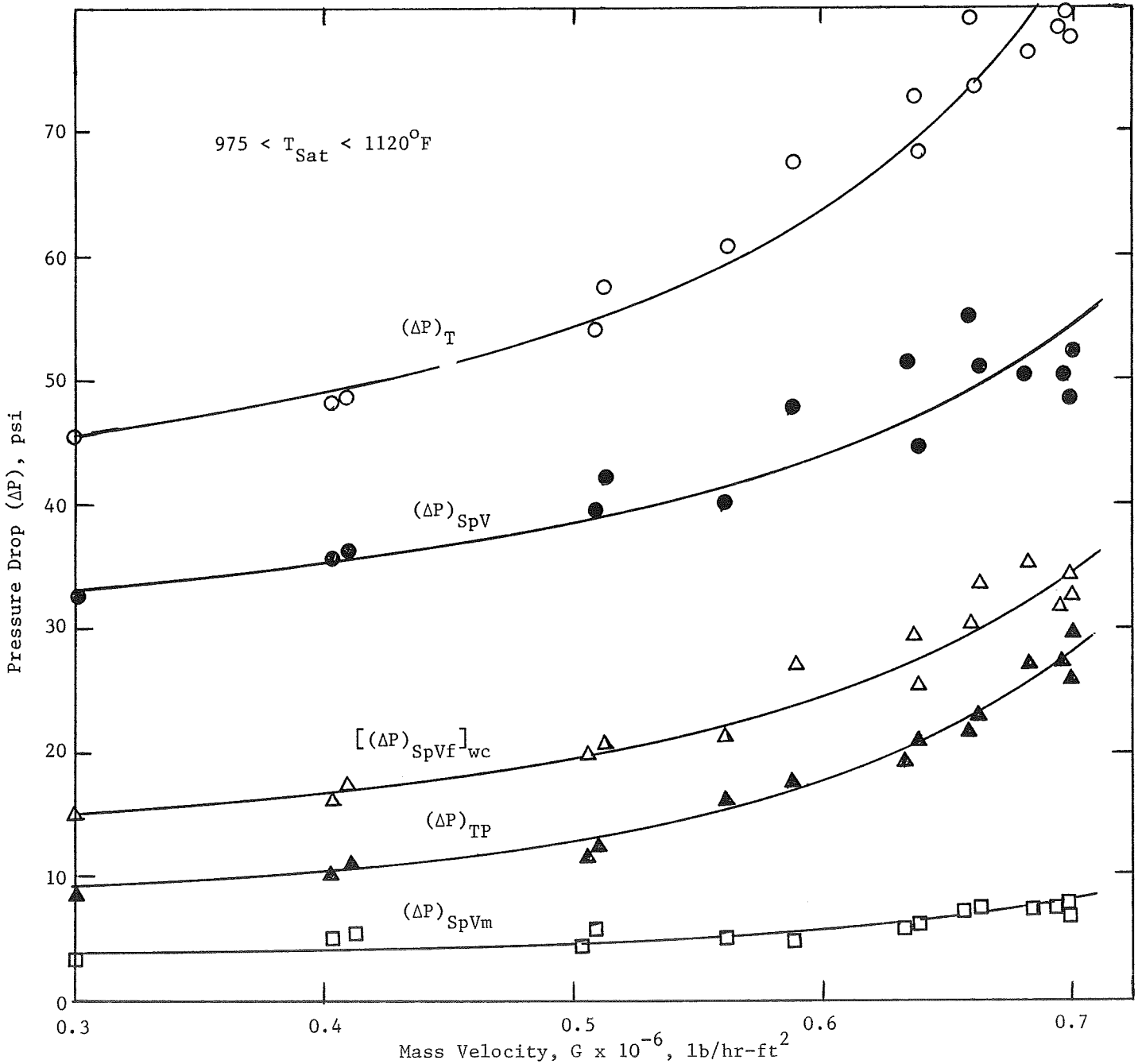

Figure 40. Mercury Single Tube Test Pressure Drop Results.

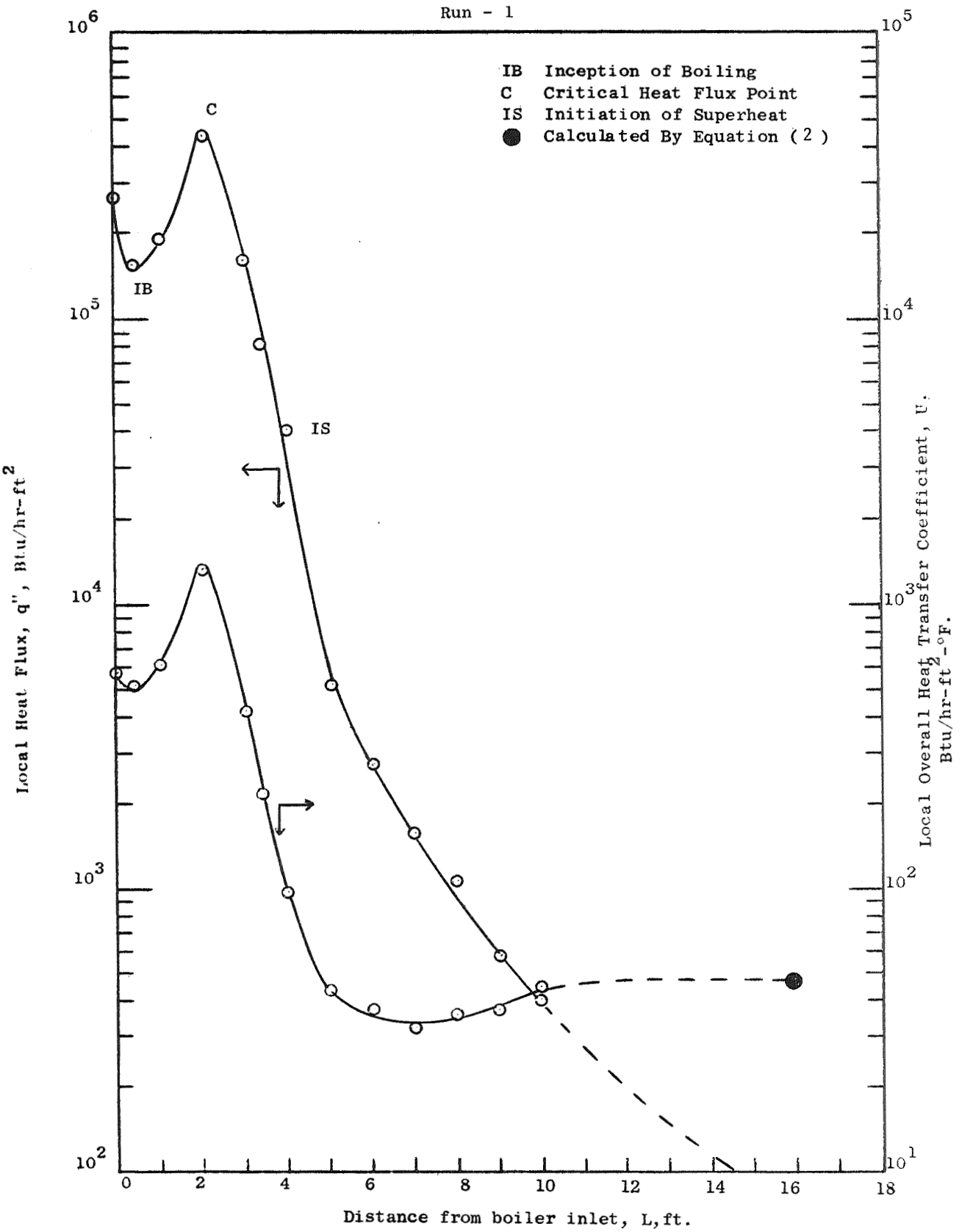

Figure 41. Local Values of Heat Flux and Overall Heat Transfer Coefficient for Mercury Once-Through Boiling Runs.

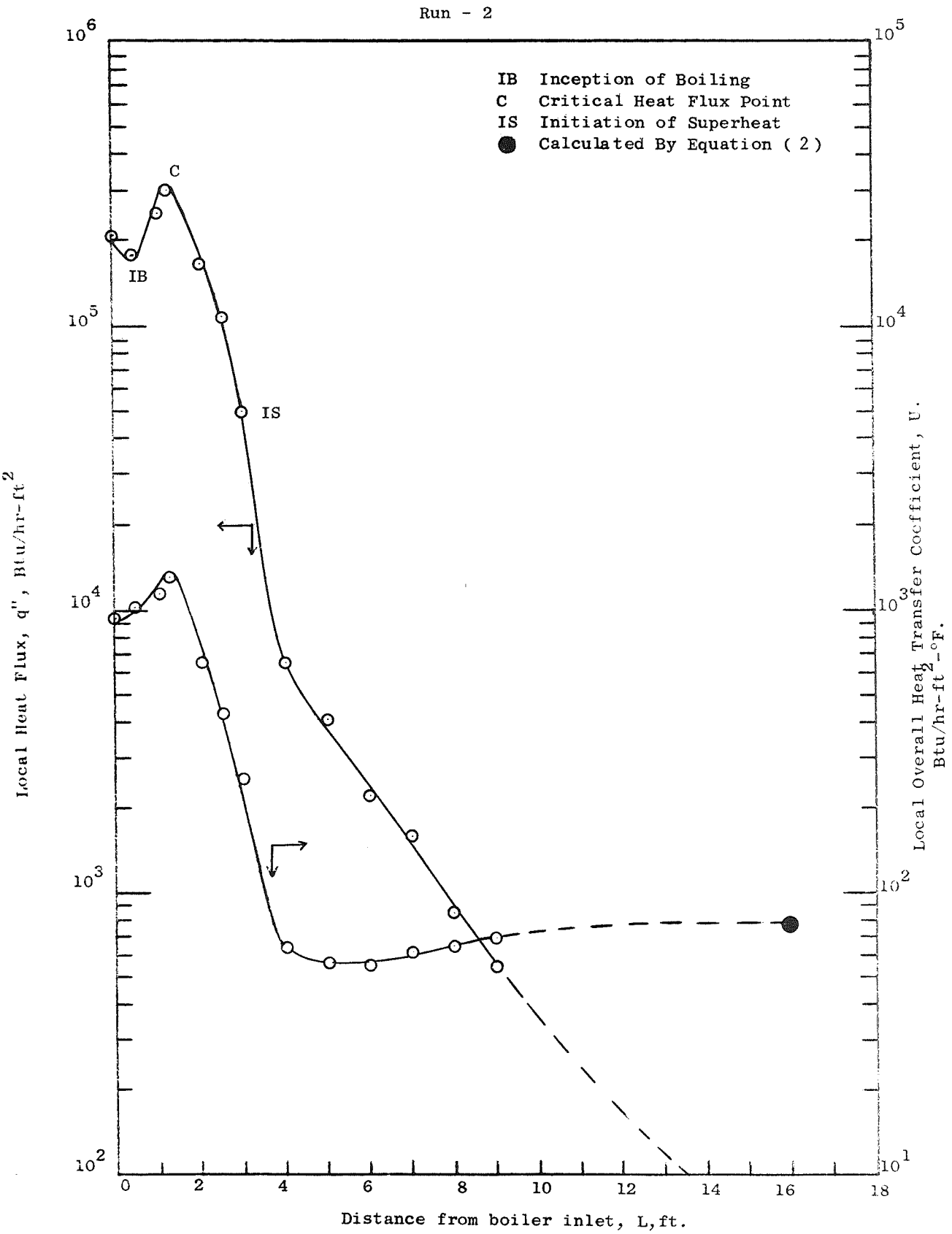

Figure 42. Local Values of Heat Flux and Overall Heat Transfer Coefficient for Mercury Once-Through Boiling Runs.

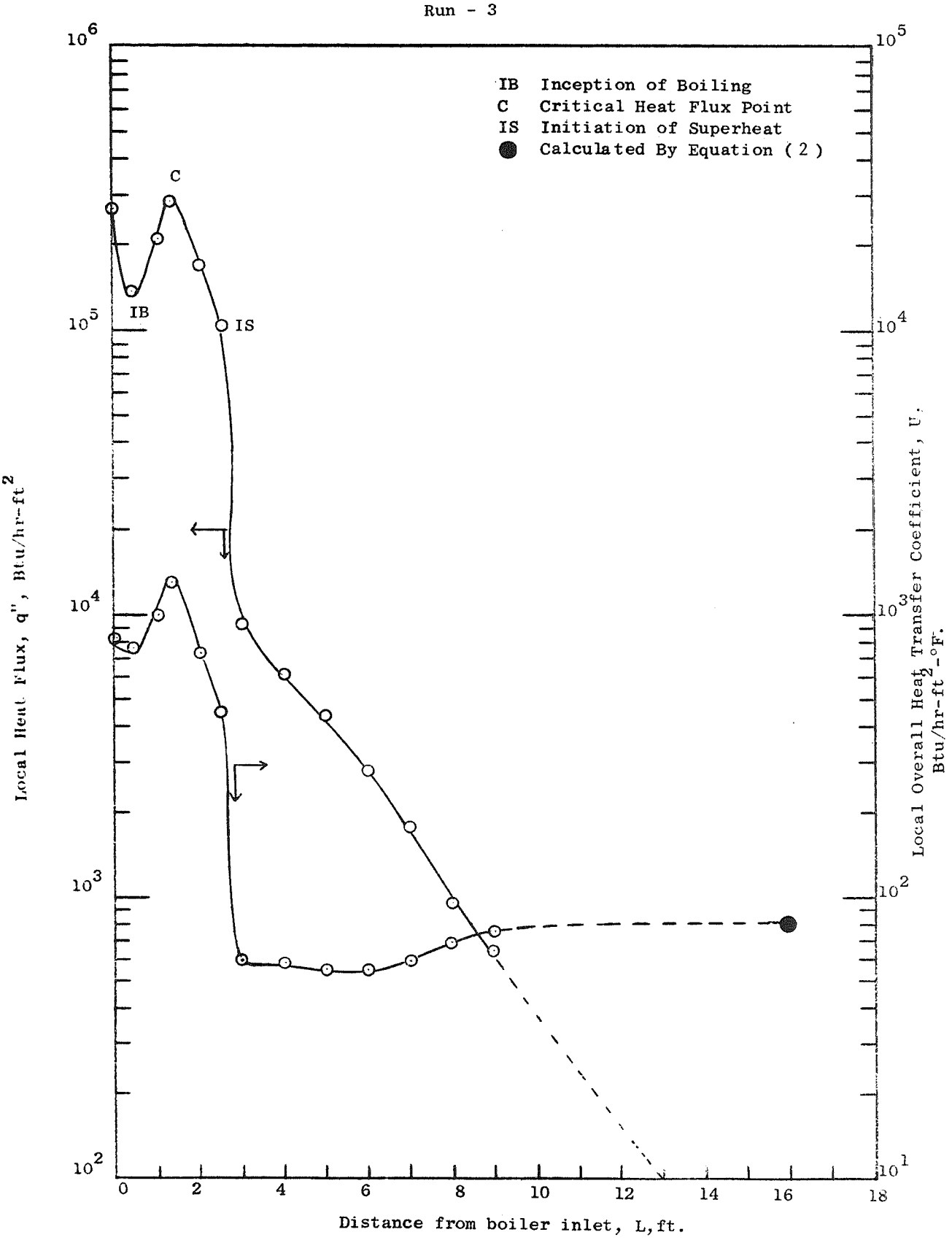

Figure 43. Local Values of Heat Flux and Overall Heat Transfer Coefficient for Mercury Once-Through Boiling Runs.

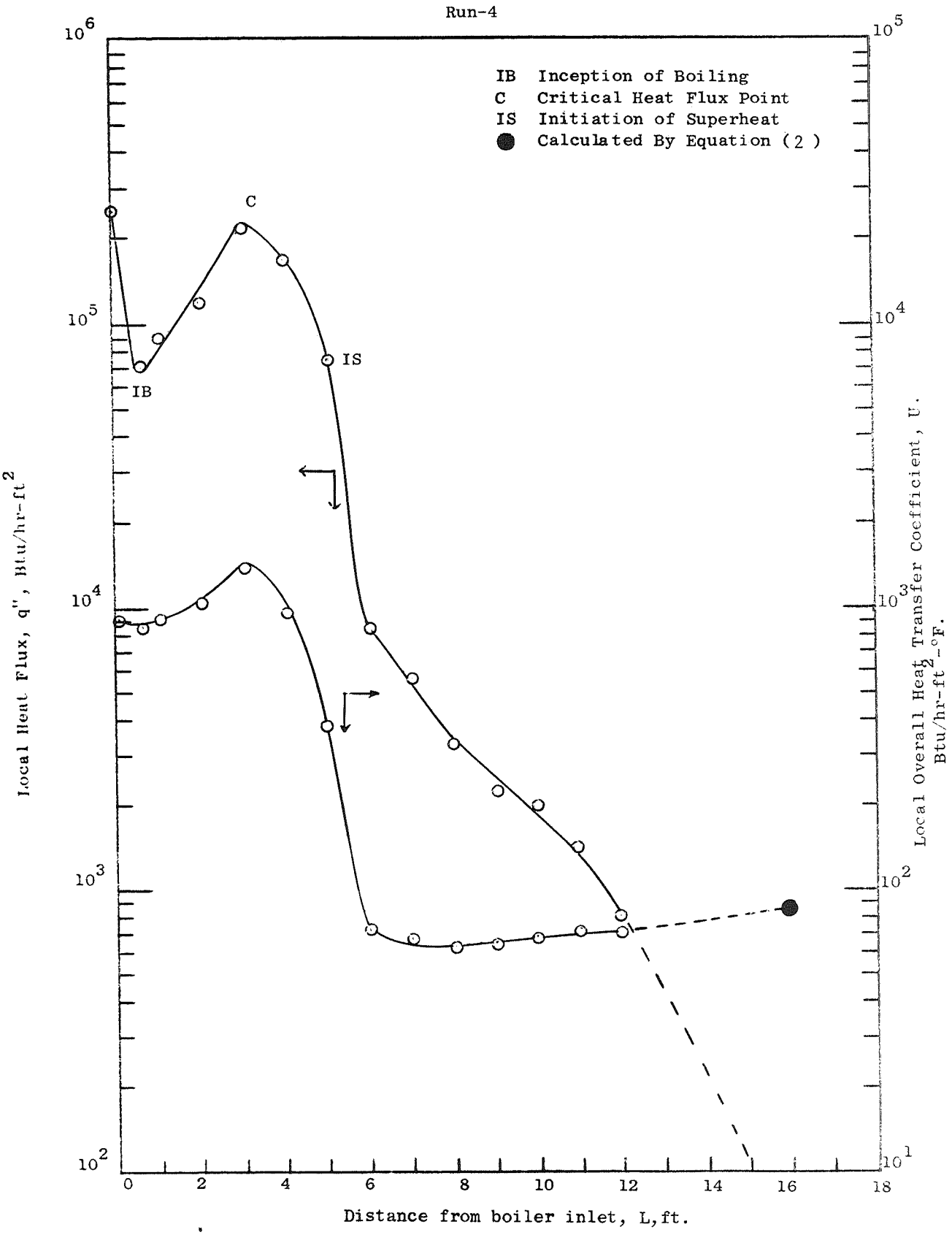

Figure 44. Local Values of Heat Flux and Overall Heat Transfer Coefficient for Mercury Once-Through Boiling Runs.

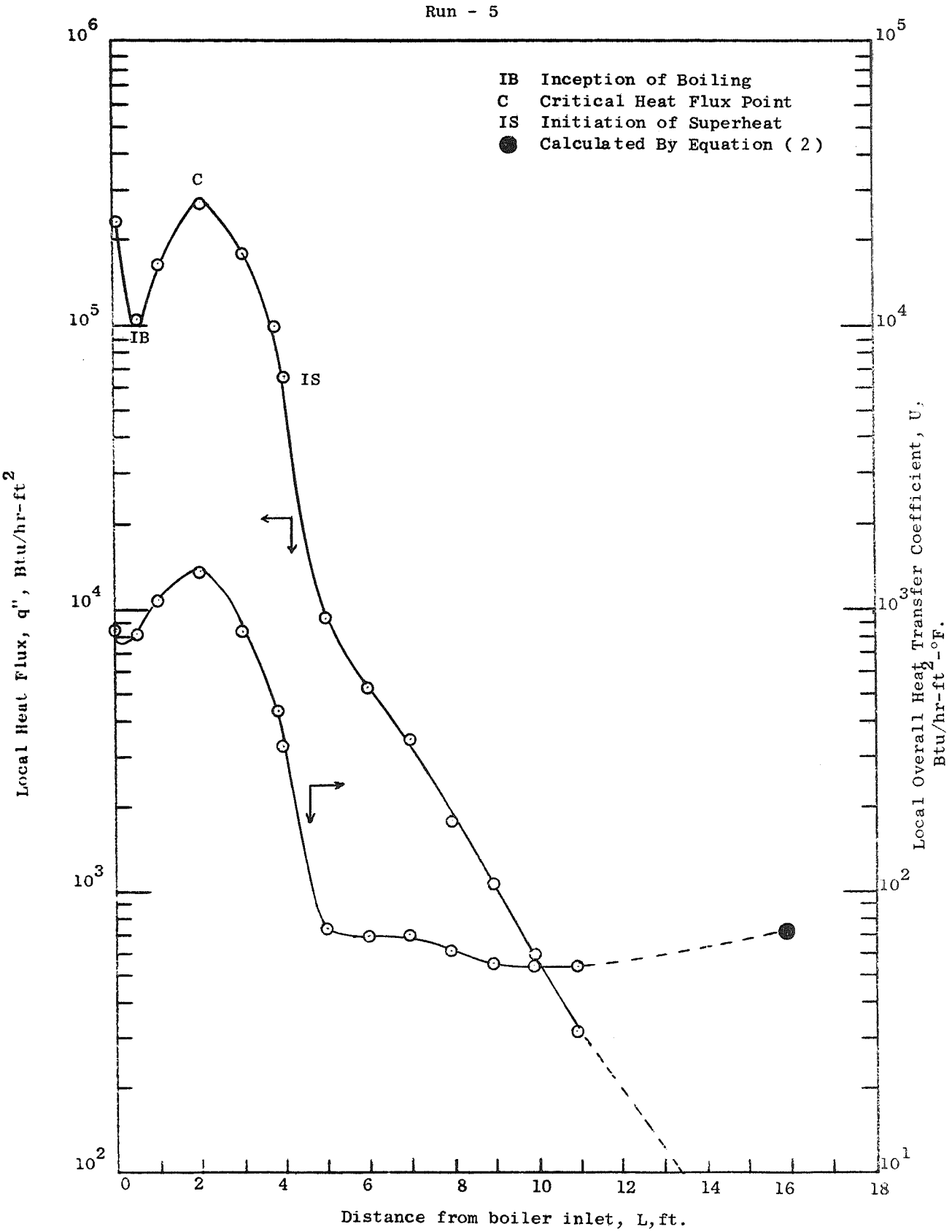

Figure 45. Local Values of Heat Flux and Overall Heat Transfer Coefficient for Mercury Once-Through Boiling Runs.

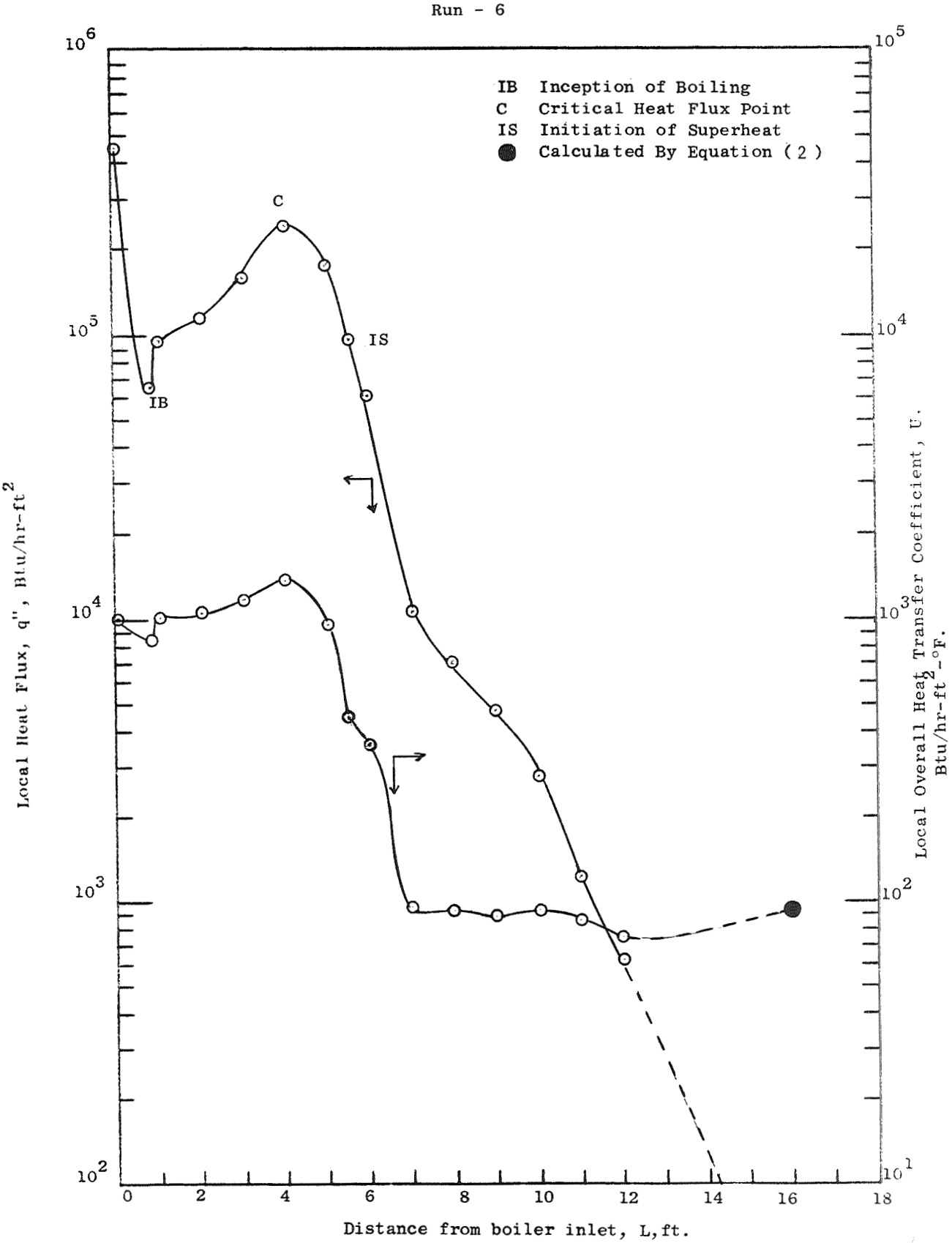

Figure 46. Local Values of Heat Flux and Overall Heat Transfer Coefficient for Mercury Once-Through Boiling Runs.

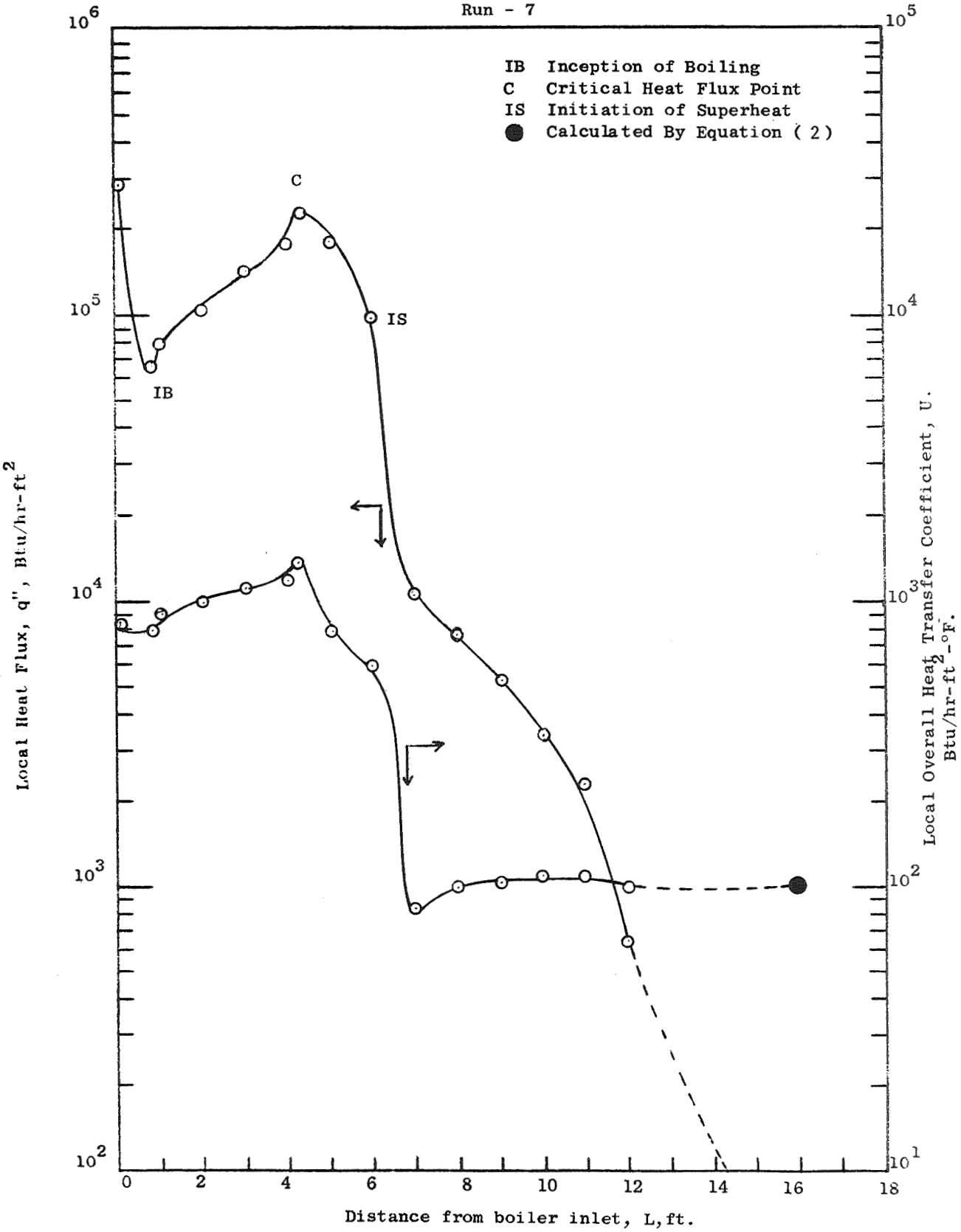

Figure 47. Local Values of Heat Flux and Overall Heat Transfer Coefficient for Mercury Once-Through Boiling Runs.

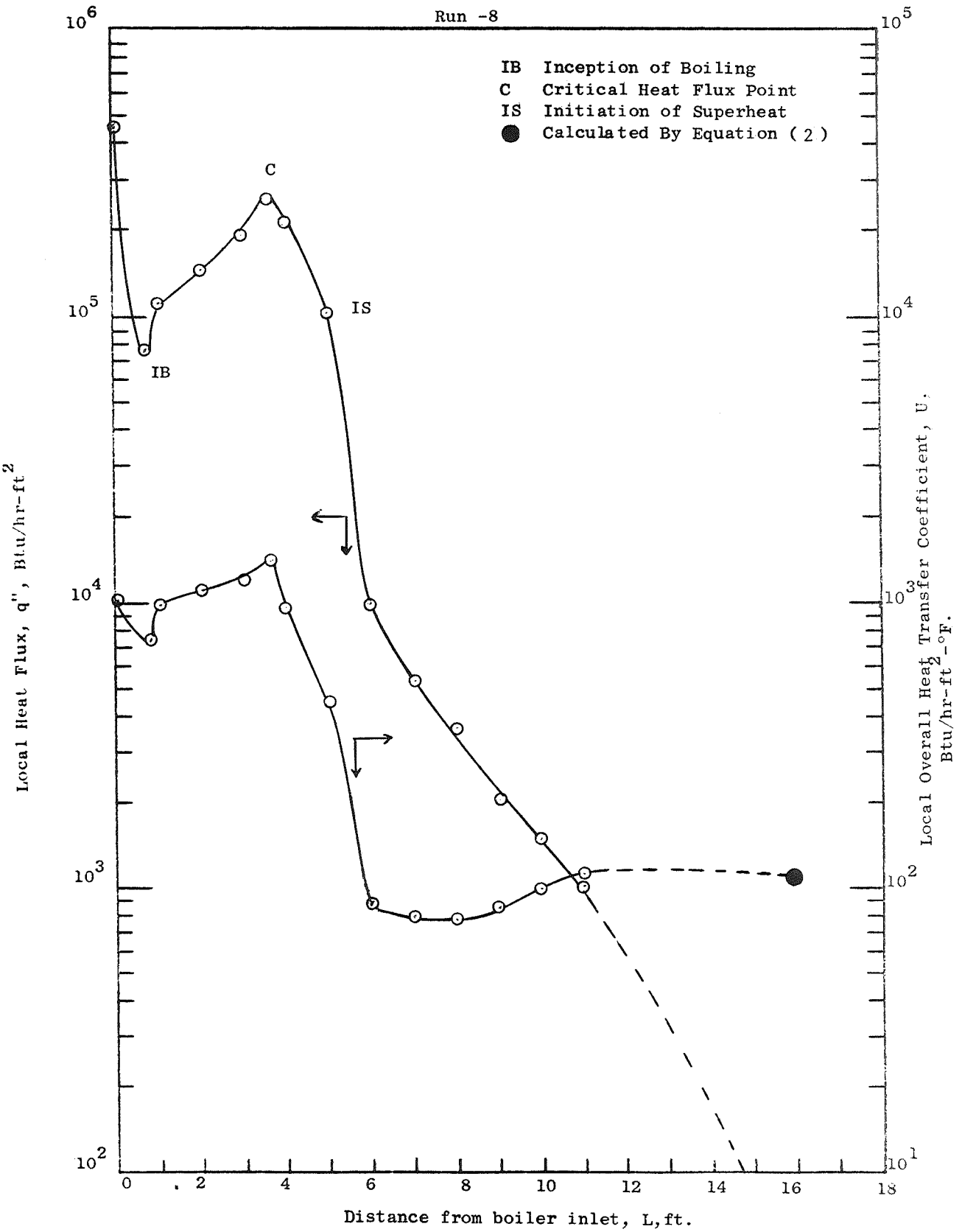

Figure 48. Local Values of Heat Flux and Overall Heat Transfer Coefficient for Mercury Once-Through Boiling Runs.

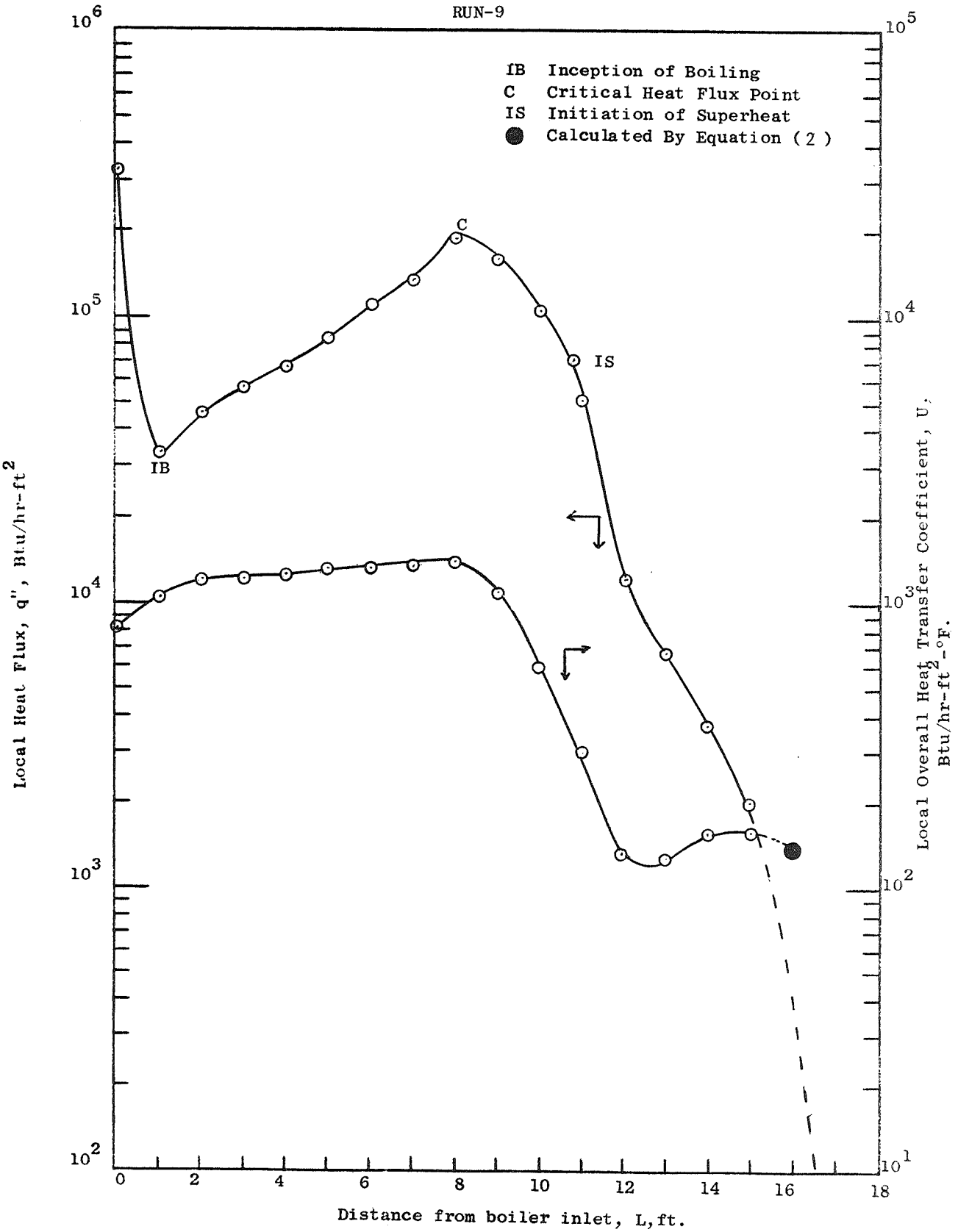

Figure 49. Local Values of Heat Flux and Overall Heat Transfer Coefficient for Mercury Once-Through Boiling Runs.

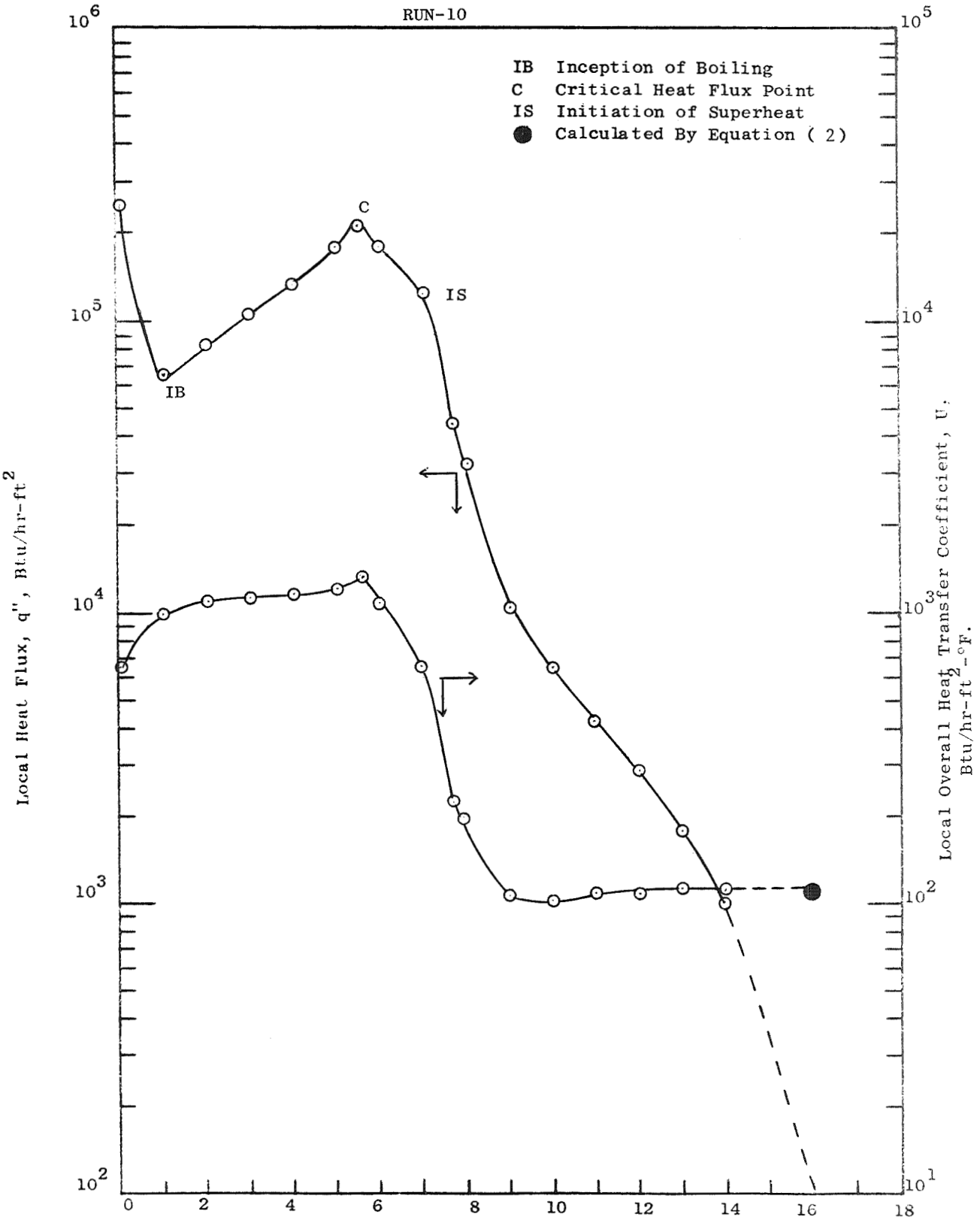

Figure 50. Local Values of Heat Flux and Overall Heat Transfer Coefficient for Mercury Once-Through Boiling Runs.

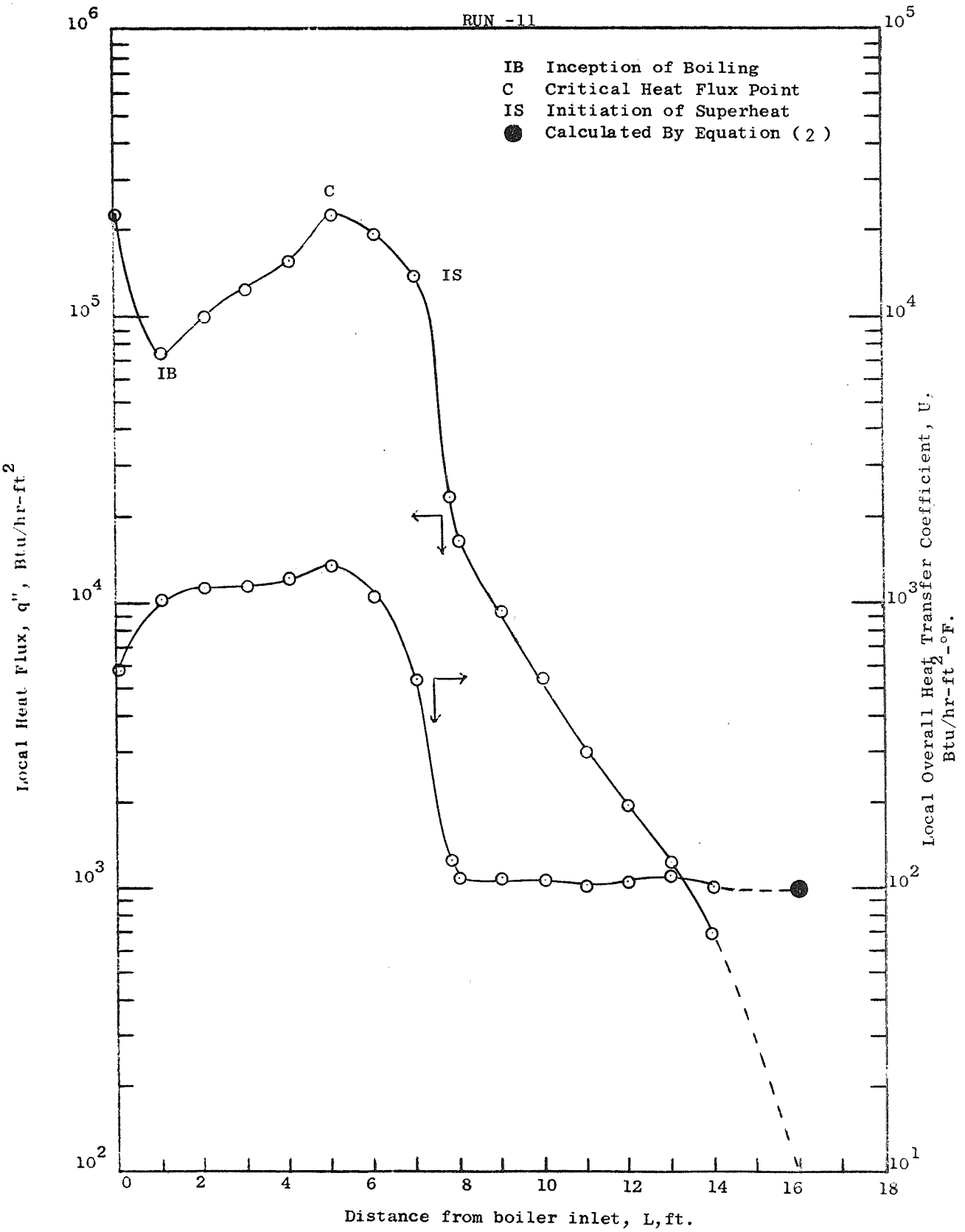

Figure 51. Local Values of Heat Flux and Overall Heat Transfer Coefficient for Mercury Once-Through Boiling Runs.

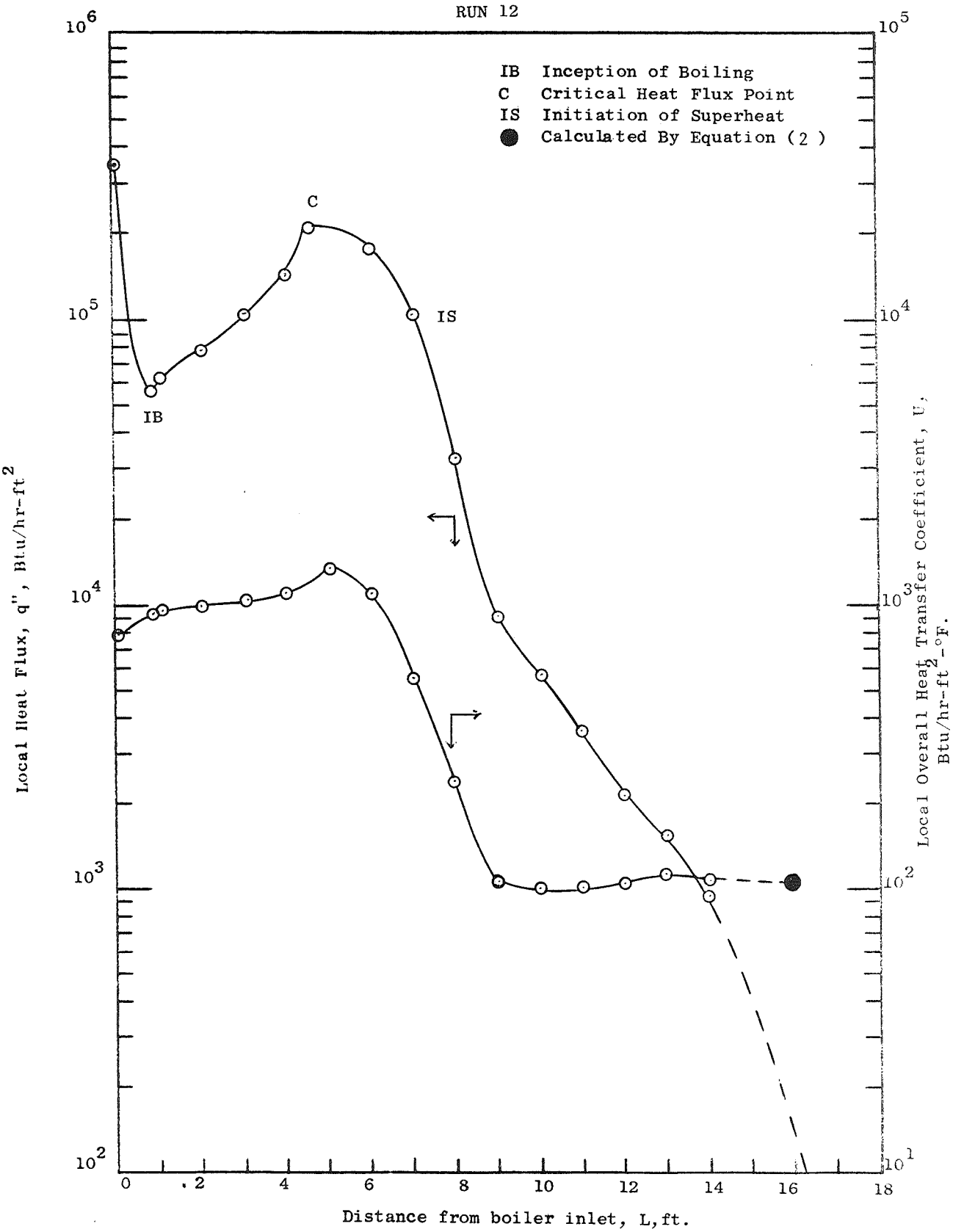

Figure 52. Local Values of Heat Flux and Overall Heat Transfer Coefficient for Mercury Once-Through Boiling Runs.

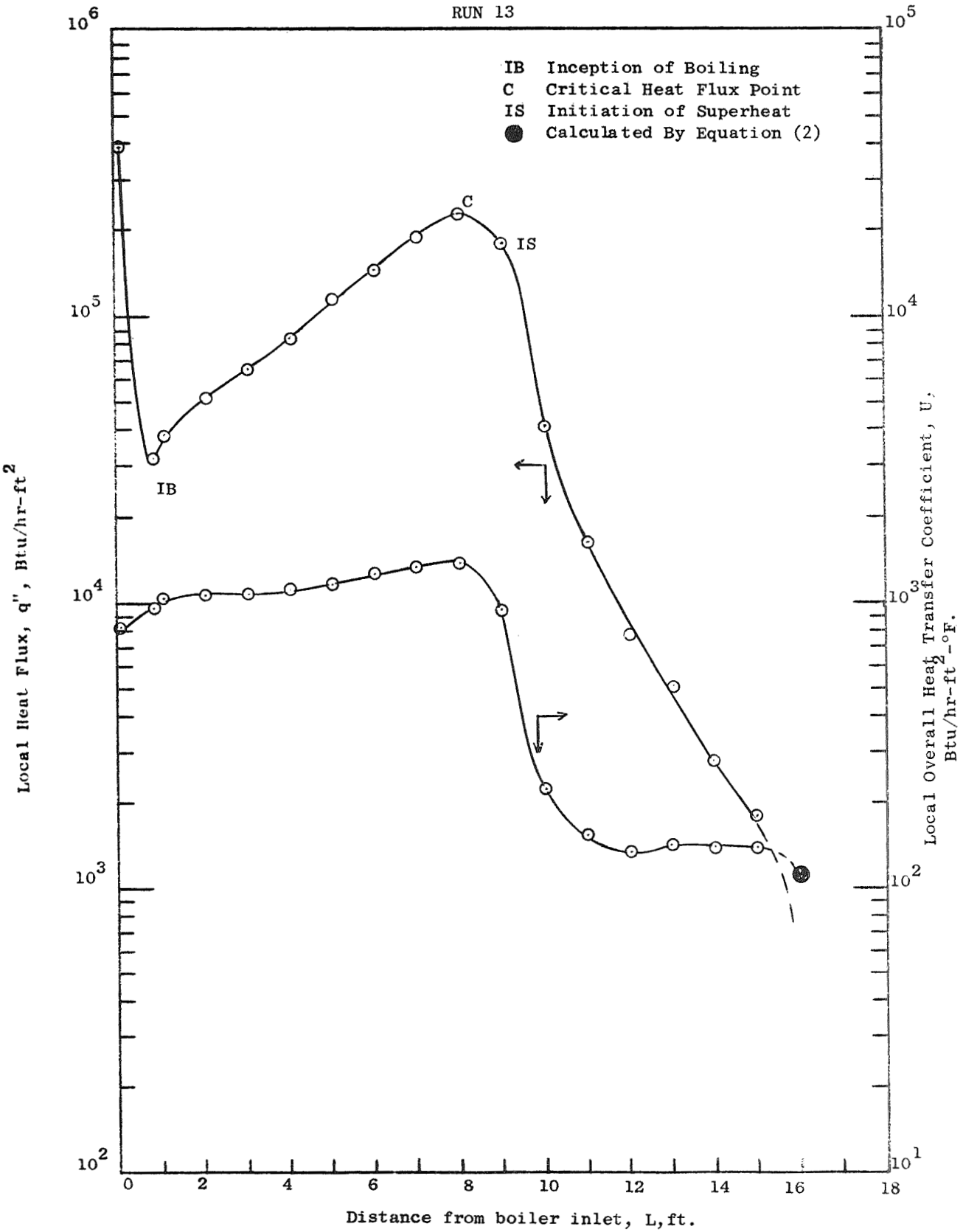

Figure 53. Local Values of Heat Flux and Overall Heat Transfer Coefficient for Mercury Once-Through Boiling Runs.

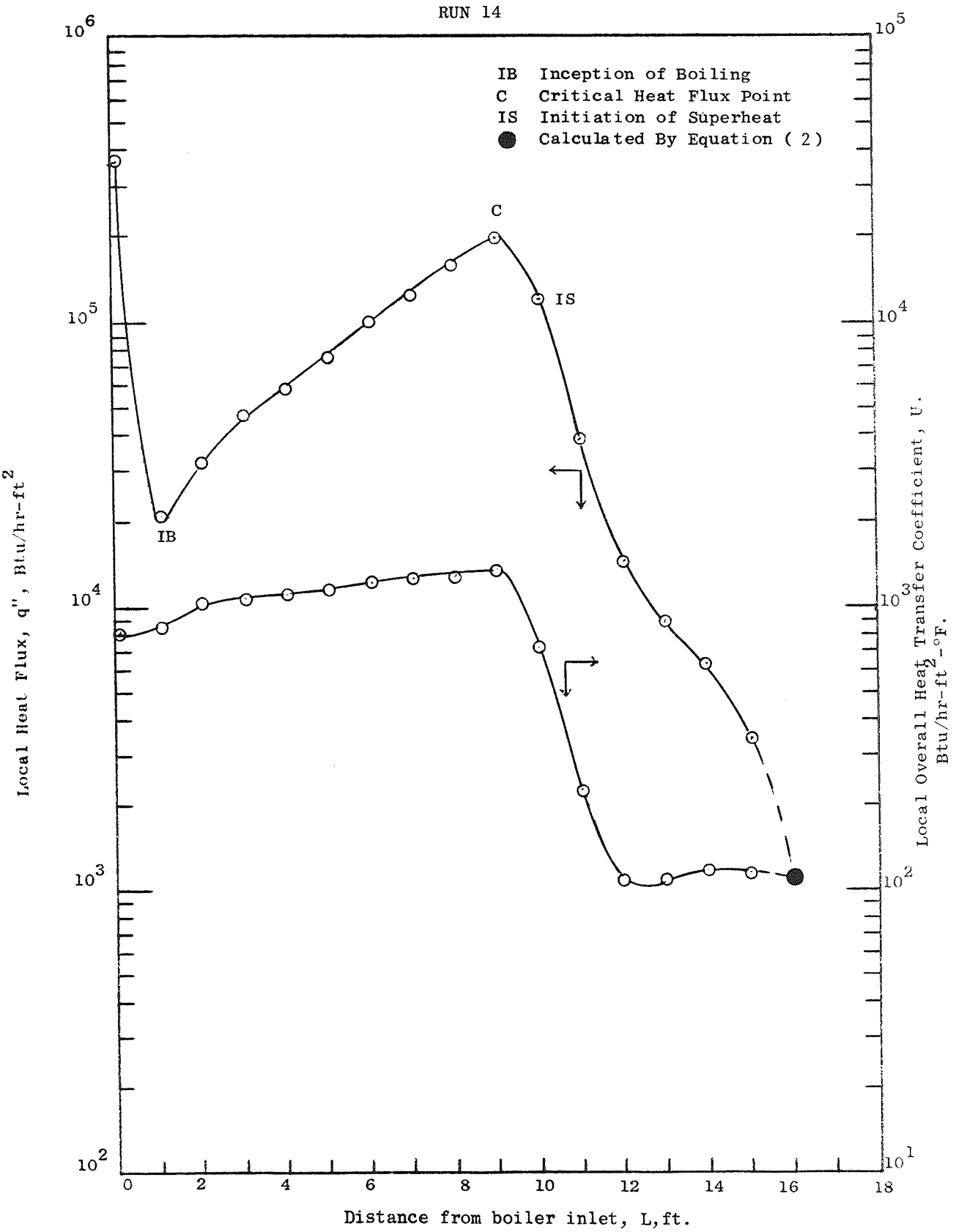

Figure 54. Local Values of Heat Flux and Overall Heat Transfer Coefficient for Mercury Once-Through Boiling Runs.

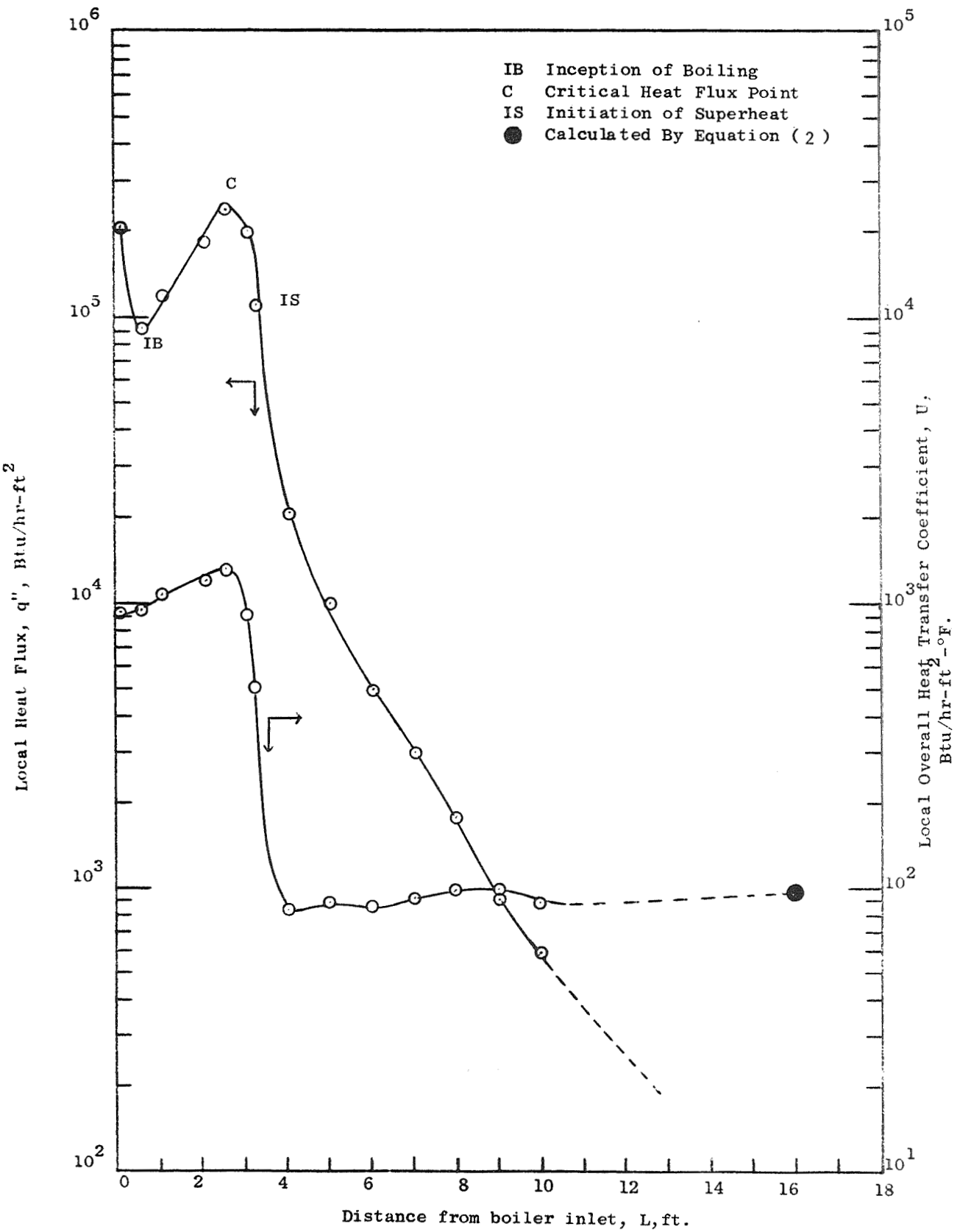

Figure 55. Local Values of Heat Flux and Overall Heat Transfer Coefficient for Mercury Once-Through Boiling Runs.

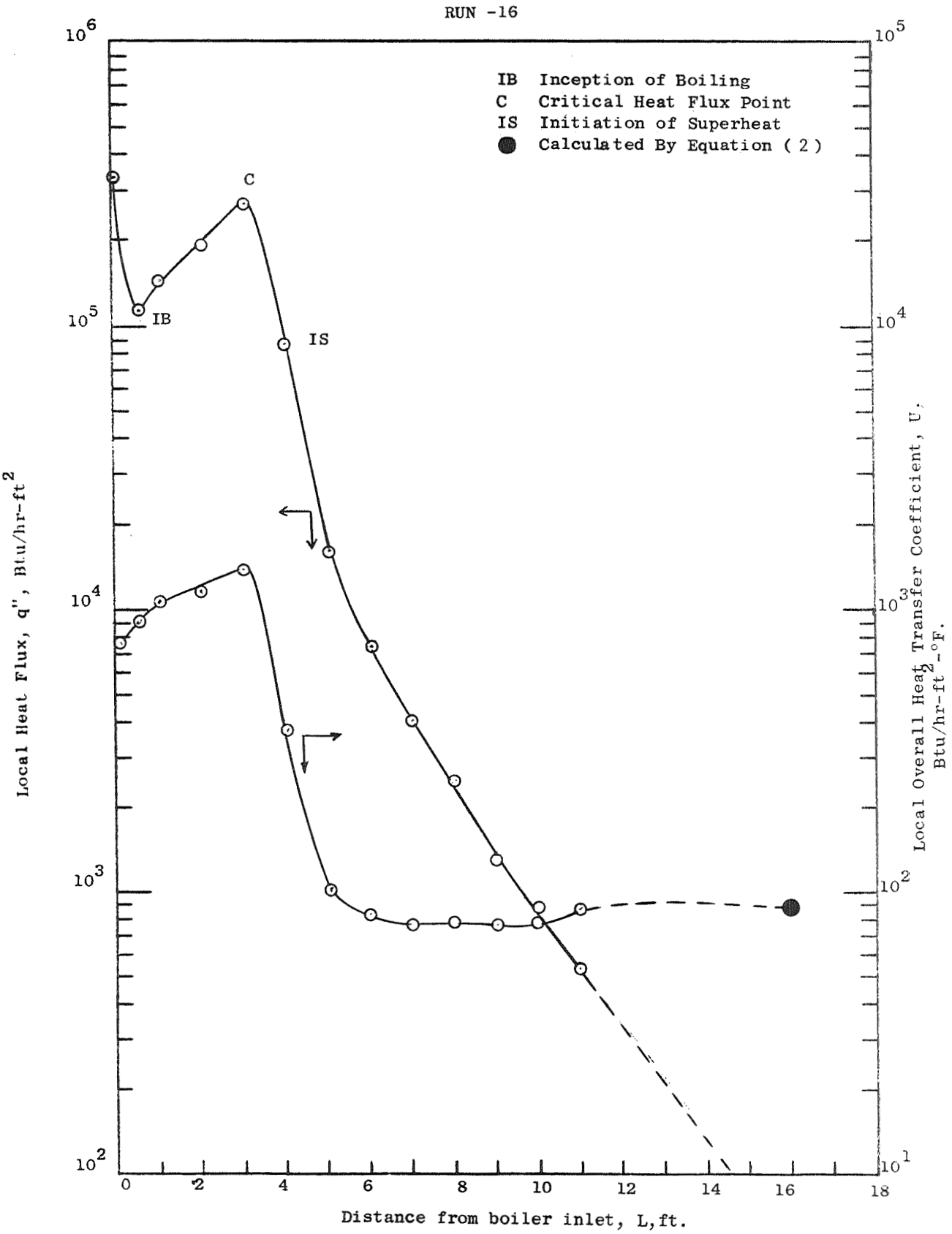

Figure 56. Local Values of Heat Flux and Overall Heat Transfer Coefficient for Mercury Once-Through Boiling Runs.

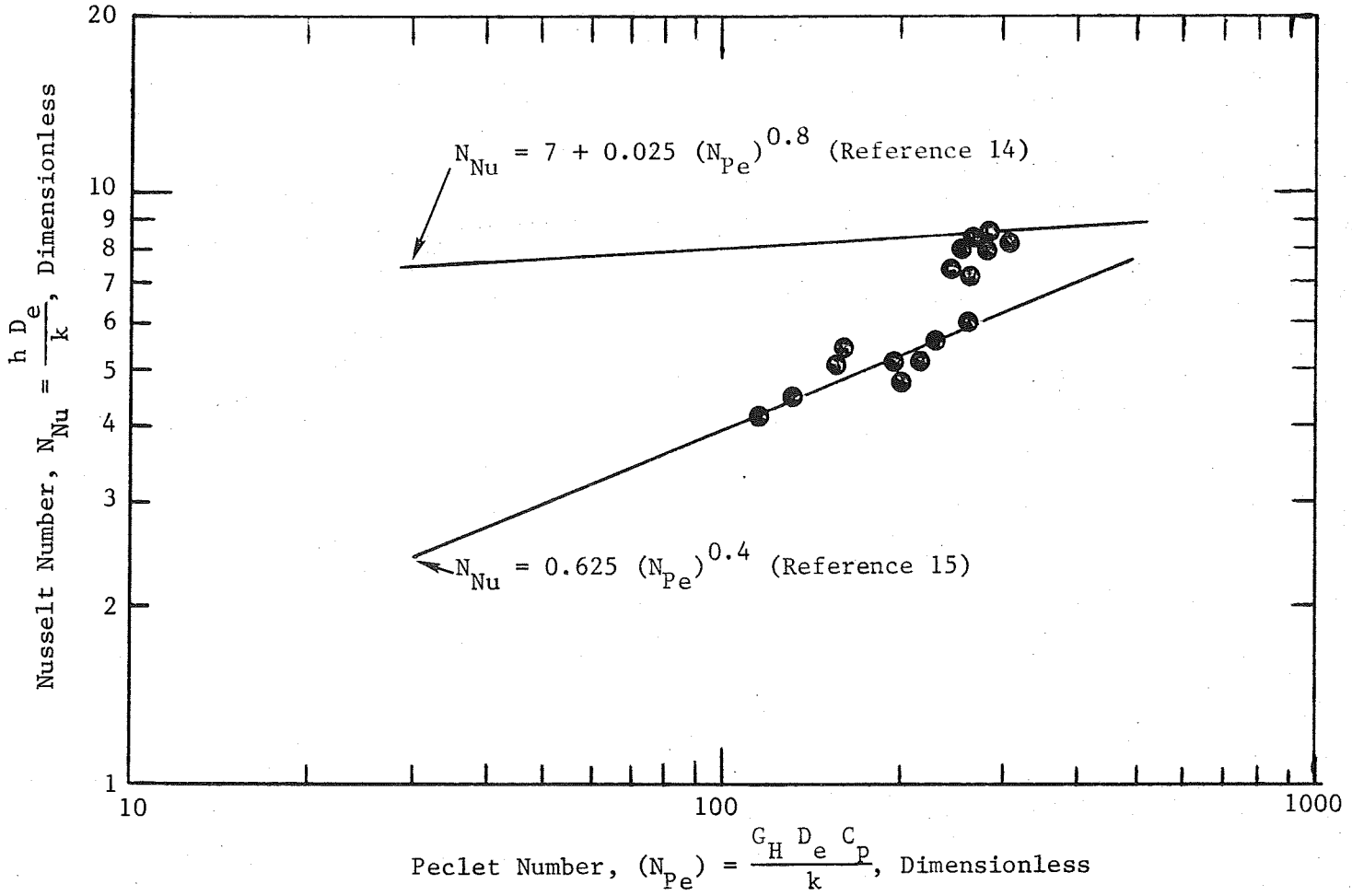

Figure 57. Mercury Liquid Heat Transfer Data from 0.67-inch ID Tube with Helical Insert (P/D = 2.0) Evaluated Assuming Helical Flow, Nusselt Number Vs. Peclet Number.

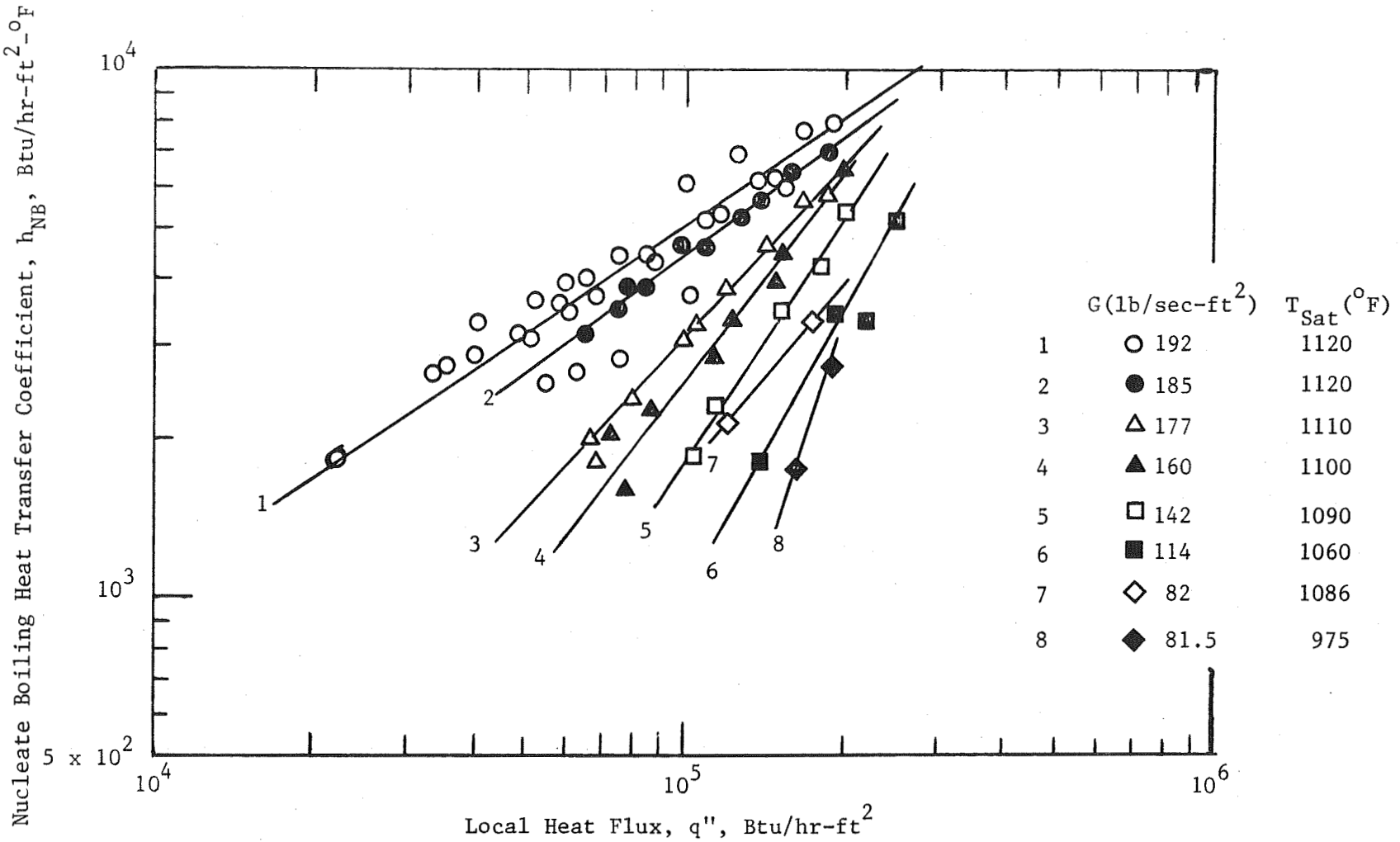

Figure 58. Mercury Nucleate Boiling Data from 0.67-inch ID Tube with Helical Insert (P/D = 2.0), h_{NB} vs. q".

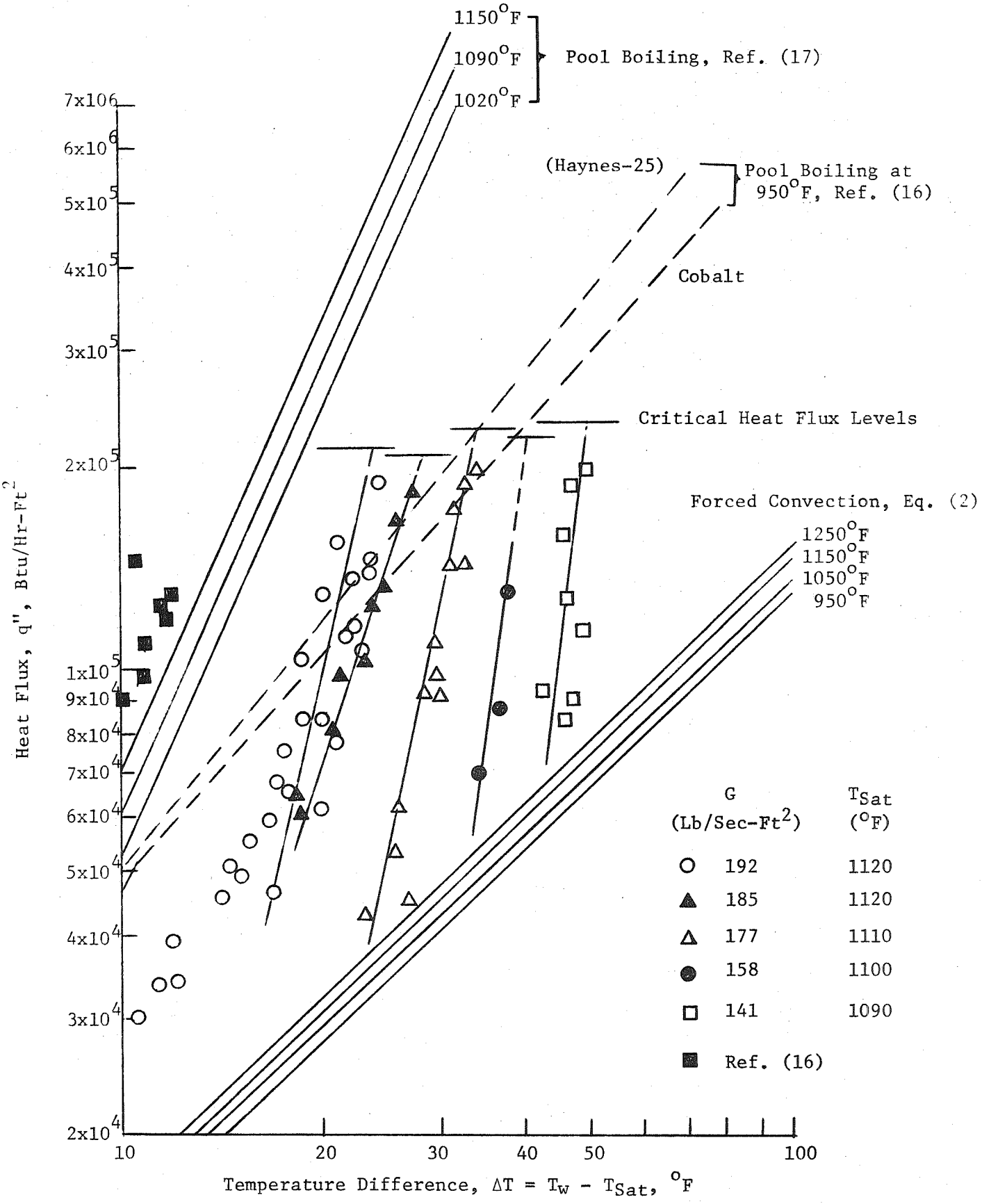

Figure 59. Mercury Nucleate Boiling Heat Transfer Data From a 0.67-Inch ID Tube With Helical Insert (P/D = 2.0), q" Versus ΔT.

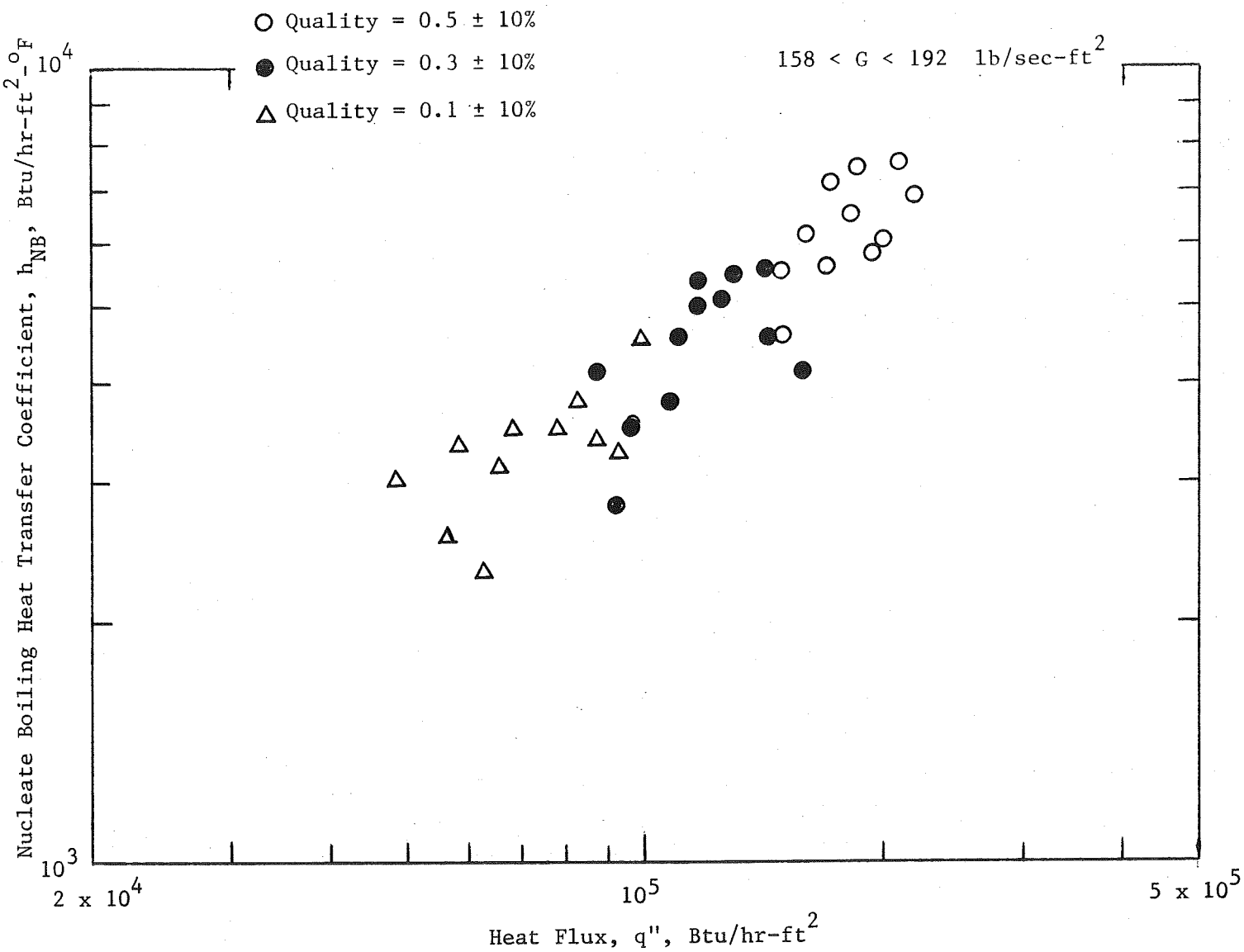

Figure 60. Nucleate Boiling Heat Transfer Data, h_{NB} vs. q", at Various Qualities.

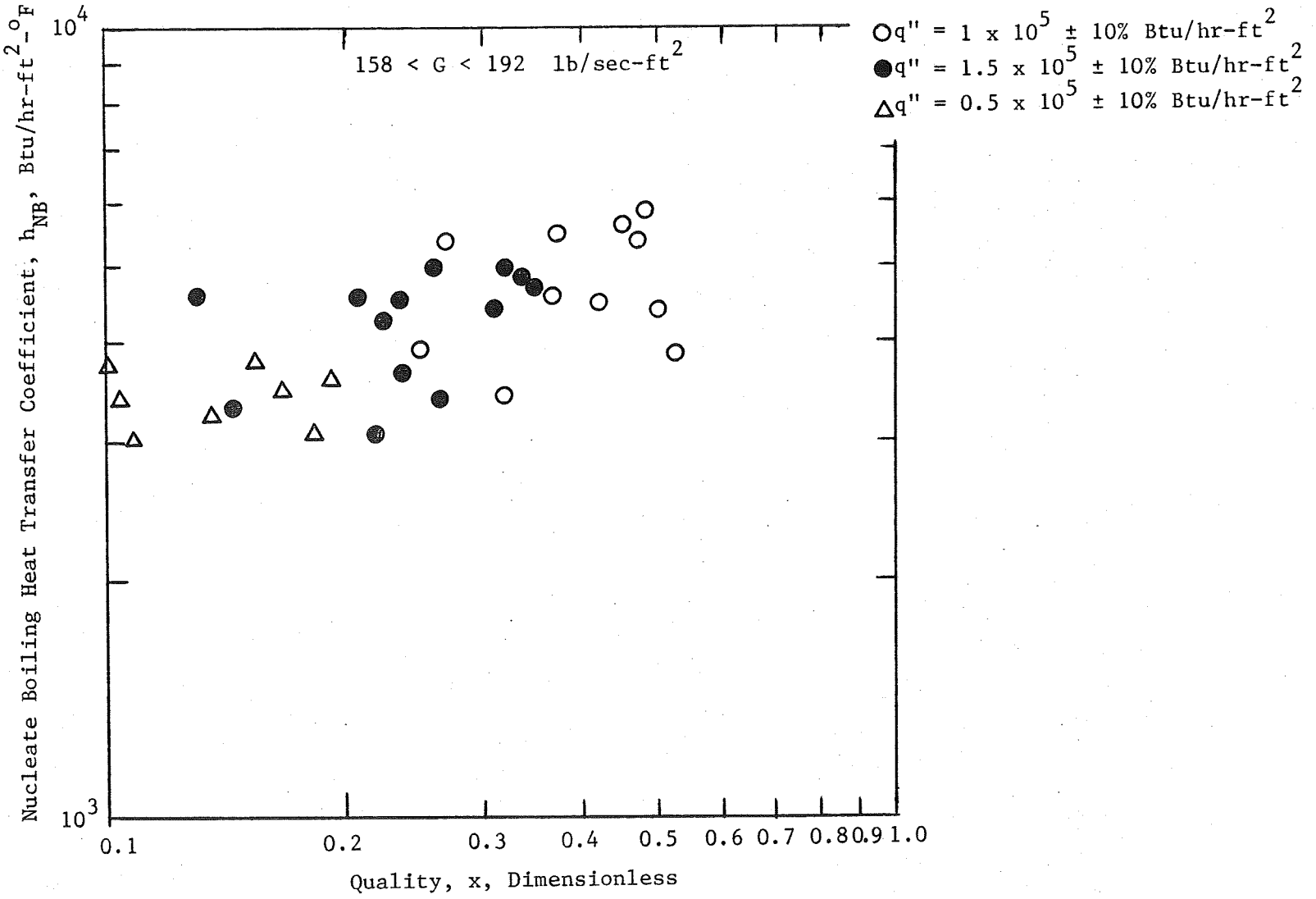

Figure 61. Nucleate Boiling Heat Transfer Results, h_{NB} vs. x, at Various Heat Fluxes.

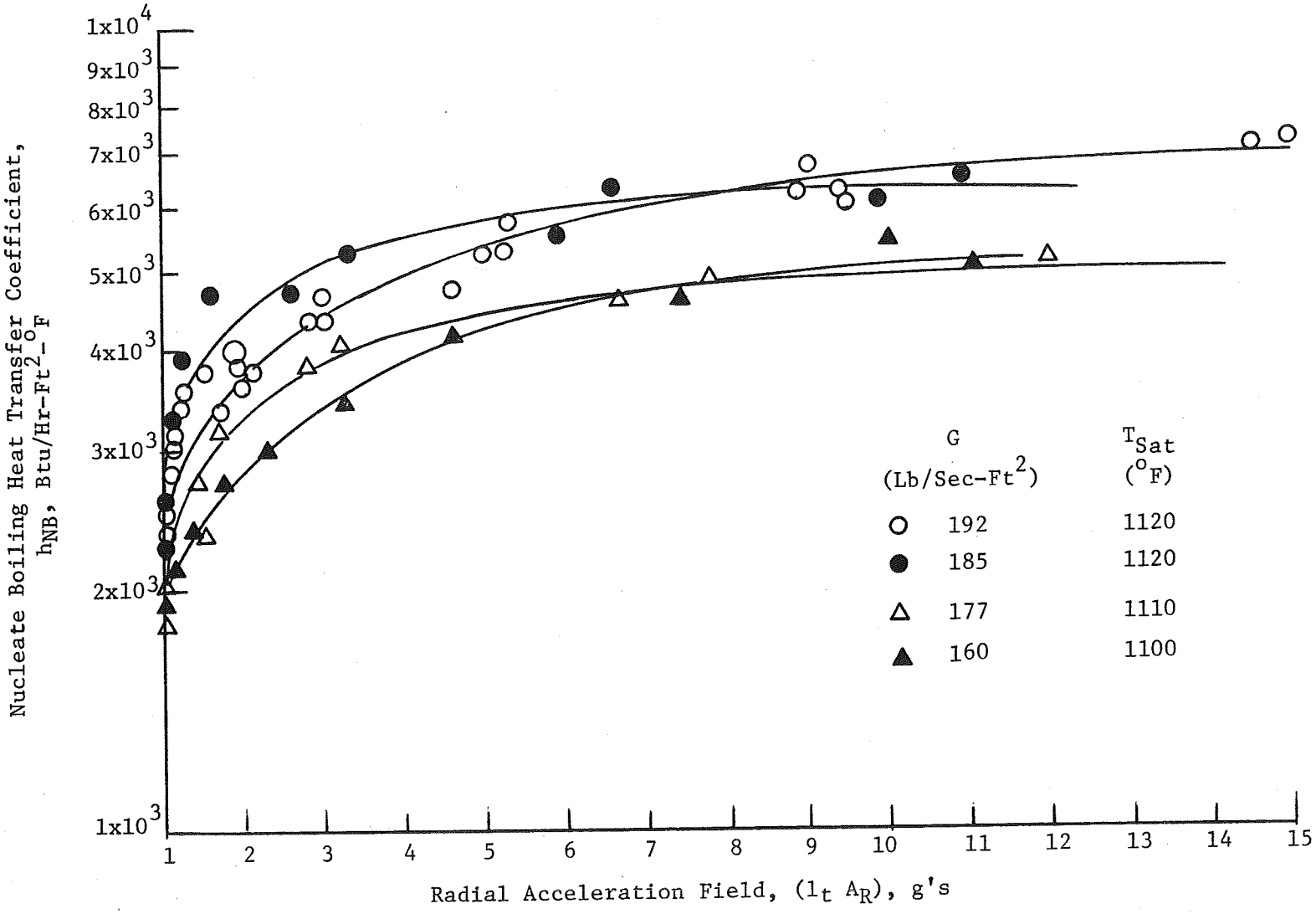

Figure 62. Mercury Nucleate Boiling Heat Transfer Coefficient as Affected by Local Radial Acceleration Field.

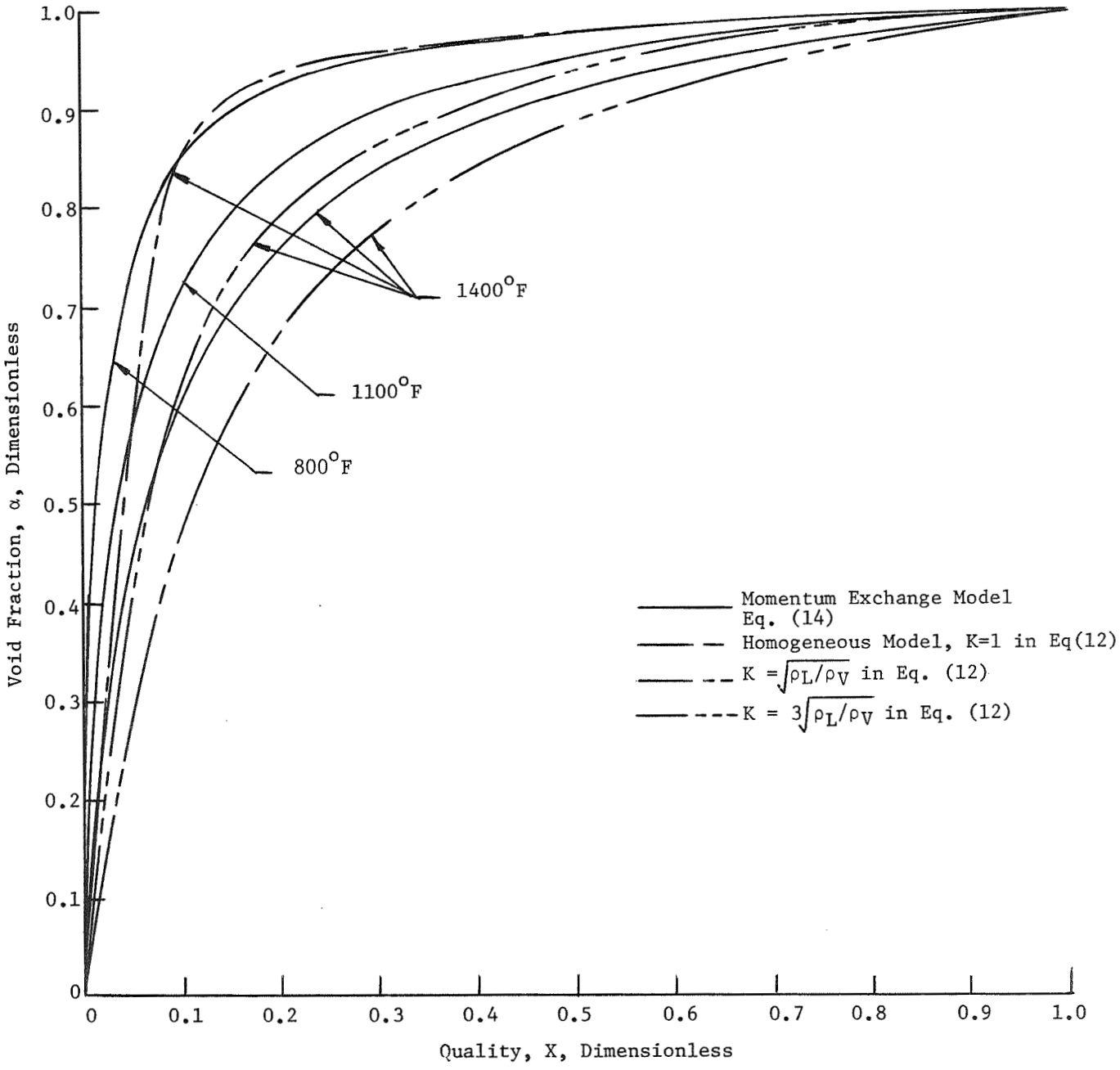

Figure 63. Mercury Void Fraction as a Function of Quality for Various Flow Models.

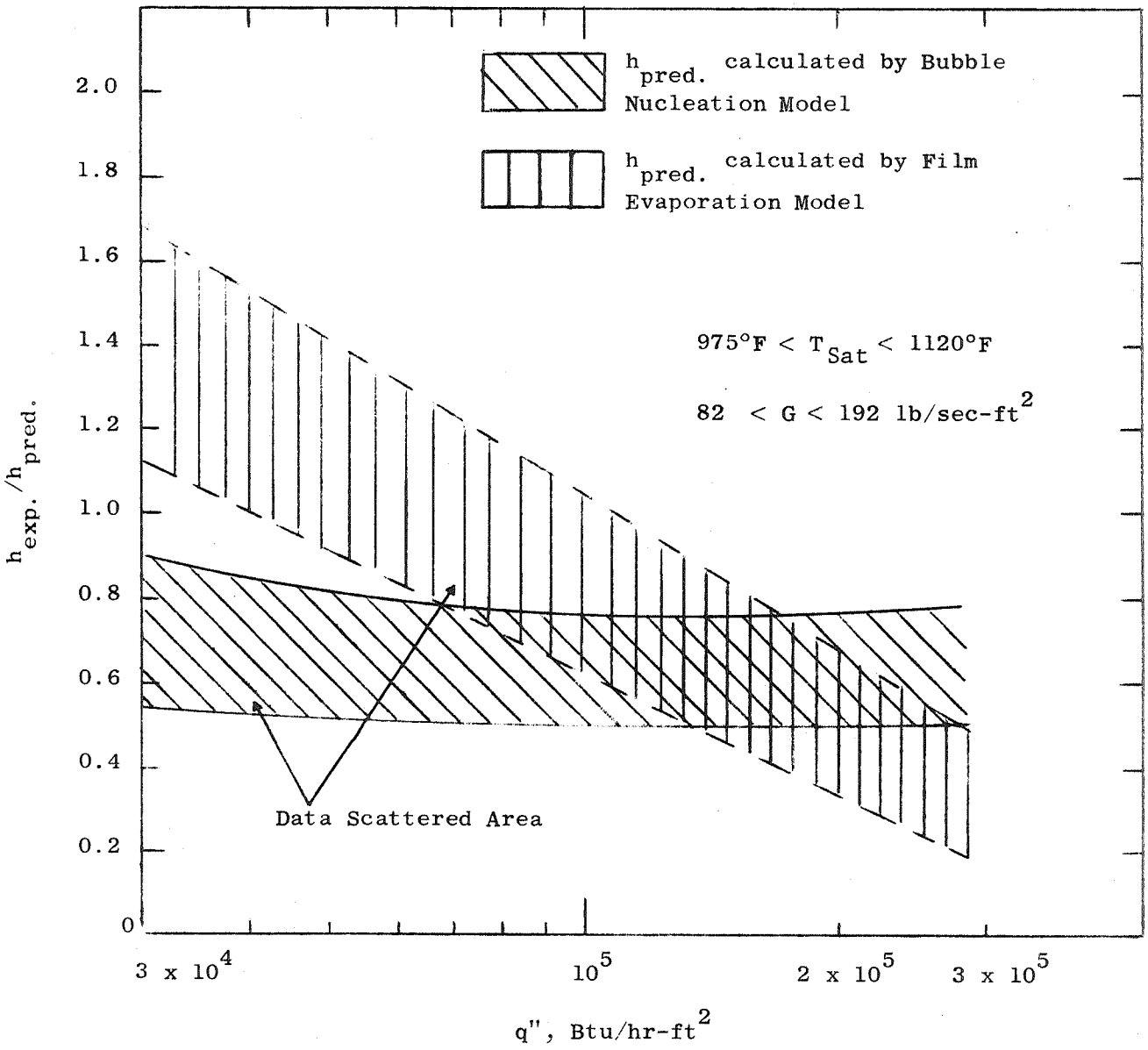

Figure 64. Comparison of Heat Transfer Models for Mercury Boiling at Wetted Conditions.

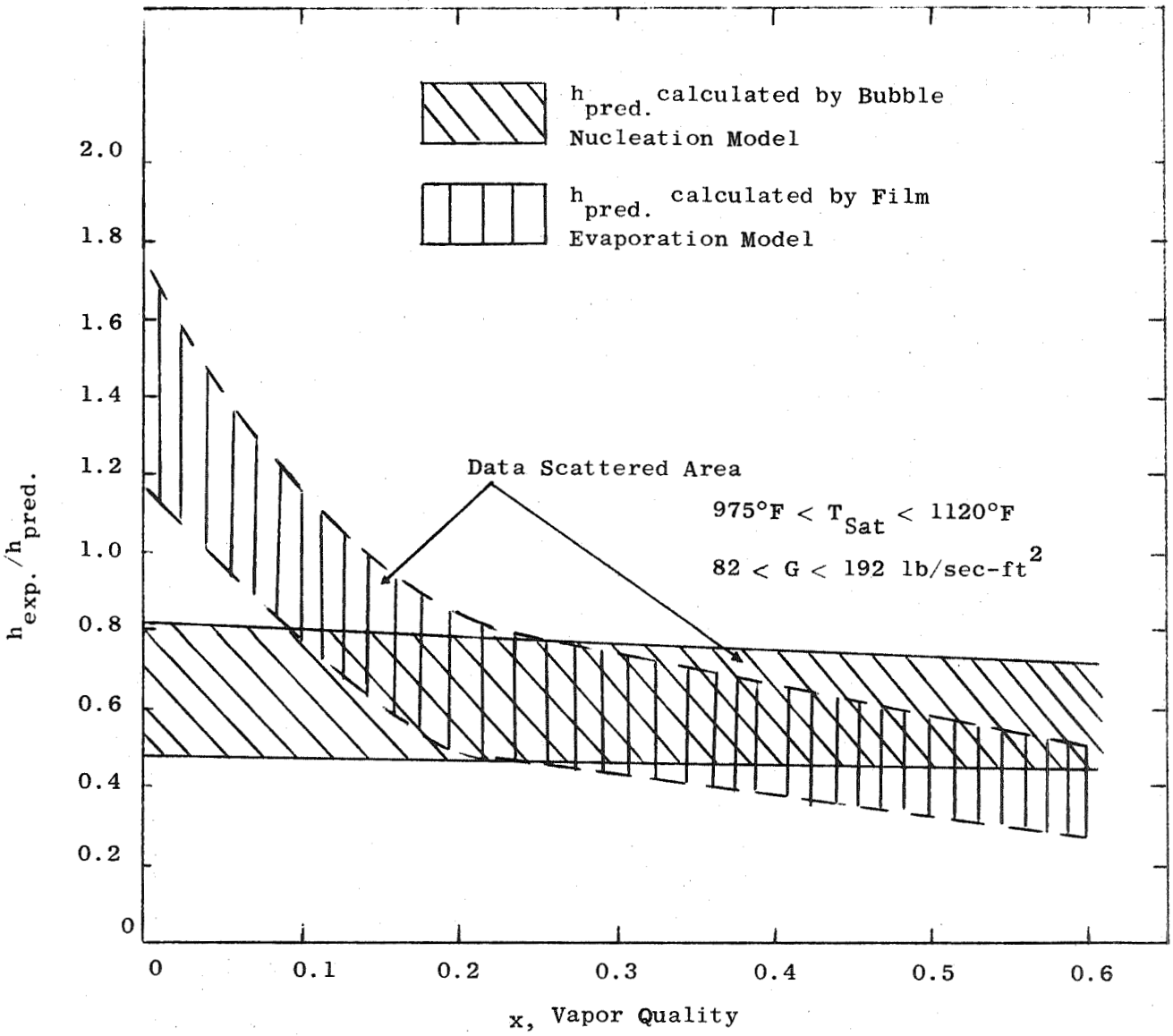

Figure 65. Comparison of Heat Transfer Models for Mercury Boiling at Wetted Conditions.

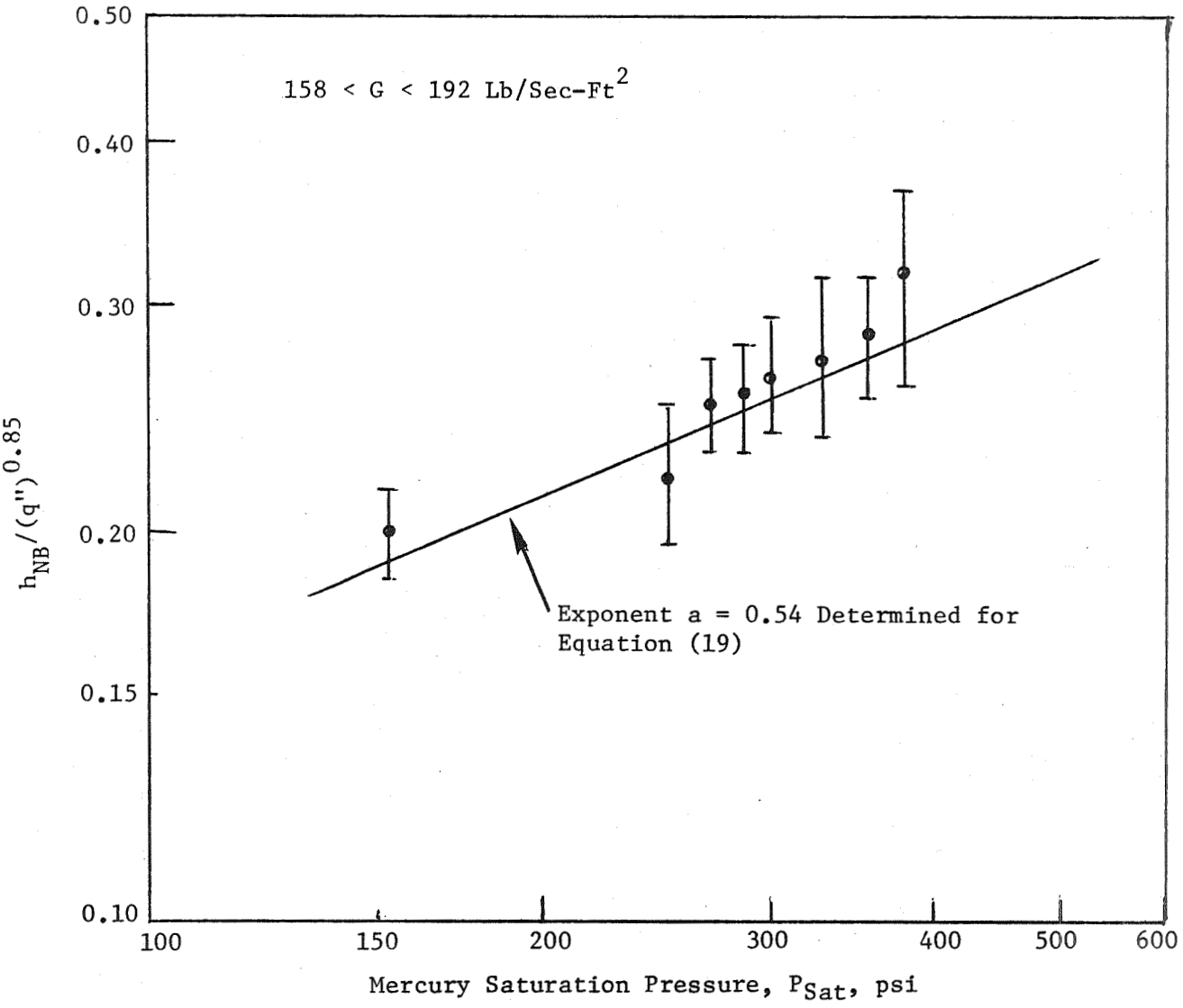

Figure 66. Functional Relation Between $h_{NB}/(q'')^{0.85}$ and P_{Sat} According to the Mercury Nucleate Boiling Data.

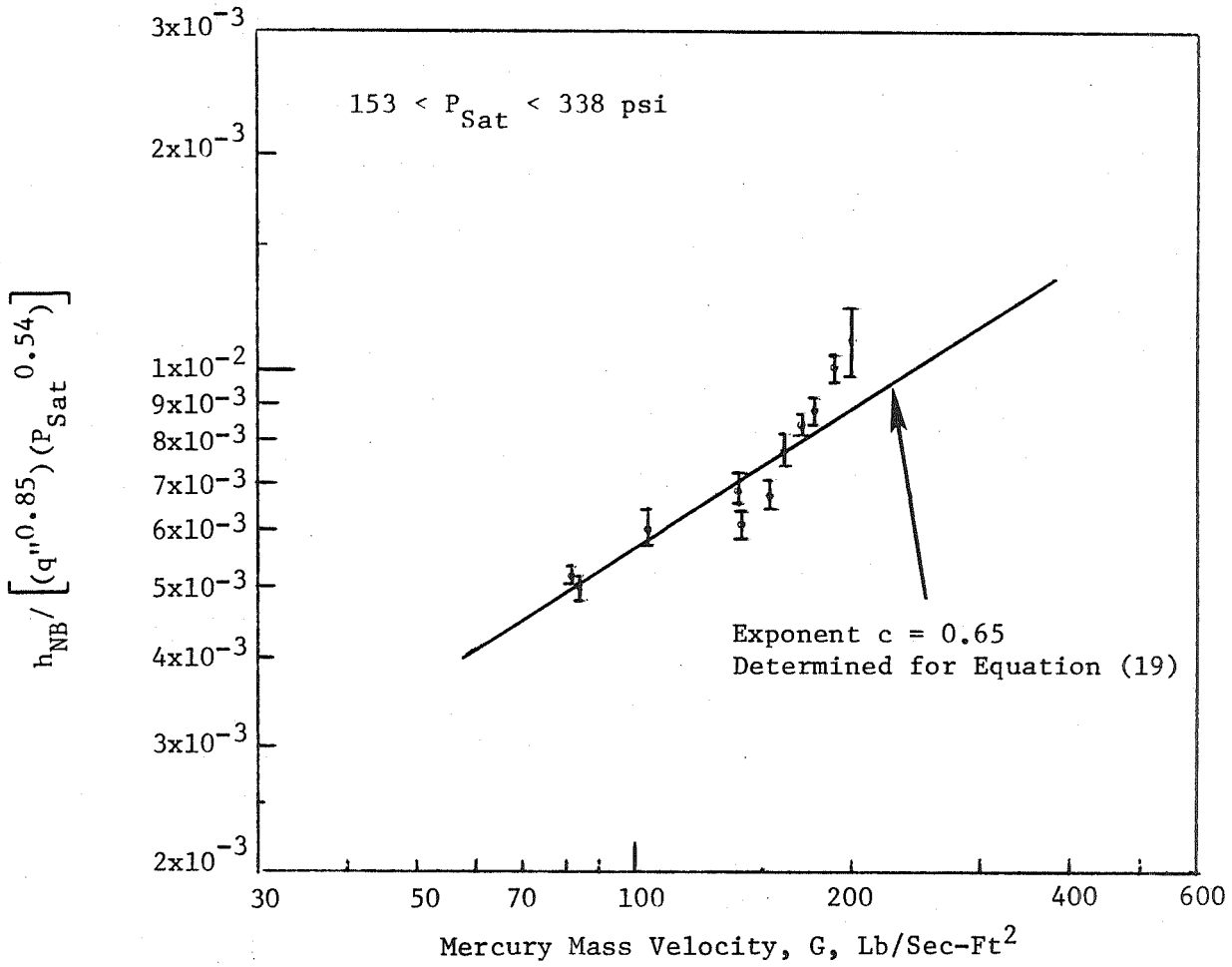

Figure 67. Functional Relation Between $h_{NB}/[(q''^{0.85})(P_{Sat}^{0.54})]$ and G According to the Mercury Nucleate Boiling Data.

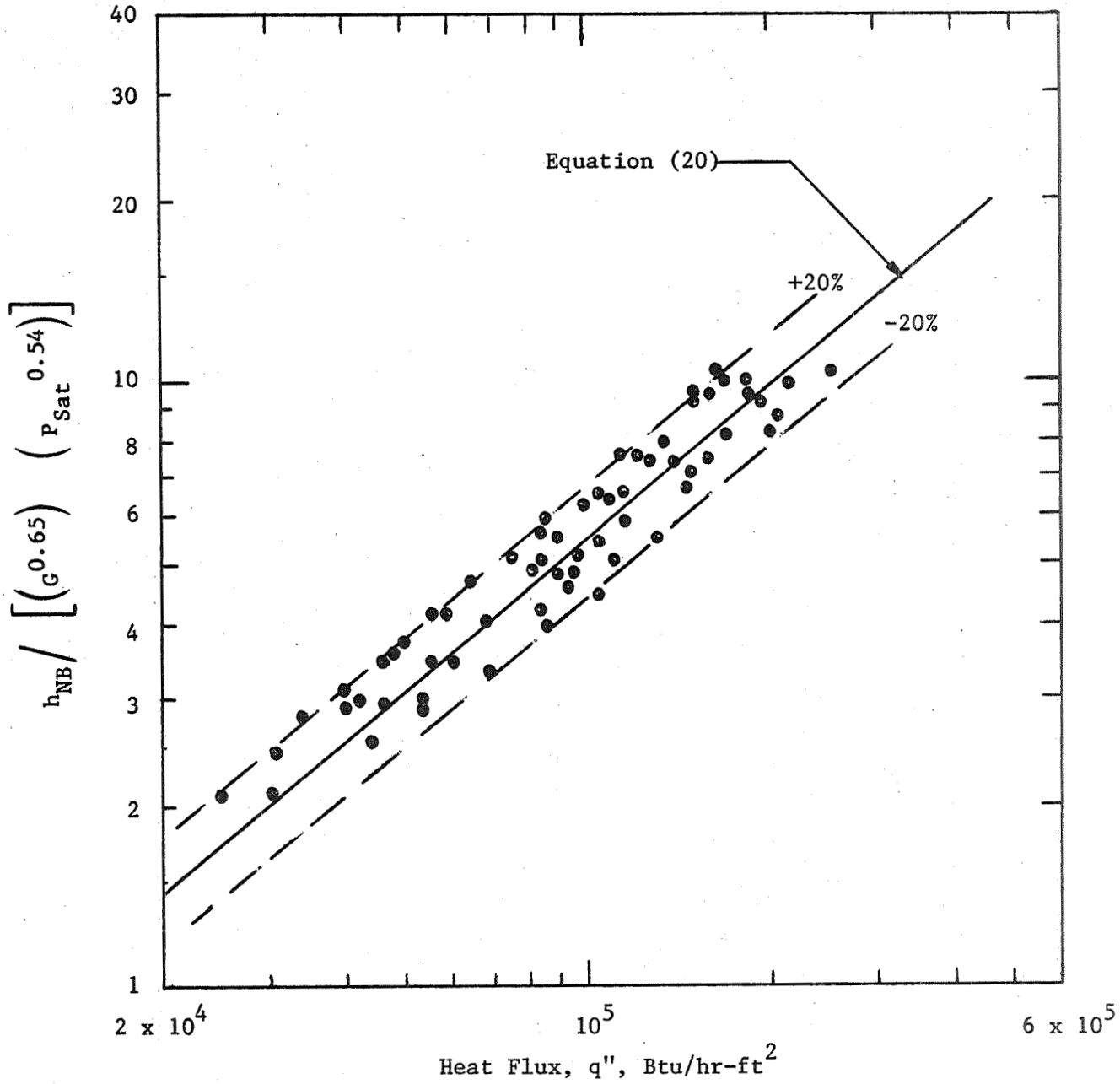

Figure 68. Correlation Plot of Mercury Nucleate Boiling Data.

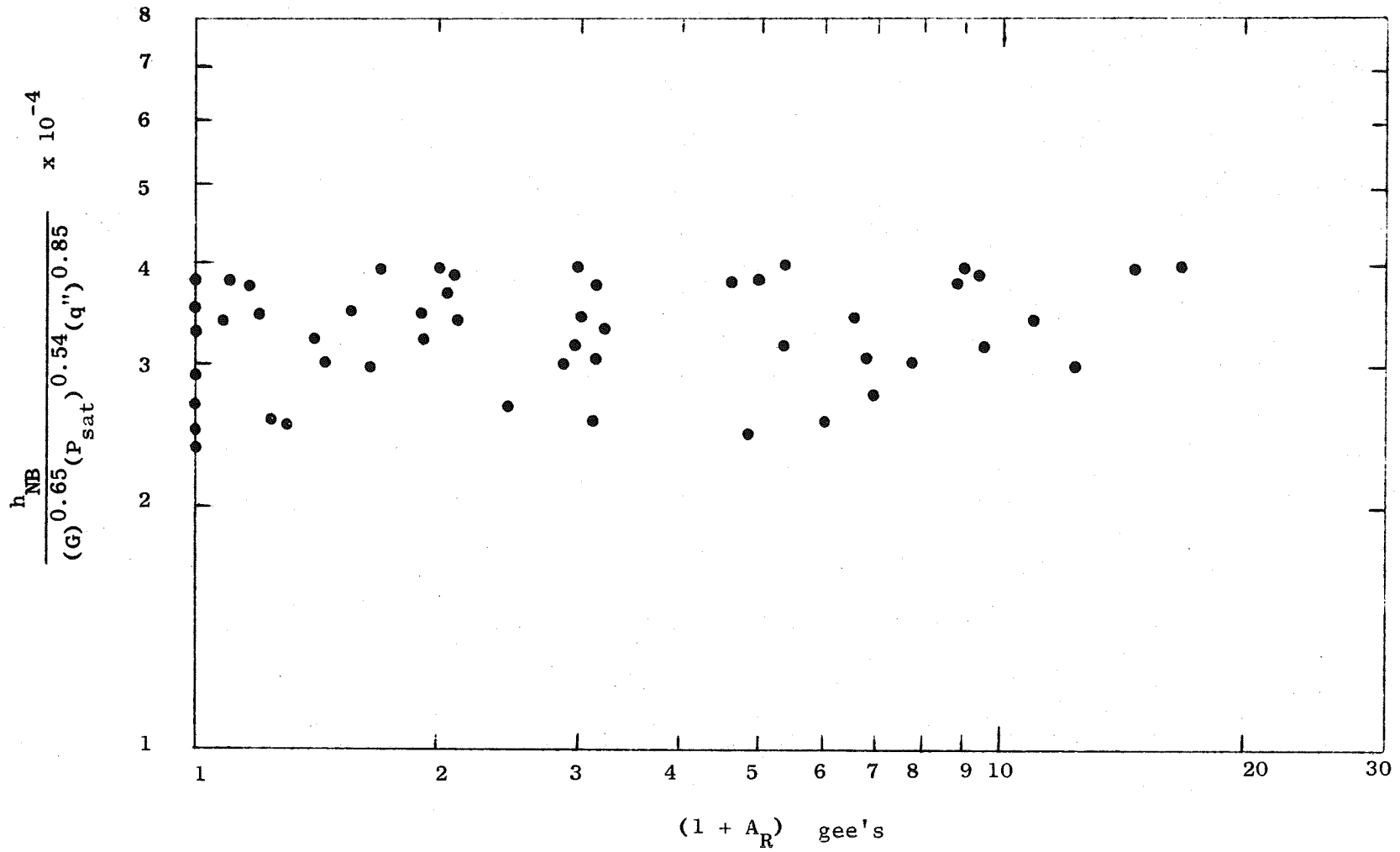

Figure 69. Functional Plot Between $\frac{h_{NB}}{(G)^{0.65}(P_{sat})^{0.54}(q'')^{0.85}}$ and $(1 + A_R)$ according to the Mercury Nucleate Boiling Data

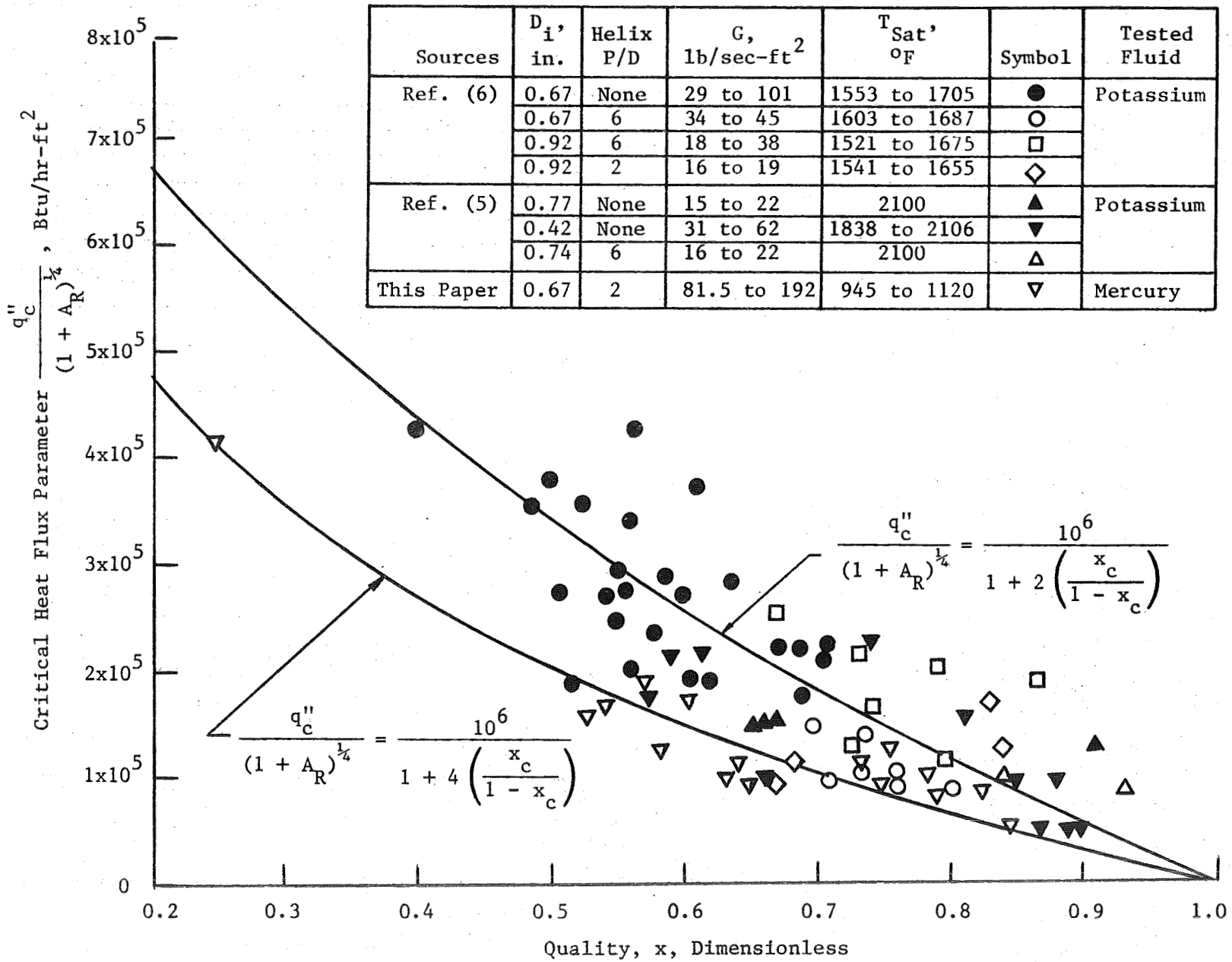

Figure 70. Mercury Critical Heat Flux Results and Correlations Compared with Potassium Results from References (5) and (6).

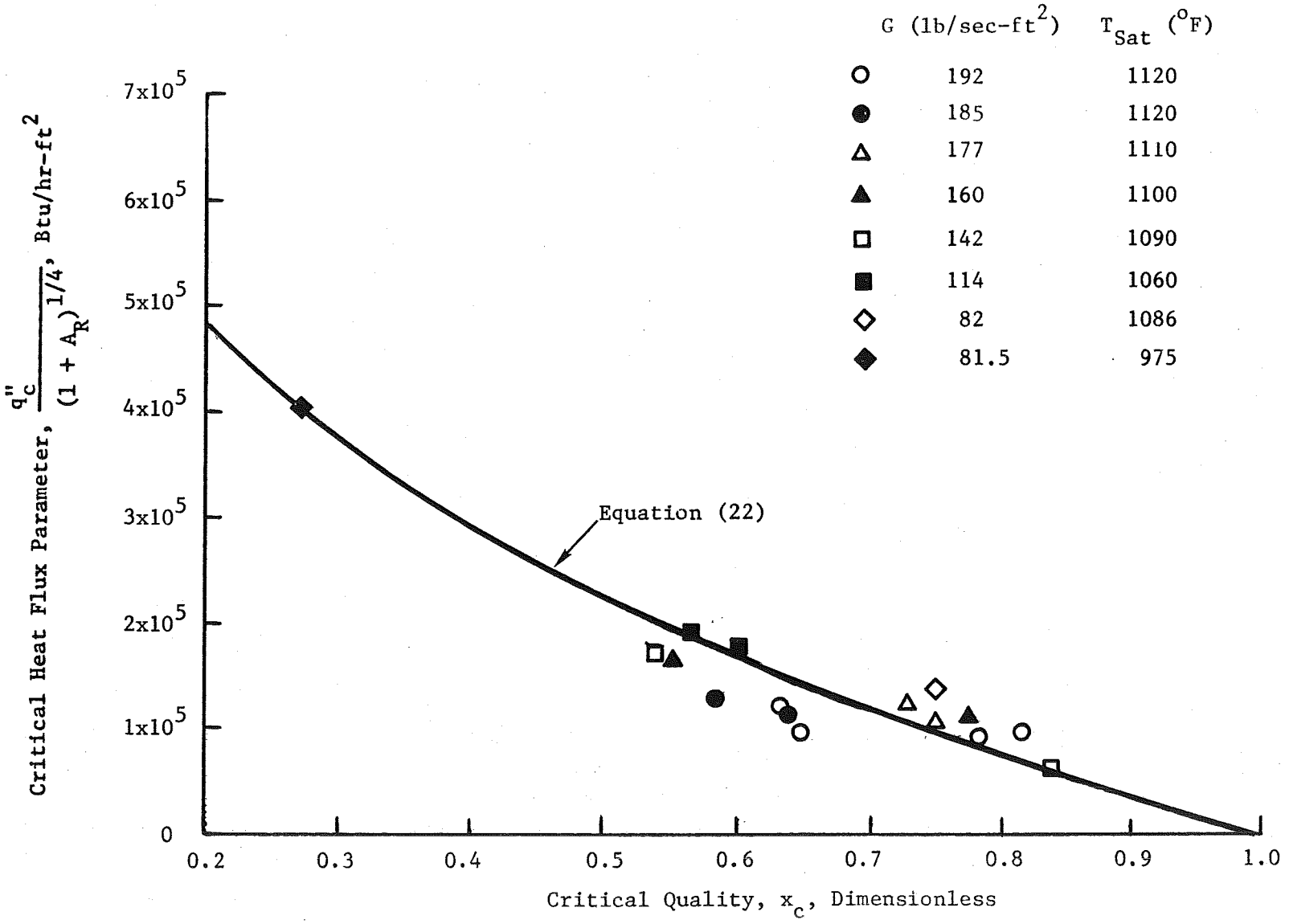

Figure 71. Mercury Critical Heat Flux Results Obtained from a 0.67-inch ID Tube with Helical Insert (P/D = 2.0).

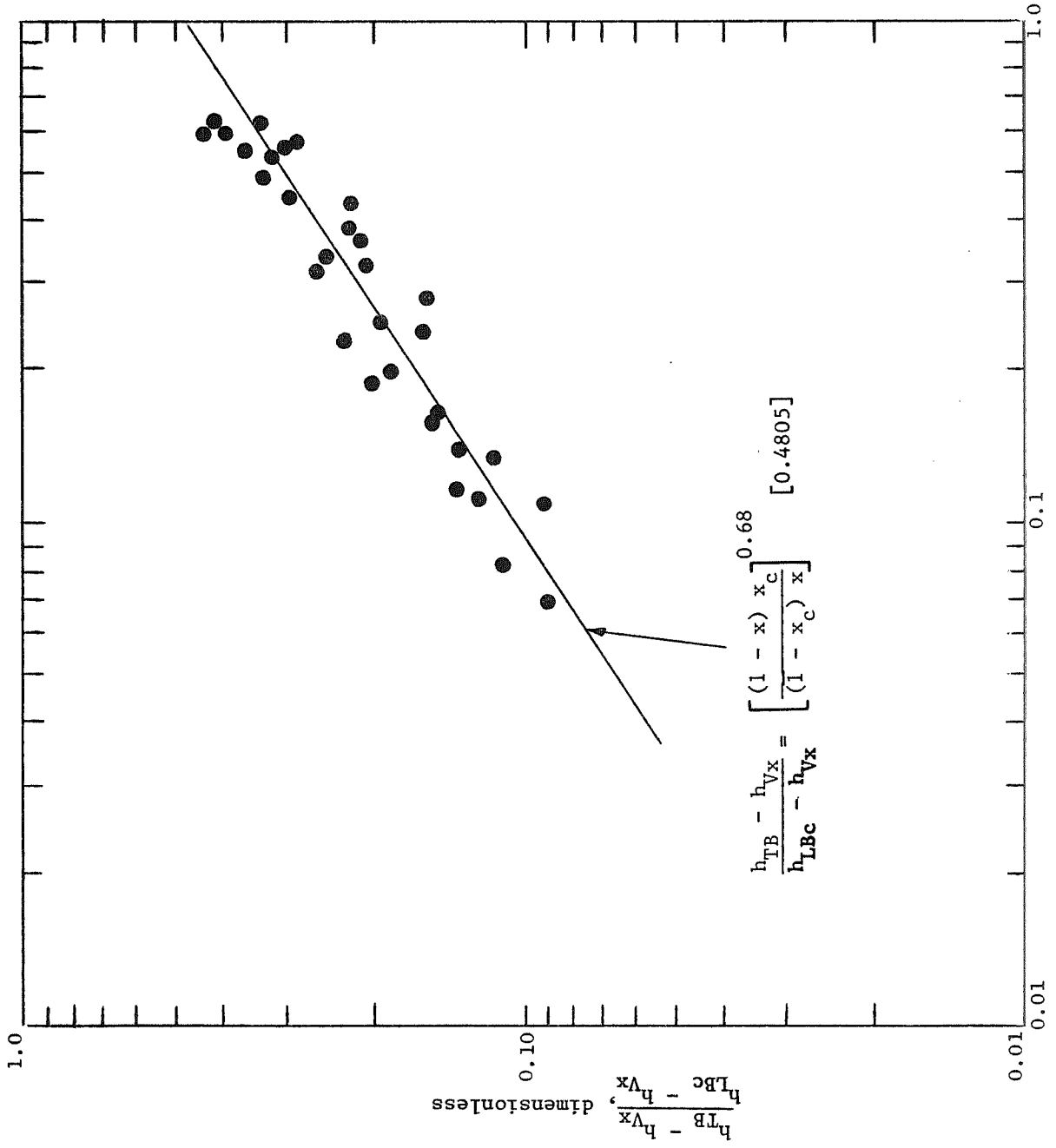

Figure 72. Transition Boiling Data Correlation Plot.

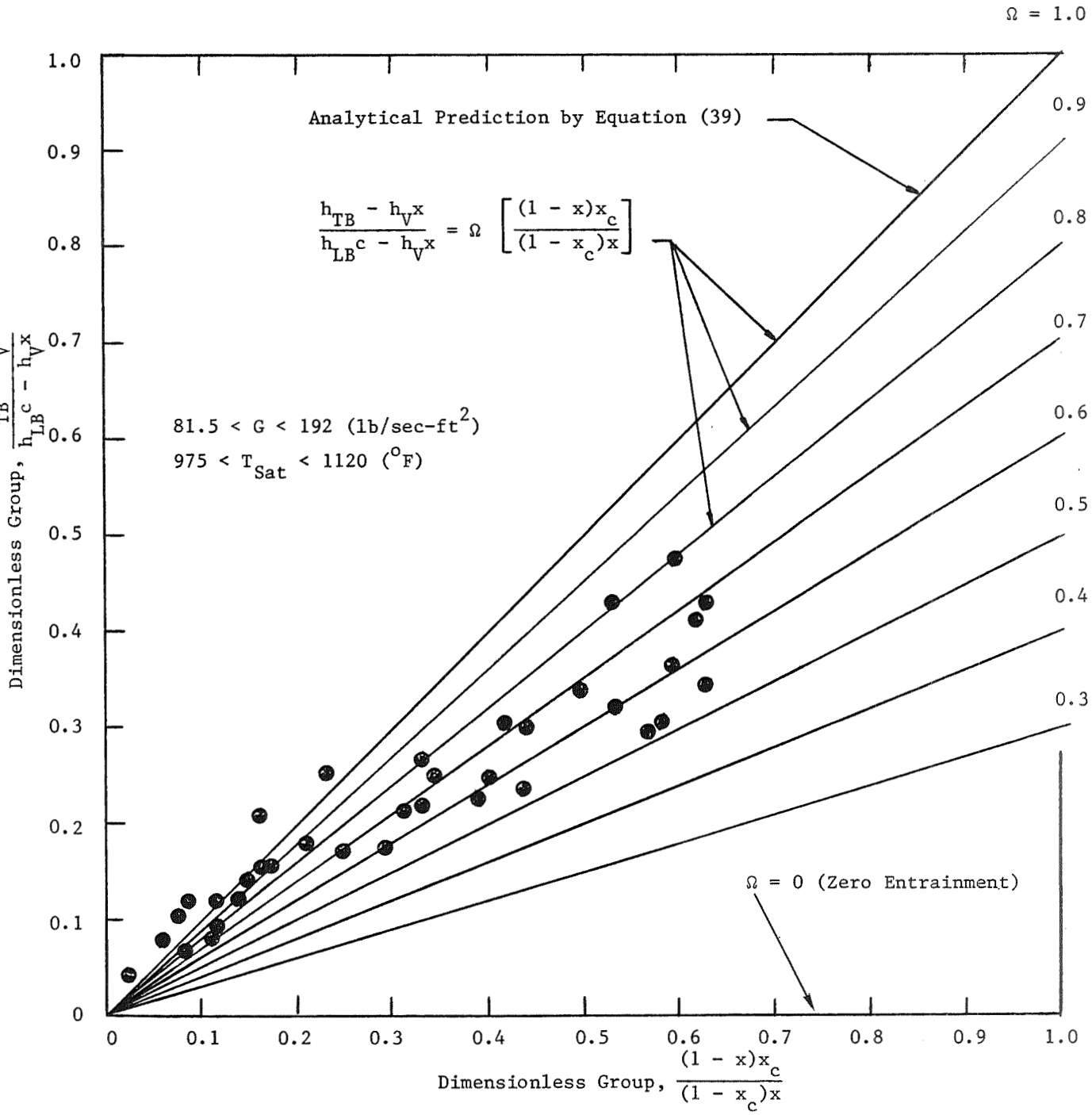

Figure 73. Correlation Plot of Transition Boiling Data by Assuming Flow Model with Constant Droplet Size.

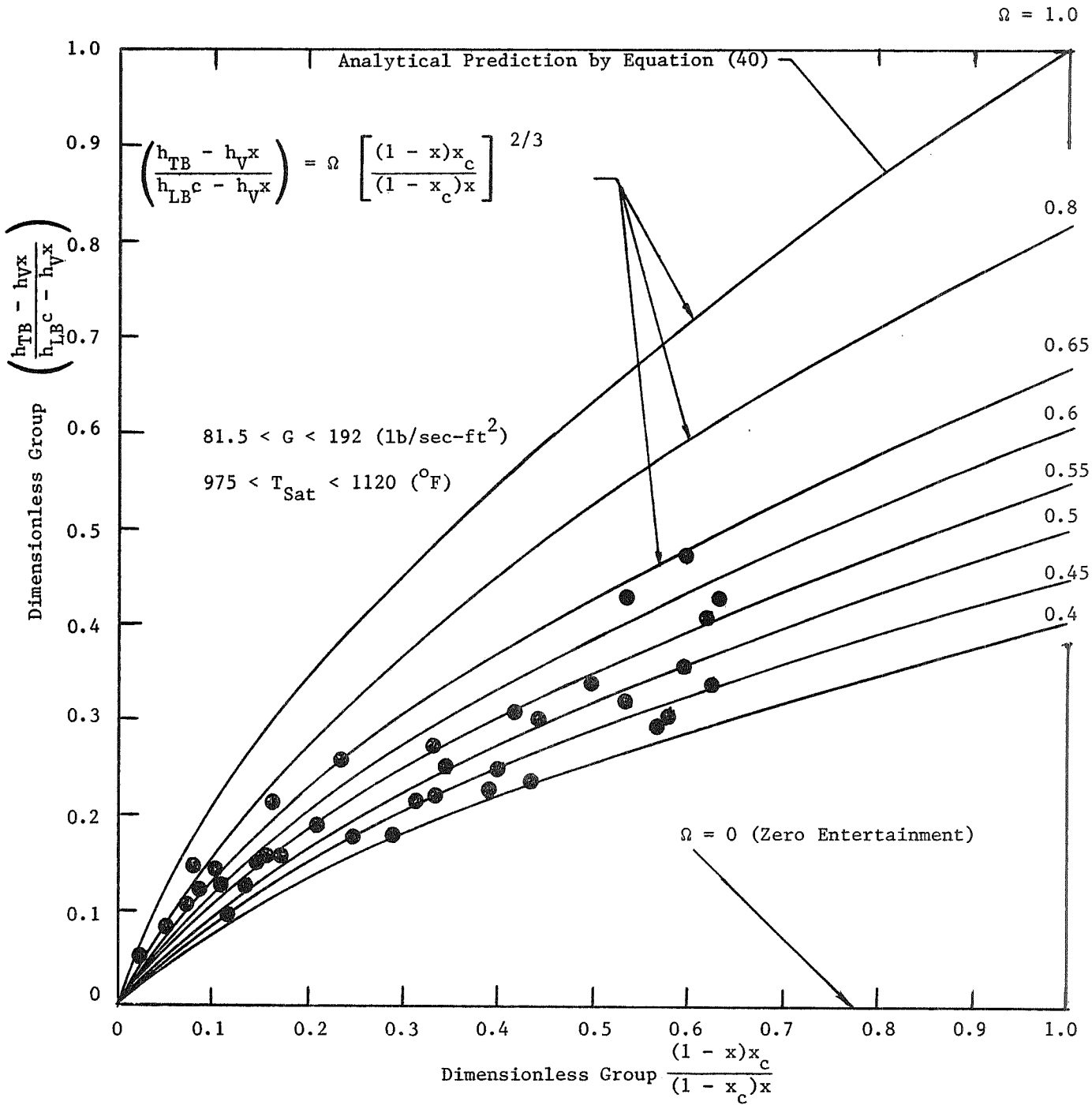

Figure 74. Correlation Plot of Transition Boiling Data by Assuming Flow Model with Constant Density of Droplets.

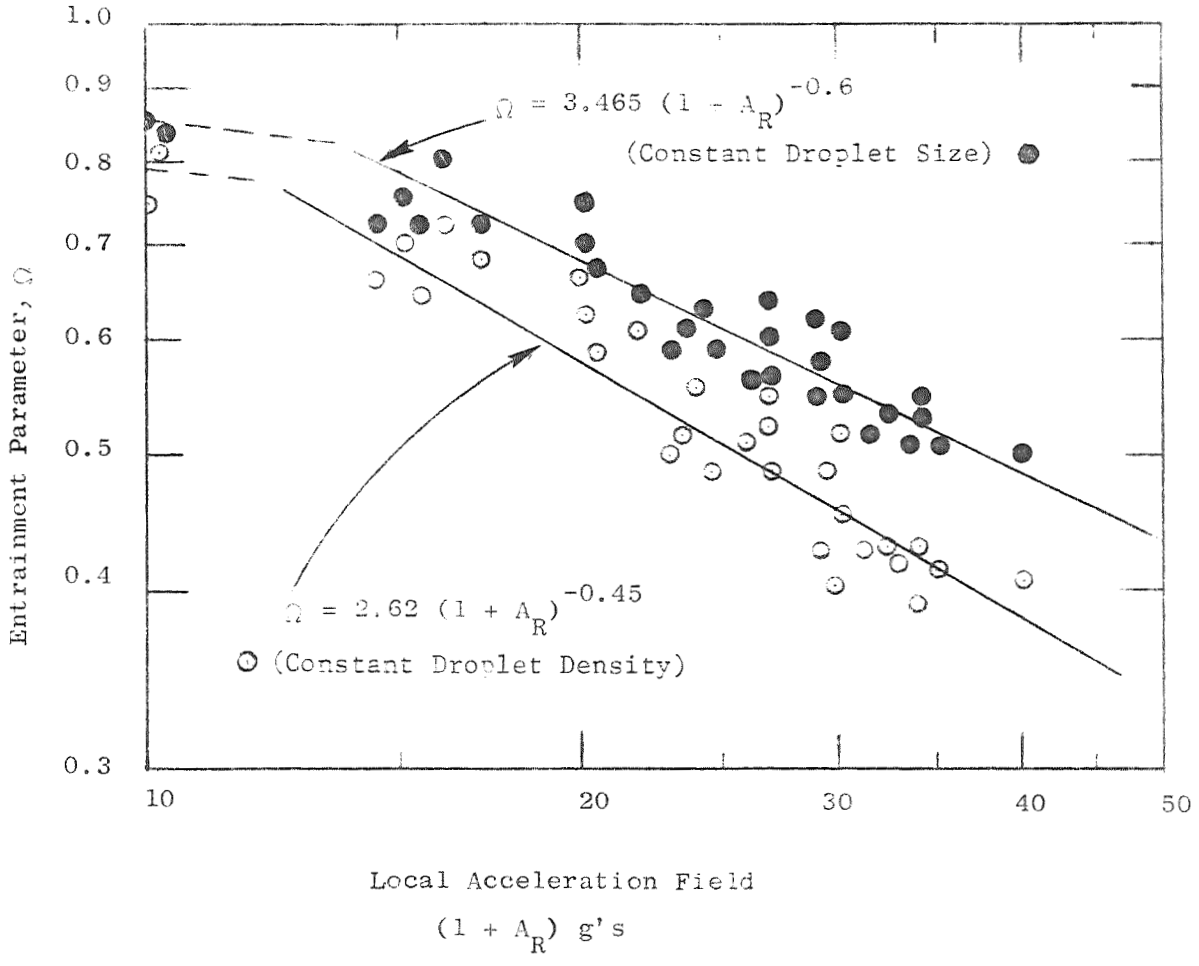

Figure 75. Liquid Entrainment as Affected by Local Acceleration Field in the Transition Boiling Region.

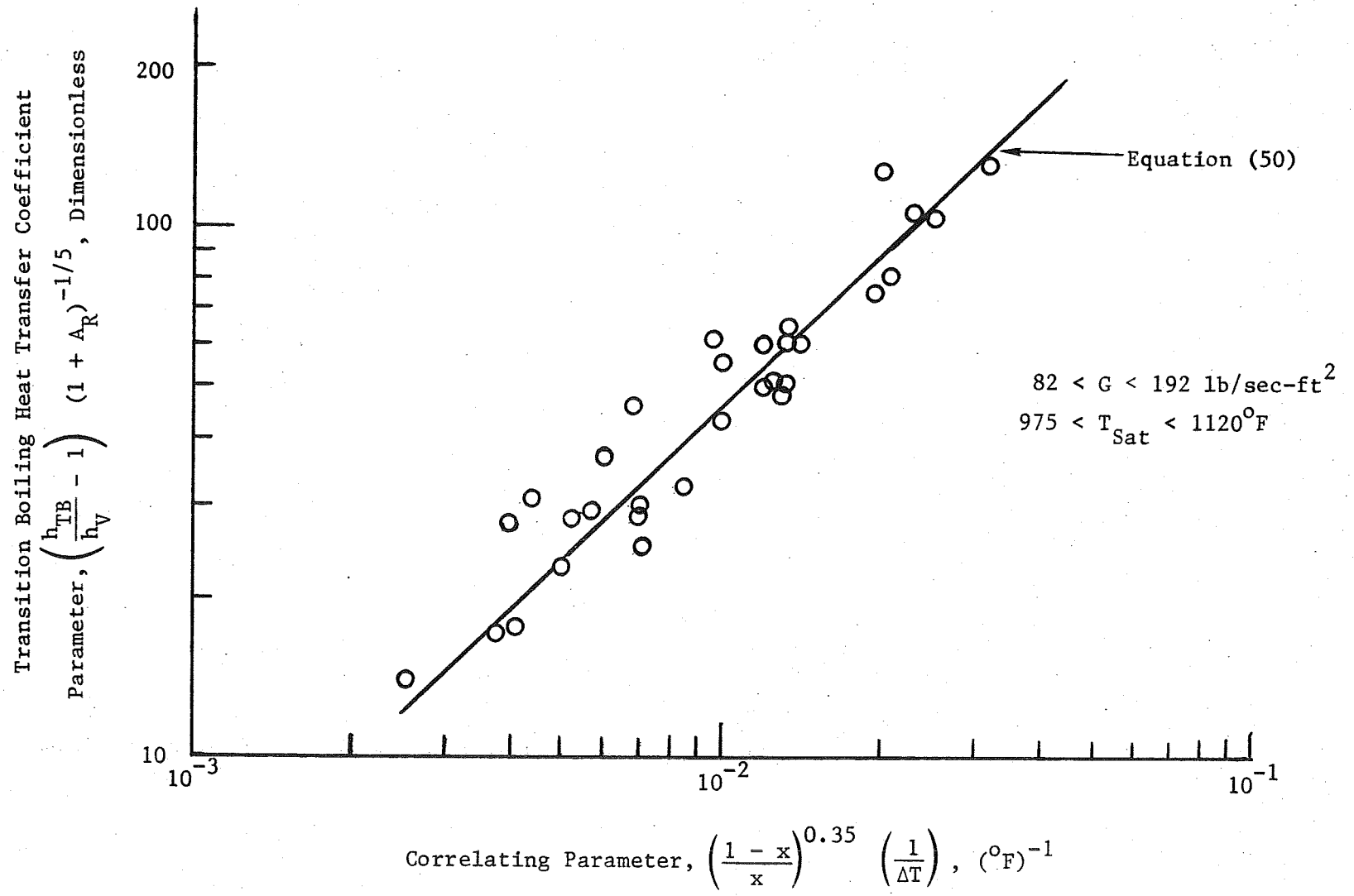

Figure 76. Mercury Transition Boiling Heat Transfer Data and Correlation.

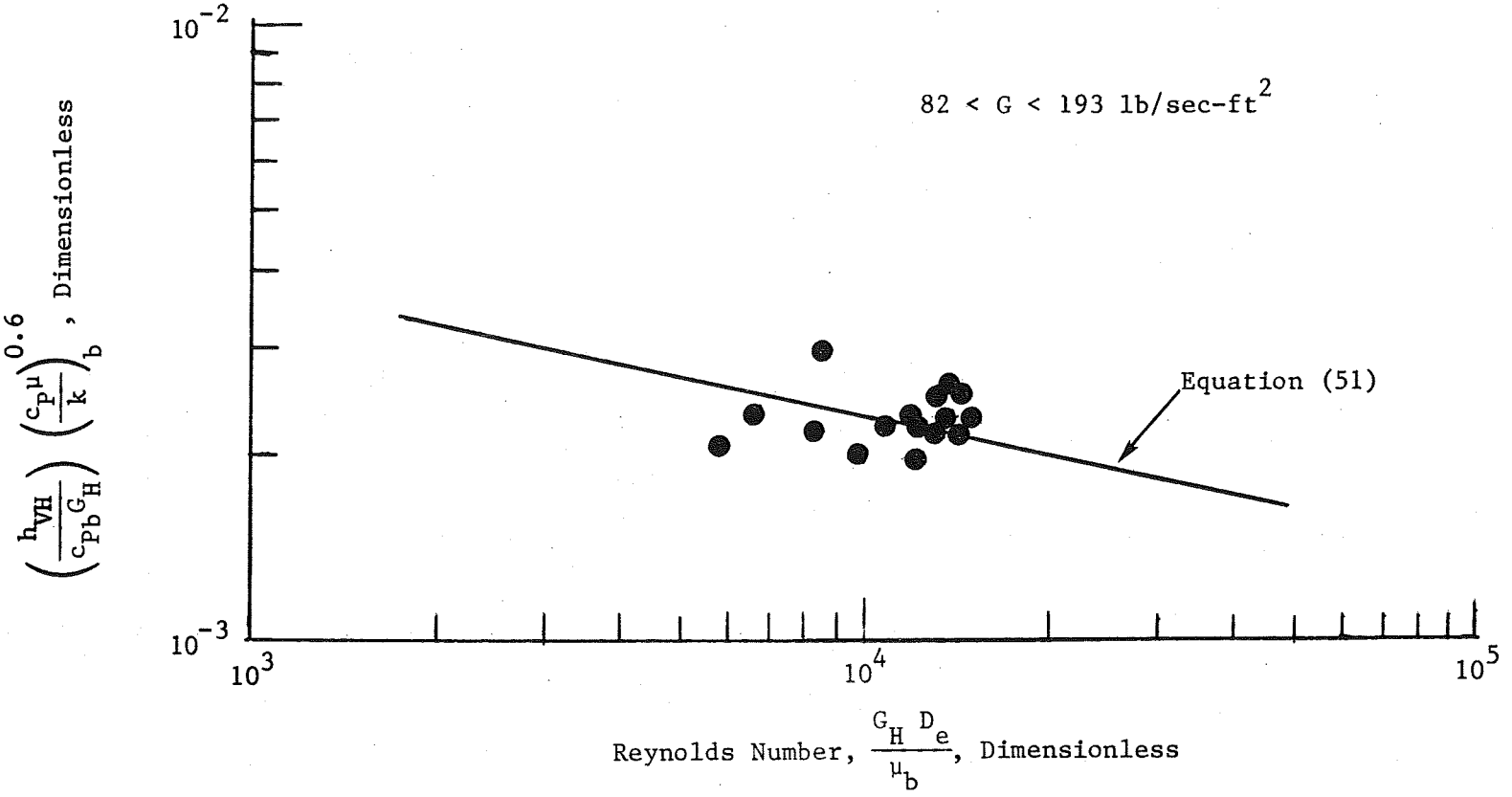

Figure 77. Mercury Superheated Vapor Results Obtained from a 0.67-inch ID Tube with Helical Insert (P/D = 2.0). Evaluated for Helical Flow.

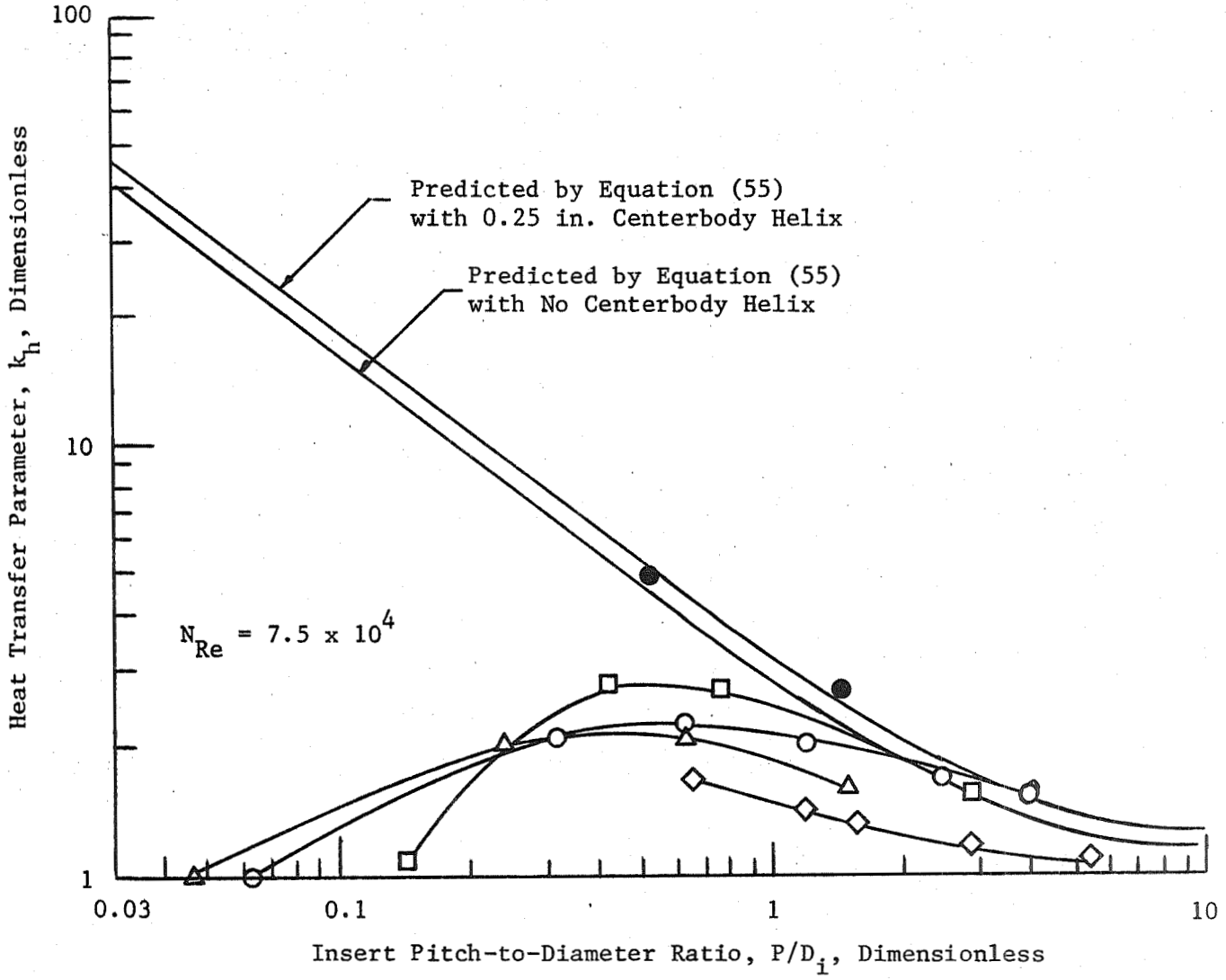

◇ △ ○ □ Wire Coil Insert	d/D_i	= 0.0317	Ref. (28)
		= 0.0463	Ref. (28)
		= 0.0634	Ref. (28)
		= 0.1428	Ref. (27)
● Helical Vane Insert	D_{cb}	= 0.25	Ref. (27)

Figure 78. Measured Heat Transfer Parameter vs. Insert Twist Ratio.

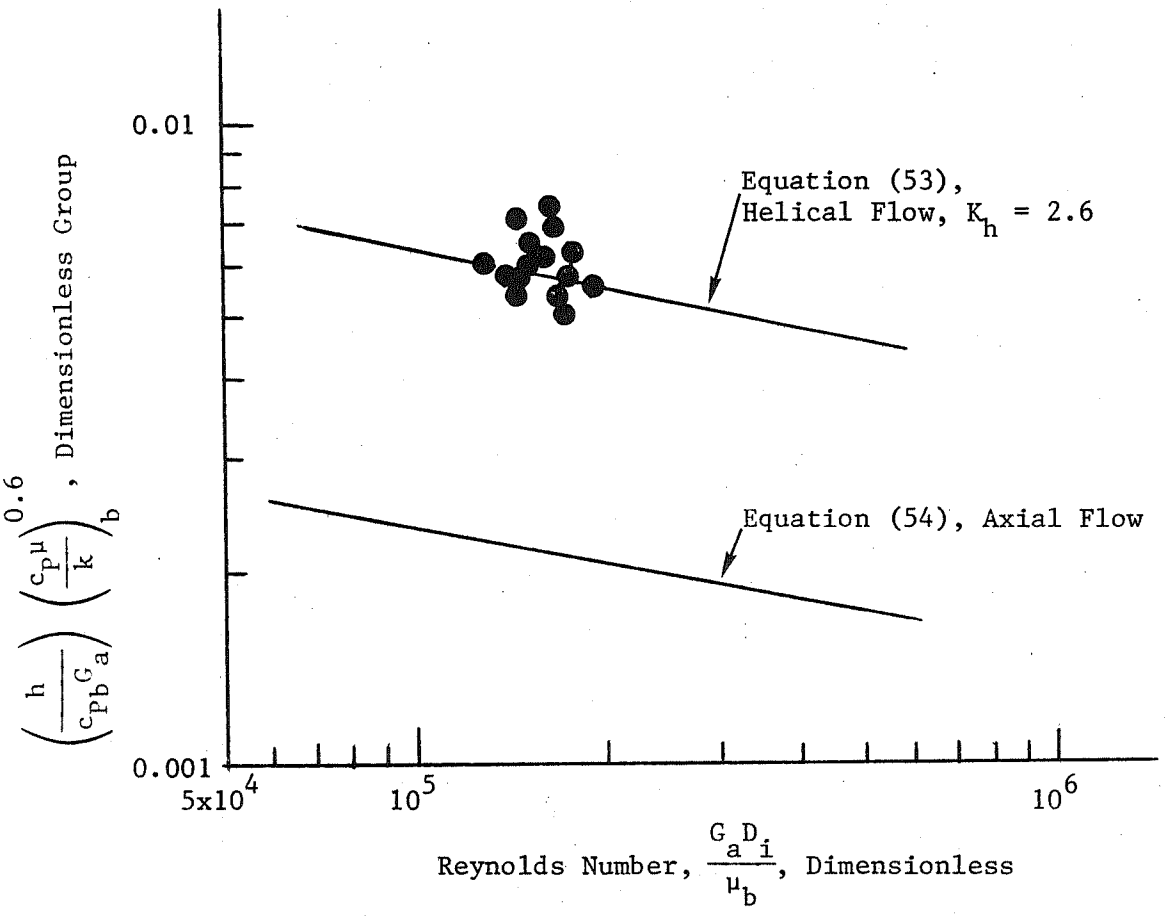

Figure 79. Superheated Mercury Vapor Heat Transfer Data in the Wire Coil Insert Region.

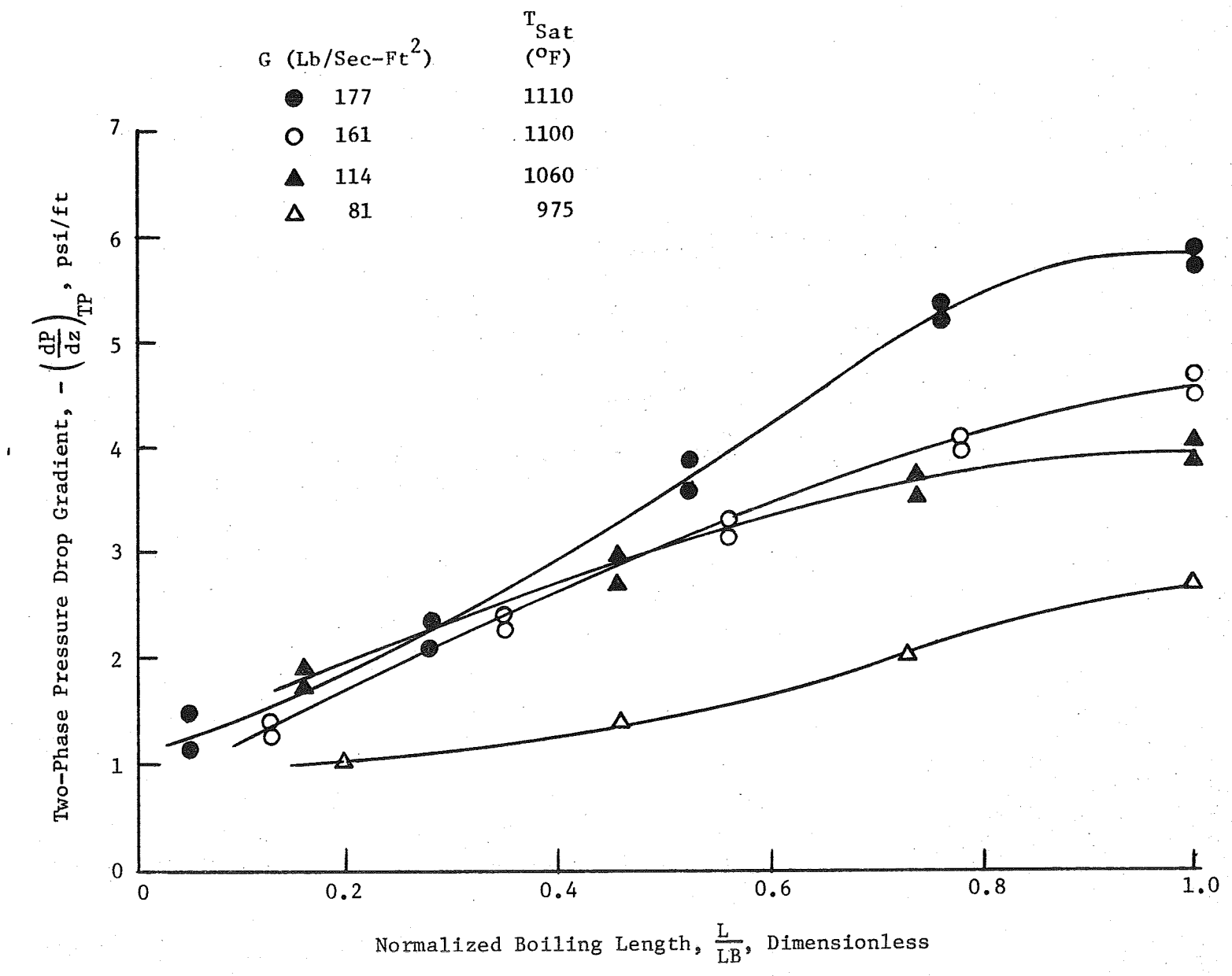

Figure 80. Local Variation of Two-Phase Pressure Gradient Along the Boiling Length.

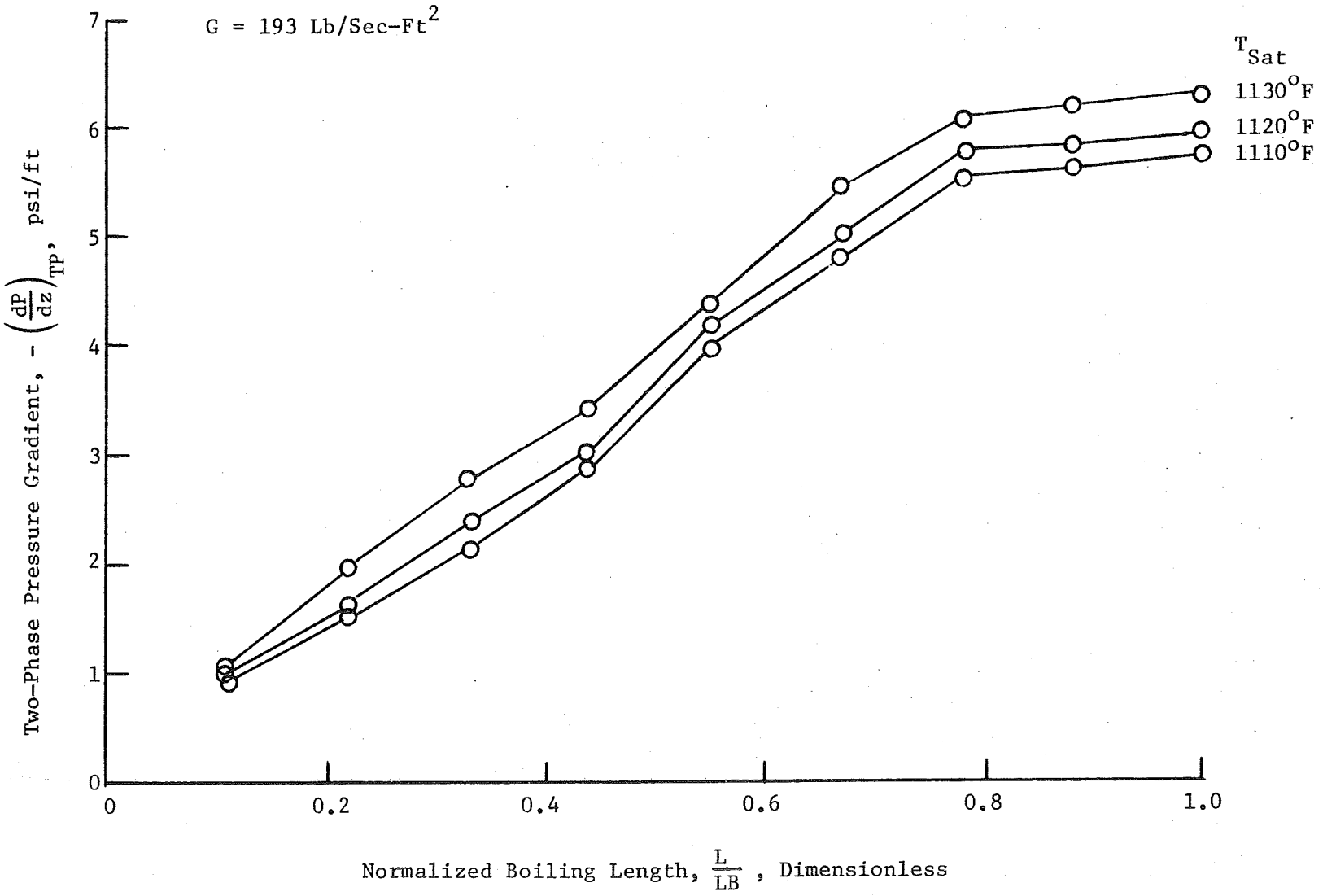

Figure 81. Local Variation of Two-Phase Pressure Gradient Along the Boiling Length as Affected by the Boiling Pressure.

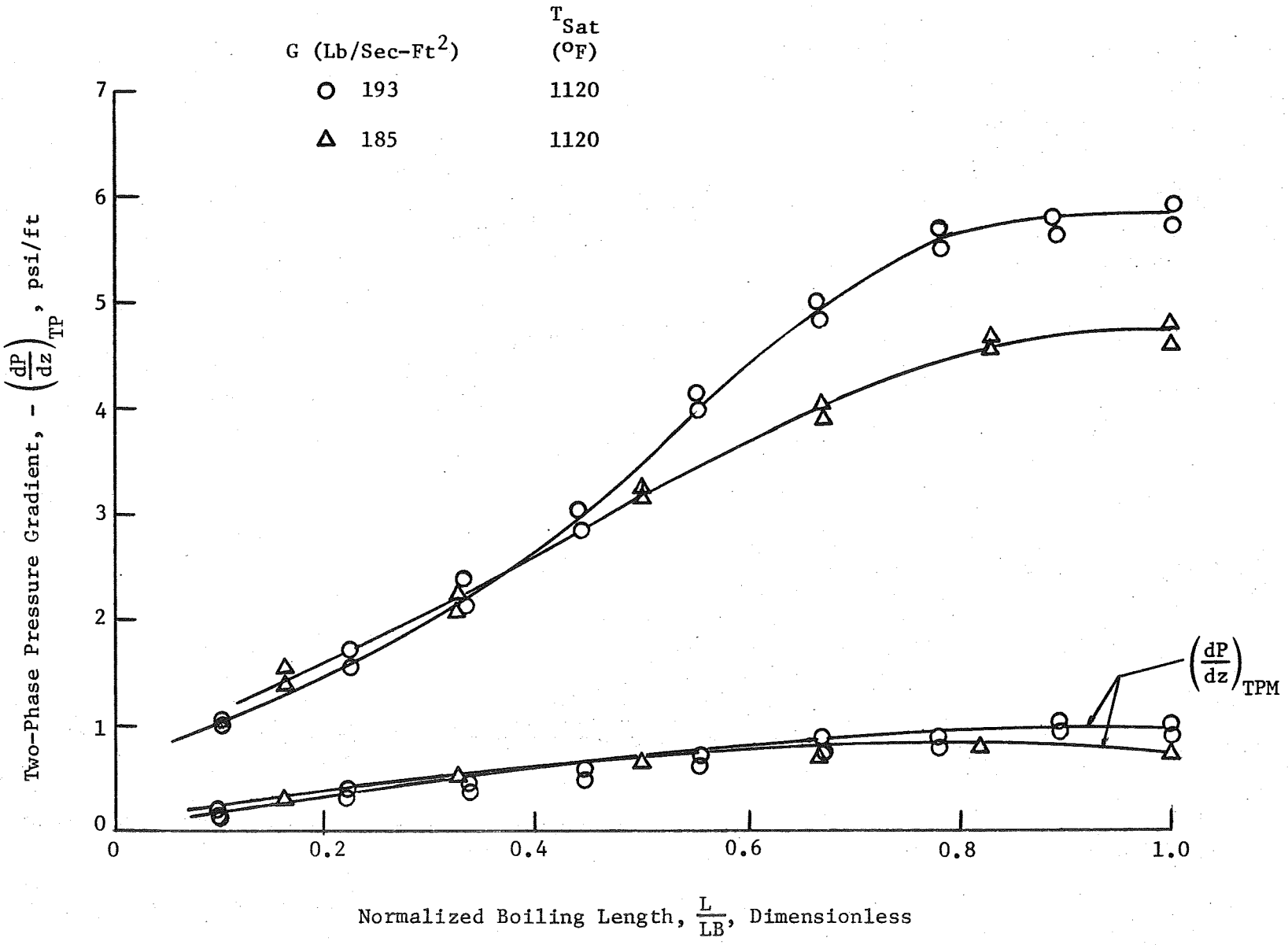

Figure 82. Local Variation of Two-Phase Pressure Gradient Along the Boiling Length as Affected by Mass Velocity.

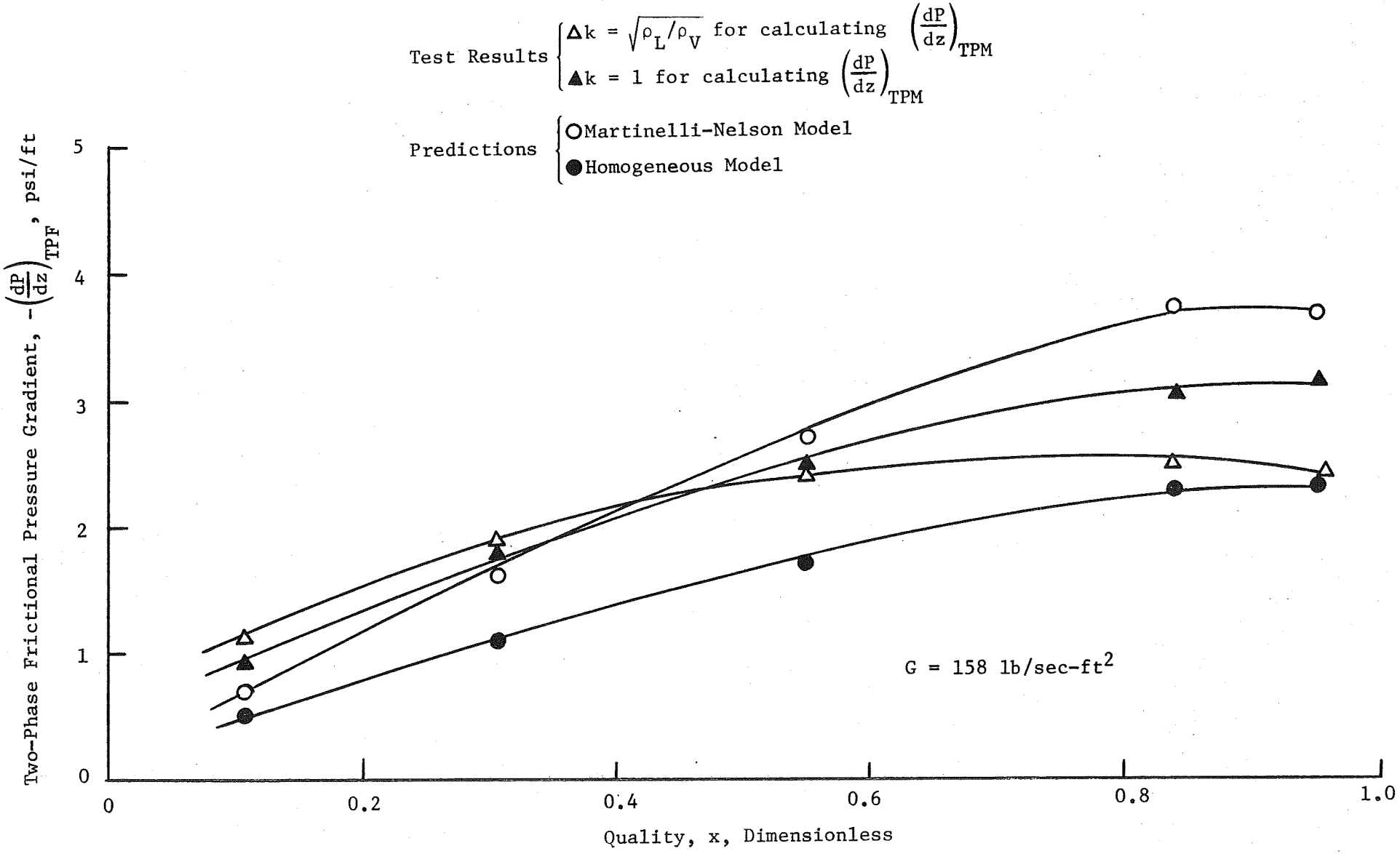

Figure 83. Local Variation of Two-Phase Frictional Pressure Gradient in the Boiling Region at T_{Sat} = 1100°F.

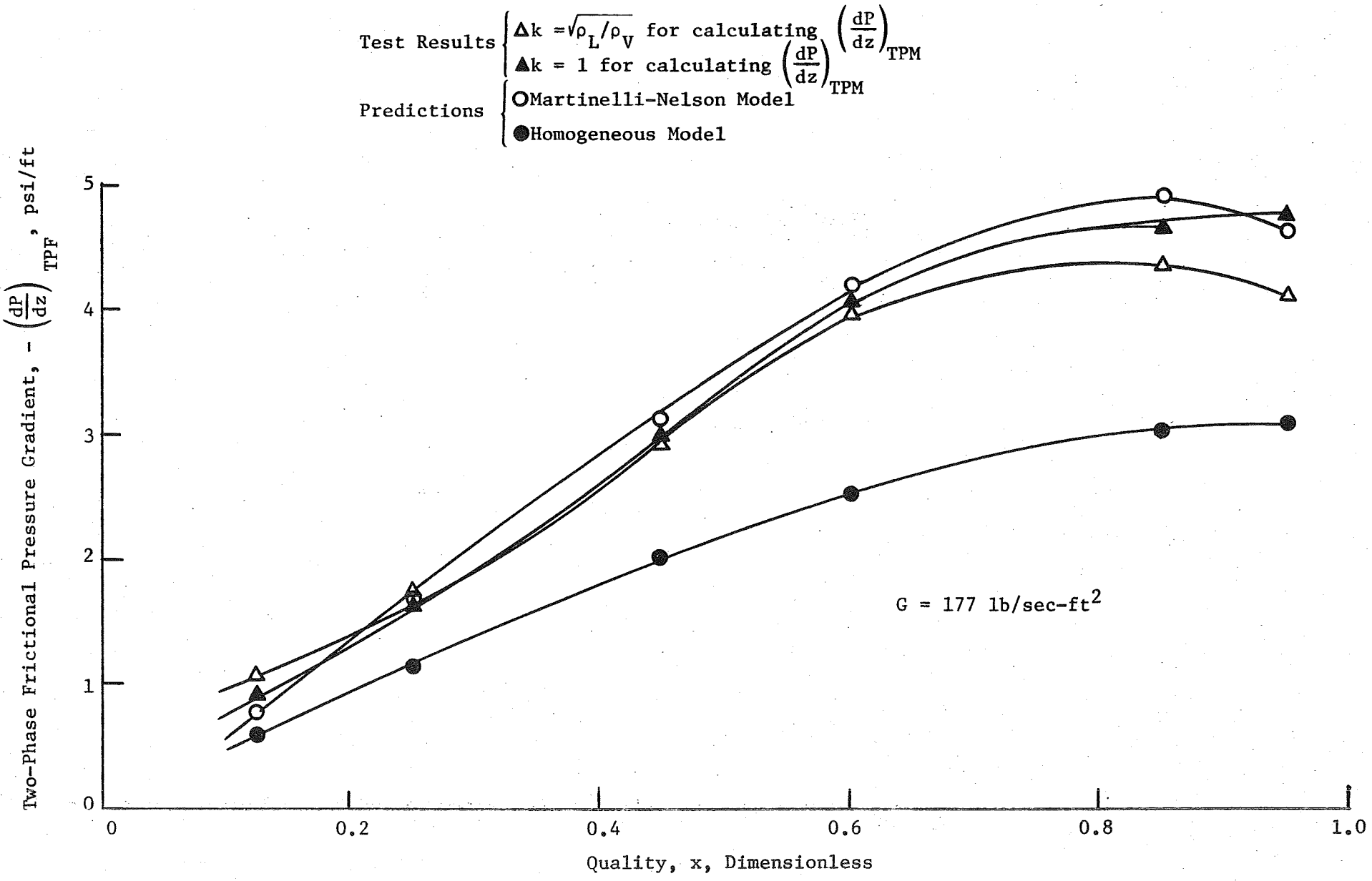

Figure 84. Local Variation of Two-Phase Frictional Pressure Gradient in the Boiling Region at T_{Sat} = 1110°F.

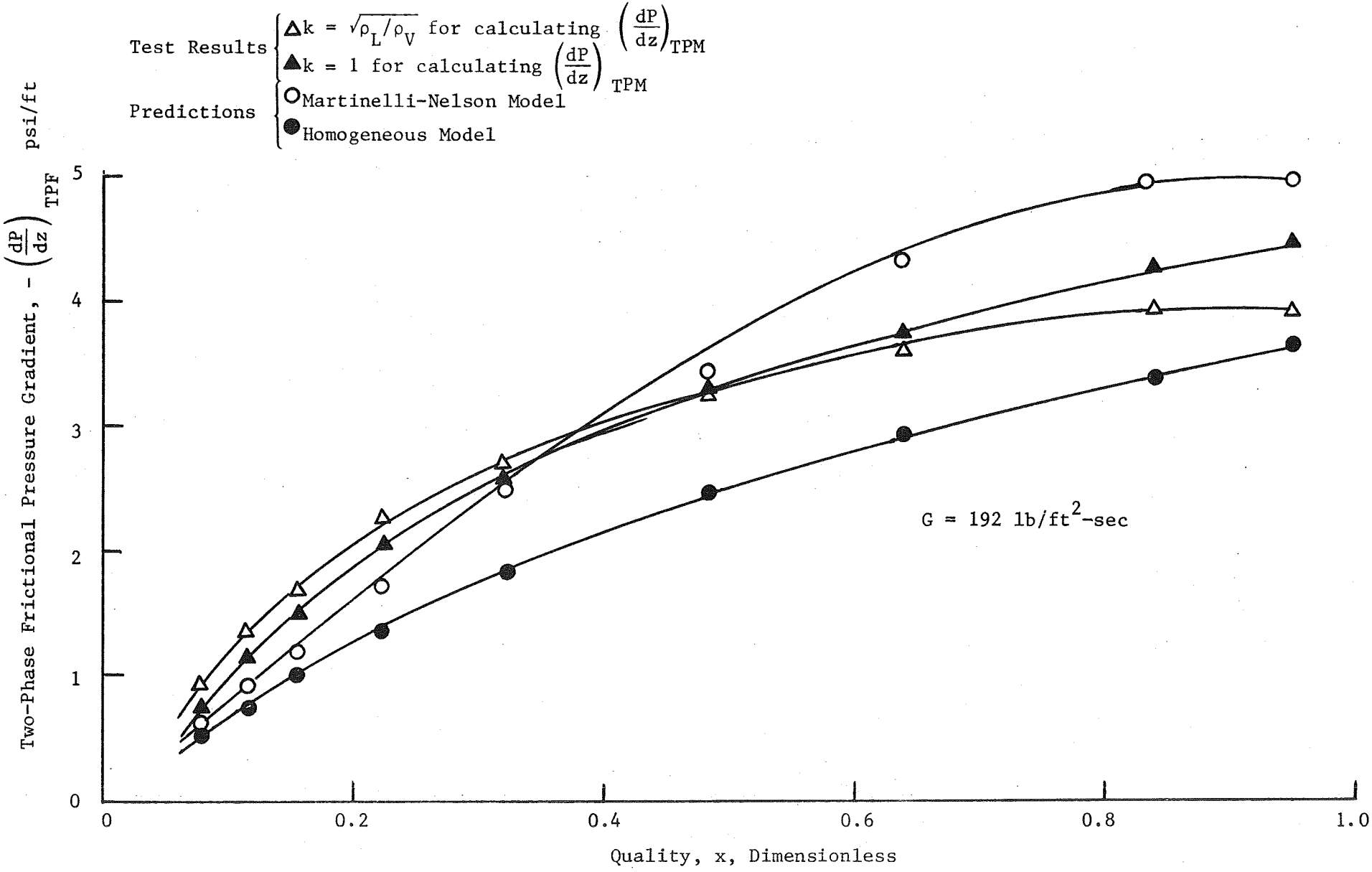

Figure 85. Local Variation of Two-Phase Frictional Pressure Gradient in the Boiling Region at T_{Sat} = 1120°F.

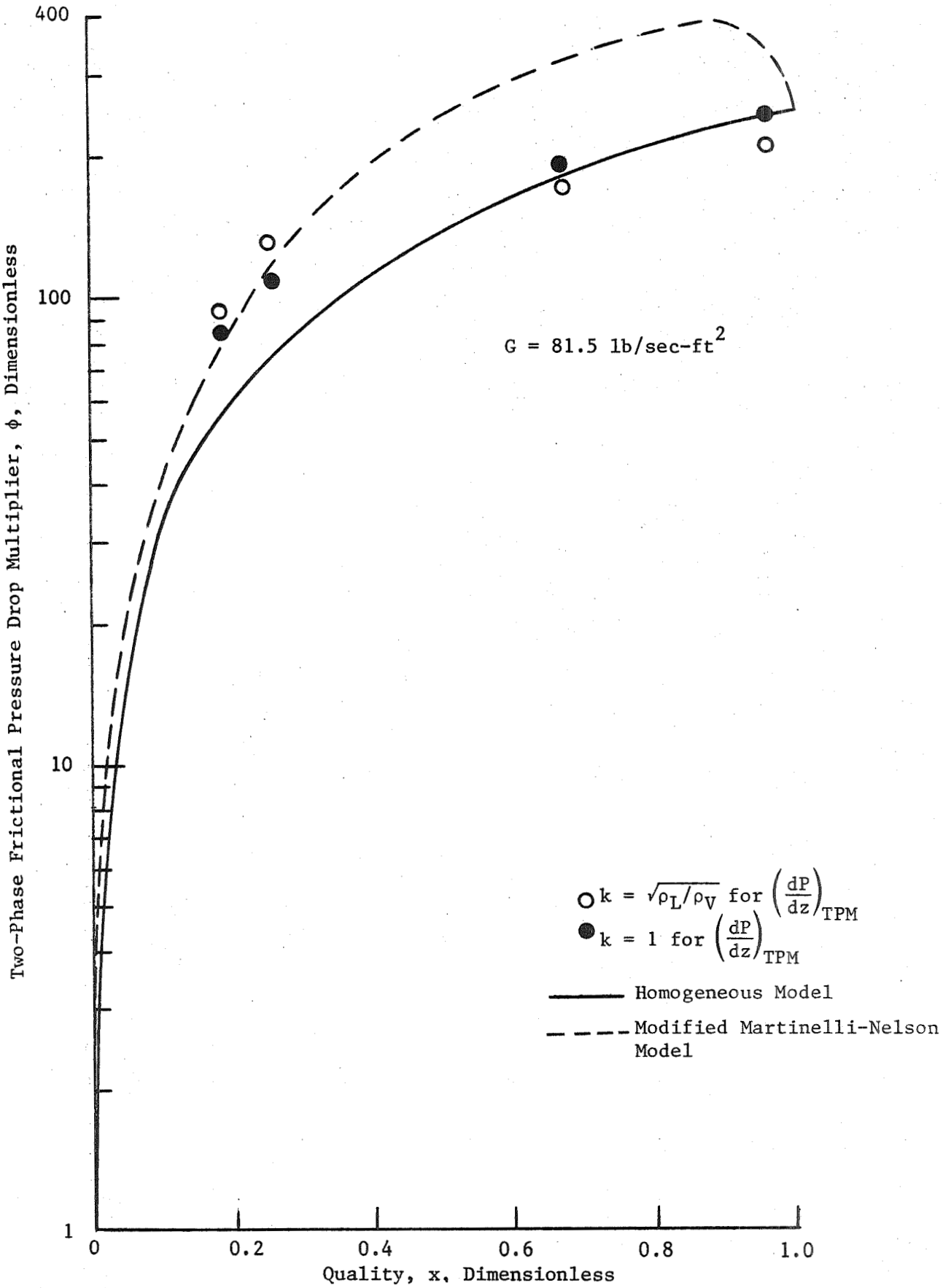

Figure 86. Comparison of Experimental and Predicted Two-Phase Friction Pressure Drop Multiplier at T_{Sat} = 975°F.

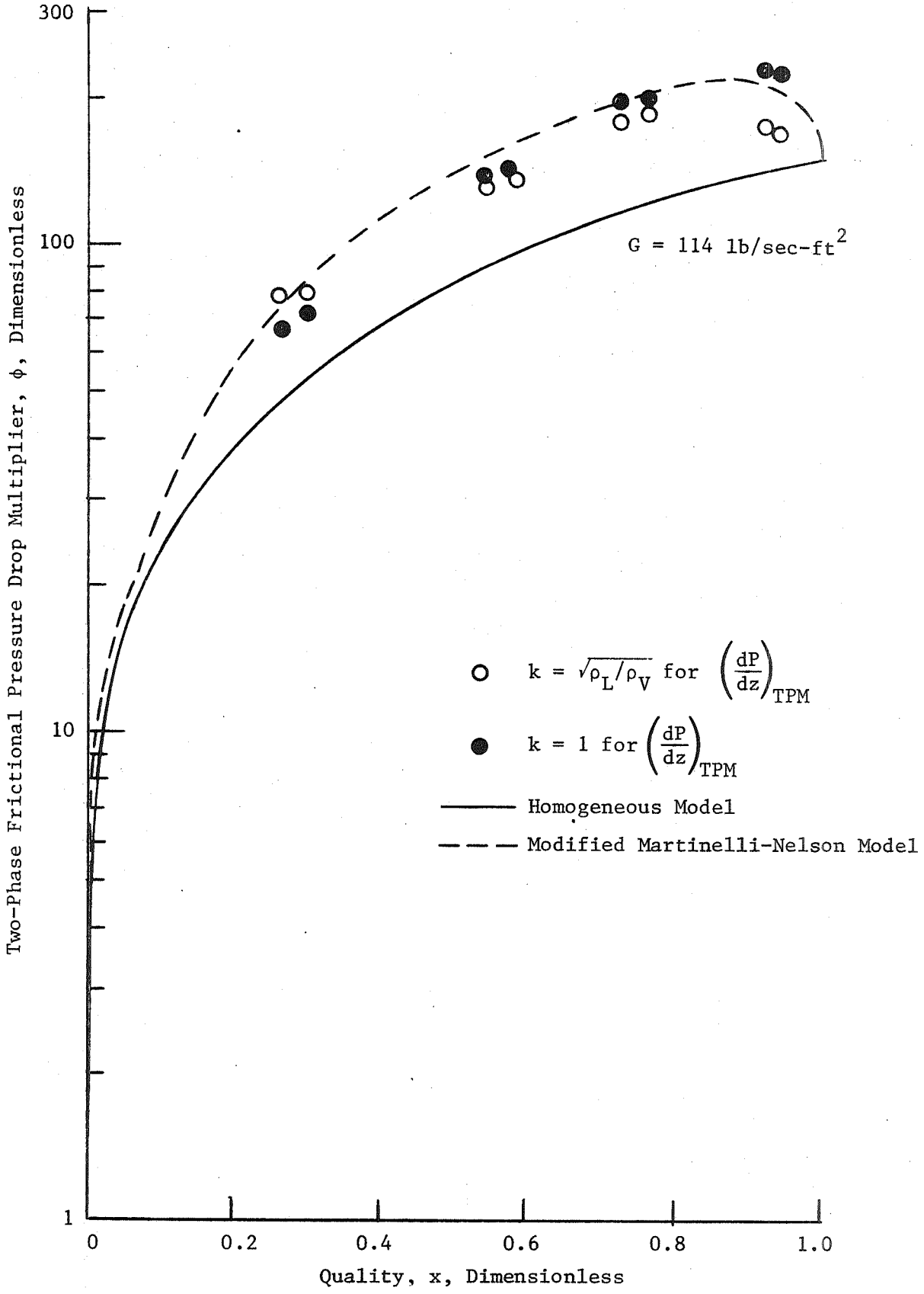

Figure 87. Comparison of Experimental and Predicted Two-Phase Friction Pressure Drop Multiplier at T_{Sat} = 1060°F.

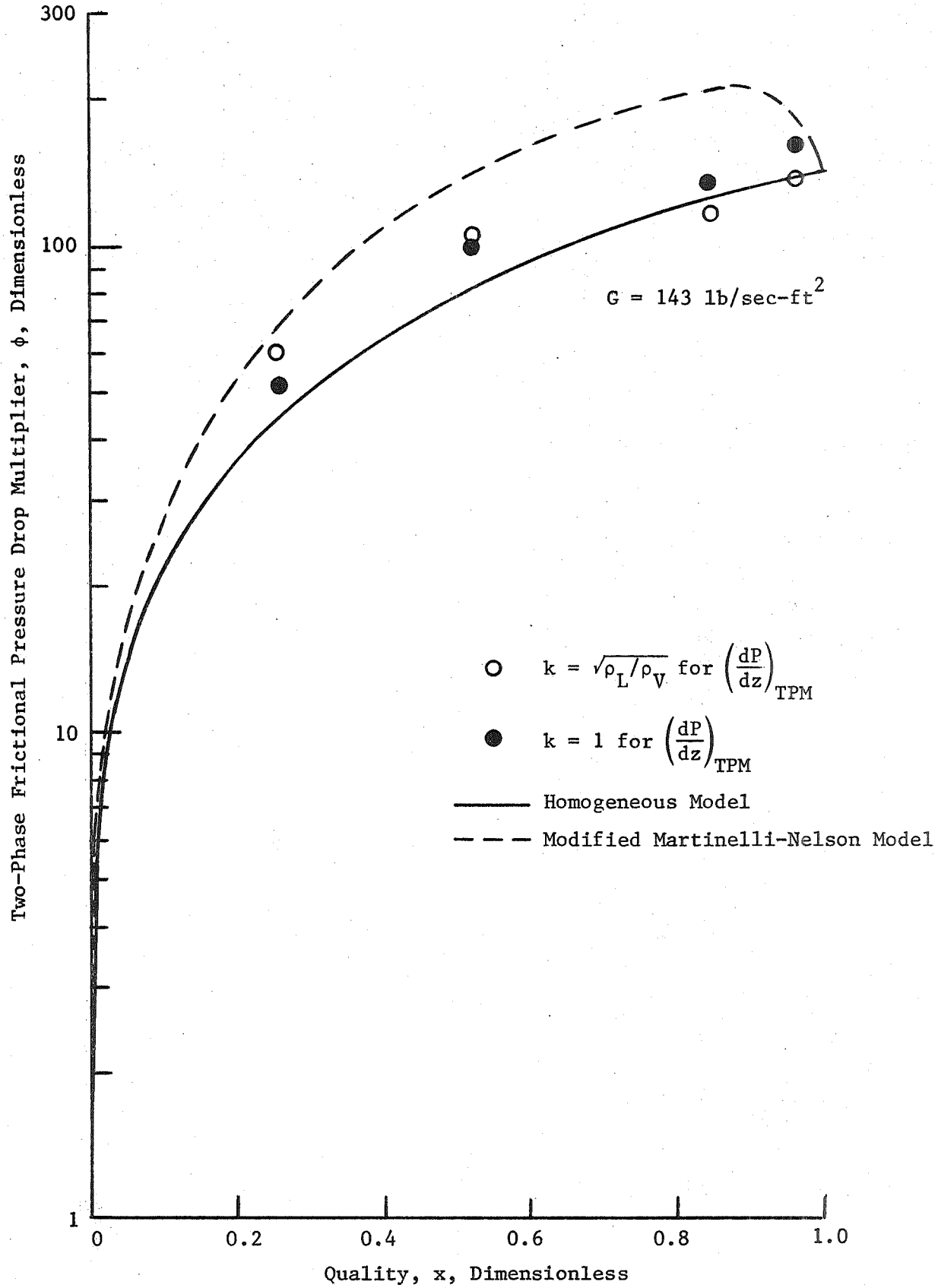

Figure 88. Comparison of Experimental and Predicted Two-Phase Friction Pressure Drop Multiplier at T_{Sat} = 1080°F.

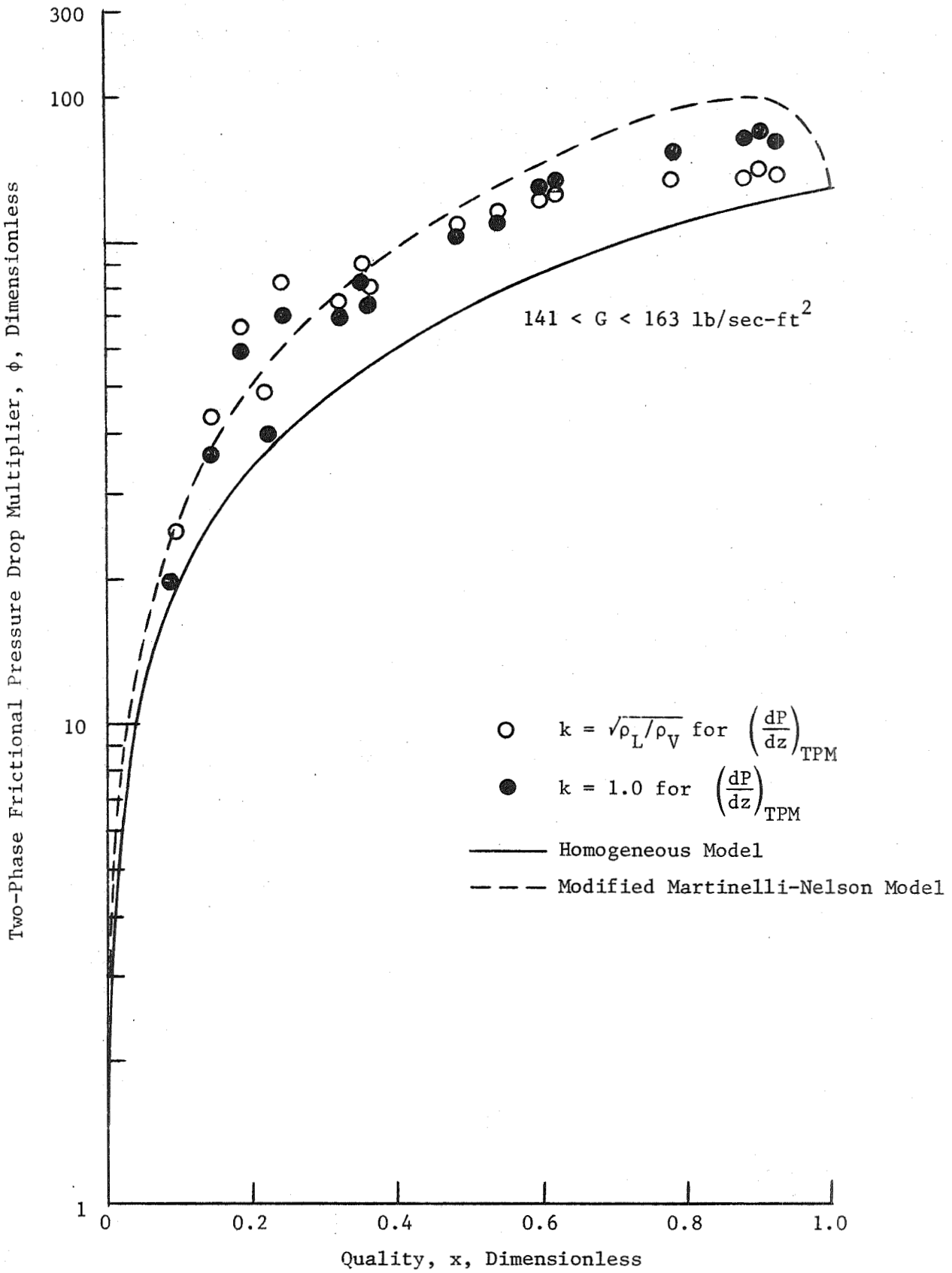

Figure 89. Comparison of Experimental and Predicted Two-Phase Friction Pressure Drop Multiplier at T_{Sat} = 1100°F.

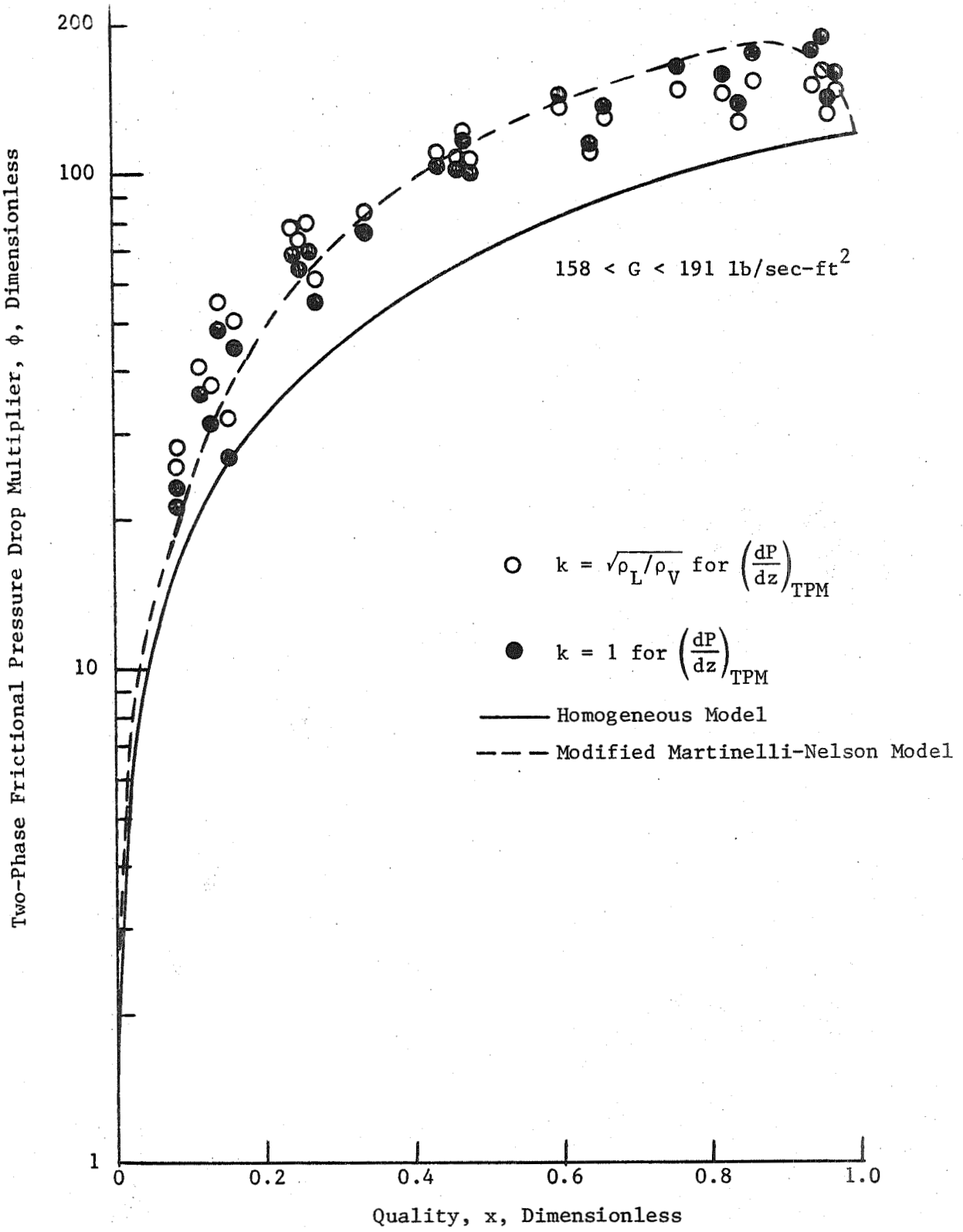

Figure 90. Comparison of Experimental and Predicted Two-Phase Friction Pressure Drop Multiplier at T_{Sat} = 1110°F.

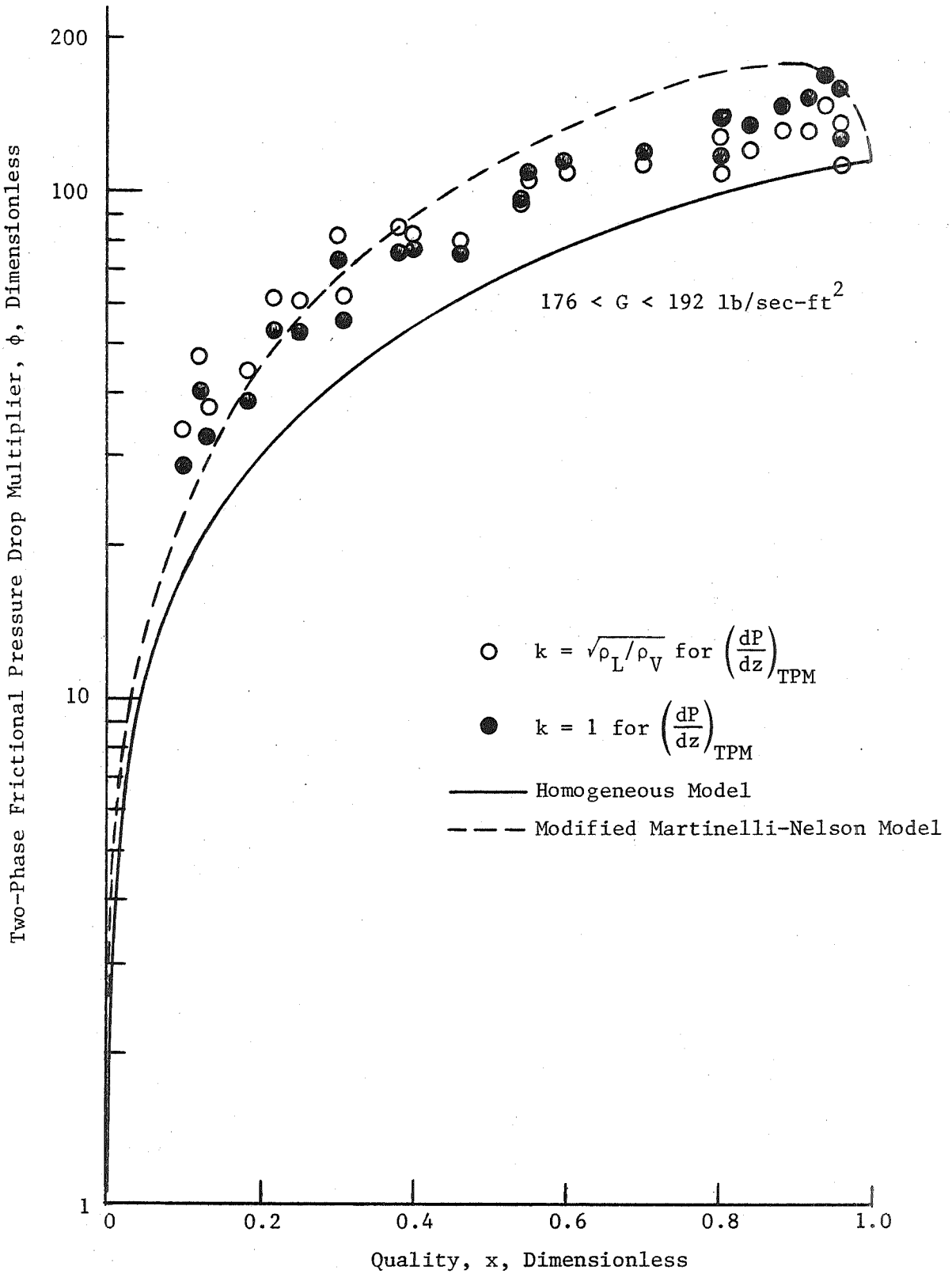

Figure 91. Comparison of Experimental and Predicted Two-Phase Friction Pressure Drop Multiplier at T_{Sat} = 1120°F.

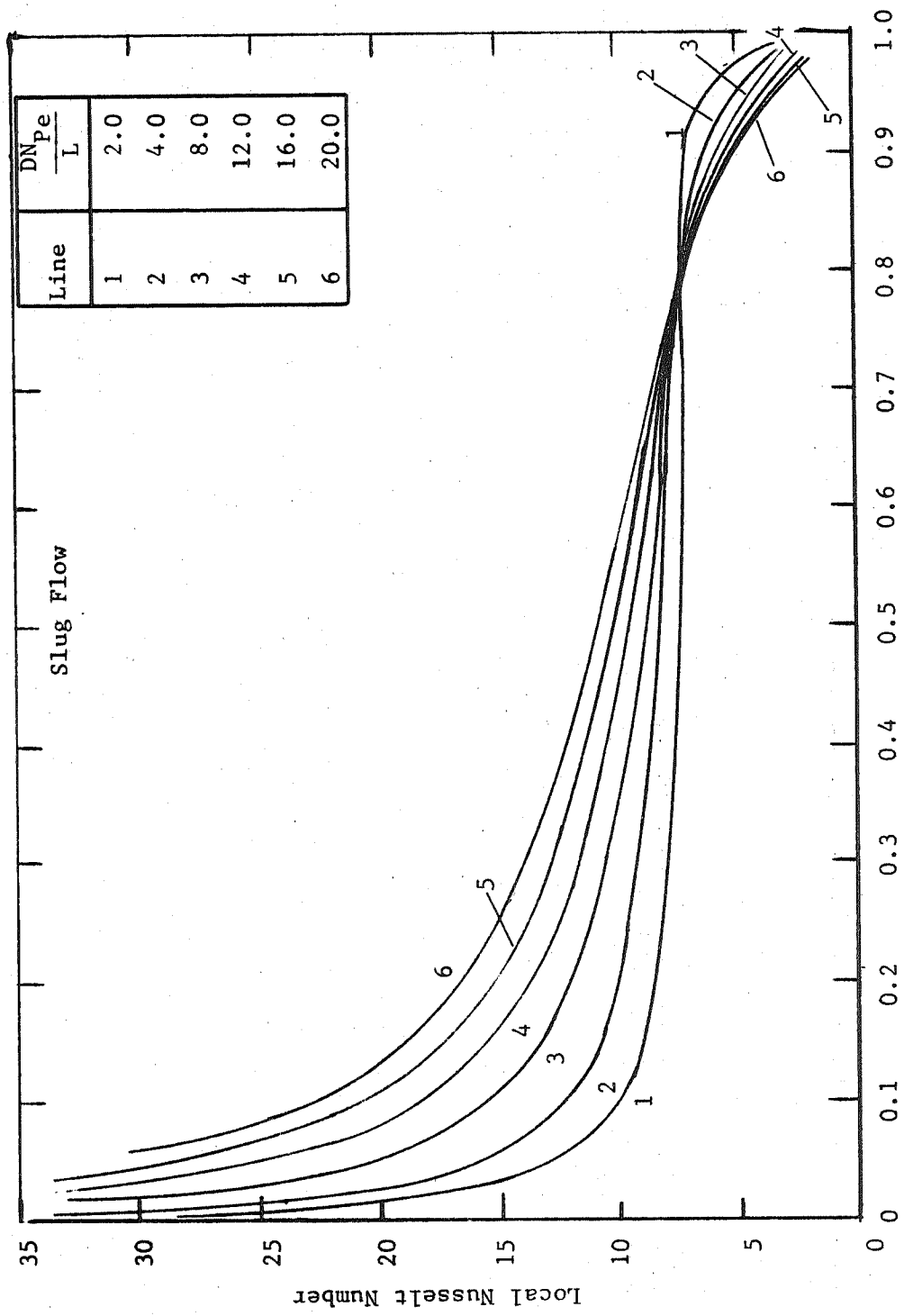

Figure 92. Local Nusselt Number vs. z/L for Slug Flow with Sinusoidal Wall Heat Flux Distribution. (Reference 30)

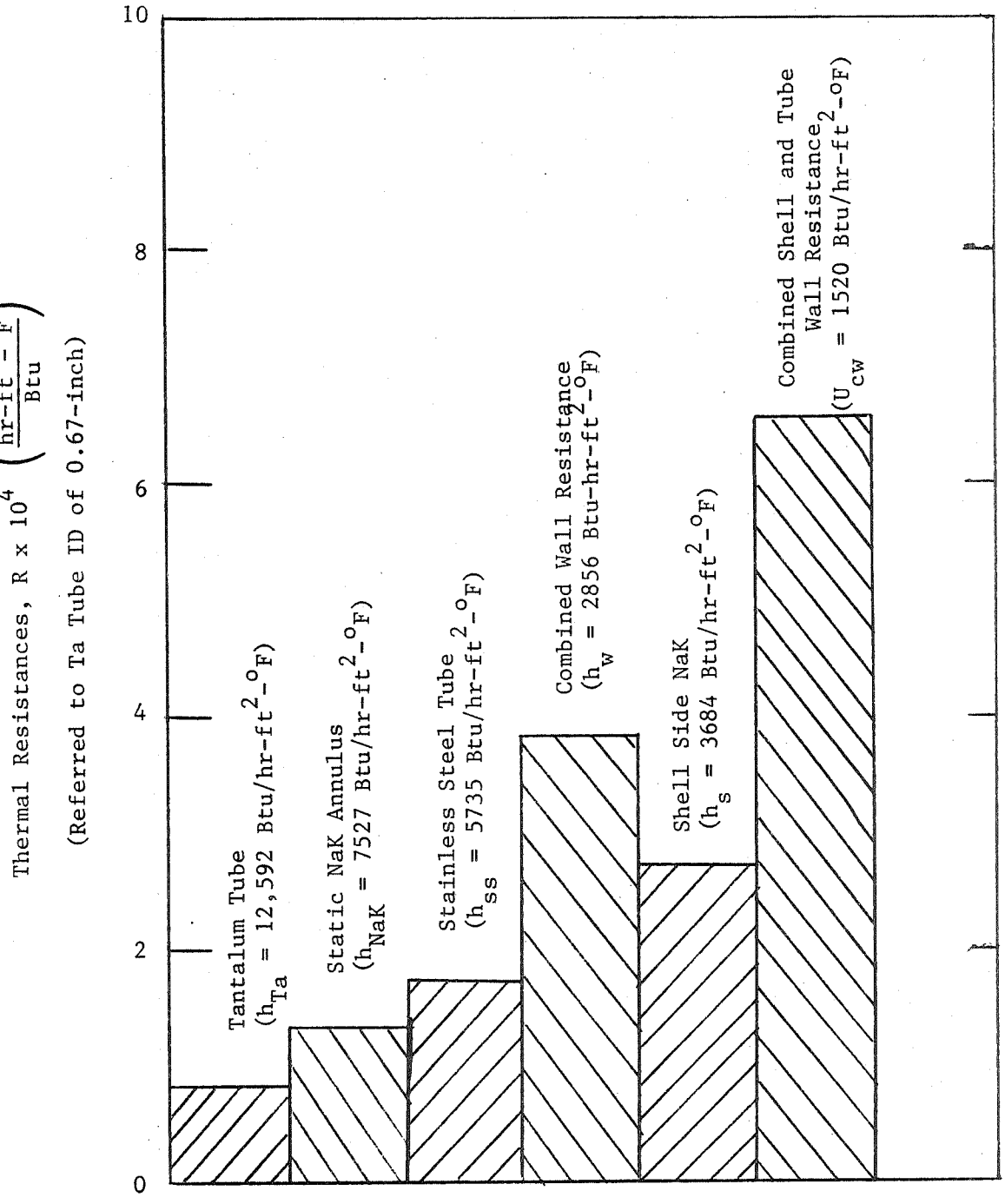

Figure 93. Shell Side and Composite Wall Thermal Resistance of the GE Single Tube Boiler.

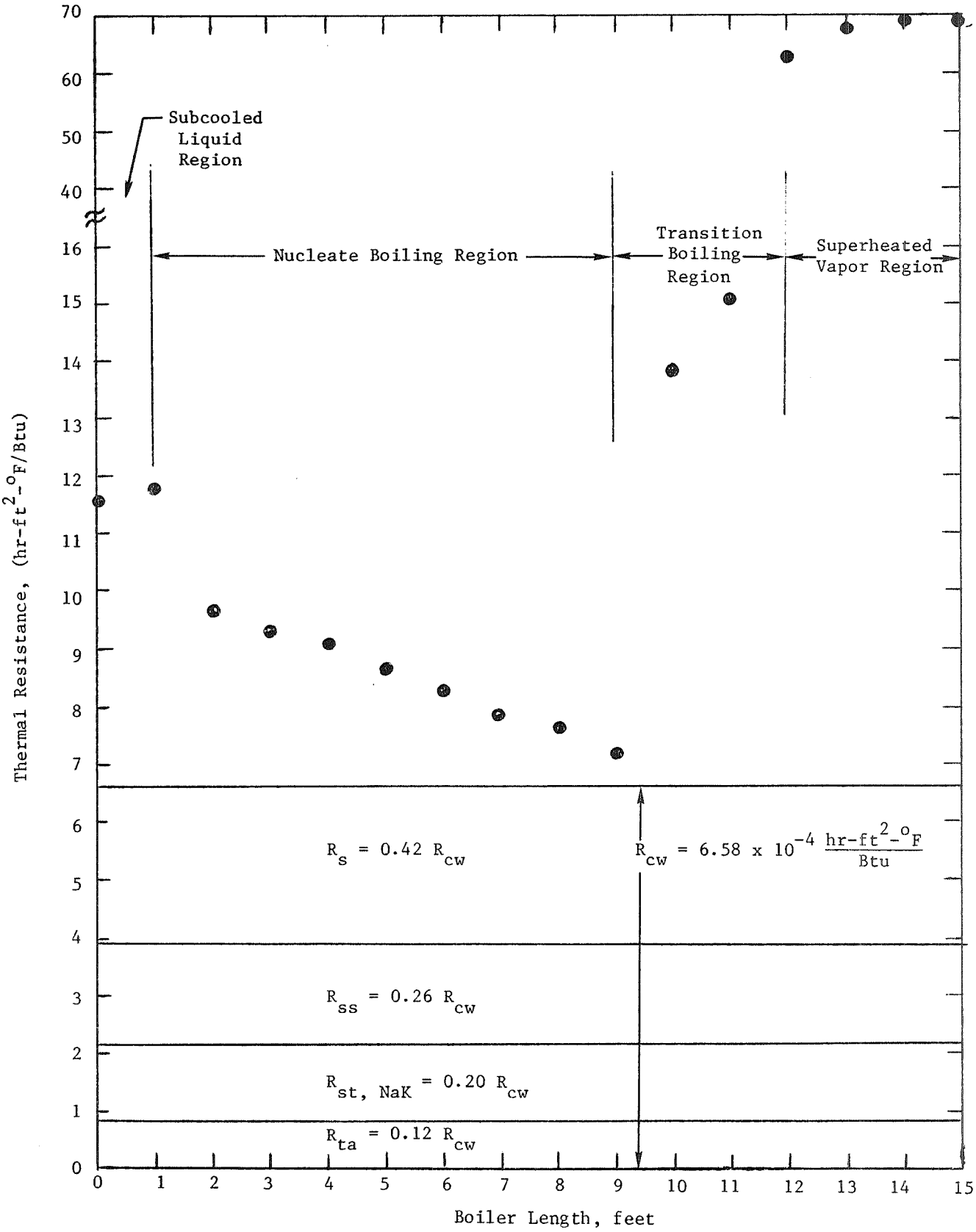

Figure 94. Typical Data for Local Heat Transfer Resistance from Test Run No. 14.

APPENDIX I

CALCULATIONAL PROCEDURES

APPENDIX I CALCULATIONAL PROCEDURES

A. Determination of Conceptual Heat Transfer Regions

As shown schematically in Figure (95), the test section temperature profiles for primary NaK flow and secondary mercury flow were recorded from the measurements of 60 shell thermocouples, 7 boiler insert thermocouples and 8 inlet and outlet well thermocouples. With the aid of these temperature profiles, the various conceptual heat transfer regions discussed in Chapter (IV) were determined as follows:

The length of the subcooled liquid heating region, L_{sc}, assumed numerically equal to the distance from the start of the heated length to the point of boiling inception, z_{IB}, was obtained directly from the calculation of z_{IB}. A single-phase heat transfer calculation gives:

$$L_{sc} = z_{IB} = \frac{W_{Hg}\, C_{Hg}\, (T_{HgIB} - T_{Hgi})}{\overline{U}_{sc}\, \Delta\overline{T}_{sc}\, (\pi D_i)} \qquad (A1)$$

The mercury temperature at the boiling inception point, T_{HgIB}, was obtained either from the insert thermocouple measurement or from the mercury saturation curve by assuming that T_{HgIB} is equal to the saturation temperature corresponding to the measured mercury inlet pressure P_{Hgi}. Thus, the liquid mercury pressure change between boiler inlet and boiling inception point was small and could be neglected.

The average overall NaK-to-mercury temperature difference in the subcooled heating region, $\overline{\Delta T}_{sc}$, was calculated as follows:

$$\overline{\Delta T}_{sc} = \frac{\left(T_{NaKo} - T_{Hgi}\right) - \left(T_{NaKIB} - T_{HgIB}\right)}{1\ n\left(\frac{T_{NaKo} - T_{Hgi}}{T_{NaKIB} - T_{HgIB}}\right)} \tag{A2}$$

with the NaK temperature at boiling inception, T_{NaKIB}, given by:

$$T_{NaKIB} = T_{NaKo} + \frac{W_{Hg} C_{pHg} \left(T_{HgIB} - T_{Hgo}\right)}{W_{NaK} C_{pNaK}} \tag{A3}$$

The overall heat transfer coefficient in the subcooled heating region, $\overline{U}_{sc}$, was calculated from the individual NaK, composite wall and liquid mercury heat transfer coefficients as follows: (see Figure 9)

$$\overline{U}_{cw} = \left\{ \frac{1}{h_s\left(\frac{D_{oa}}{D_i}\right)} + \frac{D_i 1n\left(\frac{D_{oa}}{D_{ia}}\right)}{2\ k_{ss}} + \frac{D_i 1n\left(\frac{D_{ia}}{D_o}\right)}{2k_{NaK}} + \frac{D_i 1n\left(\frac{D_o}{D_i}\right)}{2\ k_{ta}} + \frac{1}{h_{HgL}} \right\}^{-1} \tag{A4}$$

The shell-side NaK flow heat transfer coefficient, h_s, was calculated from Dwyer's equation for concentric annuli as follows:[33]

$$h_s = \frac{k_{NaK}}{D_e}\left[\alpha + \beta\ (EN_{Re}\ N_{Pr})^{\gamma}\right] \tag{A5}$$

where $\alpha = 4.82 + 0.69(Y)$

$\beta = 0.0222$

$\gamma = 0.758(Y)^{0.053}$

$Y = \frac{\text{inner radius}}{\text{outer radius}}$

and

$$E = 1 - \frac{1.82}{P_r\left[\left(\frac{\varepsilon_m}{\nu}\right)_{max}\right]^{1.4}} \tag{A6}$$

Values of $\left(\frac{\varepsilon_m}{\nu}\right)_{max}$ are provided as a function of the Reynolds number in Reference (7) for the condition of fully developed turbulent flow of liquid metal.

In the present experiment, the shell-side NaK flows were held almost constant at about 7075 lb/hr ($\pm$ 3%) and the NaK average temperatures were kept at about 1270°F ($\pm$ 3.5%). In this manner the shell-side heat transfer coefficient calculated from Equation (A5) had almost a constant value of about 2830 Btu/hr-ft^2-°F ($\pm$ 1%). In Figure (94), the shell-side and composite wall thermal resistances of the single test boiler are given. A shell flow and wall combined heat transfer coefficient, U_{cw} was then calculated to have a value of 1520 Btu/hr-ft^2-°F when referred to the tantalum boiler tube inside diameter. Lyon's equation was employed to calculate the mercury liquid heat transfer coefficient, h_{HgL}, as follows:

$$h_{HgL} = \frac{12k_{HgL}}{D_e}\left[7 + 0.025\left(\frac{G_H D_e C_p}{\mu}\right)^{0.8}\right] \tag{A7}$$

where G_H, denoted as the helical mass velocity is:

$$G_H = G_a\sqrt{1 + \left(\frac{\pi D_i}{P}\right)^2} \tag{A8}$$

and the equivalent diameter, D_e, following its usual definition, is evaluated as:

$$D_e = \frac{D_i \left[1 + \left(\frac{D_{cb}}{D_i} \right)^2 \right]}{1 + \frac{D_{cb}}{D_i} + \frac{1}{\Pi} \left(1 - \frac{D_{cb}}{D_i} \right)} \qquad \text{(A9)}$$

Equations (A1) through (A6) were then used to predict the length of the subcooled heating region, L_{sc}.

The critical heat flux point, z_c, as shown in Figure (95), was determined by assuming that the maximum heat flux occurs at this point. This was done by employing a local graphical differentiation along the smooth curve of the NaK temperature profile, since the local heat flux is proportional to the shell-side flow temperature gradient. The axial position at which vapor superheating commences, z_{IS}, is assumed to be the point at which the mercury temperature begins to rise, as shown in Figure (95).

Finally, the lengths of the various heat transfer regions of a once-through boiler are determined as follows:

Length of subcooled liquid region	$L_{sc} = z_{IB}$
Length of nucleate boiling region	$L_{NB} = z_c - z_{IB}$
Length of transition boiling region	$L_{TB} = z_{IS} - z_c$
Length of superheated vapor region	$L_{SH} = z_t - z_{IS}$

With the total boiler heated length z_t = 16 feet and predetermined values of L_{sc} and L_{SH} for each test run, the nucleate boiling and transition boiling regions were easily determined by:

$$L_{NB} = z_c - L_{sc} \quad \text{and} \quad L_{TB} = 16 - L_{sc} - L_{SH} - L_{NB} \qquad \text{(A10)}$$

B. Average and Overall Results

AVERAGE HEAT FLUX, $\bar{q}''$

The net rate of heat transfer for the mercury boiler was given by:

$$Q_{T,net} = W_{NaK} C_{NaK} \left(T_{NaKi} - T_{NaKo} \right) - Q_{Loss} \tag{A11}$$

where Q_{Loss}, the heat loss, was obtained at the average NaK temperature from the heat loss calibration runs given in Figure (19).

The heat transferred in the subcooled liquid region was given by:

$$Q_{sc} = W_{Hg} C_{Hg} \left(T_{HgIB} - T_{Hgi} \right) \tag{A12}$$

where T_{HgIB} was evaluated from the saturation curve by knowing P_{Hgi}.

The amount of the heat transferred in the superheated vapor region, Q_{SH}, was determined from the mercury temperature rise as follows:

$$Q_{SH} = W_{Hg} C_{HgV} \left(T_{Hgo} - T_{HgIS} \right) \tag{A13}$$

where T_{HgIS} was provided by the mercury temperature profile as measured by the boiler insert thermocouples.

Hence, the net heat transferred to boil the mercury was calculated by:

$$Q_B = Q_{T,net} - Q_{sc} - Q_{SH} \tag{A14}$$

With the heating lengths for the individual heat transfer regions determined, the average heat flux in each region was thus calculated by these equations:

$$\bar{q}''_{sc} = \frac{Q_{sc}}{\pi D_i L_{sc}} \tag{A15}$$

$$\bar{q}''_{B} = \frac{Q_B}{\pi D_i L_B}, \text{ with } L_B = z_t - L_{sc} - L_{SH} \tag{A16}$$

$$\bar{q}''_{SH} = \frac{Q_{SH}}{\pi D_i L_{SH}} \tag{A17}$$

Furthermore, the average heat flux in the nucleate boiling region was obtained from the NaK temperature profile provided by the boiler shell thermocouple measurements. Assuming that the temperature gradient along the shell is approximately equal to the shell-side flowing NaK temperature gradient, the following average shell temperature gradient was used to calculate the average heat flux in the nucleate boiling region:

$$\bar{q}''_{NB} = \frac{W_{NaK} C_{NaK}}{\pi D_i} \overline{\left(\frac{dT_{NaK}}{dz}\right)} - \bar{q}''_{Loss} \tag{A18}$$

where the average heat flux due to heat losses is given by:

$$\bar{q}''_{Loss} = \frac{Q_L}{\pi D_i z_t} \tag{A19}$$

Hence, with the heating length of the nucleate boiling region determined, the amount of heat transferred in the nucleate boiling region was easily calculated by:

$$Q_{NB} = \pi D_i L_{NB} \bar{q}''_{BN} \tag{A20}$$

Finally, the heat transferred in the transition boiling region was obtained from the following equation:

$$\begin{aligned} Q_{TB} &= Q_{Tnet} - Q_{sc} - Q_{SH} - Q_{NB} \\ &= Q_B - Q_{NB} \end{aligned} \tag{A21}$$

and the average heat flux in this region was obtained by:

$$\overline{q}''_{TB} = \frac{Q_{TB}}{\pi D_i L_{TB}} \tag{A22}$$

with L_{TB} calculated from Equation (A10).

AVERAGE OVERALL HEAT TRANSFER COEFFICIENTS, $\overline{U}$

With the average heat fluxes for each individual heat transfer region determined, the average overall heat transfer coefficients, $\overline{U}$, for each region were calculated by:

$$\overline{U}_{sc} = \overline{q}''_{sc} \Big/ \overline{\Delta T}_{osc} \tag{A23}$$

where $\overline{\Delta T}_{osc}$ is the average overall NaK to mercury temperature difference in the subcooled liquid region calculated by:

$$\overline{\Delta T}_{osc} = \frac{(T_{NaKo} - T_{Hgi}) - (T_{NaKIB} - T_{HgIB})}{\ln\left(\frac{T_{NaKo} - T_{Hgi}}{T_{NaKIB} - T_{HgIB}}\right)} \tag{A24}$$

The temperature notation in the above equation is illustrated in Figure (95).

Similarly, the average overall heat transfer coefficients for the nucleate boiling, transition boiling, and superheated vapor regions were calculated as follows:

$$\overline{U}_{NB} = \frac{\overline{q}''_{NB}}{\overline{\Delta T}_{oNB}} \tag{A25}$$

$$\overline{U}_{TB} = \frac{\overline{q}''_{TB}}{\overline{\Delta T}_{oTB}} \tag{A26}$$

$$\overline{U}_{SH} = \frac{\overline{q}''_{SH}}{\overline{\Delta T}_{oSH}} \tag{A27}$$

The average overall NaK to mercury temperature difference, $(\overline{\Delta T})_o$, was obtained from the following equations:

$$(\overline{\Delta T})_{oNB} = \frac{(T_{NaKc} - T_{Hgc}) - (T_{NaKIB} - T_{HgIB})}{\ln\left(\frac{T_{NaKc} - T_{Hgc}}{T_{NaKIB} - T_{HgIB}}\right)} \tag{A28}$$

$$(\overline{\Delta T})_{oTB} = \frac{(T_{NaKIS} - T_{HgIS}) - (T_{NaKc} - T_{Hgc})}{\ln\left(\frac{T_{NaKIS} - T_{HgIS}}{T_{NaKc} - T_{Hgc}}\right)} \tag{A29}$$

$$(\overline{\Delta T})_{oSH} = \frac{(T_{NaKi} - T_{Hgo}) - (T_{NaKIS} - T_{HgIS})}{\ln\left(\frac{T_{NaKi} - T_{Hgo}}{T_{NaKIS} - T_{HgIS}}\right)} \tag{A30}$$

where the NaK temperature at the point where vapor superheating starts, T_{NaKIS}, and the NaK temperature at the critical heat flux point, T_{NaKc}, are:

$$T_{NaKIS} = T_{NaKi} - \frac{Q_{SH}}{W_{NaK} C_{pNaK}} \tag{A31}$$

and

$$T_{NaKc} = T_{NaKIS} - \frac{Q_{TB}}{W_{NaK} C_{pNaK}} \tag{A32}$$

with Q_{SH} and Q_{TB} previously known from Equations (A13) and (A21), respectively.

AVERAGE MERCURY HEAT TRANSFER COEFFICIENTS, $\overline{h}$

The average mercury heat transfer coefficient for each heat transfer region was calculated from the average overall heat transfer coefficient,

$\overline{U}$, and the combined wall and shell-side heat transfer coefficient, $\overline{U}_{cw}$. For instance, in the subcooled liquid region $\overline{h}_{sc}$ was calculated by the equation:

$$\overline{h}_{sc} = \left[\frac{1}{\overline{U}_{sc}} - \frac{1}{\overline{U}_{cw}} \right]^{-1} \tag{A33}$$

where the combined wall and shell-side heat transfer coefficient, $\overline{U}_{cw}$, is given by:

$$\overline{U}_{cw} = \left[\frac{1}{h_s \left(\frac{D_{oa}}{D_i} \right)} + \frac{D_i \ln \left(\frac{D_{oa}}{D_{ia}} \right)}{2\, k_{ss}} + \frac{D_i \ln \left(\frac{D_{ia}}{D_o} \right)}{2k_{NaK}} + \frac{D_i \ln \left(\frac{D_o}{D_i} \right)}{2k_{ta}} \right]^{-1} \tag{A34}$$

Similarly, the average mercury heat transfer coefficients in regions other than the subcooled liquid region were then successfully calculated as follows:

$$\overline{h}_{NB} = \left[\frac{1}{\overline{U}_{NB}} - \frac{1}{\overline{U}_{cw}} \right]^{-1} \tag{A35}$$

$$\overline{h}_{TB} = \left[\frac{1}{\overline{U}_{TB}} - \frac{1}{\overline{U}_{cw}} \right]^{-1} \tag{A36}$$

$$\overline{h}_{SH} = \left[\frac{1}{\overline{U}_{SH}} - \frac{1}{\overline{U}_{cw}} \right]^{-1} \tag{A37}$$

with the predetermined values of $\overline{U}_{Nb}$, $\overline{U}_{TB}$, and $\overline{U}_{SH}$ given by Equations (A25), (A26), and (A27) respectively.

OVERALL PRESSURE DROP, $(\Delta P)_o$

Two Taylor slack diaphragm pressure transducers were provided for

measuring the overall pressure drop across the test section. The seven boiler insert thermocouples employed for measurement of mercury temperature in the boiling region can also be used to estimate the two-phase boiling pressure drop with the aid of the mercury saturation curve. The overall pressure drop across the test section can generally be expressed as follows:

$$(\Delta P)_o = (\Delta P)_{TP} + (\Delta P)_{SPV} + (\Delta P)_{SPL} + (\Delta P)_{elev.} + (\Delta P)_{misc.} \quad \text{(A38)}$$

where $(\Delta P)_{TP}$ = Pressure loss due to two-phase boiling.

$(\Delta P)_{SPV}$ = Pressure loss due to single-phase vapor.

$(\Delta P)_{SPL}$ = Pressure loss due to single-phase liquid.

$(\Delta P)_{elev.}$ = Elevation loss for both single-phase liquid and vapor, and two-phase fluid.

$(\Delta P)_{misc.}$ = Miscellaneous losses such as joints, contraction, expansion, etc., for both single-phase liquid and vapor.

$(\Delta P)_o$ = Overall pressure drop measured by Taylor pressure transducers.

By carefully examining the running pipe constructions and geometries between the two Taylor pressure transducers, the miscellaneous pressure drops, i.e., joints, contraction, and expansion, were estimated by the conventional pressure drop formulas and found to be in the range of 1.21 to 2.28 psi for various mercury flow rates. The test section and pipe layouts of the present experiment featured a 7 degree slope or 5/8-inch per foot elevation between the two Taylor transducers. Therefore, the elevation loss was large, especially for liquid mercury, and had to be taken into account. For various mercury flow rates, $(\Delta P)_{elev.}$ was estimated to be in the range of 7 to 8.7 psi for liquid mercury and 0.5 to 1.56 psi for mercury vapor.

In the test section, the frictional pressure and static head losses of the subcooled liquid were negligibly small due to a very short subcooled liquid region for all test runs (in the range of 0.4 to 1 foot) and a very small angle of test section orientation (7 degrees from horizontal position). On the contrary, the vapor pressure loss in the single-phase superheated vapor region constituted a large share of the total boiler pressure drop. For most test runs, the superheated vapor region covered a large portion of the test boiler, generally occupying both the helical insert region and the wire coil region. The superheated vapor pressure loss can be generally expressed by its momentum and frictional components as follows:

$$(\Delta P)_{SPV} = (\Delta P)_{SPVm} + (\Delta P)_{SPVf} \tag{A39}$$

or

$$(\Delta P)_{SPV} = (\Delta P)_{SPVm} + \left[(\Delta P)_{SPVf}\right]_{\text{helical insert region}} + \left[(\Delta P)_{SPVf}\right]_{\text{wire coil region}} \tag{A40}$$

The term $(\Delta P)_{SPVm}$, which accounts for the momentum pressure loss of mercury vapor from the superheated region to the boiler exit, was calculated by the following equation:

$$(\Delta P)_{SPVm} = \frac{G_a^2}{g_c}\left[\left(\frac{1}{\rho_V}\right)_o - \left(\frac{1}{\rho_V}\right)_{IS}\right]\overline{\left(\frac{V_H}{V_a}\right)^2} \tag{A41}$$

where G_a, defined as the axial mass velocity, is the quotient of mercury mass flow rate and the net flow area. For the boiler tube containing a

helical insert, the net flow area, A_F, is given in terms of the insert centerbody diameter, D_{cb}, and the insert tape thickness, Δt, as follows:

$$A_F = \frac{\pi \left(D_i^2 - D_{cb}^2\right)}{4 \times 144} - \frac{\left(D_i - D_{cb}\right) \Delta t}{2 \times 144} \qquad \text{(A42)}$$

The term $\overline{\left(\frac{V_H}{V_a}\right)^2}$, defined as the mean square ratio of helical velocity to axial velocity, was used in Equation (A41) as an empirical factor to account for the effect of the helical flow condition on momentum flux evaluation. For any cross section along the boiler tube, the total momentum is given by a combination of linear momentum and angular momentum. The velocity in the helical flow is considered similar to that of a solid cylindrical body rotating about its axis and translating axially in the direction of flow in such a way that the resultant velocity vector at any radius is parallel to the helical vane. Therefore, the linear momentum is independent of tube radius and helical angle, whereas the angular momentum is dependent. Thus, a mathematical expression for the total momentum flux across any cross section can be obtained by a surface integration of local momentum flux over that control surface. To avoid any mathematical difficulty in evaluating such a surface integral, an empirical factor $\overline{\left(\frac{V_H}{V_a}\right)^2}$ was thus introduced to obtain the mean total momentum flux over any cross sectional area. We define that:

$(\Delta P)_m$ = total momentum pressure loss

$$= \frac{(\rho V_a)^2}{g_c} \overline{\left(\frac{V_H}{V_a}\right)^2} \Delta \left(\frac{1}{\rho}\right) \qquad \text{(A43)}$$

with $\overline{\left(\frac{V_H}{V_a}\right)^2}$ given by the following relation:

$$\overline{\left(\frac{V_H}{V_a}\right)^2} = \iint \left(\frac{V_H}{V_a}\right)^2 dA_H \Big/ \iint dA_H \qquad \text{(A44)}$$

For a solid body rotation, the helical velocity, V_H, can be written as:

$$V_H = V_a \sqrt{1 + \left(\frac{2\pi r}{P}\right)^2}$$

and the helical cross sectional area, dA_H, can be obtained from the mass flow continuation as $dA_H = \frac{V_a}{V_H}(2\pi r)dr$. Substituting V_H and dA_H into equation (A44) and integrating, gives:

$$\overline{\left(\frac{V_H}{V_a}\right)^2} = \overline{\left(\frac{L_H}{L}\right)^2} = \frac{1}{3}\left[1 + \left(\frac{\pi D_i}{P}\right)^2 + \sqrt{1 + \left(\frac{\pi D_i}{P}\right)^2}\sqrt{1 + \left(\frac{\pi D_{cb}}{P}\right)^2} + 1 + \left(\frac{\pi D_{cb}}{P}\right)^2\right] \qquad \text{(A45)}$$

where D_{cb} is the diameter of the centerbody of the boiler insert.

The frictional pressure loss for mercury vapor in the helical vane insert region can be estimated by using the conventional pressure drop correlation for tube and multiplying by a coefficient to account for the helical insert effect. This approach was successfully used to correlate the pressure drop data for water[29] and air[27] flows. The conventional Fanning type pressure correlation gives:

$$(\Delta P)_{SPVf} = f_e \left(\frac{L_H}{D_e}\right)\frac{G_H^2}{2g_c\overline{\rho}_V} \qquad \text{(A46)}$$

$$\text{with } f_e = \frac{0.316}{\left(\frac{D_e G_H}{\mu_V}\right)^{1/4}} \qquad \text{(equivalent friction factor)} \qquad \text{(A47)}$$

$$G_H = G_a \sqrt{1 + \left(\frac{\pi D_i}{P}\right)^2} \qquad \text{(helical mass velocity)} \qquad \text{(A48)}$$

$$L_H = L \sqrt{1 + \left(\frac{\pi D_i}{P}\right)^2} \qquad \text{(helical path length)} \qquad \text{(A49)}$$

Alternatively, Equation (A46) can be rewritten as:

$$(\Delta P)_{SPVf} = (\Delta P)_a \, K_p \qquad \text{(A50)}$$

$$\text{with } (\Delta P)_a = \frac{0.316}{\left(\frac{D_i G_a}{\mu_V}\right)^{1/4}} \left(\frac{L}{D_i}\right) \frac{G_a}{2g_c \, \bar{\rho}_V} \qquad \text{(plain tube)} \qquad \text{(A51)}$$

$$\text{and } K_p = \left(\frac{L_H}{L}\right)^{2.75} \left(\frac{D_i}{D_e}\right)^{1.25} \qquad \text{(A52)}$$

K_p is then defined as a pressure loss multiplier to account for the increase in pressure loss due to helical flow conditions.

The frictional pressure loss for mercury vapor in the wire coil insert region is complicated, and as yet no analytical prediction or correlation is available. Furthermore, it was found in Reference (27) that the use of a helical flow pressure multiplier to correlate the pressure drop for air flow with wire coil inserts resulted in an underestimation of the test data. The only way to predict the frictional loss for wire coil insert is to run an experiment (such as with heated air) to obtain the actual value of the multiplier. A series of hydraulic tests using water and heated air with various geometries of wire coil inserts was completed recently,[27],[29] and some of the test results

are shown in Figure (96). As shown in Figure (97), the experimentally determined pressure loss multiplier, K_p, was found to be approximately 22 for the present wire coil geometry, and was found not to be a strong function of the Reynolds number. Thus, the mercury vapor pressure loss due to friction in the wire coil region was calculated by the following empirical equation:

$$(\Delta P)_{SPVf} = 22\ (\Delta P)_a \qquad \text{(A53)}$$

(for P/D = 0.97 and $\frac{d_w}{D_i}$ = 0.1428 wire coil insert)

With the various pressure losses, $(\Delta P)_{SPV}$, $(\Delta P)_{SPL}$, $(\Delta P)_{elev.}$, and $(\Delta P)_{misc.}$, determined by the above equations, the pressure loss in the two-phase boiling region was estimated by subtracting these known pressure losses from the total measured pressure loss which was recorded by two Taylor transducers. For comparison, the two-phase pressure loss was also obtained from the mercury saturation curve by using the insert thermocouple temperature readings in the boiling region.

The mercury single phase vapor pressure loss due to friction, $(\Delta P)_{SPVf}$, was estimated from Equation (A38) with the assumptions (1) that the two-phase pressure loss values obtained from insert thermocouples were correct, and (2) that the other pressure losses involved were evaluated with reliable equations. Since the pressure loss multiplier, K_p, was assumed to account for pressure loss in the helical vane insert region, the frictional pressure drop of mercury vapor in the wire coil region was predicted from Equation (A40). With this predicted value, the pressure loss multiplier (defined as $K_p = (\Delta P)_{wc}/(\Delta P)_a$) was then calculated and

compared with early air heating test data for the same wire coil insert.

The two-phase boiling pressure drop, $(\Delta P)_{TP}$, consists of two components, i.e., frictional and momentum, and is represented by:

$$(\Delta P)_{TP} = (\Delta P)_{TPf} + (\Delta P)_{TPm} \tag{A54}$$

The momentum term, $(\Delta P)_{TPm}$, was calculated by integrating the differential form of momentum pressure drop between the quality $x = 0$ and $x = x_e$ to yield:

$$(\Delta P)_{TPm} = \frac{G_a^2}{g_c} \overline{\left(\frac{V_H}{V_a}\right)^2} \left[\frac{1}{\rho_e} - \frac{1}{\rho_{LIB}}\right] \tag{A55}$$

where $$\frac{1}{\rho_e} = \frac{1}{\rho_V}\left[(1 - x_e)\ \frac{\rho_V}{\rho_L} + \frac{x}{K}\right]\left[1 + x_e\ (K-1)\right] \tag{A56}$$

with K defined as the slip ratio, i.e., the average velocity ratio of vapor to liquid.

For all the test runs, the mercury was always superheated 200°F to 400°F at the boiler exit. Therefore x_e was always equal to one and Equation (A56) reduced to simply $\frac{1}{\rho_e} = \frac{1}{\rho_{VIS}}$. Equation (A55) was then rewritten as:

$$(\Delta P)_{TPm} = \frac{G_a^2}{g_c} \overline{\left(\frac{V_H}{V_a}\right)^2} \left[\frac{1}{\rho_{VIS}} - \frac{1}{\rho_{LIB}}\right] \tag{A57}$$

Subsequently, the frictional two-phase pressure drop, $(\Delta P)_{TPf}$, was calculated from Equation (A54), and an integrated two-phase friction pressure drop multiplier, $\overline{\Phi}_{exp}$, was evaluated by the following equation:

$$\overline{\Phi}_{exp} = \frac{(\Delta P)_{TPf}}{(\Delta P)_L} , \tag{A58}$$

where $(\Delta P)_L$ denotes the single-phase liquid pressure drop which would result if the flow rate of the liquid in the tube were equal to the actual two-phase mixture flow rate, and is expressed by:

$$(\Delta P)_L = f_L \left(\frac{L_B}{D_e}\right) \frac{G_H^2}{2g_c \rho_L} \tag{A59}$$

$$\text{with } f_L = 0.316 \left(\frac{G_H D_e}{\mu_L}\right)^{-1/4} \tag{A60}$$

$$\text{and } L_B = L_{NB} + L_{TB} = z_{IS} - z_{IB}$$

The experimentally obtained two-phase friction pressure drop multipliers were then compared with the values from the Martinelli model[34] modified for mercury, $\overline{\Phi}_M$, and the values from a homogeneous flow model, $\overline{\Phi}_H$. Mathematically $\overline{\Phi}_M$ and $\overline{\Phi}_H$ were obtained by a numerical integration from their local values, Φ_M and Φ_H, at selected temperatures on the Φ versus x plots which are given in Figures (102) and (104). The detailed discussion about these local functions Φ_M (T,x) and Φ_H (T,x) is given in Section (D).

For the present one hundred percent boiling runs, $\overline{\Phi}_M$ and $\overline{\Phi}_H$ were calculated by the following equations:

$$\overline{\Phi}_M = \int_o^{x=1} \Phi_M \, dx \tag{A62}$$

and

$$\overline{\Phi}_H = \int_0^{x=1} \Phi_H \, dx = \int_0^{x=1} \frac{1+x\left(\frac{\rho_L}{\rho_V} - 1\right)}{\left[1+x\left(\frac{\mu_L}{\mu_V} - 1\right)\right]^n} \, dx \qquad \text{(A63)}$$

and the results are plotted in Figures (98 and (99).

C. Local Heat Transfer Results

By using the shell temperature profiles and assuming that the axial bulk NaK temperature gradient, $\frac{dT_{NaK}}{dz}$, is equal to the axial shell temperature gradient, $\frac{dT_s}{dz}$, the local heat flux q" was calculated by the following equation:

$$q'' = \frac{W_{NaK} C_{NaK}}{\pi D_i} \frac{dT_s}{dz} - q''_{Loss} \qquad \text{(A64)}$$

where q''_{Loss} is the heat flux obtained by dividing the total heat losses of the test section by the active heat transfer area. The values of $\frac{dT_s}{dz}$ needed for computation of q" in Equation (A64) were obtained by graphical differentiation of a smooth curve drawn through the shell temperature points.

The local variation of heat flux in the subcooled heating region could not be obtained directly since the length of this region was too short to permit accurate measurements. However, the heat flux at the mercury inlet was estimated by the following equation:

$$q''_{Hgi} = \overline{U}_{sc} \, (T_{NaKi} - T_{Hgi}) \qquad \text{(A65)}$$

where $\overline{U}_{sc}$, the average overall heat transfer coefficient, was given by

Equation (A23), and T_{NaK} and T_{Hgi} were provided by well thermocouple readings.

The remainder of the local heat flux profile in the subcooled heating region was estimated through the use of average heat flux, $\overline{q}''_{sc}$, in the region given by Equation (A15). The axial position at which the critical heat flux condition occurred and transition boiling commenced, z_c, was determined from the shell temperature profile as that point at which a marked change occurred in the local shell temperature gradient. From the many shell thermocouple readings along the test section it was observed that the local values of $\frac{dT_s}{dz}$ increased continuously from the boiling inception point, z_{IB}, up to its maximum value and then abruptly decreased. The point at which $\frac{dT_s}{dz}$ reached its maximum value marked the critical heat flux condition, and the critical heat flux was then determined by Equation (A64).

Equation (A64) is useful only up through the transition region because in the superheated region the shell temperature profile becomes increasingly flat, and the local differentiation of $\frac{dT_s}{dz}$ becomes very difficult and inaccurate. Therefore, in the superheated region the local heat flux was determined by the following equation with the help of the mercury temperature profiles:

$$q'' = \frac{W_{Hg} C_{Hg}}{\pi D_i} \left(\frac{dT_{Hg}}{dz} \right) \tag{A66}$$

The local bulk NaK temperature was obtained from the known bulk inlet temperature, T_{NaKi} (measured by well thermocouple), and the integration of the local heat flux with respect to z, as follows:

$$T_{NaK} = T_{NaKi} - \left(\frac{\pi D_i}{W_{NaK} C_{pNaK}}\right) \int_{z_o}^{z} q'' \, dz \qquad (A67)$$

As soon as the axial distribution of q" was obtained as described above, the integration expressed in Equation (A67) was calculated numerically as follows:

$$\int_{z_o}^{z} q'' \, dz = \sum_{i=1}^{n} q''_i \, (\Delta z)_i \qquad (A68)$$

The local quality, x, was calculated by a consideration of energy balance as follows:

$$W_{Hg}\left[x\, h_V + (1 - x)\, h_L - x_o h_{Vo} - (1-x_o)\, h_{Lo} + \frac{V_H^2 - V_{Ho}^2}{2Jg_c}\right]$$

$$= \pi D_i \int_{z_o}^{z} q'' \, dz \qquad (A69)$$

For all superheated vapor exit conditions in the present experiments, x_o was taken as the quality at the beginning of fluid bulk superheating (z_{IS}) where x_o was assumed to be 100. Hence, Equation (A69) reduced to:

$$x = \frac{\pi D_i}{W_{Hg} h_{LV}} \int_{z_{IS}}^{z} q'' \, dz + \frac{(h_{LV})_{IS}}{h_{LV}} - \frac{C_{pHgL}}{h_{LV}} \left(T_{Hg} - T_{HgIS}\right) + \frac{V_{HIS}^2 - V_H^2}{2Jg_c \, h_{LV}} \qquad (A70)$$

where h_{LV} denotes the latest heat of vaporization of mercury at local

saturation temperatures, and the helical velocities, V_H and V_{HIS}, are evaluated by the following equations:

$$V_H = \frac{xG_a}{\rho_V}\sqrt{1+\left(\frac{\pi D_i}{P}\right)^2} \tag{A71}$$

$$V_{HIS} = \frac{G_a}{\rho_V}\sqrt{1+\left(\frac{\pi D_i}{P}\right)^2} \tag{A72}$$

Local values of the overall heat transfer coefficient, U, were calculated from the local values of q" and ΔT, as follows:

$$U = \frac{q''}{\Delta T} = \frac{q''}{T_{NaK} - T_{Hg}} \tag{A73}$$

where ΔT is obtained from the calculated bulk NaK temperatures and the mercury temperatures measured by insert thermocouples.

Finally, the local values of mercury heat transfer coefficient, h_{Hg}, were calculated by subtracting the thermal resistance of the flowing NaK, static NaK layer, stainless steel annulus, and tantalum tube wall from the overall thermal resistance, as follows:

$$h_{Hg} = \left(\frac{1}{U} - \frac{1}{\overline{U}_{cw}}\right)^{-1} \tag{A74}$$

where the combined thermal resistance, $\frac{1}{\overline{U}_{cw}}$, was given in equation (A34).

D. Local Two-Phase Pressure Drop Results

The local value of saturation pressure during two-phase boiling of mercury was obtained by using measured mercury saturation temperatures together with the vapor pressure curve cited from Reference (12). The

local boiling pressure gradient $\left(\frac{dP}{dz}\right)_{TP}$ was calculated from the local boiling temperature gradient and the vapor pressure curve for mercury. In terms of the derivative of temperature with respect to pressure along the vapor pressure curve, the local boiling pressure gradient was obtained as follows:

$$\left(\frac{dP}{dz}\right)_{TP} = \left(\frac{dT_{Hg}}{dz}\right) \quad \left(\frac{dT}{dP}\right)_{Sat} \tag{A75}$$

with $\frac{dT_{Hg}}{dz}$ and $\left(\frac{dT}{dP}\right)_{Sat}$ obtained by graphical differentiation along the mercury temperature profile and the mercury vapor pressure curve, respectively.

A knowledge of the local momentum and elevation pressure gradients is needed to calculate local values of the two-phase frictional pressure gradient from the total two-phase pressure gradient, as follows:

$$\left(\frac{dP}{dz}\right)_{TPf} = \left(\frac{dP}{dz}\right)_{TP} - \left(\frac{dP}{dz}\right)_{TPm} - \left(\frac{dP}{dz}\right)_{TPe} \tag{A76}$$

Considering an annular flow model for the boiling region, i.e., liquid flowing in an annulus surrounding a core of vapor, the momentum pressure gradient for two-phase mixture was defined:

$$\left(\frac{dP}{dz}\right)_{TPm} = -\frac{G^2}{g_c} \frac{d}{dz}\left[\frac{(1-x)^2}{\rho_L(1-\alpha)} + \frac{x^2}{\rho_V \alpha}\right] \tag{A77}$$

and the elevation pressure gradient was defined:

$$\left(\frac{dP}{dz}\right)_{TPe} = -\frac{g}{g_c} \sin\theta \left[\rho_V \alpha + \rho_L (1 - \alpha)\right] \tag{A78}$$

where θ, the elevation angle of the test section, is 7 degrees in this experiment.

The void fraction, α, in equations (A77) and (A78) was eliminated by employing the continuity equation of two-phase mixtures as follows:

$$K = \frac{\rho_L}{\rho_V}\left(\frac{x}{1-x}\right)\left(\frac{1-\alpha}{\alpha}\right) \tag{A79}$$

or

$$\alpha = \frac{1}{1 + K\left(\frac{\rho_V}{\rho_L}\right)\left(\frac{1-x}{x}\right)} \tag{A80}$$

By using this expression for α, Equations (A77) and (A78) were rewritten as:

$$\left(\frac{dP}{dz}\right)_{TPm} = -\frac{G^2}{g_c}\frac{d}{dz}\left\{\frac{1}{\rho_V}\left[(1-\alpha)\frac{\rho_V}{\rho_L} + \frac{x}{K}\right]\left[1 + x\,(K-1)\right]\right\} \tag{A81}$$

and

$$\left(\frac{dP}{dz}\right)_{TPe} = -\frac{g\sin\theta}{g_c}\left[\frac{x + K\,(1-x)}{x + K\,(1-x)\,\rho_V/\rho_L}\right]\rho_V \tag{A82}$$

By assuming K, the slip ratio, constant for a particular run, the right hand side of Equation (A81) was differentiated yielding:

$$\left(\frac{dP}{dz}\right)_{TPm} = -\frac{G^2}{g_c}\left(\frac{1}{\rho_V}\right)\frac{dx}{dz}\left[\frac{1}{K} - \frac{\rho_V}{\rho_L} + \frac{\rho_V}{\rho_L}(K-1)(1-2x) + \left(\frac{K-1}{K}\right)2x\right] \tag{A83}$$

The proper value of K is uncertain at present. Some investigators[5],[35] found that $K = (\rho_V/\rho_L)^{1/2}$ in their analyses. A homogeneous model, assuming simply K = 1, is usually used in the prediction of two-phase

pressure drops. For a homogeneous model, Equations (A81) and (A82) were simplified to:

$$\left(\frac{dP}{dz}\right)_{TPm} = -\frac{G^2}{g_c}\left(\frac{1}{\rho_V} - \frac{1}{\rho_L}\right)\frac{dx}{dz} \tag{A84}$$

and

$$\left(\frac{dP}{dz}\right)_{TPe} = -\frac{g}{g_c}\sin\theta\left[\frac{\rho_V}{x + (1-x)(\rho_V/\rho_L)}\right] \tag{A85}$$

In order to calculate $\left(\frac{dP}{dz}\right)_{TPm}$ in Equation (A84), the local quality variation must be known. A consideration of energy balance gives:

$$\frac{dx}{dz} = \frac{\pi D_i L_B}{Wh_{LV}}\left(\frac{dq''}{dz}\right) - \frac{C_L}{h_{LV}}\left(\frac{dT_{Hg}}{dz}\right) \tag{A86}$$

With $\frac{dq''}{dz}$ and $\frac{dT_{Hg}}{dz}$ evaluated locally by graphical differentiation from their profiles presented in Figures (41) to (56) and Figures (21) to (36), respectively. The boiling length ($L_B = L_{NB} + L_{TB}$) was given previously in Equation (A10) for each experimental run.

The mass velocity, G, used in Equation (A84) must be corrected to account for the helical flow effect. As discussed previously, an equation was proposed for G as follows:

$$G^2 = G_a^2\,\overline{\left(\frac{V_H}{V_a}\right)^2} \tag{A87}$$

with $\overline{\left(\frac{V_H}{V_a}\right)^2}$ given in Equation (A45). Then, the frictional pressure gradient $\left(\frac{dP}{dz}\right)_{TPf}$ was calculated from Equation (A76). The local two-phase pressure drop multiplier is the ratio of two-phase to single-phase liquid frictional pressure gradient:

$$\phi = \frac{\left(\frac{dP}{dz}\right)_{TPf}}{\left(\frac{dP}{dz}\right)_{SPLf}} \tag{A88}$$

where the liquid frictional pressure gradient is calculated by the conventional Fanning equation modified for helical flow conditions as follows:

$$\left(\frac{dP}{dz}\right)_{SPLf} = \left(\frac{f_e}{D_e}\right) \frac{G_H^2}{2g_c\rho_L} \tag{A89}$$

with

$$f_e = 0.316 \left(\frac{G_H D_e}{\mu_L}\right)^{-1/4} \tag{A90}$$

One of the earliest efforts in the prediction of two-phase pressure drop was that of Martinelli et al.[37] in which a substantial amount of two-phase, two-component data was successfully correlated. A further improvement of this work by Lockhart-Martinelli[37] gave the most widely applied method for predicting two-phase pressure drop. Later, Martinelli-Nelson[34] successfully correlated their forced-convection boiling water data with the method developed in Reference (37). They then constructed a series of curves by plotting the two-phase multiplier defined in Equation (A88) versus the quality with the saturation pressure (or temperature) used as a parameter.

The Martinelli-Nelson curves, shown in Figure (100), were primarily deduced from high pressure steam data; consequently, these curves were proposed for use only with steam. However, these curves can be generalized and used for many other fluids including liquid metals. In References (5) and (6), the Martinelli-Nelson curves were modified successfully to

correlate the potassium boiling pressure drop data. An attempt was then made to modify the Martinelli-Nelson curves for predicting the current mercury boiling pressure drop data. This modification is described below.

Introducing a scale factor, defined $\frac{\rho_L}{\rho_V}\left(\frac{\mu_V}{\mu_L}\right)^{1/4}$, the Martinelli-Nelson curves were replotted in Figure (101) to show the two-phase multiplier (ϕ) as a function of the scale factor, with the quality used as a parameter. The scale factor, which involves only the physical properties for both phases of any single- or two-component, two-phase fluid, was used as a common basis to scale out the two-phase multiplier for a particular fluid in a forced-convection boiling process. Since the scale factor is primarily temperature (or pressure) dependent, there are corresponding mercury temperatures for selected values of the scale factor, as shown in Figure (101). Based upon this transformation, a series of curves for mercury similar to the Martinelli-Nelson curves for water were constructed in Figure (102).

Another frequently used two-phase pressure drop correlation is the so-called "homogeneous model" which was derived from the definition of the two-phase pressure drop multiplier as follows:

$$\phi_H = \frac{\left(\frac{dP}{dz}\right)_{TPf}}{\left(\frac{dP}{dz}\right)_{SPLf}} = \left(\frac{f_{TP}}{f_{SPL}}\right)\frac{\rho_L}{\rho_{TP}} = \left(\frac{\mu_{TP}}{\mu_L}\right)^{1/4}\frac{\rho_L}{\rho_{TP}} \qquad \text{(A91)}$$

In Equation (A91) the Fanning type pressure drop correlation and the Blasius relation for the friction factor have been used.

With the density and viscosity for a homogeneous two-phase mixture written as:

$$\frac{1}{\rho_{TP}} = \frac{1}{\rho_L}\ (1 - x) + \frac{x}{\rho_V} \tag{A92}$$

and

$$\frac{1}{\mu_{TP}} = \frac{1}{\mu_L}\ (1 - x) + \frac{x}{\mu_V} \tag{A93}$$

Equation (A91) becomes:

$$\phi_H = \frac{1 + x\left(\frac{\rho_L}{\rho_V} - 1\right)}{\left[1 + x\left(\frac{\mu_L}{\mu_V} - 1\right)\right]^{1/4}} \tag{A94}$$

Equation (A94) is a general expression for predicting two-phase, pressure drop for any single- or two-component, two-phase fluid. In Figure (103) Equation (A94) was generalized by using the scale factor. A plot similar to that of the Martinelli-Nelson curves is given in Figure (104) for various mercury temperatures.

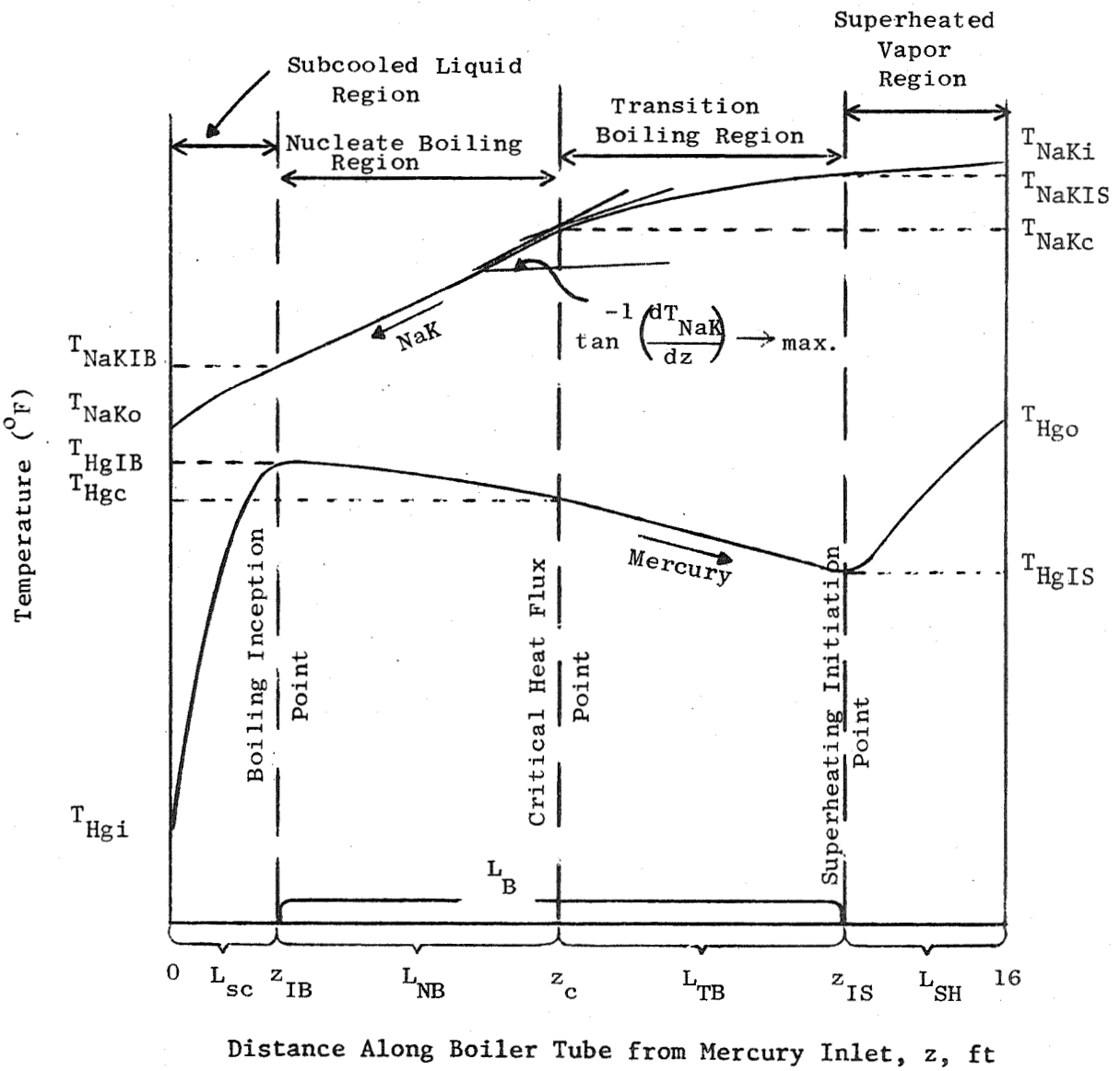

Figure 95. Diagrammatic Definition of Terminology Employed in the Calculational Procedures for Counter-Current Once-Through Mercury Boiler.

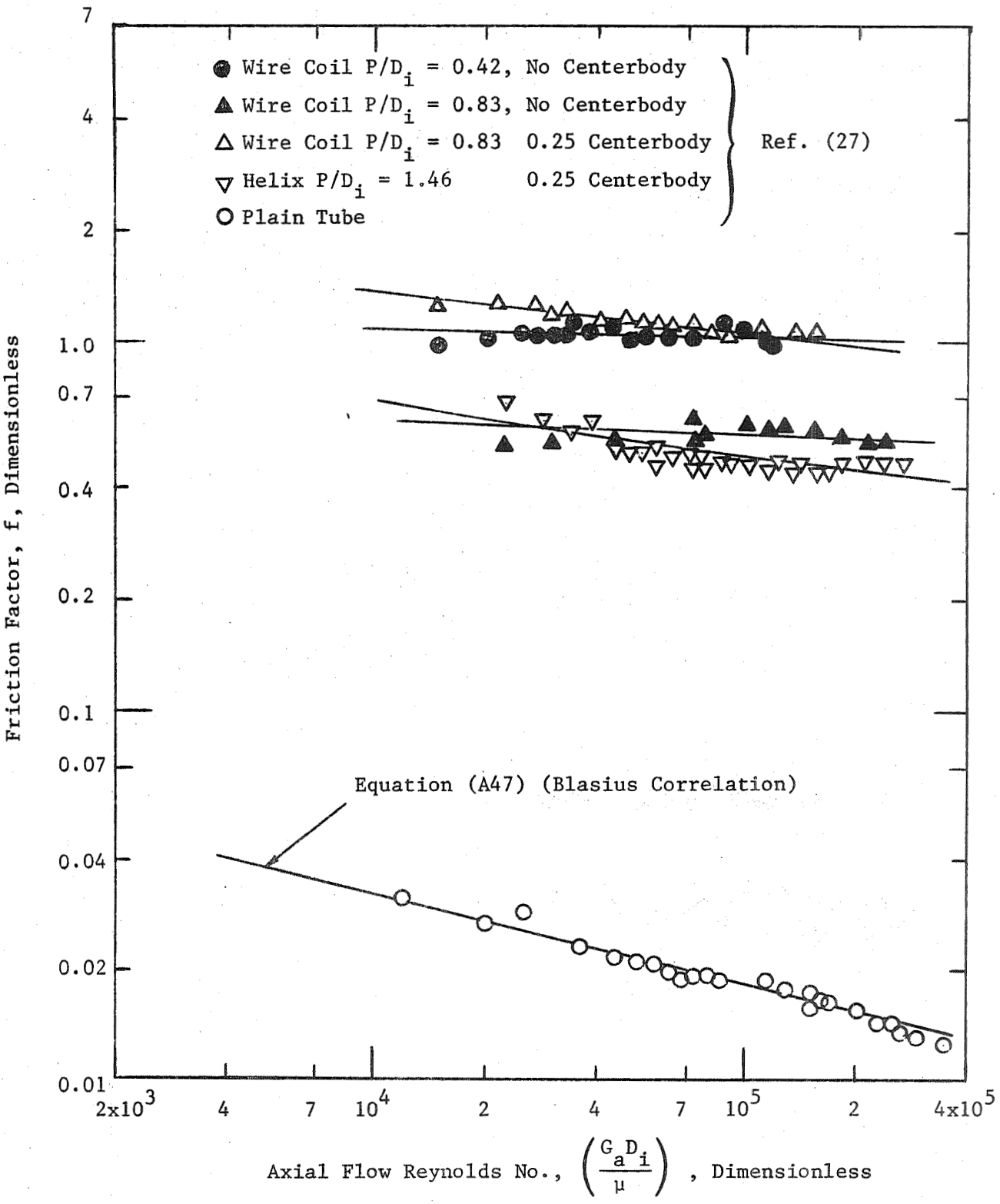

Figure 96. Friction Factor Vs. Axial Flow Reynolds Number for Tubes Containing Inserts with Forced Air Flow.

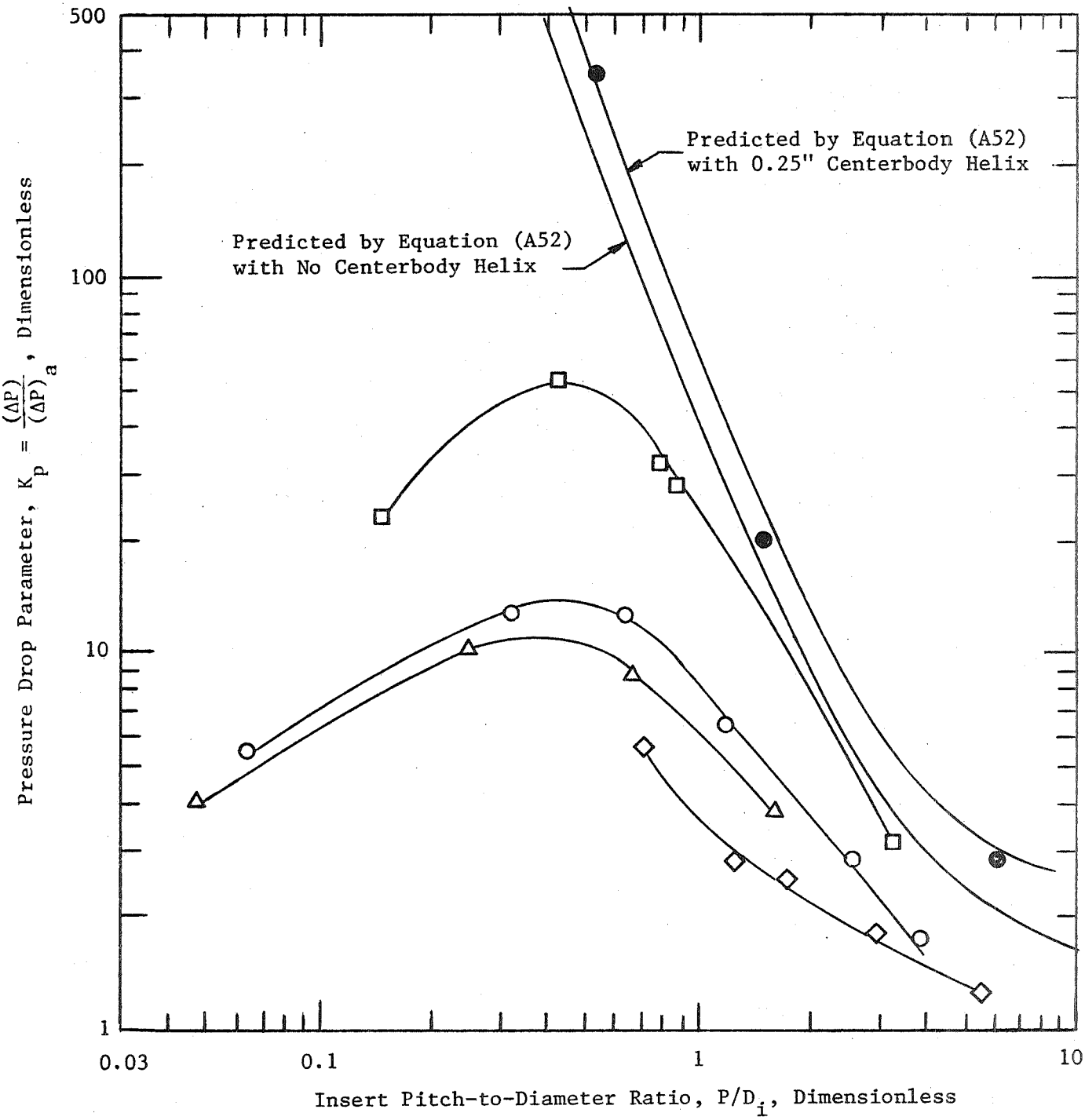

◇ △ ○ □ Wire Coil Insert d/D_i = 0.0317, 0.0463, 0.0634 Ref. (28); = 0.1428 Ref. (27)

● Helical Vane Insert D_{cb} = 0.25" Ref. (27)

Figure 97. Measured Pressure Drop Parameter vs. Insert Twist Ratio.

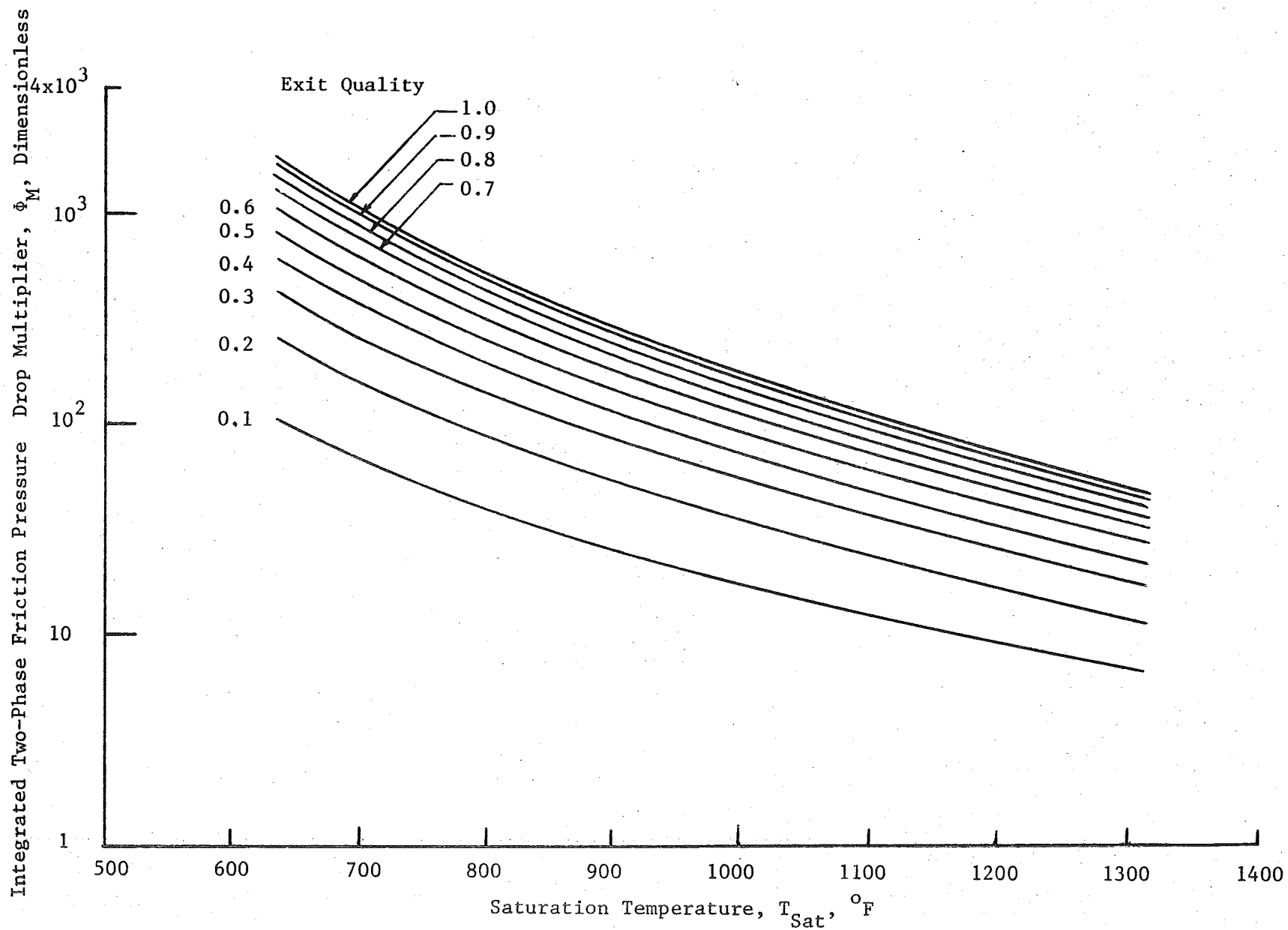

Figure 98. Integrated Two-Phase Friction Pressure Drop Multiplier for Mercury from the Modified Martinelli-Nelson Model.

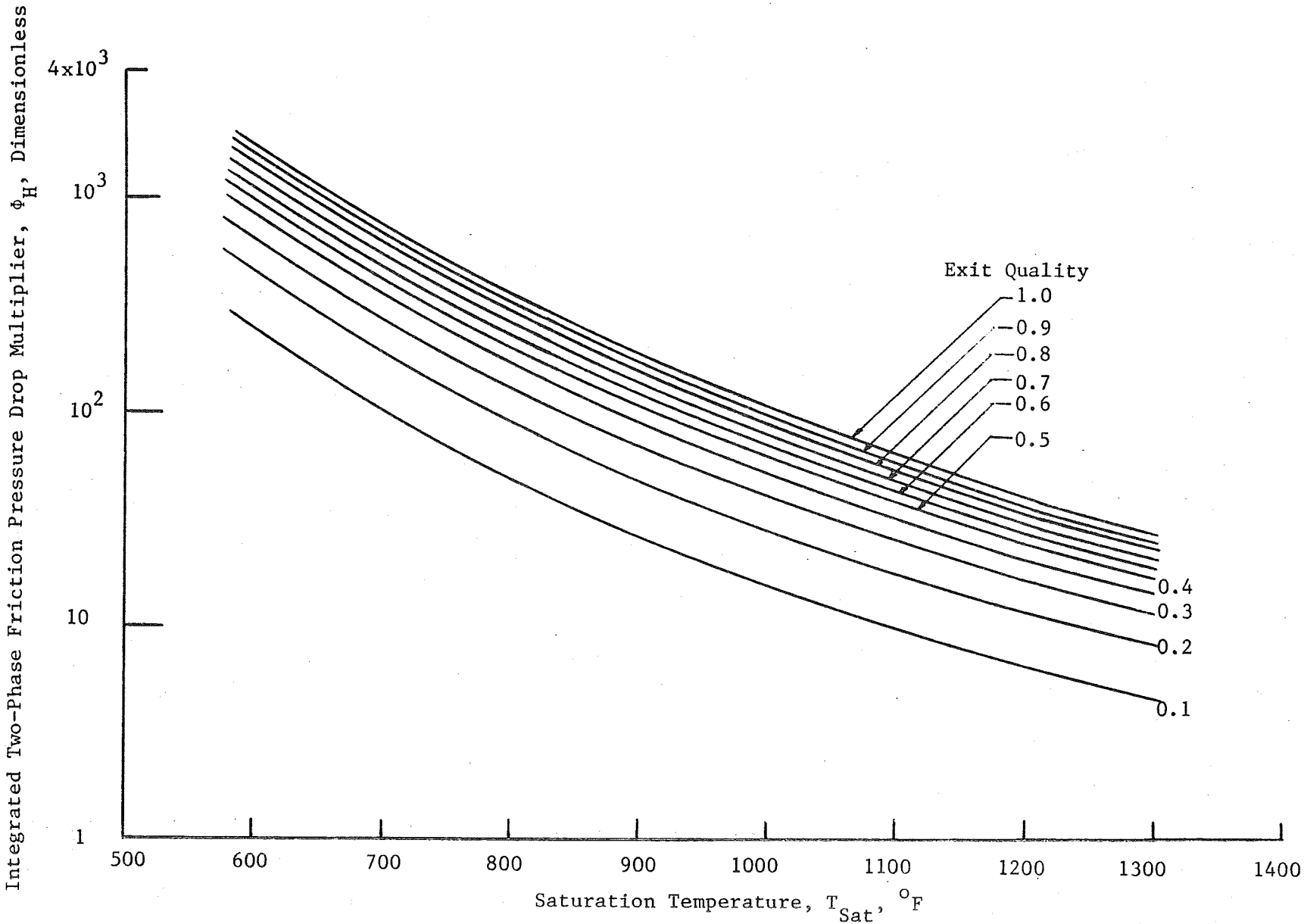

Figure 99. Integrated Two-Phase Friction Pressure Drop Multiplier for Mercury from the Homogeneous Flow Model.

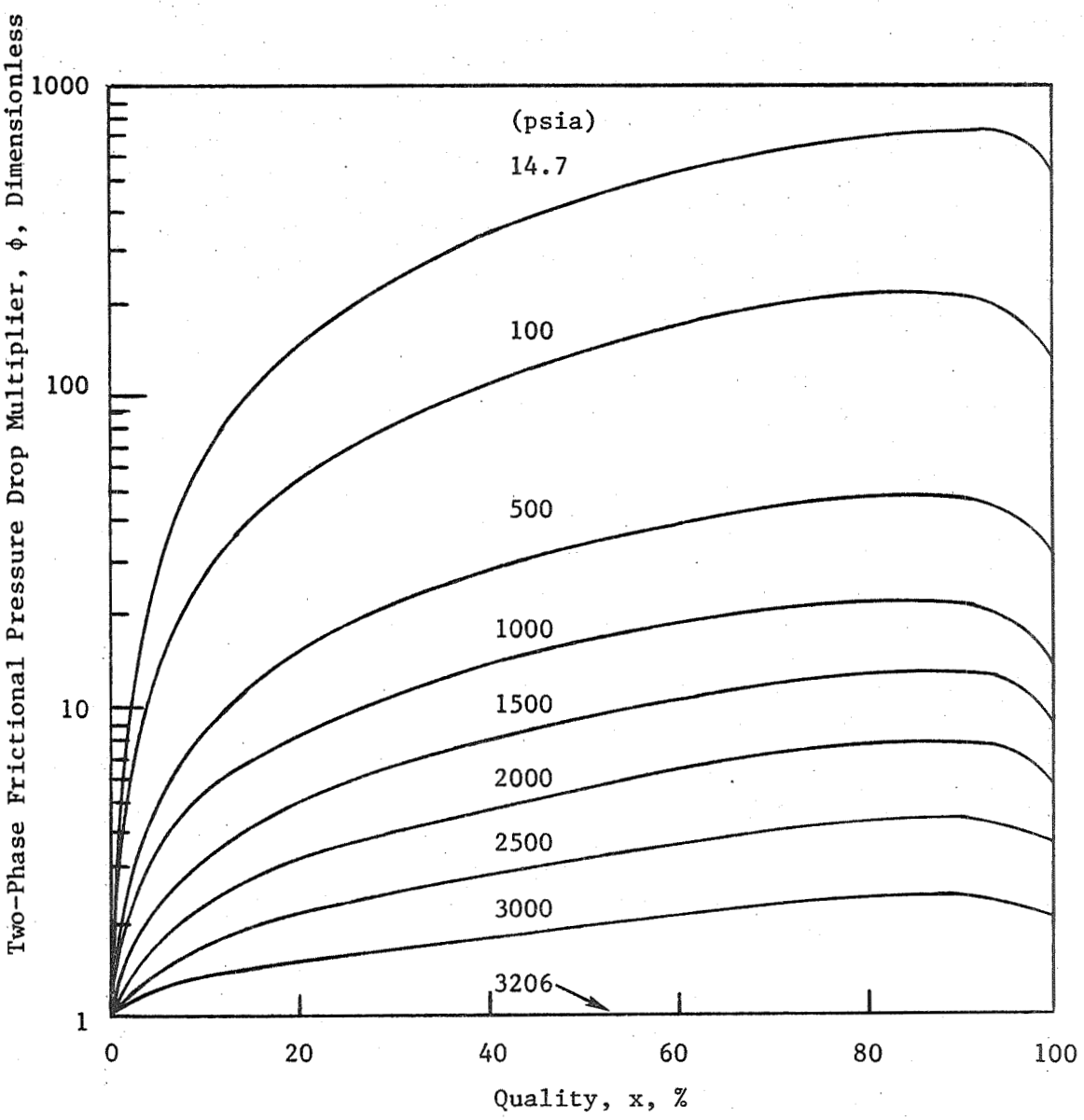

Figure 100. Ratio of Two-Phase Friction Pressure Gradient to Liquid-Phase Gradient at the Same Mass Velocity for Water at Various Pressures and Qualities. (Reference 34)

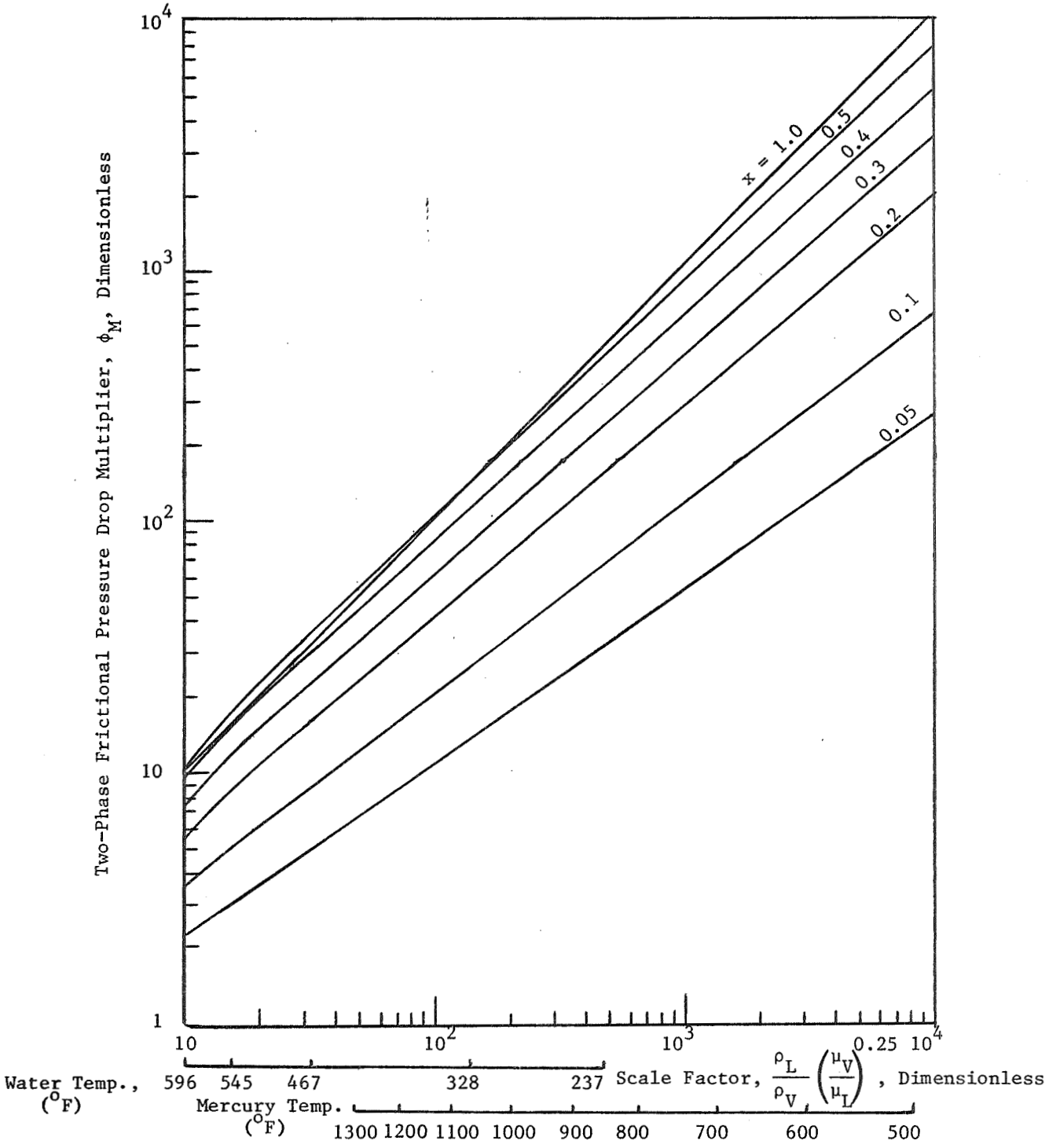

Figure 101. Generalized Martinelli-Nelson Model Two-Phase Frictional Pressure Drop Multiplier.

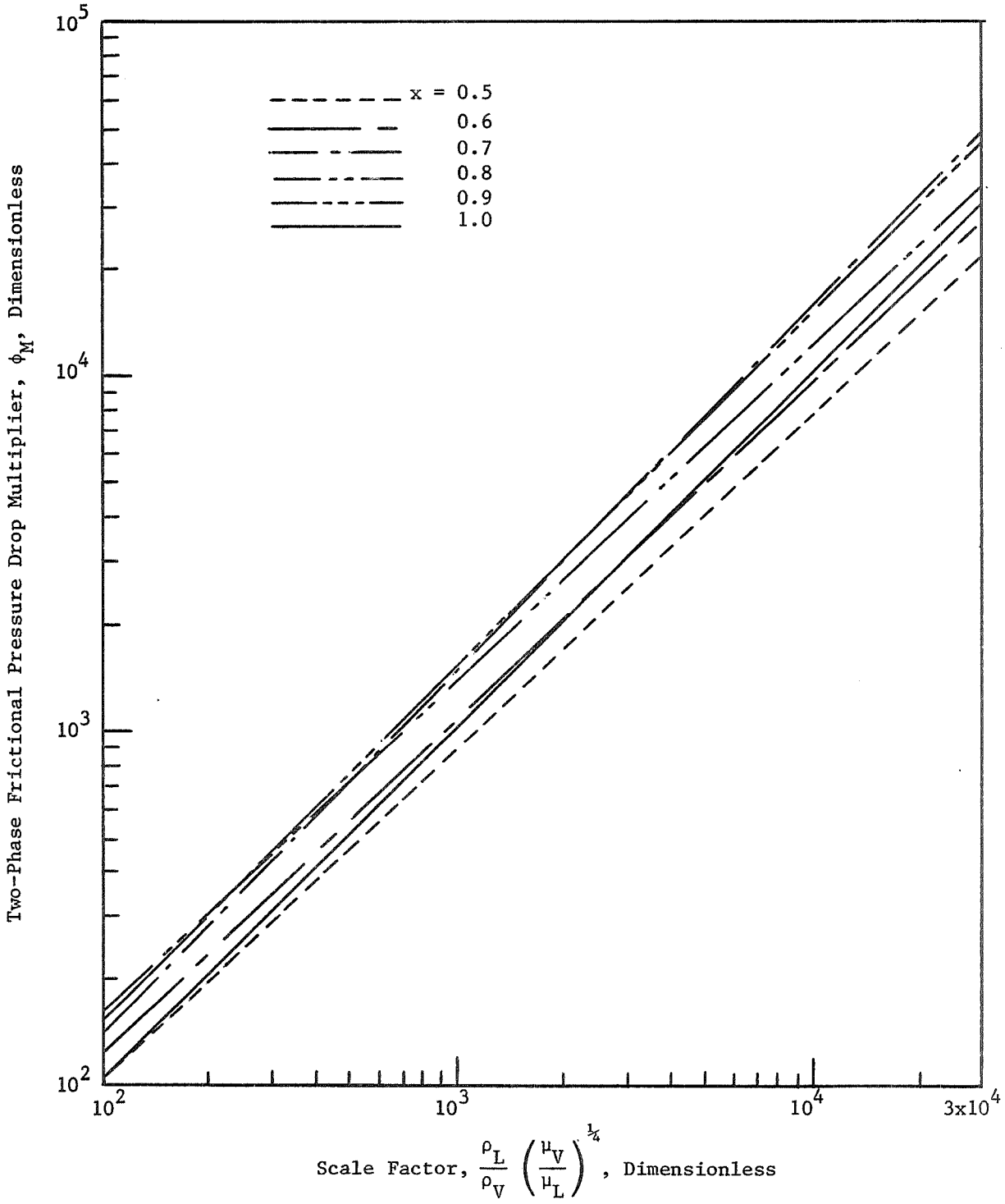

Figure 101 (Cont'd). Generalized Martinelli-Nelson Model Two-Phase Frictional Pressure Drop Multiplier for the Region of $0.5 < x < 1.0$.

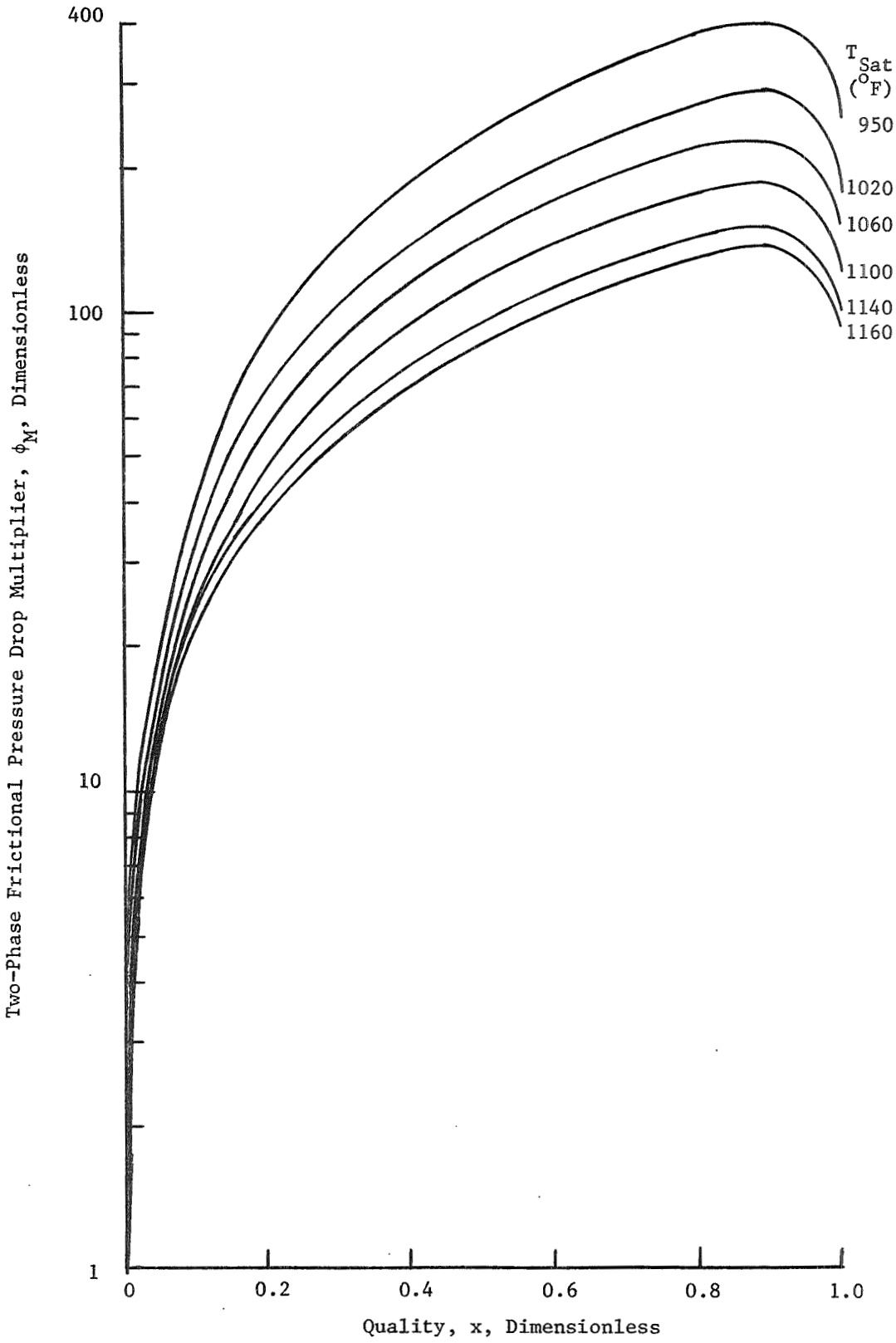

Figure 102. Two-Phase Frictional Pressure Drop Multiplier for Mercury from Modified Martinelli-Nelson Model.

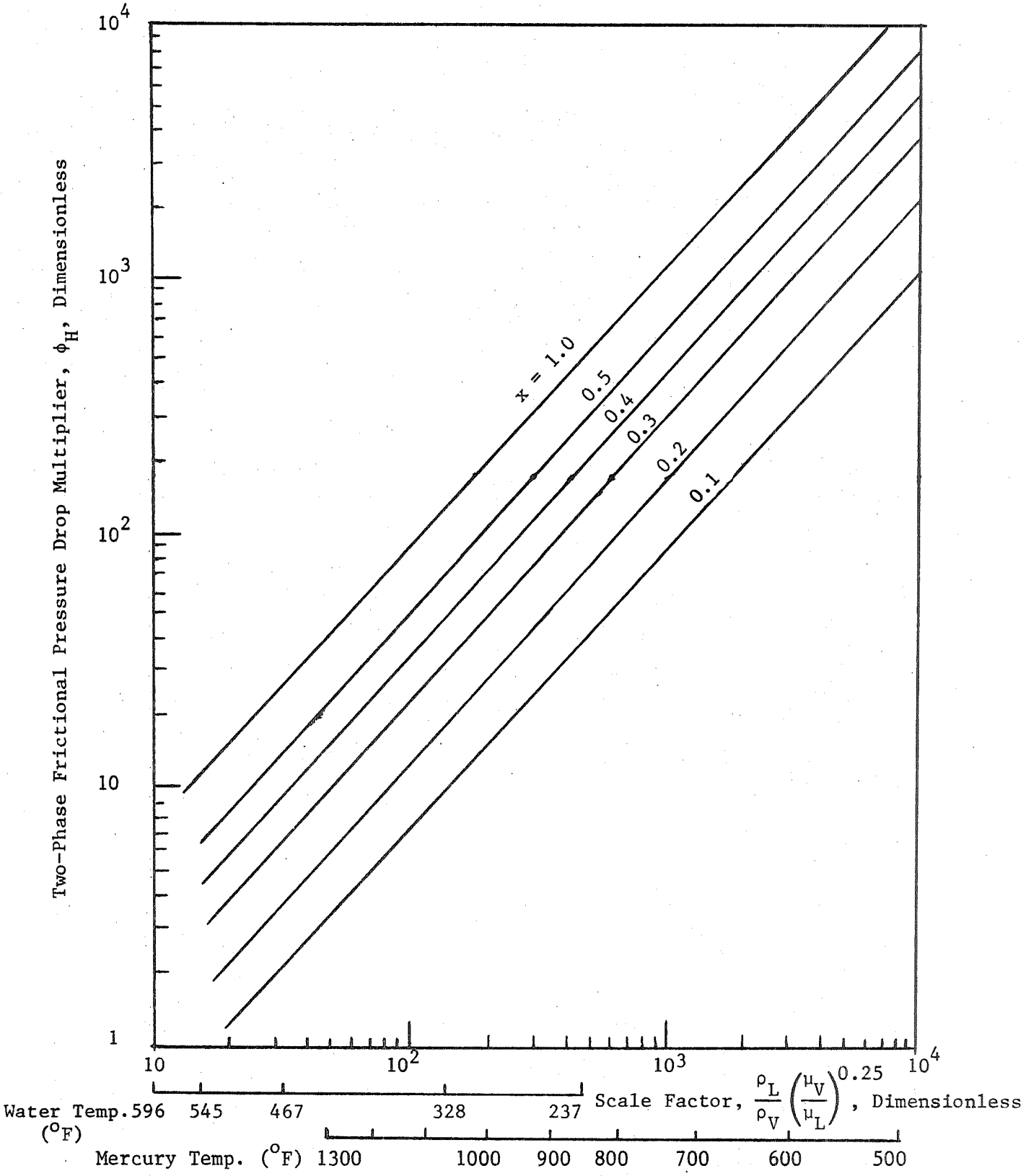

Figure 103. Generalized Homogeneous Model Two-Phase Frictional Pressure Drop Multiplier.

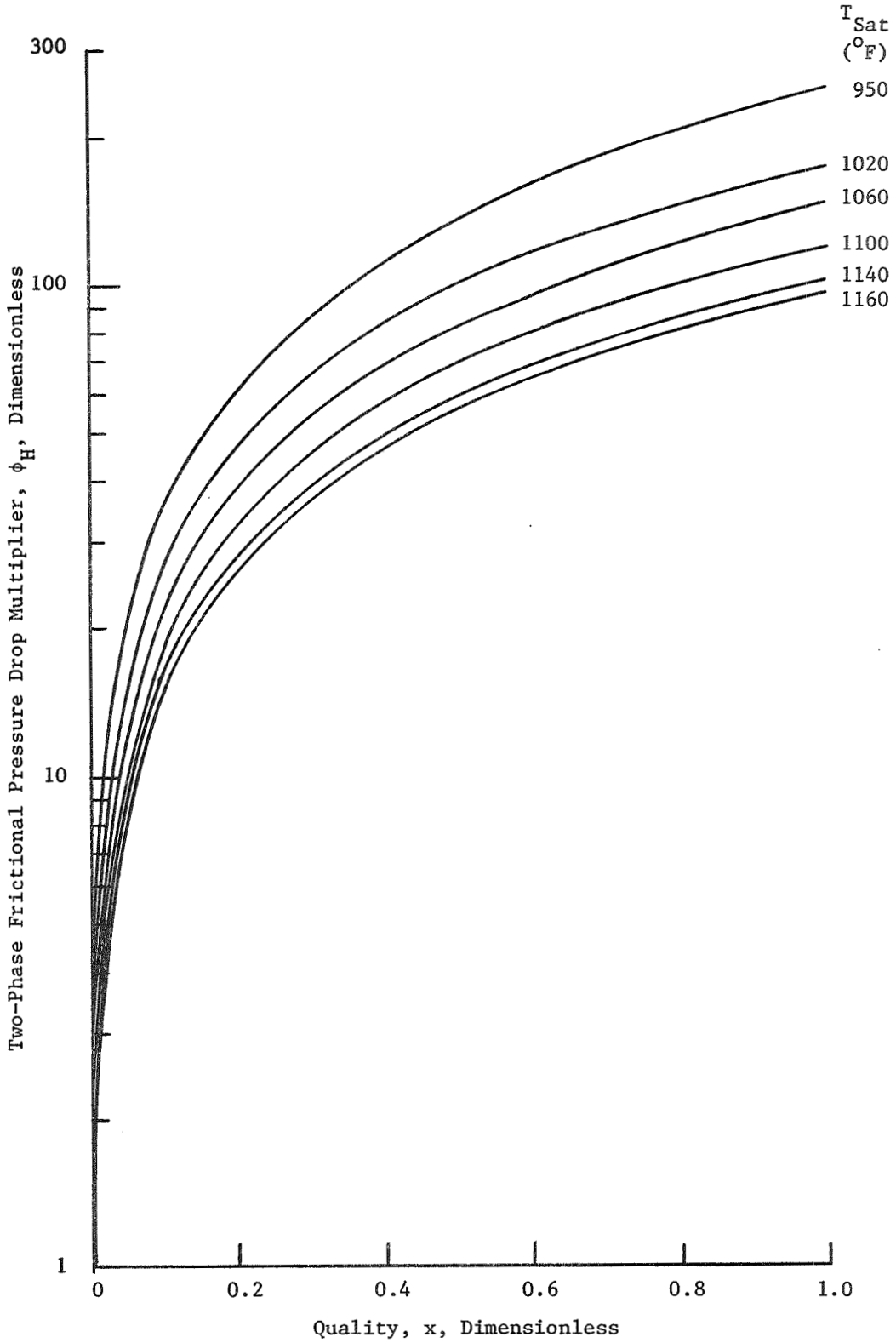

Figure 104. Two-Phase Frictional Pressure Drop Multiplier for Mercury from Homogeneous Model (n = 0.25).

APPENDIX II

TABULATION OF EXPERIMENTAL DATA

TABLE 1

LOOP THERMOCOUPLE DESCRIPTION

Thermo-couple Number	Junction Type	Outside Dia., in.	Wire Size (GA)	Digital Channel	Location
1	CNG	0.062	28	507	Boiler Inlet Well
2	CNG	0.062	28	508	Boiler Inlet Well
3	CNG	0.062	28	509	Boiler Exit Well
4	CNG	0.062	28	510	Boiler Exit Well
5	CNG	0.062	28	505	Condenser Upper Drum Well
6	CNG	0.062	28	504	Condenser Lower Drum Well
7	CNG	0.062	28	506	Pump Exit Well
8	CNG	0.062	28	503	Preheater Inlet Well
9	CNG	0.062	28	528	Preheater Exit Well
49	OSJ	0.125	24	524	Pressure Gage P6 (Pump Exit)
50	OSJ	0.125	24	526	Pressure Gage P7 (Liq. Diff. High)
51	OSJ	0.125	24	527	Pressure Gage P7 (Liq. Diff. Low)
52	OSJ	0.125	24	525	Pressure Gage P8 (Boiler Inlet)
53	OSJ	0.125	24	520	Pressure Gage P3 (Boiler Exit)
54	OSJ	0.125	24	521	Pressure Gage P4 (Vap. Diff. High)
55	OSJ	0.125	24	522	Pressure Gage P4 (Vap. Diff. Low)
56	OSJ	0.125	24	523	Pressure Gage P5 (Cond. Top Drum)
60	OLJ	See Note (2)	24	498	Reference Box B
61	OLJ	See Note (2)	24	499	Reference Box C
101	CNG	0.062	28	511	Boiler Inlet
102	CNG	0.062	28	512	Boiler Inlet
103	CNG	0.062	28	513	Boiler Exit
104	CNG	0.062	28	514	Boiler Exit
106	OSJ	0.125	24	515	Gas Heater Inlet
116	OSJ	0.125	24	517	Pressure Gage P1 (Heater Inlet)
117	OSJ	0.125	24	518	Pressure Gage P2 (Heater Diff. High)
118	OSJ	0.125	24	519	Pressure Gage P2 (Heater Diff. Low)
119	OSJ	0.125	24	516	Flowmeter Duct
120	OSJ	0.125	24	501	Flowmeter Magnet
124	OSJ	0.125	24	502	Static NaK Expansion Tank

(1) Heat Junction Reference Temperature, 150°F for all T/C's

(2) 0.125-inch OD Cu Wire (All other are Chromel-Alumel)

(3) Junction Type:
CNG Capped and Non-Grounded
OSJ Open Surface Junction
OLJ Open Loop Junction

TABLE 2

BOILER INSERT THERMOCOUPLE DESCRIPTION

Thermocouple Description				Thermocouple Location			Constant Temperature Junction		Digital Channel
Thermocouple Number	Type of Junction	Outside Dia., in.	Wire Size (B&S Gage)	Station Number	Distance from Station #1, in.	Circumferential Position	Box	Alloy Input Circuit	
301	SSW*	0.125	24	1	0	A	B	4A	531
302	SSW*	0.125	24			B	B	4B	532
303	SSW*	0.125	24			C	B	4C	533
304	SSW*	0.125	24	2	12	A	B	4D	534
305	SSW*	0.125	24			B	B	4E	535
306	SSW*	0.125	24			C	B	4F	536
307	SSW*	0.125	24	4	24	A	B	4G	537
308	SSW*	0.125	24			B	B	4H	538
309	SSW*	0.125	24			C	B	4I	539
310	SSW*	0.125	24	5	36	A	B	4J	540
311	SSW*	0.125	24			B	B	5A	541
312	SSW*	0.125	24			C	B	5B	542
313	SSW*	0.125	24			D	B	5C	543
314	SSW*	0.125	24			E	B	5D	544
315	SSW*	0.125	24			F	B	5E	545
316	SSW*	0.125	24	7	48	A	B	5F	546
317	SSW*	0.125	24			B	B	5G	547
318	SSW*	0.125	24			C	B	5H	548
319	SSW*	0.125	24	8	60	A	B	5I	549
320	SSW*	0.125	24			B	B	5J	550
321	SSW*	0.125	24			C	B	1A	551
322	SSW*	0.125	24	10	72	A	C	1B	552
323	SSW*	0.125	24			B	C	1C	553
324	SSW*	0.125	24			C	C	1D	554
325	SSW*	0.125	24	11	84	A	C	1E	555
326	SSW*	0.125	24			B	C	1F	556
327	SSW*	0.125	24			C	C	1G	557
328	SSW*	0.125	24			D	C	1H	558
329	SSW*	0.125	24			E	C	1I	559
330	SSW*	0.125	24			F	C	1J	560
331	SSW*	0.125	24	13	96	A	C	2A	561
332	SSW*	0.125	24			B	C	2B	562
333	SSW*	0.125	24			C	C	2C	563
334	SSW*	0.125	24	14	108	A	C	2D	564
335	SSW*	0.125	24			B	C	2E	565
336	SSW*	0.125	24			C	C	2F	566
337	SSW*	0.125	24	16	120	A	C	2G	567
338	SSW*	0.125	24			B	C	2H	568
339	SSW*	0.125	24			C	C	2I	569
340	SSW*	0.125	24	17	132	A	C	2J	570
341	SSW*	0.125	24			B	C	3A	571
342	SSW*	0.125	24			C	C	3B	572
343	SSW*	0.125	24			D	C	3C	573
344	SSW*	0.125	24			E	C	3D	574
345	SSW*	0.125	24			F	C	3E	575
346	SSW*	0.125	24	19	144	A	C	3F	576
347	SSW*	0.125	24			B	C	3G	577
348	SSW*	0.125	24			C	C	3H	578
349	SSW*	0.125	24	20	156	A	C	3I	579
350	SSW*	0.125	24			B	C	3J	580
351	SSW*	0.125	24			C	C	4A	581
352	SSW*	0.125	24	21	168	A	C	4B	582
353	SSW*	0.125	24			B	C	4C	583
354	SSW*	0.125	24			C	C	4D	584
355	SSW*	0.125	24	22	180	A	C	4E	585
356	SSW*	0.125	24			B	C	4F	586
357	SSW*	0.125	24			C	C	4G	587
358	SSW*	0.125	24	23	192	E	C	4H	588
359	SSW*	0.125	24			B	C	4I	589
360	SSW*	0.125	24			C	C	4J	590

*Surface Spot Weld

TABLE 3

BOILER INSERT THERMOCOUPLE DESCRIPTION

Thermocouple Description			Thermocouple Location		Constant Temperature Junction		
Thermocouple Number	Type of Junction	Outside Dia., in.	Station Number	Distance from Station #1, in.	Box	Alloy Input Circuit	Digital Channel
371	CNG*	0.040	1	0	C	5A	591
372	CNG*	0.040	3	23	C	5B	592
373	CNG*	0.040	6	46	C	5C	593
374	CNG*	0.040	9	69	C	5D	594
375	CNG*	0.040	12	92	C	5E	595
376	CNG*	0.040	15	115	C	5F	596
377	CNG*	0.040	18	136.6	C	5G	597

*Capped Not Grounded

TABLE 4

OVERALL AND AVERAGE RESULTS*

Run No.	Date	Time	G_{Hg}	T_{Hgi}	T_{Hgo}	G_{NaK}	T_{NaKi}	T_{NaKo}	T_{Sat}	P_{in}	P_{out}	ΔP	Q_T	Q_{net}	Q_{sc}	Q_B	$\bar{q}''_T$	L_{sc}	L_{NB}	L_{TB}	$\bar{q}''_{sc}\times10^{-4}$	$\bar{h}_{sc}$	$\bar{q}''_B\times10^{-4}$	$\bar{h}_B$	$\bar{q}''_{NB}\times10^{-4}$	$\bar{h}_{NB}$	$\bar{q}''_{TB}\times10^{-4}$	$\bar{h}_{TB}$	$q''_{SH}\times10^{-4}$	$\bar{h}_{SH}$	$(\Delta T)_{SH}$
1	12/29/67	1350	81.52	938	1345	315	1345	1265	975	131	75	56	36	28.6	4.21	24.4	3.48	0.3	2.3	1.8	8.5	980	3.05	938	27.1	2120	8.5	792	0.3	37.5	280
2	12/29/67	1800	115	925	1325	317	1325	1221	1060	252	202	50	48	40.8	7.32	32.9	4.89	0.4	1.8	1.4	13.9	1260	4.11	1050	25.5	9050	21.8	2380	0.27	63	303
3	12/29/67	1850	112.6	917	1326	316	1326	1226	1060	247	198	49	46.5	39.3	7.15	32.2	4.78	0.4	2.1	1.2	13.9	1210	4.02	1010	25.1	8800	28.3	5440	0.47	84	316
4	12/29/67	2005	158	760	1308	326	1308	1177	1110	326	262	64	61	54.4	11	43.4	6.62	0.6	2.4	2.0	18.3	1208	5.45	2310	15.7	8700	21.2	4050	0.37	68	245
5	12/29/67	2130	141	795	1325	324	1325	1200	1100	298	242	56	58	51	9.5	41.5	6.2	0.5	1.5	1.8	14	1220	5.2	1460	20.1	8400	25.7	4800	0.33	61	274
6	12/29/67	2230	176	708	1315	328	1316	1166	1120	334	256	78	68.8	62	12.3	49.6	7.53	0.8	3.2	2.0	23.9	1530	6.23	2730	15.1	8100	21.8	4260	0.45	97	254
7	12/29/67	2255	177.6	705	1307	329	1309	1161	1110	327	257	70	69.1	62	12.3	50	7.58	0.8	3.5	1.9	14.7	1470	6.35	2520	15.9	8250	21.7	4600	0.46	105	245
8	12/29/67	2315	163	729	1310	324	1310	1168	1100	309	237	72	64	57	11	46	6.95	0.7	2.9	1.4	24.6	1310	5.75	2280	17.4	8500	24.2	5700	0.42	92	263
9	1/3/68	1145	191.4	726	1280	309	1286	1118	1110	315	267	48	74	67.6	12.5	55	8.23	1.0	7.0	2.8	12.15	1800	7.16	3780	8.5	5000	17.4	4440	0.74	123	212
10	1/3/68	1300	185	744	1307	305	1317	1145	1120	336	250	86	75	68.3	12.3	55.9	8.3	1.0	4.3	2.2	11.2	1400	7.25	3000	13.9	8400	18.6	3710	0.61	118	250
11	1/3/68	1500	186	749	1325	310	1330	1156	1120	338	262	76	75.4	68.4	12.4	56	8.32	1.0	4.3	2.7	11.3	1215	7.14	2750	14.1	8300	16.7	2320	0.64	120	261
12	1/3/68	1900	193	722	1314	304	1323	1148	1120	337	254	83	75.6	68.6	12.9	55.8	8.35	0.8	3.7	2.5	15.5	1820	7.14	2770	13.4	8320	21.3	3400	0.60	110	254
13	1/6/68	2300	192	660	1291	311	1297	1129	1130	349	268	81	74.8	68.3	13	55.3	8.3	1.0	7.0	1.9	18.1	1850	7.08	3350	10.4	6800	18.8	3900	0.67	125	222
14	1/7/68	2110	193	657	1293	311	1296	1116	1110	330	256	74	75	68.8	12.9	55.8	8.30	1.1	7.9	2.1	13.5	1830	7.24	3790	8.33	6250	18.6	4000	0.77	130	205
15	1/9/68	0515	82	898	1331	118	1333	1111	1086	290	259	31	36	29.1	4.7	24.4	3.53	0.6	2.0	0.6	10.1	1520	3.06	2270	17.7	8080	16.3	2770	0.65	68	268
16	1/9/68	2200	143	827	1300	326	1302	1176	1080	268	200	68	59.5	52.7	8.8	43.9	6.4	0.5	1.5	2.0	11.7	1070	5.5	1840	20.4	8300	25.5	5150	0.36	81.5	281

*See Nomenclature for symbols used in the data table.
Units given in Tables 4 to 12 are given as follows:

A_R	Radial Acceleration	g's
G	Mass Velocity	$lbm/sec\text{-}ft^2$
$h,\bar{u}$	Heat Transfer Coefficient	$Btu/hr\text{-}ft^2\text{-}^oF$
L	Length	ft
P	Pressure	psia
q"	Heat Flux	$Btu/hr\text{-}ft^2$
Q	Heat Transfer Rate	kilo-watts
T	Temperature	^oF

TABLE 5

OVERALL PRESSURE DROP RESULTS

Run No.	G_{Hg}	T_{Hgi}	T_{Hgo}	P_{in}	P_{out}	$(\Delta P)_o$	$(\Delta P)_{misc.}$	$(\Delta P)_{elev.}$	L_B	L_V	$(L_V)_{WC}$	$(L_V)_{HV}$	$(\Delta P)_{HVf}$	$(\Delta P)_{WCf}$	$(\Delta P)_{SpV}$	$(\Delta P)_{SpVm}$	$(\Delta P)_{TP}$*	$(\Delta P)_{TP}$**	$\frac{(\Delta P)_{TP}*}{(\Delta P)_{TP}**}$
1	81.5	938	1345	131	75	56	1.21	9.41	4.1	12.4	4.8	7.6	15.1	14.6	33	3.3	11.4	8.44	1.35
2	115	924	1325	260	202	58	1.44	8.69	3.4	13	4.8	8.2	13.8	16.3	35.2	5.06	12.4	11.1	1.11
3	113	917	1326	255	198	57	1.81	8.49	3.2	13.2	4.8	8.4	13.1	17	35.1	5.01	11.6	10.4	1.11
4	158	760	1308	334	262	71	1.65	7.85	4.4	11.8	4.8	7	18.5	20.3	39.4	4.6	18	16.5	1.09
5	141	795	1325	306	242	64	2.01	7.69	3.3	13	4.8	8.2	17.9	19.6	40.2	3.66	13.1	10.4	1.26
6	176	708	1315	342	256	86	2.11	7.99	5.2	10.8	4.8	6	15.7	31.5	52.9	5.73	23	19.4	1.18
7	178	705	1307	335	258	77	1.86	8.04	5.4	10.6	4.8	5.8	13.6	24	44.2	5.82	23.8	21.5	1.11
8	163	729	1310	317	237	80	2.28	7.97	4.3	11.8	4.8	7	18.2	27.4	50.5	4.84	19.2	16.9	1.14
9	191	726	1280	343	257	86	2.08	8.61	9.8	6.0	4.8	1.2	4.4	37.5	48.8	6.91	26.6	27.5	0.966
10	185	744	1307	344	250	94	2.10	8.19	6.7	9.1	4.8	4.3	14.9	36.5	57.6	6.25	26.1	23.4	1.12
11	186	749	1325	346	262	84	2.20	8.19	7.0	8.8	4.8	4.0	14	30.5	50.8	6.3	23	23.6	0.98
12	193	721	1314	345	254	91	2.21	8.06	6.2	9.8	4.8	5.0	14.6	31.4	52.8	6.78	28	26.3	1.07
13	192	660	1291	357	268	89	2.20	8.33	8.9	6.9	4.8	2.1	8	31.2	46.1	6.9	30	32.1	0.94
14	193	657	1293	338	256	85	2.18	8.56	10	5.7	4.8	0.9	2.3	32.3	41.6	6.95	37.2	40.5	0.92
15	82	898	1331	290	259	31	1.13	7.01	2.6	13	4.8	8.2	5.78	8.36	15.34	1.21	8.24	7.1	1.16
16	143	827	1300	276	200	70	1.65	8.0	3.5	12.8	4.8	8.0	17.6	19.8	44	6.6	13.9	12.1	1.15

*Calculated from the inlet and exit Taylor pressure transducers

**Estimated from measured saturation temperatures

TABLE 6

OVERALL PRESSURE DROP RESULTS IN TWO PHASE REGION

Run No.	G_{Hg}	T_{Sat}	P_{Sat}	$(\Delta P)_{TP}$*	$(\Delta P)_{TPm}$	$(\Delta P)_{L}$	$(\Delta P)_{TPf}$	Φ_{exp}	Φ_{H} (n=¼)	Φ_{H} (n=0)	Φ_{MN}	$\Phi_{exp}/\Phi_{H(n=¼)}$	Φ_{exp}/Φ_{M}
1	81.5	975	123.1	8.44	1.37	3.72×10^{-2}	7.07	190	130	210	200	1.47	0.935
2	115	1060	252	11.1	2.14	5.8×10^{-2}	8.9	164	90	145	150	1.73	1.04
3	113	1060	247	10.4	2.11	5.5×10^{-2}	8.3	149	90	145	150	1.62	0.976
4	158	1110	326	16.5	3.01	11×10^{-2}	13.4	125	70	105	110	1.76	1.12
5	141	1100	298	10.4	2.16	5.8×10^{-2}	9.24	138	75	120	125	1.8	1.13
6	176	1120	334	19.4	3.06	15.8×10^{-2}	18.8	116	70	110	110	1.56	0.995
7	178	1110	327	21.5	3.17	15.5×10^{-2}	18.63	118	70	115	115	1.65	1.08
8	163	1100	309	16.9	2.31	11.8×10^{-2}	14.6	128	75	120	125	1.68	1.05
9	191	1110	335	27.5	3.21	25.9×10^{-2}	24.3	87	70	115	115	1.26	0.82
10	185	1120	336	23.4	4.46	17.6×10^{-2}	19	112	70	110	110	1.57	1.00
11	186	1120	338	23.6	4.12	18.2×10^{-2}	19.5	98	70	100	110	1.44	0.93
12	193	1120	337	26.3	4.26	18.8×10^{-2}	22.04	111	70	105	110	1.58	1.01
13	192	1130	349	32.1	4.8	26.2×10^{-2}	27.3	103	70	110	110	1.33	0.85
14	193	1110	330	40.5	4.5	33×10^{-2}	36	106	75	120	120	1.27	0.804
15	82	1086	282	7.1	1.12	4.6×10^{-2}	6.0	130	81	120	125	1.61	1.05
16	143	1080	268	12.1	2.43	8.7×10^{-2}	9.7	125	85	130	135	1.47	0.944

*Obtained from insert thermocouple readings.

TABLE 7

SUBCOOLED LIQUID RESULTS

Run No.	Date	Time	G_{Hg}	T_{Sat}	ΔT_{sc}	h_L	N_{Nu}	N_{pe}	L_{sc}
1	12-29-67	1350	81.52	975	37	980	4.2	114	0.3
2	12-29-67	1800	115	1060	135	1260	5.4	160	0.4
3	12-29-67	1850	112.6	1060	143	1210	5.2	158	0.4
4	12-29-67	2005	158	1110	350	1208	5.21	210	0.6
5	12-29-67	2130	141	1100	305	1220	5.2	198	0.5
6	12-29-67	2230	176	1120	412	1530	7.15	247	0.8
7	12-29-67	2255	178	1110	405	1470	6.3	247	0.8
8	12-29-67	2315	163	1100	370	1310	5.65	228	0.7
9	1-03-68	1145	191.4	1110	384	1800	7.7	266	1.0
10	1-03-68	1300	185	1120	376	1400	6.05	257	1.0
11	1-03-68	1500	186	1120	370	1215	5.21	259	1.0
12	1-03-68	1900	193	1120	398	1820	7.75	270	0.8
13	1-06-68	2300	192	1130	470	1850	7.8	270	1.0
14	1-07-68	2110	193	1110	453	1830	7.8	270	1.1
15	1-09-68	0515	82	1086	225	1240	5.4	130	0.5
16	1-09-68	2200	143	1080	253	1070	4.6	201	0.5

TABLE 8

LOCAL NUCLEATE BOILING HEAT TRANSFER RESULTS

Run No.	T_{Sat}	G_{Hg}	L_{NB}	$q'' \times 10^{-5}$	x	h_{NB}	$(T_W - T_{Sat})$	A_R
1	975	81.52	2.3	1.13	0	1885	58	0
				1.87	0.176	2970	63	0.133
2	1060	115	1.8	0.96	0	2100	45.5	0
3	1060	113	2.1	1.08	0	2200	49	0
				1.82	0.493	3610	50.5	3.96
4	1110	158	2.4	0.70	0	2070	34	0
				0.875	0.108	2380	36.8	0.266
				1.31	0.304	3410	38.6	2.11
5	1100	141	1.5	0.86	0	1850	46.4	0
				2.02	0.32	4100	49.8	2.06
6	1120	176	3.2	0.537	0	2030	25.6	0
				0.92	0.146	3250	28	0.67
				1.07	0.242	3700	29	4.84
				1.49	0.467	4700	31.5	6.85
7	1110	178	3.5	0.434	0	1885	23	0
				0.615	0.121	2380	25.7	0.474
				1.07	0.262	3890	28.1	2.22
				1.415	0.421	4590	31	5.74
				1.64	0.597	5090	32.4	11.52
8	1100	163	2.9	0.546	0	1960	27	0
				0.92	0.221	2940	30.4	1.31
				1.48	0.369	4590	32.2	3.65
				1.82	0.6	5670	33	9.65

TABLE 8 (Cont.)

LOCAL NUCLEATE BOILING HEAT TRANSFER RESULTS

Run No.	T_{Sat}	G_{Hg}	L_{NB}	$q'' \times 10^{-5}$	x	h_{NB}	$(T_W - T_{Sat})$	A_R
9	1120	191.4	7.0	0.338	0	2510	12.8	0
				0.461	0.0616	3160	14.7	0.14
				0.555	0.115	3650	15.5	0.49
				0.671	0.154	3850	17.2	0.88
				0.84	0.231	4640	18.6	1.97
				1.132	0.338	5260	21.4	4.23
				1.345	0.477	6120	22.1	8.44
10	1120	185	4.3	0.42	0	2310	18.4	0
				0.82	0.08	3900	20.5	0.22
				1.07	0.216	4650	23	1.61
				1.35	0.376	5500	24.6	4.89
				1.85	0.535	6350	28.7	9.9
11	1120	186	4.3	0.46	0	2500	18.2	0
				0.995	0.13	4760	21	0.596
				1.25	0.254	5310	23.6	2.28
				1.68	0.398	6670	25.2	5.56
12	1120	193	3.7	0.28	0	2410	11.8	0
				0.41	0.05	3030	13.5	0.093
				0.57	0.171	3580	16.1	1.09
				0.86	0.31	4640	18.6	3.6
				1.47	0.456	6250	22.6	7.8
13	1130	192	7.0	0.301	0	2320	11.4	0
				0.398	0.023	3410	11.7	0.02
				0.515	0.066	3700	14.2	0.16
				0.648	0.174	3740	17.4	1.12
				0.84	0.235	4270	19.7	20.5
				1.15	0.326	5240	22.2	3.96
				1.45	0.477	6250	23.3	8.45
				1.71	0.65	7250	23.6	15.7

TABLE 8 (Cont.)

LOCAL NUCLEATE BOILING HEAT TRANSFER RESULTS

Run No.	T_{Sat}	G_{Hg}	L_{NB}	$q'' \times 10^{-5}$	x	h_{NB}	$(T_W - T_{Sat})$	A_R
14	1120	193	7.9	0.25	0	2210	11.2	0
				0.334	0.047	2850	11.7	0.082
				0.484	0.137	3200	15.1	0.7
				0.583	0.167	3550	16.5	1.03
				0.75	0.227	4300	17.4	1.91
				1.16	0.341	5850	19.8	4.31
				1.45	0.466	6750	21.6	8.05
				1.62	0.606	7080	23.1	13.6
15	1086	82	2.1	0.89	0	1870	47.4	0
				1.12	0.143	2250	49.6	0.088
				1.84	0.536	3460	53.3	1.24
16	1080	143	1.5	0.93	0	2300	40.6	0
				1.61	0.253	3890	42.5	1.42
				2.08	0.516	4750	44	5.9

TABLE 9

CRITICAL HEAT FLUX RESULTS

Run No.	Date	Time	G_{Hg}	T_{Sat}	x_c	$q''_c \times 10^{-5}$	A_{Rc}
1	12-29-67	1350	81.52	975	0.246	4.5	0.26
2	12-29-67	1800	115	1060	0.6	3.06	6.1
3	12-29-67	1850	112.6	1060	0.56	2.97	5.1
4	12-29-67	2005	158	1110	0.544	2.28	17.2
5	12-29-67	2130	141	1100	0.537	2.67	5.8
6	12-29-67	2230	176	1120	0.754	2.4	17.75
7	12-29-67	2255	178	1110	0.728	2.3	17.1
8	12-29-67	2315	163	1100	0.77	2.58	15.9
9	1-03-68	1145	191.4	1110	0.637	1.86	15.05
10	1-03-68	1300	185	1120	0.64	2.05	14.15
11	1-03-68	1500	186	1120	0.587	2.16	12.15
12	1-03-68	1900	193	1120	0.643	2.12	15.50
13	1-06-68	2300	192	1130	0.81	2.2	24.3
14	1-07-68	2110	193	1110	0.78	1.96	22.6
15	1-09-68	0515	82	1086	0.75	2.14	2.5
16	1-09-68	2200	143	1080	0.835	2.14	15.4

TABLE 10

LOCAL TRANSITION BOILING HEAT TRANSFER RESULTS

Run No.	G_{Hg}	T_{Sat}	$q''_{TB} \times 10^{-5}$	x_{TB}	h_{TB}	A_R	L_{TB}
1	81.52	975	3.14	0.667	2270	1.92	1.8
			1.61	0.965	610	4.0	
2	115	1060	1.68	0.93	1760	14.6	1.4
3	112.6	1060	1.78	0.92	1560	13.75	1.2
4	158	1110	2.12	0.695	8700	11.1	2.0
			2.01	0.837	5000	16.2	
5	141	1100	2.5	0.702	6670	9.9	1.8
			2.26	0.881	4200	15.6	
6	176	1120	2.12	0.852	5280	22.8	2.0
			1.78	0.951	2440	28.4	
7	178	1110	2.04	0.86	4590	23.8	1.9
8	163	1100	2.08	0.895	4350	21.4	1.4
9	191.4	1110	1.77	0.737	7150	20.1	2.8
			1.68	0.838	4080	26	
			1.6	0.896	2940	29.8	
			1.36	0.955	1940	33.7	

TABLE 10 (Cont.)

LOCAL TRANSITION BOILING HEAT TRANSFER RESULTS

Run No.	G_{Hg}	T_{Sat}	$q''_{TB} \times 10^{-5}$	x_{TB}	h_{TB}	A_R	L_{TB}
10	185	1120	1.97	0.75	6500	19.4	2.2
			1.88	0.80	4000	22.1	
			1.56	0.88	2250	26.7	
			1.23	0.96	1320	31.8	
11	186	1120	2.08	0.696	6400	17.1	2.7
			1.97	0.805	4020	22.9	
			1.87	0.86	2500	26.1	
			1.75	0.914	2150	29.5	
12	193	1120	1.95	0.76	5750	21.6	2.5
			1.92	0.877	3940	28.8	
			1.38	0.938	1530	33	
13	192	1130	1.95	0.88	4950	28.7	1.9
			1.51	0.97	1850	35	
14	193	1110	1.74	0.85	4380	28.7	2.1
			1.68	0.918	2750	31.2	
15	82	1086	1.84	0.92	2430	3.68	0.5
16	143	1080	2.1	0.94	3450	19.5	2.0

TABLE 11

LOCAL SUPERHEATED VAPOR RESULTS

Run No.	G_{Hg}	T_{Sat}	L	h_{SH}	q''_{SH}	L_{SH}	$(\Delta T)_{SH}$
1	81.5	975	5	45	5150	12.7	400
			6	38.2	2780		
			7	33.6	1550		
			8	38.7	1080		
			9	39.9	556		
			10	47.3	422		
2	115	1060	4	66	6520	13.4	304
			5	58	4130		
			6	56	2220		
			7	64	1590		
			8	67	855		
			9	69.7	550		
3	112.6	1060	3	63	9370	13.5	315
			4	65.5	6400		
			5	75.4	4550		
			6	76.6	2800		
			7	80	1775		
			8	84.3	909		
			9	87.6	554		
4	158	1110	6	72.6	8650	11	245
			7	69.4	5870		
			8	62.6	3380		
			9	67	2190		
			10	70.8	1462		
			11	71.8	796		

TABLE 11 (Cont.)

LOCAL SUPERHEATED VAPOR RESULTS

Run No.	G_{Hg}	T_{Sat}	L	h_{SH}	q''_{SH}	L_{SH}	$(\Delta T)_{SH}$
5	141	1100	5	76	9150		
			6	70.4	5490		
			7	71	3540		
			8	60.2	1770		
			9	56.4	1150		
			10	53.6	585		
			11	53	318		
6	176	1120	7	98.6	10600	10.0	253
			8	97.2	7240		
			9	93.6	4700		
			10	98	2800		
			11	91	1240		
			12	73	645		
7	178	1110	7	90.6	10500	9.9	245
			8	87	7840		
			9	90	5400		
			10	92.2	3510		
			11	101	2300		
			12	103	620		
8	163	1100	6	94	9840	11.0	262
			7	85	5540		
			8	80.4	3690		
			9	91	2050		
			10	101	1540		
			11	103	1025		
9	191.4	1110	12	146	11800	5.2	212
			13	145.2	6800		
			14	179	4410		
			15	182	2650		

TABLE 11 (Cont.)

LOCAL SUPERHEATED VAPOR RESULTS

Run No.	G_{Hg}	T_{Sat}	L	h_{SH}	q''_{SH}	L_{SH}	$(\Delta T)_{SH}$
10	185	1120	9	114.3	10680	8.3	250
			10	114	6600		
			11	116	4250		
			12	120.8	2805		
			13	127.4	1710		
			14	116.5	974		
11	186	1120	8	113	16400	8.3	261
			9	105	9350		
			10	107	5560		
			11	109	2990		
			12	118.5	1965		
			13	119.6	1250		
			14	94	890		
12	193	1120	8	113	12900	9.0	254
			9	105.4	9000		
			10	109	5760		
			11	111.1	3600		
			12	115	2150		
			13	118	1570		
			14	109	940		
13	192	1130	11	166.4	15700	6.5	222
			12	142	7600		
			13	176	5180		
			14	170	2900		
			15	165	1880		

TABLE 11 (Cont.)

LOCAL SUPERHEATED VAPOR RESULTS

Run No.	G_{Hg}	T_{Sat}	L	h_{SH}	q''_{SH}	L_{SH}	$(\Delta T)_{SH}$
14	193	1110	12	119	14150	5.0	206
			13	124	8950		
			14	138.6	6380		
			15	141.5	3380		
15	82	1086	4	52	7200	13.0	268
			5	44	4680		
			6	41.5	2790		
			7	43	1260		
			8	41.3	865		
16	143	1080	5	108.8	15700	12.0	281
			6	93	7300		
			7	78.5	4070		
			8	81.3	2540		
			9	81.4	1265		
			10	86	905		
			11	90.6	532		

TABLE 12

LOCAL PRESSURE DROP DATA IN TWO-PHASE REGION

Run No.	G_{Hg}	T_{Sat}	z	$-\left(\frac{dT}{dz}\right)$	$\left(\frac{dT}{dP}\right)_{Sat}$	$-\left(\frac{dP}{dz}\right)_{L}$	$-\left(\frac{dP}{dz}\right)_{TP}$	$\left(\frac{dx}{dz}\right)$	$-\left(\frac{dP}{dz}\right)^{*}_{TPm}$	$-\left(\frac{dP}{dz}\right)^{**}_{TPm}$	$-\left(\frac{dP}{dz}\right)^{*}_{TPf}$	$-\left(\frac{dP}{dz}\right)^{*}_{TPf}$	ϕ^{*}_{exp}	ϕ^{**}_{exp}	x	ϕ_H	ϕ_M
1	81.5	975	0.3		0.69	0.94×10^{-2}											
			1	0.715			1.03	0.288	0.214	0.107	0.81	0.92	86	95	0.176	56	80
			2	1.0			1.45	0.371	0.300	0.180	1.05	1.27	112	134	0.246	76	115
			3	1.5			2.18	0.48	0.474	0.603	1.7	1.57	183	168	0.667	170	312
			4	2.0			2.90	0.36	0.58	1.05	2.3	1.85	246	197	0.965	250	330
2	115	1060	0.4		0.66	1.40×10^{-2}											
			1	1.67			2.54	0.34	0.485	0.52	2.05	2.02	146	144	0.54	86	150
			2	2.5			3.80	0.46	0.85	1.15	2.95	2.65	208	188	0.72	110	202
			3	3.0			4.54	0.34	1.26	2.12	3.28	2.42	233	172	0.92	140	225
3	113	1060	0.4		0.66	1.38×10^{-2}											
			1	1.61			2.48	0.334	0.48	0.51	2.00	1.97	145	142	0.56	90	155
			2	2.42			3.73	0.44	0.81	1.10	2.92	2.63	206	190	0.76	115	210
			3	2.95			4.47	0.36	1.21	2.06	3.26	2.41	230	175	0.93	142	220
4	158	1110	0.4		0.64	2.14×10^{-2}											
			1	0.84			1.31	0.141	0.392	0.135	0.90	1.17	42	54	0.108	21	27
			2	1.5			2.34	0.166	0.56	0.39	1.80	1.94	85	90	0.304	48	74
			3	2.0			3.12	0.271	0.71	0.76	2.41	2.36	112	110	0.544	74	126
			4	2.5			3.90	0.244	0.98	1.51	2.98	2.40	135	117	0.837	106	180
			5	3.0			4.70	0.21	0.89	1.56	3.81	3.14	172	146	0.96	114	170

TABLE 12 (Cont.)

LOCAL PRESSURE DROP DATA IN TWO-PHASE REGION

Run No.	G_{Hg}	T_{Sat}	z	$-\left(\frac{dT}{dz}\right)$	$\left(\frac{dT}{dP}\right)_{Sat}$	$-\left(\frac{dP}{dz}\right)_{L}$	$-\left(\frac{dP}{dz}\right)_{TP}$	$\left(\frac{dx}{dz}\right)$	$-\left(\frac{dP}{dz}\right)^{*}_{TPm}$	$-\left(\frac{dP}{dz}\right)^{**}_{TPm}$	$-\left(\frac{dP}{dz}\right)^{*}_{TPf}$	$-\left(\frac{dP}{dz}\right)^{*}_{TPf}$	ϕ^{*}_{exp}	ϕ^{**}_{exp}	x	ϕ_H	ϕ_M
5	141	1100	0.4		0.65	1.73×10^{-2}											
			1	1.02			1.55	0.182	0.352	0.248	1.20	1.30	69.5	75	0.32	50	78
			2	1.7			2.58	0.222	0.69	0.715	1.89	1.86	109	107	0.537	74	128
			3	2.5			3.80	0.2	0.95	1.54	2.85	2.26	165	135	0.881	110	180
6	176	1120	0.8		0.64	2.64×10^{-2}											
			1	0.97			1.04	0.080	0.326	0.13	0.72	0.91	27.5	34.5	0.146	26	35
			2	1.5			2.34	0.101	0.54	0.34	1.80	2.00	66	75	0.242	38	58
			3	2.5			3.90	0.286	0.68	0.66	3.20	3.24	120	121	0.467	65	115
			4	3.5			5.47	0.182	0.84	1.31	4.63	4.16	170	156	0.754	98	170
			5	4.0			6.24	0.128	1.07	1.88	5.17	4.33	190	163	0.951	115	171
7	178	1110	0.8		0.64	2.68×10^{-2}											
			1	1.0			1.56	0.096	0.34	0.133	0.92	1.12	34	41	0.121	24	30
			2	1.5			2.04	0.117	0.52	0.312	1.52	1.73	56	64	0.262	42	62
			3	2.5			3.60	0.166	0.73	0.65	2.87	2.95	106	110	0.421	60	102
			4	3.5			5.17	0.238	1.04	1.20	4.13	3.97	154	147	0.597	80	140
			5	4.0			5.94	0.188	1.24	1.95	4.70	4.40	175	162	0.86	108	180
			5.5	4.0			5.94	0.11	1.11	1.87	4.83	4.07	180	158	0.94	114	175
8	163	1100	0.7		0.64	2.25×10^{-2}											
			1	0.86			1.34	0.11	0.47	0.26	0.87	1.08	38.5	48	0.221	37	51
			2	1.5			2.34	0.18	0.68	0.51	1.66	1.83	74	81	0.364	54	86
			3	2.5			3.90	0.21	0.83	0.97	3.03	2.93	135	131	0.600	82	140
			4	3.0			4.68	0.22	0.85	1.38	3.83	3.30	171	147	0.895	110	180

TABLE 12 (Cont.)

LOCAL PRESSURE DROP DATA IN TWO-PHASE REGION

Run No.	G_{Hg}	T_{Sat}	z	$-\left(\frac{dT}{dz}\right)$	$\left(\frac{dT}{dP}\right)_{Sat}$	$-\left(\frac{dP}{dz}\right)_{L}$	$-\left(\frac{dP}{dz}\right)_{TP}$	$\left(\frac{dx}{dz}\right)$	$-\left(\frac{dP}{dz}\right)^{*}_{TPm}$	$-\left(\frac{dP}{dz}\right)^{**}_{TPm}$	$-\left(\frac{dP}{dz}\right)^{*}_{TPf}$	$-\left(\frac{dP}{dz}\right)^{*}_{TPf}$	ϕ^{*}_{exp}	ϕ^{**}_{exp}	x	ϕ_H	ϕ_M
9	191	1110	1		0.64	3.14×10^{-2}											
			2	0.65			1.01	0.05	0.24	0.075	0.77	0.93	24	29.5	0.080	18	22
			3	0.96			1.50	0.04	0.26	0.113	1.24	1.38	39	44	0.115	23	28
			4	1.20			1.86	0.06	0.32	0.128	1.54	1.73	48	55	0.154	28	41
			5	1.75			2.74	0.09	0.45	0.24	2.30	2.50	72	79.5	0.231	38	58
			6	2.0			3.12	0.110	0.62	0.44	2.50	2.68	78	85	0.338	52	84
			7	2.5			3.90	0.134	0.70	0.68	3.20	3.22	100	102	0.477	68	113
			8	3.0			4.68	0.170	0.87	1.04	3.81	3.64	116	114	0.637	85	140
			9	3.5			5.46	0.07	0.99	1.50	4.45	3.96	139	126	0.838	104	180
			10	3.5			5.46	0.02	0.68	1.14	4.78	4.32	142	137	0.955	114	170
10	185	1120	1		0.64	2.95×10^{-2}											
			2	0.85			1.31	0.09	0.430	0.13	0.87	1.18	29	40	0.090	20	28
			3	1.5			2.34	0.143	0.705	0.36	1.63	1.98	54	66	0.216	38	54
			4	2.0			3.12	0.170	0.84	0.66	2.28	2.46	76	83	0.376	56	90
			5	2.5			3.90	0.185	0.96	0.99	2.94	2.90	97	98	0.535	72	121
			6	3.0			4.68	0.241	1.18	1.71	3.50	2.97	116	101	0.80	100	172
			7	3.0			4.68	0.091	0.86	1.52	3.82	3.16	126	108	0.96	115	170
11	186	1120	1		0.64	2.98×10^{-2}											
			2	0.95			1.48	0.110	0.49	0.182	0.99	1.30	33	43.5	0.130	25	34
			3	1.5			2.34	0.135	0.66	0.386	1.68	1.95	54	65	0.250	40	58
			4	2.0			3.12	0.166	0.82	0.68	2.30	2.44	76	81.5	0.398	58	96
			5	3.0			4.68	0.220	1.22	1.34	3.46	3.34	115	112	0.589	82	140
			6	3.5			5.47	0.143	1.08	1.62	4.39	3.85	141	128	0.800	100	170
			7	3.5			5.47	0.111	0.93	1.53	4.54	3.94	150	132	0.914	112	174

TABLE 12 (Cont.)

LOCAL PRESSURE DROP DATA IN TWO-PHASE REGION

Run No.	G_{Hg}	T_{Sat}	z	$-\left(\frac{dT}{dz}\right)$	$\left(\frac{dT}{dP}\right)_{Sat}$	$-\left(\frac{dP}{dz}\right)_{L}$	$-\left(\frac{dP}{dz}\right)_{TP}$	$\left(\frac{dx}{dz}\right)$	$-\left(\frac{dP}{dz}\right)^{*}_{TPm}$	$-\left(\frac{dP}{dz}\right)^{**}_{TPm}$	$-\left(\frac{dP}{dz}\right)^{*}_{TPf}$	$-\left(\frac{dP}{dz}\right)^{*}_{TPf}$	ϕ^{*}_{exp}	ϕ^{**}_{exp}	x	ϕ_H	ϕ_M
12	193	1120	0.8		0.64	3.18×10^{-2}											
			1	1.0			1.56	0.090	0.31	0.125	1.25	1.43	39	45	0.171	31	42
			2	1.5			2.34	0.125	0.50	0.33	1.80	2.01	56	63	0.310	48	70
			3	2.0			3.12	0.135	0.70	0.63	2.42	2.50	75	78.5	0.456	64	110
			4	3.0			4.70	0.168	0.79	1.02	3.96	3.68	122	115	0.701	92	160
			5	3.7			5.75	0.201	0.89	1.41	4.88	4.34	150	136	0.877	108	180
			6	4.3			6.70	0.158	1.14	1.91	5.50	4.80	170	151	0.95	114	170
13	192	1130	1		0.64	3.14×10^{-2}											
			2	0.6			0.94	0.050	0.24	0.072	0.70	0.87	22	27	0.080	18	24
			3	1.3			2.03	0.080	0.40	0.150	1.63	1.88	51	60	0.114	23	29
			4	1.8			2.80	0.085	0.52	0.286	2.28	2.51	72	80	0.235	38	58
			5	2.2			3.44	0.111	0.61	0.43	2.83	3.01	90	95	0.326	50	82
			6	2.7			3.72	0.153	0.80	0.75	3.32	3.37	106	108	0.477	68	114
			7	3.5			4.46	0.182	0.96	1.20	4.50	4.26	140	135	0.65	86	150
			8	4.0			6.25	0.162	0.85	1.30	5.40	4.95	168	157	0.81	101	180
			9	4.0			6.25	0.095	0.68	1.21	5.55	5.04	172	160	0.97	118	165
14	193	1110	1		0.64	3.2×10^{-2}											
			2	0.6			0.93	0.055	0.30	0.090	0.63	0.84	19.5	26	0.080	19	24
			3	1.0			1.56	0.053	0.34	0.130	1.22	1.43	38	44	0.137	26	36
			4	1.5			2.34	0.048	0.39	0.157	1.95	2.17	60	68	0.161	28	41
			5	1.8			2.81	0.072	0.43	0.25	2.38	2.76	74	85	0.227	38	58
			6	2.1			3.30	0.105	0.57	0.41	2.70	2.90	84	90	0.341	54	86
			7	2.7			4.70	0.115	0.68	0.63	3.50	3.57	105	111	0.466	67	115
			8	3.5			5.46	0.145	0.90	1.04	4.56	4.42	142	138	0.606	83	142
			9	4.0			6.25	0.166	1.14	1.65	5.11	4.60	160	143	0.78	98	172
			10				6.25	0.117	1.08	1.72	5.17	4.53	163	141	0.92	111	173

TABLE 12 (Cont.)

LOCAL PRESSURE DROP DATA IN TWO-PHASE REGION

Run No.	G_{Hg}	T_{Sat}	z	$-\left(\frac{dT}{dz}\right)$	$\left(\frac{dT}{dP}\right)_{Sat}$	$-\left(\frac{dP}{dz}\right)_{L}$	$-\left(\frac{dP}{dz}\right)_{TP}$	$\left(\frac{dx}{dz}\right)$	$-\left(\frac{dP}{dz}\right)^{*}_{TPm}$	$-\left(\frac{dP}{dz}\right)^{**}_{TPm}$	$-\left(\frac{dP}{dz}\right)^{*}_{TPf}$	$-\left(\frac{dP}{dz}\right)^{*}_{TPf}$	ϕ^{*}_{exp}	ϕ^{**}_{exp}	x	ϕ_H	ϕ_M
15	82	1086	0.4		0.66	0.126×10^{-2}											
			1	0.92			1.40	0.33	0.234	0.111	1.16	1.28	91	101	0.143	44	62
			2	1.23			1.88	0.41	0.34	0.21	1.54	1.69	121	133	0.535	81	135
			3	1.86			2.89	0.37	0.59	0.98	2.3	1.91	182	152	0.98	136	174
16	143	1080	0.5		0.66	1.75×10^{-2}											
			1	0.8			1.21	0.25	0.30	0.15	0.91	1.06	50	60.5	0.25	46	66
			2	1.5			2.28	0.306	0.43	0.43	1.85	1.85	101	101	0.52	78	130
			3	2.0			3.04	0.168	0.75	1.18	2.29	1.86	127	106	0.84	120	180
			4	2.5			3.8	0.098	0.78	1.32	3.0	2.48	165	141	0.96	130	171

*Values obtained by taking slip ratio equal to one (Homogeneous Model).

**Values obtained by taking slip ratio equal to $\left(\frac{\rho_V}{\rho_L}\right)$.

APPENDIX III

SNAP-8 SINGLE TUBE BOILER DATA REDUCTION RESULTS

COMPUTER OUTPUT TABLE NOMENCLATURE

CATSB	Reference Temperature Box "B" Cu-Const. T/C	°F
CATSC	Reference Temperature Box "C" Cu-Const. T/C	°F
DTPPEX	Pinch-point Temperature Difference at Boiler Exit	°F
DTS-AM	$T_{Shell}-T_{Amb.}$	°F
DTSH	Degree of Superheat at Boiler Exit	°F
GAHR	Axial Mercury Mass Velocity in the Helix Region	lb sec-ft^2
GAWC	Axial Mercury Mass Velocity in the Wire Coil Region	lb/ sec-ft^2
GPR1	Mass Velocity of NaK Flow	lb/sec-ft^2
GSEC	Superficial Mass Velocity of Mercury Flow	lb/sec-ft^2
NRELS	Superficial Reynolds Number	———
P3	Boiler Exit Pressure	psi
P5	Condenser Pressure, Top Drum	psi
P6	Pump Exit Pressure	psi
P8	Boiler Inlet Pressure	psi
QB	Heat Transferred after Boiling Inception	Kw
QNET	Net Thermal Power to Boiler Tube,	Kw
QSC	Heat Transferred in Subcooled Liquid Mercury	Kw
QT	Total Thermal Power to Boiler	Kw
Q/A	Average Test Section Heat Flux	Btu/hr-ft^2
T (1,2, 4,5,7,8, 10,11,13, 14,16,17, 19,20,21, 22,23)-A, B,C,D.E.	Boiler Shell T/C (station number) -Circular Location	°F
TBS(1,2--23)	Average Shell Temperature	°F
TAMB	Ambient Temperature	°F
TBEND (1,2)	Exit Bend Mercury Skin Temperature	°F
TBEW (1,2)	Boiler Exit Well Temperature	°F

TBIW (1,2)	Boiler Inlet Well Temperature	°F
TBI (1,3,6,9, 12,15,18)	Boiler Insert T/C (Station Number)	°F
TCLDW	Condenser Lower Drum Wall Temperature	°F
TCUDW	Condenser Upper Drum Wall Temperature	°F
TESAT	Boiler Exit Saturation Temperature	°F
TEXBHG	Mercury Temperature at Boiler Exit	°F
TFMD	NaK Flowmeter Duct Temperature	°F
TFMM	NaK Flowmeter Magnet Temperature	°F
TGHIN	Gas Heater Inlet Temperature	°F
TINW	Boiler Inlet Wall Temperature	°F
TNAKI (1,2)	NaK Inlet Well Temperature	°F
TNAKE (1,2)	NaK Exit Well Temperature	°F
TOUTW	Boiler Outlet Wall Temperature	°F
TPEW	Pump Exit Well Temperature	°F
TPG1	Gas Heater Inlet Pressure Transducer Temperature	°F
TPG2 (HI,LO)	NaK Pressure Gage Temperature	°F
TPG3	Boiler Exit Pressure Transducer Temperature	°F
TPG4 (HI,LO)	Vapor Venturi High and low Pressure Tranducer Temp.	°F
TPG5	Condenser Top Drum Pressure Transducer Temp.	°F
TPG6	Pump Exit Pressure Transducer Temperature	°F
TPG7 (HI,LO)	Liquid Venturi High and Low Pressure Transducer Temp.	°F
TPG8	Boiler Inlet Pressure Transducer Temperature	°F
TPHIW	Preheater Inlet Well Temperature	°F
TSING	Mercury Inlet Saturation Temperature	°F
TSNAKX	Static NaK Expansion Tank Temperature	°F
WHGLV	Mercury Flow Rate (Liquid Venturi)	lb/sec

WNAK	NaK Flow Rate (NaK Flowmeter)	lb/sec
X	Quality	———

SNAP-8 SINGLE-TUBE BOILER DATA REDUCTION

	291	292	299	300	301
	DATE	TIME	DRNAK	WHGLV	WHGVV
1	1,2297E 04	1,3500E 03	0,	1,9485E-01	0,
2	1,2297E 04	1,8000E 03	0,	2,8408E-01	0,
3	1,2297E 04	1,8500E 03	0,	2,7955E-01	0,
4	1,2297E 04	2,0050E 03	0,	3,9023E-01	0,
5	1,2297E 04	2,1300E 03	0,	3,4881E-01	0,
6	1,2297E 04	2,2300E 03	0,	4,3461E-01	0,
7	1,2297E 04	2,2550E 03	0,	4,3830E-01	0,
8	1,2297E 04	2,3150E 03	0,	4,0223E-01	0,
9	1,0380E 03	1,1450E 03	0,	4,7125E-01	0,
10	1,0380E 03	1,3000E 03	0,	4,9467E-01	0,
11	1,0380E 03	1,5000E 03	0,	4,9710E-01	0,
12	1,0380E 03	1,9000E 03	0,	4,7450E-01	0,
13	1,0680E 03	2,3000E 03	0,	4,7285E-01	0,
14	1,0780E 03	2,1100E 03	0,	4,7523E-01	0,
15	1,0980E 03	9,1500E 02	0,	1,9578E-01	0,
16	1,0980E 03	2,2000E 03	0,	5,5370E-01	0,

SNAP-8 SINGLE-TUBE BOILER DATA REDUCTION

	311	312	313	314	315
	P1	P3	P5	P6	P8
1	0.	7.4775E 01	2.9926E 01	2.4122E 02	1.3408E n2
2	0.	2.0239E 02	3.1148E 01	2.9926E 02	2.6076E n2
3	0.	1.9818E 02	3.1044E 01	2.9360E 02	2.5575E n2
4	0.	2.6187E 02	3.2864E 01	3.6338E 02	3.3427E n2
5	0.	2.4259E 02	3.5508E 01	3.4294E 02	3.0663E n2
6	0.	2.5648E 02	3.6218E 01	3.7368E 02	3.4259E n2
7	0.	2.5773E 02	3.6205E 01	3.6956E 02	3.3549E n2
8	0.	2.3704E 02	3.5919E 01	3.5941E 02	3.1739E n2
9	0.	2.6719E 02	3.2708E 01	4.4015E 02	3.2302E n2
10	0.	2.5079E 02	3.2812E 01	4.5076E 02	3.4455E n2
11	0.	2.6195E 02	2.7950E 01	4.5000E 02	3.4675E n2
12	0.	2.5397E 02	2.8132E 01	4.5272E 02	3.4565E n2
13	0.	2.6786E 02	2.9757E 01	4.3676E 02	3.5727E n2
14	0.	2.5608E 02	2.9913E 01	4.2309E 02	3.3855E n2
15	0.	2.5958E 02	3.0537E 01	3.8574E 02	2.9036E n2
16	0.	2.0047E 02	2.9731E 01	4.0279E 02	2.7617E n2

SNAP-8 SINGLE-TUBE BOILER DATA REDUCTION

	318	319	420	421	422
	CATSB	CATSC	TAMB	TBEND1	TBEND2
1	1.5000E 02	1.4892E 02	7.7111E 01	1.2938E 03	1.2883E 03
2	1.4976E 02	1.4996E 02	7.7111E 01	1.2906E 03	1.2847E 03
3	1.5018E 02	1.4883E 02	7.7111E 01	1.2919E 03	1.2889E 03
4	1.4900E 02	1.5040E 02	7.7111E 01	1.2789E 03	1.2751E 03
5	1.4942E 02	1.4902E 02	7.7111E 01	1.2921E 03	1.2887E 03
6	1.4942E 02	1.4975E 02	7.7111E 01	1.2852E 03	1.2818E 03
7	1.4883E 02	1.5020E 02	7.7111E 01	1.2771E 03	1.2741E 03
8	1.4983E 02	1.4971E 02	7.7111E 01	1.2784E 03	1.2724E 03
9	1.5000E 02	1.4929E 02	7.7111E 01	1.2478E 03	1.2430E 03
10	1.4904E 02	1.4912E 02	7.7111E 01	1.2811E 03	1.2768E 03
11	1.5052E 02	1.5032E 02	7.7111E 01	1.2970E 03	1.2919E 03
12	1.5004E 02	1.4987E 02	7.7111E 01	1.2871E 03	1.2820E 03
13	1.4362E 02	1.4900E 02	7.7111E 01	1.2603E 03	1.2561E 03
14	1.4929E 02	1.4954E 02	7.7111E 01	1.2359E 03	1.2311E 03
15	1.4987E 02	1.4992E 02	7.7111E 01	1.2750E 03	1.2703E 03
16	1.4971E 02	1.4883E 02	7.7111E 01	1.2638E 03	1.2591E 03

SNAP-8 SINGLE-TUBE BOILER DATA REDUCTION

	426 TFMM	427 TSWAKX	428 TRMIW	429 TCLDW	430 TCUBW
1	1.3652E 02	1.5000E 02	7.3114E 01	1.1130E 02	1.5000E 02
2	1.3687E 02	1.4978E 02	1.0204E 02	1.1370E 02	1.4978E 02
3	1.3390E 02	1.5016E 02	9.9893E 01	1.1563E 02	1.5016E 02
4	1.3217E 02	1.4913E 02	1.3383E 02	1.1996E 02	1.4913E 02
5	1.3080E 02	1.4949E 02	1.2541E 02	6.0742E 01	1.4949E 02
6	1.3114E 02	1.4949E 02	1.5023E 02	5.9833E 01	1.4949E 02
7	1.3038E 02	1.4899E 02	1.5007E 02	5.8485E 01	1.4899E 02
8	1.3103E 02	1.4986E 02	1.4146E 02	5.6939E 01	1.4986E 02
9	1.1317E 02	1.5000E 02	1.7013E 02	1.7621E 02	1.5000E 02
10	1.1521E 02	1.4917E 02	1.6834E 02	1.7472E 02	1.4917E 02
11	1.2163E 02	1.5068E 02	1.7275E 02	7.3138E 01	1.5068E 02
12	1.2001E 02	1.5005E 02	1.7175E 02	6.7555E 01	1.5005E 02
13	1.1707E 02	1.4880E 02	1.6594E 02	6.5523E 01	1.4880E 02
14	1.0769E 02	1.4935E 02	1.6483E 02	4.9682E 01	1.4935E 02
15	1.0971E 02	1.4989E 02	1.1987E 01	5.5932E 01	1.4989E 02
16	1.2366E 02	1.4975E 02	1.3444E 02	6.4235E 01	1.4975E 02

SNAP-8 SINGLE-TUBE BOILER DATA REDUCTION

	431 TPEW	432 TBIW1	434 TBIW2	434 TBEW1	435 TBEW2
1	5,3083E 02	3,7031E 02	3,1920E 02	1,2657E 03	1,2657E 03
2	1,4978E 02	3,2196E 02	2,8400E 02	1,2706E 03	1,2732E 03
3	1,5016E 02	3,2314E 02	2,8078E 02	1,2787E 03	1,2787E 03
4	1,4913E 02	2,9600E 02	2,6471E 02	1,2717E 03	1,2713E 03
5	1,4949E 02	3,0770E 02	2,6979E 02	1,2823E 03	1,2814E 03
6	1,4949E 02	2,9929E 02	2,6397E 02	1,2806E 03	1,2797E 03
7	1,4899E 02	3,0030E 02	2,6276E 02	1,2728E 03	1,2720E 03
8	1,4986E 02	3,0454E 02	2,6879E 02	1,2720E 03	1,2733E 03
9	4,0827E 02	3,2036E 02	3,2022E 02	1,2487E 03	1,2487E 03
10	4,0986E 02	3,1973E 02	3,1853E 02	1,2743E 03	1,2743E 03
11	4,1944E 02	3,2203E 02	3,2136E 02	1,2928E 03	1,2928E 03
12	4,1855E 02	3,2108E 02	3,1996E 02	1,2815E 03	1,2828E 03
13	4,0611E 02	3,1722E 02	3,1602E 02	1,2590E 03	1,2595E 03
14	3,9502E 02	3,1427E 02	3,1320E 02	1,2350E 03	1,2354E 03
15	3,6439E 02	3,8300E 02	3,8140E 02	1,2546E 03	1,2554E 03
16	3,8099E 02	3,3755E 02	3,3042E 02	1,2574E 03	1,2583E 03

SNAP-8 SINGLE-TUBE BOILER DATA REDUCTION

	436	437	438	439	440
	TNAKI1	TNAKI2	TNAKE1	TNAKE2	TGHIN
1	1.3520E 03	1.3513E 03	1.2717E 03	1.2691E 03	1.2530E 03
2	1.3315E 03	1.3323E 03	1.2230E 03	1.2226E 03	1.2068E 03
3	1.3336E 03	1.3344E 03	1.2272E 03	1.2276E 03	1.2119E 03
4	1.3139E 03	1.3135E 03	1.1781E 03	1.1768E 03	1.1653E 03
5	1.3333E 03	1.3325E 03	1.2031E 03	1.2027E 03	1.1857E 03
6	1.3225E 03	1.3230E 03	1.1708E 03	1.1708E 03	1.1563E 03
7	1.3155E 03	1.3146E 03	1.1630E 03	1.1626E 03	1.1490E 03
8	1.3142E 03	1.3184E 03	1.1720E 03	1.1720E 03	1.1575E 03
9	1.2913E 03	1.2930E 03	1.1183E 03	1.1179E 03	1.1066E 03
10	1.3235E 03	1.3244E 03	1.1462E 03	1.1449E 03	1.1288E 03
11	1.3370E 03	1.3379E 03	1.1613E 03	1.1609E 03	1.1464E 03
12	1.3518E 03	1.3513E 03	1.1513E 03	1.1509E 03	1.1339E 03
13	1.3042E 03	1.3054E 03	1.1301E 03	1.1297E 03	1.1172E 03
14	1.2885E 03	1.2902E 03	1.1144E 03	1.1140E 03	1.0983E 03
15	1.3333E 03	1.3329E 03	1.1119E 03	1.1116E 03	1.0782E 03
16	1.3046E 03	1.3055E 03	1.1732E 03	1.1723E 03	1.1587E 03

SNAP-8 SINGLE-TUBE BOILER DATA REDUCTION

	441	442	443	444	445
	TFMD	TRG1	TPG2HI	TPG2LO	TPG3
1	1.2589E 03	1.0022E 02	9.7111E 01	1.0067E 02	9.2667E 01
2	1.2116E 03	9.5556E 01	9.1111E 01	9.3333E 01	9.1111E 01
3	1.2174E 03	9.6382E 01	9.2827E 01	9.4604E 01	9.1049E 01
4	1.1587E 03	9.5383E 01	9.4000E 01	9.2667E 01	9.1778E 01
5	1.1925E 03	9.8815E 01	9.6594E 01	9.6593E 01	9.3481E 01
6	1.1518E 03	9.9259E 01	9.7926E 01	9.8370E 01	9.4815E 01
7	1.1537E 03	9.8741E 01	9.7407E 01	9.7852E 01	9.5185E 01
8	1.1509E 03	1.0052E 02	9.6219E 01	1.0007E 02	9.6074E 01
9	1.1083E 03	9.2687E 01	9.0889E 01	9.1778E 01	9.1778E 01
10	1.1322E 03	9.2704E 01	9.1370E 01	9.3148E 01	9.0926E 01
11	1.1490E 03	9.6471E 01	9.4249E 01	9.5138E 01	9.4249E 01
12	1.1386E 03	9.4942E 01	9.2720E 01	9.4053E 01	9.2276E 01
13	1.1193E 03	8.8778E 01	8.6111E 01	9.1889E 01	8.8333E 01
14	1.1009E 03	8.0000E 01	7.8667E 01	8.3556E 01	7.8667E 01
15	1.0976E 03	8.6778E 01	8.3667E 01	8.9000E 01	8.5000E 01
16	1.1621E 03	9.5963E 01	9.3296E 01	9.7741E 01	9.3741E 01

SNAP-8 SINGLE-TUBE BOILER DATA REDUCTION

	446	447	448	449	450
	TPG4HI	TPG4LO	TPG5	TPG6	TPG8
1	1.0289E 02	1.0378E 02	1.7930E 02	1.0289E 02	9.9333E 01
2	9.7333E 01	9.7383E 01	1.7574E 02	1.1022E 02	9.2889E 01
3	9.9930E 01	9.6827E 01	1.8122E 02	1.1277E 02	9.3716E 01
4	9.8000E 01	9.6687E 01	1.8362E 02	1.1478E 02	9.3556E 01
5	1.0197E 02	9.8815E 01	1.1732E 02	1.1819E 02	9.5259E 01
6	1.0326E 02	1.0015E 02	1.0815E 02	1.1775E 02	9.6593E 01
7	1.0319E 02	1.0052E 02	1.0630E 02	1.1986E 02	9.7487E 01
8	1.0407E 02	1.0274E 02	1.0452E 02	1.2377E 02	9.7487E 01
9	1.2747E 03	1.2782E 03	2.0435E 02	9.3111E 01	9.2667E 01
10	1.3037E 03	1.3071E 03	2.0612E 02	9.4481E 01	9.4037E 01
11	1.3185E 03	1.3220E 03	1.0847E 02	9.6471E 01	9.5582E 01
12	1.3114E 03	1.3157E 03	1.0020E 02	9.5387E 01	9.4942E 01
13	1.2850E 03	1.2884E 03	9.4111E 01	9.3222E 01	9.1444E 01
14	1.2689E 03	1.2732E 03	7.9256E 01	8.2667E 01	8.2222E 01
15	1.3039E 03	1.3082E 03	7.6111E 01	8.4556E 01	8.0556E 01
16	1.2863E 03	1.2898E 03	9.7741E 01	9.5074E 01	9.6852E 01

SNAP-8 SINGLE-TUBE BOILER DATA REDUCTION

	451	452	453	514	515
	TPG7MI	TPG7LO	TPME	TBI-1	TBI-3
1	9.5638E 02	9.5778E 01	4.0022E 02	9.3844E 02	9.6652E n2
2	1.1349E 03	9.7778E 01	3.3159E 02	9.1975E 02	1.0695E n3
3	1.2757E 03	9.9089E 01	3.3607E 02	9.1752E 02	1.0618E n3
4	1.3057E 03	1.0022E 02	3.0291E 02	7.6072E 02	1.1142E n3
5	1.4099E 03	1.0459E 02	3.1748E 02	7.9504E 02	1.0967E n3
6	1.4650E 03	1.0593E 02	3.0765E 02	7.0804E 02	1.1148E n3
7	1.4545E 03	1.0674E 02	3.0758E 02	7.0504E 02	1.1157E n3
8	1.2373E 03	1.0763E 02	3.0758E 02	7.2933E 02	1.1038E n3
9	1.1502E 03	8.4222E 01	3.4318E 02	7.2642E 02	1.1182E n3
10	1.1854E 03	8.3370E 01	3.3958E 02	7.4415E 02	1.1197E n3
11	1.1509E 03	8.5804E 01	3.4271E 02	7.4956E 02	1.1266E n3
12	1.4070E 03	8.5184E 01	3.4824E 02	7.2181E 02	1.1232E n3
13	7.4713E 02	8.4788E 01	3.3330E 02	6.6000E 02	1.1237E n3
14	7.6851E 02	7.6889E 01	3.3841E 02	6.5743E 02	1.1184E n3
15	7.0467E 02	8.1000E 01	4.4678E 02	8.9868E 02	1.0828E n3
16	9.5613E 02	9.1074E 01	3.6837E 02	8.2688E 02	1.0799E n3

SNAP-8 SINGLE-TUBE BOILER DATA REDUCTION

	516	517	518	519	520
	TBI-6	TBI-9	TBI-12	TBI-15	TBI-18
1	1,0853E 03	1,2580E 03	1,3121E 03	1,3321E 03	1,3389E 03
2	1,2061E 03	1,2827E 03	1,3083E 03	1,3182E 03	1,3243E 03
3	1,2099E 03	1,2839E 03	1,3099E 03	1,3194E 03	1,3246E 03
4	1,1098E 03	1,1731E 03	1,2505E 03	1,2833E 03	1,2977E 03
5	1,0993E 03	1,2495E 03	1,2934E 03	1,3130E 03	1,3199E 03
6	1,1119E 03	1,1108E 03	1,2328E 03	1,2800E 03	1,2983E 03
7	1,1107E 03	1,1056E 03	1,2209E 03	1,2698E 03	1,2920E 03
8	1,0978E 03	1,1778E 03	1,2515E 03	1,2834E 03	1,2978E 03
9	1,1144E 03	1,1104E 03	1,1111E 03	1,1026E 03	1,1609E 03
10	1,1159E 03	1,1103E 03	1,1433E 03	1,2392E 03	1,2778E 03
11	1,1208E 03	1,1103E 03	1,1896E 03	1,2666E 03	1,2989E 03
12	1,1182E 03	1,1157E 03	1,1648E 03	1,2529E 03	1,2886E 03
13	1,1192E 03	1,1103E 03	1,1150E 03	1,1096E 03	1,2177E 03
14	1,1155E 03	1,1150E 03	1,1100E 03	1,1020E 03	1,1109E 03
15	1,1556E 03	1,2652E 03	1,2953E 03	1,3091E 03	1,3147E 03
16	1,0724E 03	1,2022E 03	1,2562E 03	1,2801E 03	1,2899E 03

SNAP-8 SINGLE-TUBE BOILER DATA REDUCTION

	522	524	526	647	648
	TNAKI	WNAK	TNAKE	T1A	T1B
1	1.3520E 03	1.9452E 00	1.2704E 03	1.2669E 03	1.2577E 03
2	1.3319E 03	1.9882E 00	1.2232E 03	1.2270E 03	1.2445E 03
3	1.3340E 03	1.9634E 00	1.2274E 03	1.2244E 03	1.2427E 03
4	1.3137E 03	2.0271E 00	1.1774E 03	1.1759E 03	1.1781E 03
5	1.3329E 03	2.0128E 00	1.2029E 03	1.1994E 03	1.2027E 03
6	1.3228E 03	2.0397E 00	1.1709E 03	1.1660E 03	1.1640E 03
7	1.3151E 03	2.0466E 00	1.1628E 03	1.1609E 03	1.1588E 03
8	1.3153E 03	2.0132E 00	1.1720E 03	1.1673E 03	1.1681E 03
9	1.2921E 03	1.9180E 00	1.1181E 03	1.1244E 03	1.1326E 03
10	1.3239E 03	1.8982E 00	1.1456E 03	1.1542E 03	1.1607E 03
11	1.3375E 03	1.9244E 00	1.1611E 03	1.1672E 03	1.1745E 03
12	1.3315E 03	1.8856E 00	1.1511E 03	1.1538E 03	1.1641E 03
13	1.3048E 03	1.9291E 00	1.1299E 03	1.1308E 03	1.1369E 03
14	1.2894E 03	1.9329E 00	1.1142E 03	1.1171E 03	1.1244E 03
15	1.3331E 03	7.3198E-01	1.1116E 03	1.1163E 03	1.1430E 03
16	1.3051E 03	2.0285E 00	1.1727E 03	1.1757E 03	1.1859E 03

SNAP-8 SINGLE-TUBE BOILER DATA REDUCTION

	649	650	651	652	653
	T1C	T2A	T2B	T2C	T4A
1	1,2752E 03	1,2869E 03	1,3118E 03	1,2818E 03	1,2933E 03
2	1,1901E 03	1,2743E 03	1,2637E 03	1,2727E 03	1,3097E 03
3	1,2105E 03	1,2751E 03	1,2863E 03	1,2760E 03	1,3143E 03
4	1,1784E 03	1,2088E 03	1,2212E 03	1,2148E 03	1,2272E 03
5	1,1979E 03	1,2485E 03	1,2703E 03	1,2457E 03	1,2711E 03
6	1,1589E 03	1,2036E 03	1,2271E 03	1,2087E 03	1,2195E 03
7	1,1630E 03	1,1958E 03	1,2159E 03	1,2001E 03	1,2126E 03
8	1,1706E 03	1,2078E 03	1,2386E 03	1,2138E 03	1,2245E 03
9	1,0986E 03	1,1485E 03	1,1518E 03	1,1490E 03	1,1547E 03
10	1,1207E 03	1,1806E 03	1,1862E 03	1,1837E 03	1,1948E 03
11	1,1280E 03	1,1979E 03	1,2020E 03	1,1979E 03	1,2121E 03
12	1,1262E 03	1,1892E 03	1,1935E 03	1,1896E 03	1,2025E 03
13	1,1218E 03	1,1611E 03	1,1664E 03	1,1637E 03	1,1693E 03
14	1,1065E 03	1,1483E 03	1,1488E 03	1,1462E 03	1,1498E 03
15	1,0889E 03	1,1787E 03	9,1056E 02	1,1767E 03	1,2233E 03
16	1,1650E 03	1,2115E 03	1,2175E 03	1,2154E 03	1,2372E 03

SNAP-8 SINGLE-TUBE BOILER DATA REDUCTION

	654	655	656	657	658
	T4B	T4C	T5A	T5B	T5C
1	1.2933E 03	1.2918E 03	1.3359E 03	1.3289E 03	1.3352E 03
2	1.3088E 03	1.3113E 03	1.3179E 03	1.3135E 03	1.3187E 03
3	1.3121E 03	1.3138E 03	1.3204E 03	1.3152E 03	1.3217E 03
4	1.2330E 03	1.2350E 03	1.2510E 03	1.2525E 03	1.2552E 03
5	1.2741E 03	1.2746E 03	1.3046E 03	1.3013E 03	1.3051E 03
6	1.2202E 03	1.2276E 03	1.2383E 03	1.2373E 03	1.2456E 03
7	1.2120E 03	1.2182E 03	1.2310E 03	1.2268E 03	1.2389E 03
8	1.2307E 03	1.2340E 03	1.2491E 03	1.2519E 03	1.2547E 03
9	1.1566E 03	1.1559E 03	1.1607E 03	1.1590E 03	1.1639E 03
10	1.1939E 03	1.1948E 03	1.2093E 03	1.2066E 03	1.2113E 03
11	1.2128E 03	1.2134E 03	1.2296E 03	1.2251E 03	1.2303E 03
12	1.2037E 03	1.2043E 03	1.2200E 03	1.2156E 03	1.2190E 03
13	1.1711E 03	1.1714E 03	1.1787E 03	1.1774E 03	1.1811E 03
14	1.1504E 03	1.1519E 03	1.1562E 03	1.1541E 03	1.1602E 03
15	1.2333E 03	1.2221E 03	1.2902E 03	1.2885E 03	1.2906E 03
16	1.2427E 03	1.2378E 03	1.2675E 03	1.2667E 03	1.2644E 03

SNAP-8 SINGLE-TUBE BOILER DATA REDUCTION

	659	660	661	662	663
	T5D	T5E	T5F	T7A	T7B
1	1.3338E 03	1.3354E 03	1.3360E 03	1.3385E 03	1.3409E 03
2	1.3362E 03	1.3199E 03	1.3179E 03	1.3205E 03	1.3198E 03
3	1.3366E 03	1.3220E 03	1.3200E 03	1.3222E 03	1.3224E 03
4	1.2657E 03	1.2619E 03	1.2532E 03	1.2742E 03	1.2811E 03
5	1.3260E 03	1.3110E 03	1.3078E 03	1.3180E 03	1.3195E 03
6	1.2593E 03	1.2519E 03	1.2457E 03	1.2631E 03	1.2695E 03
7	1.2485E 03	1.2409E 03	1.2382E 03	1.2523E 03	1.2553E 03
8	1.2753E 03	1.2626E 03	1.2548E 03	1.2783E 03	1.2826E 03
9	1.1564E 03	1.1687E 03	1.1623E 03	1.1686E 03	1.1738E 03
10	1.2124E 03	1.2120E 03	1.2106E 03	1.2257E 03	1.2307E 03
11	1.2324E 03	1.2381E 03	1.2321E 03	1.2492E 03	1.2504E 03
12	1.2213E 03	1.2222E 03	1.2209E 03	1.2381E 03	1.2389E 03
13	1.2023E 03	1.1843E 03	1.1808E 03	1.1887E 03	1.1953E 03
14	1.1884E 03	1.1609E 03	1.1587E 03	1.1642E 03	1.1681E 03
15	1.3177E 03	1.2951E 03	1.2924E 03	1.3039E 03	1.3057E 03
16	1.2688E 03	1.2732E 03	1.2688E 03	1.2901E 03	1.2906E 03

SNAP-8 SINGLE-TUBE BOILER DATA REDUCTION

	664	665	666	667	668
	T7C	T8A	T8B	T8C	T10A
1	1,3386E 03	1,3417E 03	1,3406E 03	1,3355E 03	1,3407E 03
2	1,3202E 03	1,3211E 03	1,3209E 03	1,3163E 03	1,3217E 03
3	1,3219E 03	1,3237E 03	1,3226E 03	1,3184E 03	1,3224E 03
4	1,2781E 03	1,3016E 03	1,3009E 03	1,2955E 03	1,3042E 03
5	1,3177E 03	1,3213E 03	1,3202E 03	1,3151E 03	1,3216E 03
6	1,2725E 03	1,2939E 03	1,2965E 03	1,2912E 03	1,3098E 03
7	1,2584E 03	1,2787E 03	1,2819E 03	1,2762E 03	1,3035E 03
8	1,2831E 03	1,3019E 03	1,3025E 03	1,2971E 03	1,3034E 03
9	1,1746E 03	1,1800E 03	1,1859E 03	1,1777E 03	1,1920E 03
10	1,2513E 03	1,2489E 03	1,2556E 03	1,2457E 03	1,2769E 03
11	1,2545E 03	1,2716E 03	1,2806E 03	1,2732E 03	1,3041E 03
12	1,2417E 03	1,2586E 03	1,2672E 03	1,2590E 03	1,2886E 03
13	1,1934E 03	1,2015E 03	1,2112E 03	1,2012E 03	1,2268E 03
14	1,1584E 03	1,1730E 03	1,1784E 03	1,1736E 03	1,1875E 03
15	1,3044E 03	1,3082E 03	1,3068E 03	1,3014E 03	1,3091E 03
16	1,2898E 03	1,2924E 03	1,2934E 03	1,2872E 03	1,2933E 03

SNAP-8 SINGLE-TUBE BOILER DATA REDUCTION

	669	670	671	672	673
	T10B	T10C	T11A	T11B	T11C
1	1.3406E 03	1.3413E 03	1.3415E 03	1.3418E 03	1.3409E 03
2	1.3229E 03	1.3219E 03	1.3228E 03	1.3228E 03	1.3219E 03
3	1.3228E 03	1.3227E 03	1.3227E 03	1.3236E 03	1.3222E 03
4	1.3028E 03	1.3049E 03	1.3044E 03	1.3053E 03	1.3049E 03
5	1.3211E 03	1.3223E 03	1.3215E 03	1.3228E 03	1.3214E 03
6	1.3102E 03	1.3101E 03	1.3109E 03	1.3118E 03	1.3109E 03
7	1.3021E 03	1.3042E 03	1.3041E 03	1.3051E 03	1.3050E 03
8	1.3046E 03	1.3033E 03	1.3054E 03	1.3046E 03	1.3049E 03
9	1.1980E 03	1.1958E 03	1.2113E 03	1.2152E 03	1.2134E 03
10	1.2845E 03	1.2777E 03	1.3053E 03	1.3062E 03	1.3044E 03
11	1.3083E 03	1.3052E 03	1.3237E 03	1.3237E 03	1.3237E 03
12	1.2950E 03	1.2886E 03	1.3149E 03	1.3154E 03	1.3145E 03
13	1.2277E 03	1.2232E 03	1.2446E 03	1.2506E 03	1.2457E 03
14	1.1919E 03	1.1917E 03	1.2047E 03	1.2086E 03	1.2080E 03
15	1.3086E 03	1.3086E 03	1.3098E 03	1.3103E 03	1.3107E 03
16	1.2928E 03	1.2928E 03	1.2948E 03	1.2949E 03	1.2944E 03

SNAP-8 SINGLE-TUBE BOILER DATA REDUCTION

	674	675	676	677	678
	T11D	T11E	T11F	T13A	T13B
1	1,3421E 03	1,3408E 03	1,3425E 03	1,3367E 03	1,3421E 03
2	1,3234E 03	1,3222E 03	1,3226E 03	1,3187E 03	1,3223E 03
3	1,3248E 03	1,3225E 03	1,3229E 03	1,3190E 03	1,3226E 03
4	1,3046E 03	1,3052E 03	1,3038E 03	1,3020E 03	1,3048E 03
5	1,3234E 03	1,3217E 03	1,3221E 03	1,3186E 03	1,3218E 03
6	1,3124E 03	1,3109E 03	1,3120E 03	1,3077E 03	1,3126E 03
7	1,3043E 03	1,3058E 03	1,3035E 03	1,3017E 03	1,3054E 03
8	1,3051E 03	1,3044E 03	1,3056E 03	1,3000E 03	1,3062E 03
9	1,2102E 03	1,2104E 03	1,2095E 03	1,2247E 03	1,2330E 03
10	1,3050E 03	1,3065E 03	1,3030E 03	1,3059E 03	1,3104E 03
11	1,3220E 03	1,3231E 03	1,3232E 03	1,3204E 03	1,3253E 03
12	1,3142E 03	1,3104E 03	1,3130E 03	1,3129E 03	1,3178E 03
13	1,2452E 03	1,2510E 03	1,2420E 03	1,2611E 03	1,2724E 03
14	1,2031E 03	1,2090E 03	1,2034E 03	1,2185E 03	1,2281E 03
15	1,3104E 03	1,3101E 03	1,3096E 03	1,3057E 03	1,3110E 03
16	1,2941E 03	1,2939E 03	1,2937E 03	1,2899E 03	1,2952E 03

SNAP-8 SINGLE-TUBE BOILER DATA REDUCTION

	679	680	681	682	683
	T13C	T14A	T14B	T14C	T16A
1	1.3418E 03	1.3427E 03	1.3423E 03	1.3425E 03	1.3429E 03
2	1.3240E 03	1.3228E 03	1.3237E 03	1.3239E 03	1.3226E 03
3	1.3243E 03	1.3232E 03	1.3245E 03	1.3233E 03	1.3242E 03
4	1.3060E 03	1.3056E 03	1.3058E 03	1.3072E 03	1.3055E 03
5	1.3235E 03	1.3228E 03	1.3237E 03	1.3230E 03	1.3238E 03
6	1.3130E 03	1.3131E 03	1.3140E 03	1.3133E 03	1.3142E 03
7	1.3057E 03	1.3072E 03	1.3060E 03	1.3078E 03	1.3065E 03
8	1.3057E 03	1.3057E 03	1.3063E 03	1.3064E 03	1.3069E 03
9	1.2339E 03	1.2529E 03	1.2591E 03	1.2590E 03	1.2750E 03
10	1.3111E 03	1.3139E 03	1.3135E 03	1.3136E 03	1.3128E 03
11	1.3253E 03	1.3283E 03	1.3259E 03	1.3270E 03	1.3274E 03
12	1.3182E 03	1.3193E 03	1.3188E 03	1.3199E 03	1.3203E 03
13	1.2700E 03	1.2886E 03	1.2899E 03	1.2895E 03	1.2926E 03
14	1.2286E 03	1.2457E 03	1.2507E 03	1.2479E 03	1.2633E 03
15	1.3118E 03	1.3120E 03	1.3112E 03	1.3126E 03	1.3126E 03
16	1.2951E 03	1.2953E 03	1.2949E 03	1.2958E 03	1.2959E 03

SNAP-8 SINGLE-TUBE BOILER DATA REDUCTION

	684	685	686	687	688
	T16B	T16C	T17A	T17B	T17C
1	1.3424E 03	1.3439E 03	1.3423E 03	1.3362E 03	1.3424E 03
2	1.3240E 03	1.3230E 03	1.3246E 03	1.3178E 03	1.3234E 03
3	1.3241E 03	1.3243E 03	1.3249E 03	1.3188E 03	1.3250E 03
4	1.3075E 03	1.3059E 03	1.3074E 03	1.3008E 03	1.3063E 03
5	1.3237E 03	1.3234E 03	1.3241E 03	1.3182E 03	1.3246E 03
6	1.3140E 03	1.3142E 03	1.3148E 03	1.3088E 03	1.3149E 03
7	1.3076E 03	1.3074E 03	1.3072E 03	1.3009E 03	1.3069E 03
8	1.3059E 03	1.3077E 03	1.3063E 03	1.3002E 03	1.3064E 03
9	1.2765E 03	1.2785E 03	1.2812E 03	1.2745E 03	1.2804E 03
10	1.3136E 03	1.3141E 03	1.3151E 03	1.3085E 03	1.3140E 03
11	1.3281E 03	1.3279E 03	1.3276E 03	1.3213E 03	1.3277E 03
12	1.3210E 03	1.3208E 03	1.3206E 03	1.3143E 03	1.3207E 03
13	1.2933E 03	1.2930E 03	1.2946E 03	1.2879E 03	1.2939E 03
14	1.2677E 03	1.2678E 03	1.2775E 03	1.2709E 03	1.2768E 03
15	1.3133E 03	1.3130E 03	1.3128E 03	1.3070E 03	1.3129E 03
16	1.2960E 03	1.2963E 03	1.2957E 03	1.2895E 03	1.2958E 03

SNAP-8 SINGLE-TUBE BOILER DATA REDUCTION

	689	690	691	692	693
	T17D	T17E	T17F	T19A	T19B
1	1.3439E 03	1.3428E 03	1.3442E 03	1.3430E 03	1.3441E 03
2	1.3249E 03	1.3233E 03	1.3244E 03	1.3240E 03	1.3238E 03
3	1.3235E 03	1.3254E 03	1.3238E 03	1.3248E 03	1.3250E 03
4	1.3073E 03	1.3061E 03	1.3077E 03	1.3069E 03	1.3070E 03
5	1.3235E 03	1.3246E 03	1.3239E 03	1.3240E 03	1.3246E 03
6	1.3139E 03	1.3148E 03	1.3144E 03	1.3143E 03	1.3153E 03
7	1.3084E 03	1.3076E 03	1.3075E 03	1.3083E 03	1.3072E 03
8	1.3070E 03	1.3079E 03	1.3061E 03	1.3083E 03	1.3067E 03
9	1.2811E 03	1.2806E 03	1.2806E 03	1.2827E 03	1.2832E 03
10	1.3142E 03	1.3143E 03	1.3141E 03	1.3159E 03	1.3156E 03
11	1.3284E 03	1.3285E 03	1.3279E 03	1.3279E 03	1.3282E 03
12	1.3213E 03	1.3219E 03	1.3209E 03	1.3213E 03	1.3211E 03
13	1.2940E 03	1.2955E 03	1.2948E 03	1.2957E 03	1.2954E 03
14	1.2770E 03	1.2783E 03	1.2774E 03	1.2786E 03	1.2787E 03
15	1.3140E 03	1.3137E 03	1.3127E 03	1.3136E 03	1.3137E 03
16	1.2965E 03	1.2965E 03	1.2960E 03	1.2960E 03	1.2961E 03

SNAP-8 SINGLE-TUBE BOILER DATA REDUCTION

	694	695	696	697	698
	T19C	T20A	T20B	T20C	T21A
1	1,3433E 03	1,3438E 03	1,3441E 03	1,3375E 03	1,3454E 03
2	1,3248E 03	1,3234E 03	1,3256E 03	1,3185E 03	1,3255E 03
3	1,3246E 03	1,3255E 03	1,3241E 03	1,3201E 03	1,3250E 03
4	1,3077E 03	1,3067E 03	1,3084E 03	1,3014E 03	1,3083E 03
5	1,3234E 03	1,3252E 03	1,3242E 03	1,3193E 03	1,3250E 03
6	1,3142E 03	1,3158E 03	1,3149E 03	1,3096E 03	1,3157E 03
7	1,3091E 03	1,3078E 03	1,3090E 03	1,3029E 03	1,3085E 03
8	1,3078E 03	1,3077E 03	1,3076E 03	1,3024E 03	1,3075E 03
9	1,2831E 03	1,2829E 03	1,2834E 03	1,2777E 03	1,2849E 03
10	1,3154E 03	1,3153E 03	1,3153E 03	1,3100E 03	1,3173E 03
11	1,3283E 03	1,3296E 03	1,3295E 03	1,3233E 03	1,3295E 03
12	1,3219E 03	1,3225E 03	1,3229E 03	1,3167E 03	1,3228E 03
13	1,2952E 03	1,2955E 03	1,2968E 03	1,2911E 03	1,2971E 03
14	1,2791E 03	1,2806E 03	1,2806E 03	1,2741E 03	1,2808E 03
15	1,3148E 03	1,3147E 03	1,3146E 03	1,3085E 03	1,3159E 03
16	1,2964E 03	1,2971E 03	1,2971E 03	1,2910E 03	1,2969E 03

SNAP-8 SINGLE-TUBE BOILER DATA REDUCTION

	699	700	701	702	703
	T21B	T21C	T22A	T22B	T22C
1	1,3436E 03	1,3450E 03	1,3440E 03	1,3439E 03	1,3370E 03
2	1,3254E 03	1,3242E 03	1,3263E 03	1,3241E 03	1,3122E 03
3	1,3258E 03	1,3254E 03	1,3249E 03	1,3257E 03	1,3172E 03
4	1,3079E 03	1,3071E 03	1,3087E 03	1,3065E 03	1,2887E 03
5	1,3246E 03	1,3255E 03	1,3250E 03	1,3258E 03	1,3117E 03
6	1,3152E 03	1,3158E 03	1,3148E 03	1,3160E 03	1,3000E 03
7	1,3097E 03	1,3077E 03	1,3101E 03	1,3080E 03	1,2893E 03
8	1,3092E 03	1,3072E 03	1,3088E 03	1,3075E 03	1,2914E 03
9	1,2854E 03	1,2846E 03	1,2845E 03	1,2841E 03	1,2885E 03
10	1,3173E 03	1,3185E 03	1,3164E 03	1,3159E 03	1,3227E 03
11	1,3294E 03	1,3295E 03	1,3312E 03	1,3298E 03	1,3400E 03
12	1,3227E 03	1,3283E 03	1,3241E 03	1,3231E 03	1,3365E 03
13	1,2967E 03	1,2983E 03	1,2979E 03	1,2970E 03	1,3105E 03
14	1,2817E 03	1,2818E 03	1,2817E 03	1,2809E 03	1,2758E 03
15	1,3168E 03	1,3159E 03	1,3158E 03	1,3153E 03	1,2234E 03
16	1,2969E 03	1,2970E 03	1,2978E 03	1,2969E 03	1,2294E 03

SNAP-8 SINGLE-TUBE BOILER DATA REDUCTION

	704	705	706	724	725
	T23E	T23B	T23E	TBS1	TBS2
1	1.3446E 03	1.3448E 03	1.3449E 03	1.2666E 03	1.2935E n3
2	1.3256E 03	1.3249E 03	1.3267E 03	1.2205E 03	1.2702E n3
3	1.3268E 03	1.3253E 03	1.3266E 03	1.2259E 03	1.2791E n3
4	1.3080E 03	1.3074E 03	1.3094E 03	1.1775E 03	1.2149E n3
5	1.3260E 03	1.3253E 03	1.3257E 03	1.2000E 03	1.2531E n3
6	1.3162E 03	1.3156E 03	1.3169E 03	1.1663E 03	1.2131E n3
7	1.3094E 03	1.3084E 03	1.3109E 03	1.1611E 03	1.2040E n3
8	1.3089E 03	1.3075E 03	1.3100E 03	1.1687E 03	1.2200E n3
9	1.2863E 03	1.2857E 03	1.2860E 03	1.1185E 03	1.1491E n3
10	1.3183E 03	1.3172E 03	1.3176E 03	1.1452E 03	1.1835E n3
11	1.3299E 03	1.3297E 03	1.3311E 03	1.1566E 03	1.1993E n3
12	1.3233E 03	1.3231E 03	1.3244E 03	1.1480E 03	1.1908E n3
13	1.2972E 03	1.2970E 03	1.2982E 03	1.1296E 03	1.1637E n3
14	1.2827E 03	1.2825E 03	1.2824E 03	1.1160E 03	1.1461E n3
15	1.3172E 03	1.3170E 03	1.3174E 03	1.1161E 03	1.0870E n3
16	1.2970E 03	1.2973E 03	1.2981E 03	1.1758E 03	1.2148E n3

SNAP-8 SINGLE-TUBE BOILER DATA REDUCTION

	726	727	728	729	730
	TBS4	TBS5	TBS7	TBS8	TBS10
1	1,2928E 03	1,3343E 03	1,3396E 03	1,3393E 03	1,3409E 03
2	1,3099E 03	1,3207E 03	1,3202E 03	1,3194E 03	1,3222E 03
3	1,3134E 03	1,3226E 03	1,3221E 03	1,3215E 03	1,3226E 03
4	1,2317E 03	1,2566E 03	1,2778E 03	1,2993E 03	1,3040E 03
5	1,2733E 03	1,3092E 03	1,3184E 03	1,3188E 03	1,3217E 03
6	1,2224E 03	1,2463E 03	1,2684E 03	1,2939E 03	1,3101E 03
7	1,2143E 03	1,2375E 03	1,2553E 03	1,2783E 03	1,3033E 03
8	1,2297E 03	1,2581E 03	1,2814E 03	1,3005E 03	1,3038E 03
9	1,1557E 03	1,1682E 03	1,1724E 03	1,1812E 03	1,1953E 03
10	1,1945E 03	1,2104E 03	1,2292E 03	1,2494E 03	1,2797E 03
11	1,2128E 03	1,2304E 03	1,2514E 03	1,2751E 03	1,3059E 03
12	1,2035E 03	1,2198E 03	1,2396E 03	1,2616E 03	1,2910E 03
13	1,1706E 03	1,1841E 03	1,1925E 03	1,2046E 03	1,2239E 03
14	1,1507E 03	1,1681E 03	1,1669E 03	1,1750E 03	1,1906E 03
15	1,2262E 03	1,2957E 03	1,3047E 03	1,3048E 03	1,3088E 03
16	1,2392E 03	1,2682E 03	1,2902E 03	1,2910E 03	1,2929E 03

SNAP-8 SINGLE-TUBE BOILER DATA REDUCTION

	731	732	733	734	735
	TBS11	TBS13	TBS14	TBS16	TBS17
1	1.3416E 03	1.3402E 03	1.3425E 03	1.3430E 03	1.3420E 03
2	1.3220E 03	1.3216E 03	1.3235E 03	1.3234E 03	1.3231E 03
3	1.3230E 03	1.3220E 03	1.3237E 03	1.3242E 03	1.3236E 03
4	1.3047E 03	1.3043E 03	1.3065E 03	1.3063E 03	1.3059E 03
5	1.3221E 03	1.3213E 03	1.3231E 03	1.3237E 03	1.3232E 03
6	1.3115E 03	1.3111E 03	1.3135E 03	1.3141E 03	1.3136E 03
7	1.3046E 03	1.3043E 03	1.3070E 03	1.3072E 03	1.3064E 03
8	1.3050E 03	1.3039E 03	1.3065E 03	1.3068E 03	1.3057E 03
9	1.2127E 03	1.2305E 03	1.2570E 03	1.2750E 03	1.2797E 03
10	1.3058E 03	1.3091E 03	1.3137E 03	1.3134E 03	1.3134E 03
11	1.3231E 03	1.3237E 03	1.3264E 03	1.3278E 03	1.3269E 03
12	1.3144E 03	1.3183E 03	1.3193E 03	1.3207E 03	1.3199E 03
13	1.2466E 03	1.2678E 03	1.2894E 03	1.2930E 03	1.2933E 03
14	1.2061E 03	1.2251E 03	1.2481E 03	1.2662E 03	1.2763E 03
15	1.3101E 03	1.3095E 03	1.3119E 03	1.3130E 03	1.3122E 03
16	1.2943E 03	1.2934E 03	1.2953E 03	1.2962E 03	1.2950E 03

SNAP-8 SINGLE-TUBE BOILER DATA REDUCTION

	736	737	738	739	740
	TBS19	TBS20	TBS21	TBS22	TBS23
1	1.3435E 03	1.3418E 03	1.3447E 03	1.3417E 03	1.3447E 03
2	1.3242E 03	1.3225E 03	1.3251E 03	1.3209E 03	1.3257E 03
3	1.3248E 03	1.3233E 03	1.3254E 03	1.3226E 03	1.3262E 03
4	1.3072E 03	1.3055E 03	1.3077E 03	1.3013E 03	1.3083E 03
5	1.3240E 03	1.3229E 03	1.3250E 03	1.3208E 03	1.3257E 03
6	1.3146E 03	1.3135E 03	1.3156E 03	1.3103E 03	1.3159E 03
7	1.3082E 03	1.3065E 03	1.3086E 03	1.3025E 03	1.3096E 03
8	1.3070E 03	1.3059E 03	1.3080E 03	1.3025E 03	1.3088E 03
9	1.2830E 03	1.2813E 03	1.2849E 03	1.2857E 03	1.2860E 03
10	1.3156E 03	1.3135E 03	1.3170E 03	1.3184E 03	1.3177E 03
11	1.3281E 03	1.3275E 03	1.3294E 03	1.3337E 03	1.3303E 03
12	1.3213E 03	1.3207E 03	1.3229E 03	1.3279E 03	1.3236E 03
13	1.2954E 03	1.2945E 03	1.2967E 03	1.3018E 03	1.2975E 03
14	1.2788E 03	1.2784E 03	1.2814E 03	1.2795E 03	1.2825E 03
15	1.3140E 03	1.3126E 03	1.3160E 03	1.2849E 03	1.3172E 03
16	1.2961E 03	1.2950E 03	1.2970E 03	1.2747E 03	1.2972E 03

SNAP-8 SINGLE-TUBE BOILER DATA REDUCTION

	742	751	752	753	755
	DTS-AM	QT	QNET	TSING	TINW
1	1.2542E 03	3.5331E 01	2.7943E 01	9.5290E 02	3.4476E n2
2	1.2356E 03	4.8078E 01	4.0878E 01	1.0641E 03	3.0298E n2
3	1.2374E 03	4.6554E 01	3.9337E 01	1.0608E 03	3.0196E n2
4	1.2064E 03	6.1340E 01	5.4436E 01	1.1119E 03	2.8036E n2
5	1.2303E 03	5.8102E 01	5.0996E 01	1.0942E 03	2.8874E n2
6	1.2084E 03	6.8868E 01	6.1923E 01	1.1173E 03	2.8163E n2
7	1.2005E 03	6.9176E 01	6.2382E 01	1.1127E 03	2.8303E n2
8	1.2066E 03	6.4068E 01	5.7162E 01	1.1011E 03	2.8661E n2
9	1.1471E 03	7.3985E 01	6.7672E 01	1.1047E 03	3.2029E n2
10	1.1952E 03	7.5085E 01	6.8293E 01	1.1185E 03	3.1913E n2
11	1.2116E 03	7.5396E 01	6.8440E 01	1.1199E 03	3.2169E n2
12	1.2030E 03	7.5545E 01	6.8675E 01	1.1192E 03	3.2052E n2
13	1.1567E 03	7.4833E 01	6.8329E 01	1.1261E 03	3.1662E n2
14	1.1423E 03	7.5057E 01	6.8792E 01	1.1147E 03	3.1373E n2
15	1.2020E 03	3.5974E 01	2.9119E 01	1.0836E 03	3.8220E n2
16	1.1998E 03	3.9504E 01	5.2707E 01	1.0743E 03	3.3698E n2

SNAP-8 SINGLE-TUBE BOILER DATA REDUCTION

	757	785	766	769	771
	TOUTW	QSC	QB	X	TESAT
1	1,2557E 03	4,0447E 00	2,3899E 01	9,3598E-01	9,6612E 02
2	1,2719E 03	7,3843E 00	3,3494E 01	9,0685E-01	1,0208E 03
3	1,2787E 03	7,2445E 00	3,2092E 01	8,8276E-01	1,0173E 03
4	1,2715E 03	1,1085E 01	4,8351E 01	8,5754E-01	1,0648E 03
5	1,2818E 03	9,5987E 00	4,1400E 01	9,1483E-01	1,0514E 03
6	1,2801E 03	1,2406E 01	4,9217E 01	8,7963E-01	1,0613E 03
7	1,2724E 03	1,2422E 01	4,9910E 01	8,7886E-01	1,0621E 03
8	1,2726E 03	1,1191E 01	4,5971E 01	8,8137E-01	1,0476E 03
9	1,2487E 03	1,2634E 01	5,5038E 01	9,0087E-01	1,0683E 03
10	1,2743E 03	1,2425E 01	5,5868E 01	9,4875E-01	1,0575E 03
11	1,2928E 03	1,2474E 01	5,5966E 01	9,4543E-01	1,0649E 03
12	1,2822E 03	1,2956E 01	5,5720E 01	9,0672E-01	1,0596E 03
13	1,2993E 03	1,3085E 01	5,5240E 01	9,0249E-01	1,0688E 03
14	1,2952E 03	1,3010E 01	5,5782E 01	9,0605E-01	1,0613E 03
15	1,2950E 03	4,6989E 00	2,4418E 01	9,6061E-01	1,0633E 03
16	1,2578E 03	8,9103E 00	4,3797E 01	9,5307E-01	1,0194E 03

SNAP-8 SINGLE-TUBE BOILER DATA REDUCTION

	777	793	794	795	801
	GPRI	GSEC	GAHR	GAWC	NRELS
1	3,1318E 02	7,9502E 01	8,9964E 01	8,1180E 01	8,5117E 03
2	3,2011E 02	1,1603E 02	1,3116E 02	1,1836E 02	1,2944E 04
3	3,1611E 02	1,1418E 02	1,2907E 02	1,1647E 02	1,2725E 04
4	3,2637E 02	1,5938E 02	1,8018E 02	1,6258E 02	1,8034E 04
5	3,2390E 02	1,4246E 02	1,6105E 02	1,4533E 02	1,6043E 04
6	3,2840E 02	1,7751E 02	2,0067E 02	1,8107E 02	2,0091E 04
7	3,2951E 02	1,7902E 02	2,0237E 02	1,8261E 02	2,0250E 04
8	3,2413E 02	1,6428E 02	1,8572E 02	1,6758E 02	1,8508E 04
9	3,0881E 02	1,9248E 02	2,1759E 02	1,9634E 02	2,1766E 04
10	3,0529E 02	1,8570E 02	2,0993E 02	1,8943E 02	2,1010E 04
11	3,0983E 02	1,8670E 02	2,1105E 02	1,9045E 02	2,1151E 04
12	3,0360E 02	1,9380E 02	2,1909E 02	1,9769E 02	2,1936E 04
13	3,1059E 02	1,9313E 02	2,1832E 02	1,9701E 02	2,1914E 04
14	3,1120E 02	1,9410E 02	2,1942E 02	1,9800E 02	2,1960E 04
15	1,1785E 02	7,9982E 01	9,0398E 01	8,1567E 01	9,0062E 03
16	3,2627E 02	1,4446E 02	1,6331E 02	1,4736E 02	1,6138E 04

SNAP-8 SINGLE-TUBE BOILER DATA REDUCTION

	806	821	822	823
	J/A	TEXBHG	DTPPEX	DTSH
1	3,3976E 04	1,2657E 03	7,9004E 01	3,9963E 02
2	4,9703E 04	1,3251E 03	6,6438E-01	3,0423E 02
3	4,7529E 04	1,3327E 03	-6,4903E 00	3,1539E 02
4	6,6187E 04	1,3101E 03	-1,7970E 00	2,4522E 02
5	6,2005E 04	1,3250E 03	6,8568E-01	2,7368E 02
6	7,5291E 04	1,3148E 03	1,1578E 00	2,5351E 02
7	7,5787E 04	1,3068E 03	2,8165E 00	2,4465E 02
8	6,9502E 04	1,3101E 03	-1,8057E 00	2,6248E 02
9	8,2280E 04	1,2806E 03	5,4338E 00	2,1225E 02
10	8,3035E 04	1,3074E 03	1,0294E 01	2,4989E 02
11	8,3214E 04	1,3257E 03	4,5202E 00	2,6085E 02
12	8,3500E 04	1,3139E 03	9,6895E 00	2,5429E 02
13	8,3074E 04	1,2911E 03	6,4178E 00	2,2227E 02
14	8,3542E 04	1,2689E 03	1,5680E 01	2,0558E 02
15	3,5399E 04	1,3319E 03	-1,4653E 01	2,6856E 02
16	6,4085E 04	1,3005E 03	-3,0259E 00	2,8114E 02

REFERENCES

1. Gordon, R. and Slone, H. O. "SNAP-8 Development Status." AIAA Specialists Conference on Rankine Space Power Systems, pp. 102-138, 1965.

2. Thur, G. M. "SNAP-8 Power Conversion System Assessment." Intersociety Energy Conversion Engineering Conference, pp. 329-337, 1968.

3. Brooks, R. D. SNAP-8 Refractory Boiler Development Monthly Progress Report. General Electric Company, SPPS-MSD, Contract NAS 3-10610, August 1967.

4. Poppendiek, H. F. Investigation of the Boiler Conditioning and Heat Transfer Characteristics in a Mercury-Tantalum System Monthly Technical Progress Report. Geoscience, LTD; Aerojet Contract Number OP119224, October 1967.

5. Bond, J. A. and Converse, G. L. Vaporization of High Temperature Potassium in Forced Convection at Saturation Temperatures of 1800°F to 2100°F. NASA CR-843, July 1967.

6. Peterson, J. R. High Performance Once-Through Boiling of Potassium in Single Tubes at Saturation Temperatures of 1500°F to 1750°F. NASA CR-842, August 1967.

7. Brooks, R. D. SNAP-8 Refractory Boiler Development Monthly Progress Report. General Electric Company, SPPS-MSD; Contract NAS 3-10610; October, November, and December 1967.

8. Chang, Y. P. "Wave Theory of Heat Transfer in Film Boiling." Journal of Heat Transfer, Vol. 81, February 1959.

9. Zuber, N. Hydrodynamic Aspects of Boiling Heat Transfer. Ph.D. Thesis, University of California, Los Angeles, June 1959.

10. Berenson, P. J. "Film Boiling Heat Transfer from a Horizontal Surface." Journal of Heat Transfer, Vol. 83, No. 3, 1961.

11. Sellers, A. J.; Thur, G. M.; and Wong, M. K. Recent Development in Heat Transfer and Development of the Mercury Boiler for the SNAP-8 System. Aerojet-General Corporation, SNAP-8 Division, 1965.

12. "Properties of Fluids." Design Manual H-100. Aerojet-General Corporation, January 1967.

13. Converse, G. L. and Hsia, E. S. Thermal and Hydraulic Analysis for Advanced SNAP-8 Boilers. General Electric Company, SPPS HTC-11, January 1969.

14. Lyon, R. N. "Liquid Metal Heat Transfer Coefficients." Trans. AIChE, 47:75-79, 1965.

REFERENCES (Cont'd)

15. Lubarsky, B. and Kaufmann, S. J. Review of Experimental Investigation of Liquid-Metal Heat Transfer. NASA Report No. 1270, 1956.

16. Atomics International. SNAP-8 Systems Improvement Program Progress Report. July-September 1966, Vol. I. NAA-SR-12256, January 1967.

17. Kutateladze, S. S. Liquid Metal Heat Transfer Media. New York: Consultants Bureau, Inc., 1959.

18. Cichelli, M. T. and Bonilla, C. F. Trans. AIChE, 41:755-787, 1945.

19. Zuber, N. "Stability of Boiling Heat Transfer." Trans. ASME, Vol. 80-C, April 1958.

20. Merte, J., Jr. and Clark, J. A. Study of Pool Boiling in an Accelerating System. ASME Paper 60-HT-22, 1960.

21. Longo, J. Alkali Metal Boiling and Condensing Investigation Quarterly Progress Report No. 6. General Electric Company, SPPS, Contract NAS 3-2528, April 1964.

22. Brooks, R. D. Alkali Metal Boiling and Condensing Investigation, Vol. I. General Electric Company, SPPS, Contract NAS 5-681, June 1964.

23. Levy, S. "Steam Slip-Theoretical Prediction from Momentum Model." Journal of Heat Transfer, 82:113, May 1960.

24. Kutateladze, S. S. Fundamentals of Heat Transfer. New York: Academic Press, Inc., 1963.

25. Costello, C. P. and Adams, J. M. "Burnout Heat Fluxes in Pool Boiling at High Accelerations." International Heat Transfer Conference, Paper No. 30, August 1961.

26. Veiskim, C. M. and Siegel, R. "An Experimental Study of Boiling in Reduced and Zero-Gravity Fields." Trans. ASME, 83-C:243-253, August 1961.

27. Converse, G. L. Air Heating Experiments. General Electric Company, SPPS HTC-12, April 1969.

28. Sams, E. W. "Heat Transfer and Pressure Drop Characteristics of Wire-Coil Type Turbulence Promoters." Reactor Heat Transfer Conference. U.S. AEC, November 1956.

29. Converse, G. L. and Tedesco, D. P. Air Water Experiment - Transparent Plastic Tube. General Electric Company, SPPS HTC-10, March 1968.

30. Hsu, C. J. "Heat Transfer in a Round Tube with Sinusoidal Wall Heat Flux Distribution." AIChE Journal, 11:690-695, 1965.

31. Stein, R. P. "Improved Design Predictions Through Liquid-Metal Heat Transfer Research." Power Reactor Technology, 9:174-179, 1966.

32. Nunge, R. J. and Gill, W. N. "An Analytical Study of Laminar Counter-flow Double-Pipe Heat Exchangers." AIChE Journal, 12:279-289, 1966.

33. Dwyer, O. E. "Heat Transfer to Fluids Flowing Through Pipes, Annuli and Parallel Plates" USAEC Report No. BNL-6692, 1963.

34. Martinelli, R. C. and Nelson, D. B. "Prediction of Pressure Drop During Forced-Circulation Boiling of Water." Trans. ASME, 70:695, 1948.

35. Fauske, H. K. Contribution to the Theory of Two-Phase, One-Component Critical Flow. ANL-6633, October 1962.

36. Martinelli, R. C.; Boelter, L. M. K.; Taylor, T. H. M.; Thompson, E. G.; and Morrin, E. H. "Isothermal Pressure Drop for Two-Phase, Two-Component Flow in a Horizontal Pipe." Trans. ASME, 66:139, 1944.

37. Lockhart, R. W. and Martinelli, R. C. "Proposed Correlation of Data for Isothermal Two-Phase Two-Component Flow in Pipes." Chem. Engr. Prog., 45:39, 1949.

DISTRIBUTION LIST

TOPICAL AND FINAL REPORTS

NAS 3-10610

National Aeronautics and Space Administration
Washington, D.C. 20546
Attention: P.R. Miller (RNP)
James J. Lynch (RNP)
George C. Deutsch (RR)
H. Rochen (RNP)
J. Gangler

National Aeronautics and Space Administration
Lewis Research Center
21000 Brookpark Road
Cleveland, Ohio 44135
Attention: Librarian
G.M. Ault, MS 3-13
P.L. Stone, MS 106-1 (2 copies)
Technology Utilization, MS 3-19
Report Control Office, MS 5-5
R.L. Davies, MS 106-1 (2 copies)
V.F. Hlavin, MS 3-14
E.R. Furman, MS 500-202
M.J. Saari, MS 500-202
R. English, MS 500-201
L. Schopen, MS 77-3
N.T. Saunders, MS 105-1
~~J.E. Dilley, MS 500-309~~ Howard E. Hinckley (500-206)
R.H. Johns, MS 49-2
D.A. Spera, MS 49-2
H.C. Slone, MS 500-201

National Aeronautics and Space Administration
Scientific and Technical Information Facility
P. O. Box 33
College Park, Maryland 20740
Attention: Acquisitions Branch
(SQT-34054) 2 copies

National Aeronautics and Space Administration
Ames Research Center
Moffett Field, California 94035
Attention: Librarian

National Aeronautics and Space Administration
Goddard Space Flight Center
Greenbelt, Maryland 20771
Attention: Librarian

National Aeronautics and Space Administration
Langley Research Center
Hampton, Virginia 23365
Attention: Librarian

National Aeronautics and Space Administration
Manned Spacecraft Center
Houston, Texas 77001
Attention: Librarian

National Aeronautics and Space Administration
George C. Marshall Space Flight Center
Huntsville, Alabama 35812
Attention: Librarian

National Aeronautics and Space Administration
Jet Propulsion Laboratory
4800 Oak Grove Drive
Pasadena, California 91103
Attention: Librarian

National Bureau of Standards
Washington, D.C. 20546
Attention: Librarian

AFSC
Aeronautical Systems Division
Wright-Patterson Air Force Base, Ohio 45433
Attention: Charles Armbruster (ASRPP-10)
T. Cooper
Librarian

Army Ordnance Frankford Arsenal
Bridesburg Station
Philadelphia, Pennsylvania 19137
Attention: Librarian

U.S. Atomic Energy Commission
Technical Information Service Extension
P. O. Box 62
Oak Ridge, Tennessee 37831

U.S. Atomic Energy Commission
Washington, D.C. 20545
Attention: M.J. Whitman
J.M. Simmons
C. Johnson (SNSO)
G. Newby (SNSO)

Bureau of Weapons
Research and Engineering
Materials Division
Washington, D.C. 20546
Attention: Librarian

Argonne National Laboratory
9700 South Cass Avenue
Argonne, Illinois 60440
Attention: Librarian

Battelle Memorial Institute
505 King Avenue
Columbus, Ohio 43201
Attention: R.T. Niehoff, DMIC
Librarian

Brookhaven National Laboratory
Upton, Long Island, New York 11973
Attention: Librarian
Dr. D.H. Gurinsky

Oak Ridge National Laboratory
Oak Ridge, Tennessee 37831
Attention: J. Devan
R. MacPherson
Librarian

U.S. Naval Research Laboratory
Washington, D.C. 20390
Attention: Librarian

Aerojet-General Corporation
Electronics Division
Azusa, California 91703
Attention: Librarian

AiResearch Manufacturing Company
Division of the Garrett Corporation
Sky Harbor Airport
403 South 36th Street
Phoenix, Arizona 85034
Attention: Librarian

AirResearch Manufacturing Company
Division of the Garrett Corporation
9851-9951 Sepulveda Boulevard
Los Angeles, California 90009
Attention: Librarian

AVCO
Research & Advanced Development Department
201 Lowell Street
Wilmington, Massachusetts 01887
Attention: Librarian

Babcock & Wilcox Company
Research Center
Alliance, Ohio 44601
Attention: Librarian

Battelle-Northwest Labs
P. O. Box 999
Richland, Washington 99352

The Bendix Corporation
Research Laboratories Division
Southfield, Michigan
Attention: Librarian

The Boeing Company
Seattle, Washington 98100
Attention: Librarian

Chance Vought Aircraft, Inc.
P. O. Box 5907
Dallas, Texas 75222
Attention: Librarian

Clevite Corporation
Mechanical Research Division
540 East 105th Street
Cleveland, Ohio 44108
Attention: N.C. Beerli
Project Administrator

Convair Astronautics
5001 Kerrny Villa Road
San Diego, California 92111
Attention: Librarian

Douglas Aircraft Company, Inc.
Missile and Space Systems Division
3000 Ocean Park Boulevard
Santa Monica, California
Attention: Librarian

Engineering Library
Fairchild Hiller
Republic Aviation Corporation
Farmingdale, Long Island, New York
Attention: Librarian

Ford Motor Company
Aeronautronics
Newport Beach, California 92660
Attention: Librarian

General Dynamics Corporation
General Atomic Division
John Jay Hopkins Lab.
P. O. Box 608
San Diego, California 92112
Attention: Librarian

General Dynamics/Fort Worth
P. O. Box 748
Fort Worth, Texas 76101
Attention: Librarian

General Electric Company
Missile and Space Vehicle Department
3198 Chestnut Street
Philadelphia, Pennsylvania 19104
Attention: Librarian

General Electric Company
Vallecitos Atomic Laboratory
Pleasanton, California 94566
Attention: Librarian

General Electric Company
Evendale, Ohio 45215
Technical Information Center
Building 700, Mail Drop N-32

General Motors Corporation
Allison Division
Indianapolis, Indiana 46206
Attention: Librarian

Grumman Aircraft
Bethpage, New York
Attention: Librarian

Hamilton Standard
Division of United Aircraft Corporation
Windsor Locks, Connecticut 06096
Attention: Librarian

Hughes Aircraft Company
Engineering Division
Culver City, California 90230
Attention: Librarian

IIT Research Institute
10 West 35th Street
Chicago, Illinois 60616
Attention: Librarian

Lawrence Radiation Lab.
Livermore, California 94550
Attention: Librarian

Lockheed Missiles and Space Division
Lockheed Aircraft Corporation
Sunnyvale, California 90221
Attention: Librarian

Los Alamos Scientific Laboratory
University of California
Los Alamos, New Mexico
Attention: Librarian

Materials Research & Development
Manlabs, Incorporated
21 Erie Street
Cambridge, Massachusetts 02139

Marquardt Aircraft Co.
P. O. Box 2013
Van Nuys, California
Attention: Librarian

The Martin Company
Nuclear Division
P. O. Box 5042
Baltimore, Maryland 21203
Attention: Librarian

Martin Marietta Corporation
Metals Technology Laboratory
Wheeling, Illinois 60090

Materials Research Corporation
Orangeburg, New York 10962
Attention: Librarian

McDonnell Aircraft
St. Louis, Missouri 03166
Attention: Librarian

MSA Research Corporation
Callery, Pennsylvania 16024
Attention: Librarian

National Research Corporation
70 Memorial Drive
Cambridge, Massachusetts 02142
Attention: Librarian

North American Rockwell
Los Angeles Division
Los Angeles, California 90009
Attention: Librarian

North American Rockwell Corporation
Atomics International Division
8900 DeSota Avenue
Canoga Park, California 91304
Attention: T.A. Moss
P.B. Ferry
Librarian

Philco Corporation
Aeronutronics
Newport Beach, California 92665
Attention: Librarian

Republic Aviation Corporation
Farmingdale, Long Island, New York 11735
Attention: Librarian

Rocketdyne
Canoga Park, California 91303
Attention: Librarian

Sandia Corporation
P. O. Box 5800
Albuquerque, New Mexico 87116
Attention: Librarian
Don Johnson

Solar
2200 Pacific Highway
San Diego, California 92112
Attention: Librarian

Southwest Research Institute
8500 Culebra Road
San Antonio, Texas 78228
Attention: Librarian

Superior Tube Company
Norristown, Pennsylvania 19404
Attention: Librarian

TRW, Inc.
23555 Euclid Avenue
Cleveland, Ohio 44117
Attention: Librarian
K. Sheffler

Union Carbide Corporation
Materials Systems Division
1020 West Park
Kokomo, Indiana 46901
Attention: Librarian
Technology Department

Union Carbide Metals
Niagara Falls, New York 14300
Attention: Librarian

Union Carbide Corporation
Parma Research Center
P. O. Box 6115
Cleveland, Ohio 44101
Attention: Technical Info. Services

United Aircraft Corporation
Pratt & Whitney Aircraft Division
400 Main Street
East Hartford, Connecticut 06108
Attention: Librarian

Wah Chang Corporation
Albany, Oregon 97321
Attention: Librarian

Westinghouse Electric Corporation
Astronuclear Laboratory
P. O. Box 10864
Pittsburgh, Pennsylvania 15236
Attention: R.W. Buckman
D.R. Stoner
Librarian

Westinghouse Electric Corporation
Research & Development Center
Pittsburgh, Pennsylvania 15235
Attention: Librarian
R.T. Begley

Westinghouse Electric Corporation
Materials Manufacturing Division
RD #2, Box 25
Blairsville, Pennsylvania
Attention: Librarian